The Standard Model is complete, what's next

G. Aad

AIX MARSEILLE UNIVERSITÉ
ECOLE DOCTORALE 352
UMR 7346
CENTRE DE PHYSIQUE DES PARTICULES DE MARSEILLE

Habilitation à Diriger des Recherches

The Standard Model is complete, what's next

Georges AAD

Soutenue le 15/03/2024 devant le jury composé de:

Cristinel Diaconu	CPPM	Président
Freya Blekman	University of Hamburg	Rapporteure
Gustaaf Brooijmans	Columbia University	Rapporteur
Guillaume Unal	CERN	Rapporteur
Didier Contardo	IP2I	Examinateur
Mossadek Talby	Aix-Marseille University	Examinateur

Contents

Introduction

The Standard Model of particle physics, established in the second half of the twentieth century, is very successful in describing known particles and their interactions with an astonishing precision. At the beginning of the 20^{th} century, two breakthroughs were accomplished in fundamental physics: General Relativity and Quantum Mechanics suggested new visions of our physical world. After establishing the Quantum Mechanics, several developments, both theoretical and experimental, lead to the Standard Model of particle physics as it is known nowadays. This model gathers several pieces developed during the last 50 years: the Dirac [1] relativistic quantum equation and the prediction of anti-particles, the Fermi [2] theory of weak interactions, the Gross, Wilczek and Politzer [3, 4, 5] Quantum ChromoDynamics (QCD) with asymptotic freedom, the Gell-Mann, Zweig, Han and Nambu [6, 7, 8] coloured quark model, the Englert, Brout and Higgs [9, 10, 11] spontaneous symmetry breaking, the Glashow, Weinberg and Salam [12, 13, 14] electroweak theory including the Higgs mechanism and the electroweak symmetry breaking, the Cabibbo, Kobayashi, Maskawa [15, 16] matrix and the mixing of quarks leading to CP violation, and last but not least the Hooft and Veltman [17] regularisation and renormalisation of gauge fields.

The Standard Model successfully predicted a large number of new particles that were all discovered throughout different experiments over 50 years. Arguably the most important discoveries were the observation of neutral currents by the Gargamelle neutrino collaboration [18, 19] and the observation of the W [20, 21] and Z [22, 23] bosons by the UA1 and UA2 collaborations. The Standard Model had also an important success in the QCD sector. Establishing the presence of quarks took several years due to the confinement property of QCD that does not allow quarks to be observed in an isolated state. The first evidence of the internal proton structure [24, 25] by the MIT-SLAC collaboration paved the way to establishing the quarks model. The top quark, the heaviest known particle and the only quark that can be observed in an isolated state, was discovered by the CDF and D0 collaborations [26, 27], thus ending the race for quarks search. In 2012, the last particle of the Standard Model, the Higgs boson, was discovered by the ATLAS and CMS collaborations [28, 29]. Since then, the study of the Higgs boson properties and its interaction with other particles is one of the most active area in particle physics. The Higgs boson sealed the hunt for Standard Model particles after 50 years of active searches.

Despite its great successes, the Standard Model does not provide answers for several questions that arise both from theoretical arguments and experimental observations. One of the most important established experimental observation that is not described by the Standard Model is the presence of neutrino oscillations, which suggest that the neutrino particles have a non-zero mass. In addition, the Standard Model does not explain several cosmological and astrophysics observations such as the presence of dark matter, the matter anti-matter asymmetry, and the dark energy. On the theoretical side, one can argue that the Standard Model is not an elegant or even a satisfactory theory since it does not provide an explanation to its 19 free parameters and require fine tuning for the theory to

be valid at large energy scales[1]. Finally, the Standard Model does not include a quantum theory of gravity. For all these reasons, it is thought that new physics should exist leading to new particles and phenomena. New physics can be probed by direct discoveries of new particles or by measurements that deviate from the Standard Model expectations. This document focuses on Standard Model measurements including observations in the newly discovered Higgs sector. It ends with a technical chapter describing the upgrade of the liquid argon calorimeter of the ATLAS [30] experiment. This upgrade prepares the detector for further new physics searches and a more precise characterisation of the Higgs boson at the run 3 and run 4 of the LHC [31].

The ATLAS detector

The ATLAS detector at the LHC covers nearly the entire solid angle around the collision point. It consists of an inner tracking detector surrounded by a thin superconducting solenoid magnet producing a 2 T axial magnetic field, electromagnetic and hadronic calorimeters, and an external muon spectrometer (MS) incorporating three large toroid magnet assemblies.

ATLAS uses a right-handed coordinate system with its origin at the nominal interaction point (IP) in the center of the detector and the z-axis coinciding with the axis of the beam pipe. The x-axis points from the IP to the center of the LHC ring, and the y-axis points upward. Cylindrical coordinates (r,ϕ) are used in the transverse plane, ϕ being the azimuthal angle around the beam pipe. The pseudorapidity is defined in terms of the polar angle θ as $\eta = -\ln\tan(\theta/2)$. Unless stated otherwise, angular distances are measured in units of $\Delta R \equiv \sqrt{(\Delta\eta)^2 + (\Delta\phi)^2}$.

The inner detector (ID) consists of a high-granularity silicon pixel detector and a silicon microstrip tracker, together providing precision tracking in the pseudorapidity range $|\eta| < 2.5$, complemented by a straw-tube transition radiation tracker providing tracking and electron identification information for $|\eta| < 2.0$. The electromagnetic sampling calorimeter uses lead or copper as the absorber material and liquid argon (LAr) as the active medium, and is divided into barrel ($|\eta| < 1.475$), endcap ($1.375 < |\eta| < 3.2$) and forward ($3.1 < |\eta| < 4.9$) regions. Hadron calorimetry is also based on the sampling technique and covers $|\eta| < 4.9$, with either scintillator tiles or LAr as the active medium and with steel, copper or tungsten as the absorber material. The muon spectrometer measures the deflection of muons with $|\eta| < 2.7$ using multiple layers of high-precision tracking chambers located in a toroidal field. The field integral of the toroids ranges between 2.0 and 6.0 Tm across most of the detector. The muon spectrometer is also instrumented with separate trigger chambers covering $|\eta| < 2.4$. A two-level trigger system [32], using custom hardware followed by a software-based level, is used to reduce the trigger rate to an average of around one kHz for offline storage. An extensive software suite [33] is used in data simulation, in the reconstruction and analysis of real and simulated data, in detector operations, and in the trigger and data acquisition systems of the experiment.

LHC and ATLAS upgrades

The LHC schedule can be found in [34] and is summarised in figure 1. The LHC started to deliver proton-proton collisions in 2010 at a centre-of-mass energy of $\sqrt{s} = 7$ TeV and increased to $\sqrt{s} = 8$ TeV in the year 2012. This period constitutes the run 1 of the LHC. During run 1, the ATLAS experiment collected 5 fb^{-1} at $\sqrt{s} = 7$ TeV and 20 fb^{-1} at $\sqrt{s} = 8$ TeV. The first long shutdown (LS1) took place in 2013 to 2014 and allowed the LHC to reach a centre-of-mass energy of $\sqrt{s} =$

[1] Much larger than the electroweak scale.

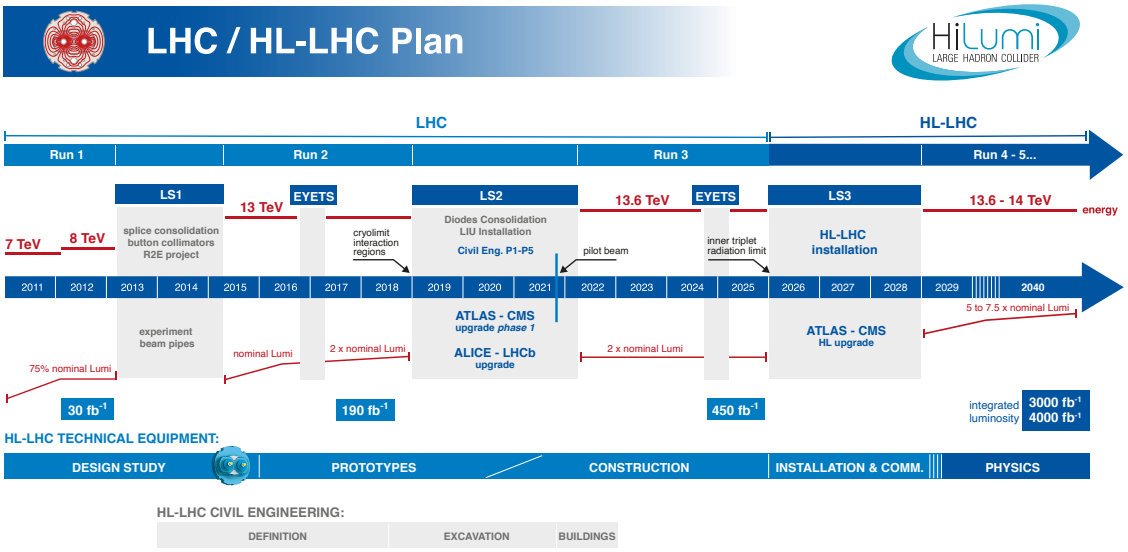

Figure 1: The LHC schedule as of January 2022 [34].

13 TeV. During LS1 a new innermost silicon pixel layer, the insertable B-layer (IBL) [35, 36], was added to the ATLAS detector. The LS1 was followed by the LHC run 2 (2015-2018) where the ATLAS experiment collected 140 fb^{-1} at $\sqrt{s} = 13$ TeV. The LHC managed to increase its luminosity by a factor 2 and its centre-of-mass energy to 13.6 TeV during the LS2 from 2019 to 2021. The so-called ATLAS Phase-I upgrade was achieved in the same period. It consisted of adding a new trigger path for the LAr calorimeter [37], upgrading the calorimeter trigger system [38], and replacing the muon system small wheels [39]. The LHC run 3 started in 2022 and will continue until 2025 followed by the LS3. During LS3 (2026-2028), the LHC will be upgraded to increase its instantaneous luminosity by a factor 5-7 with respect to the nominal luminosity. Thus, the high-luminosity LHC (HL-LHC) era will begin. The HL-LHC is expected to deliver 3000 fb^{-1} to each of the ATLAS and CMS [40] collaborations. During LS3, the ATLAS detector will undergo a major upgrade called the Phase-II upgrade. It consists of completely exchanging the inner tracker [41], improving the muon trigger system by the addition or replacement of some muon chambers [42], and replacing the full trigger and readout electronics for all sub-detectors [43, 44, 42, 45]. A new High-Granularity Timing Detector (HGTD) [46] will be also added to the ATLAS detector. The LAr calorimeter Phase-I and Phase-II upgrades are discussed in chapter 3.

Standard Model measurements at the LHC

The LHC is designed to be a discovery machine. The ATLAS and CMS detectors cover a wide energy range for the detection of a variety of particles. This allowed them to perform a plethora of measurements targeting Standard Model processes. Figure 2 shows a summary of fiducial cross-section measurements performed by the ATLAS collaboration during run 1 and run 2 of the LHC. The measurements extend over 14 orders of magnitude in cross-section values and target a variety of processes such as inelastic proton-proton collisions, jets production, top quark production, sin-

gle and multi bosons production, and Higgs boson production. The measured cross sections are compared with theoretical predictions when available. An impressive agreement between the measurements and the Standard Model predictions is found. The largest deviation is found in the WWW production cross section measurement at $\sqrt{s} = 13$ TeV [47], which is 2.6 standard deviations from the Standard Model prediction. All other values are within 2 standard deviations from the predictions. Figure 3 shows a selection of production cross section measurements as function of $\sqrt{s}$. An excellent agreement between the measurements and the predictions is found.

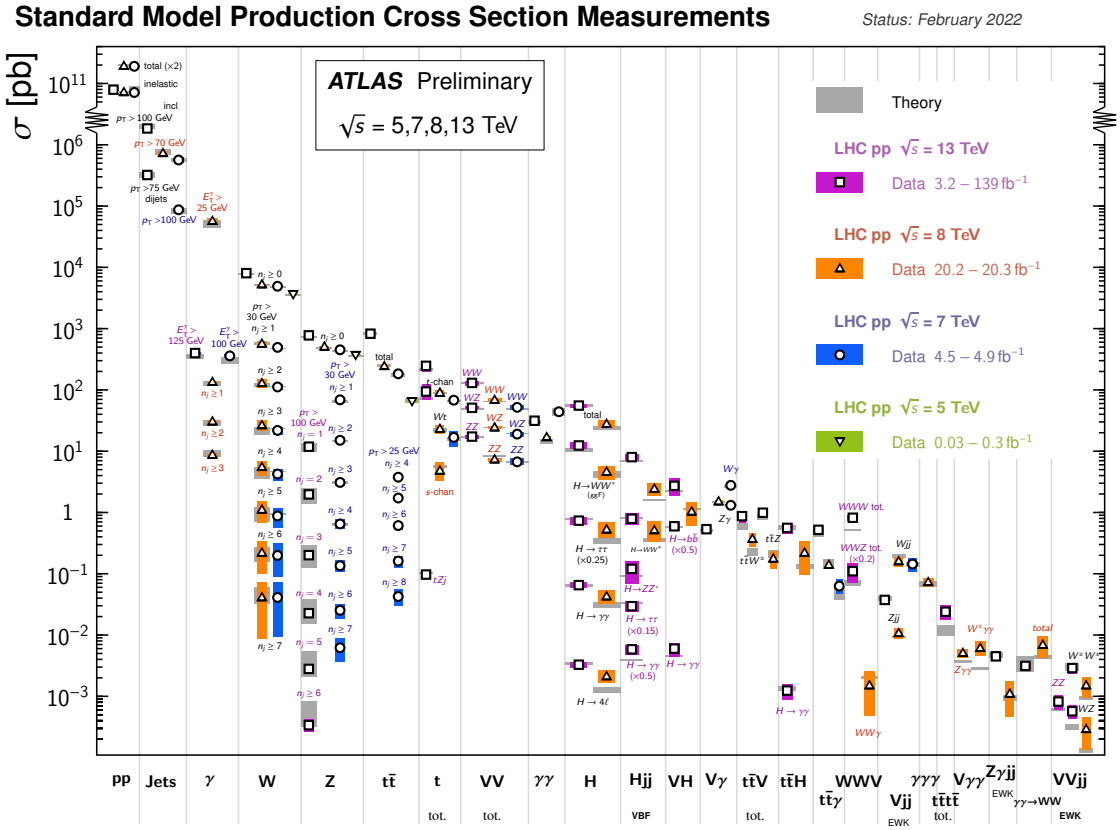

Figure 2: Summary of several Standard Model total and fiducial production cross-section measurements [48]. The measurements are corrected for branching fractions and compared to the corresponding theoretical predictions.

The determination of Parton Distribution Functions (PDFs) of the proton is of great importance at the LHC. The uncertainties on the PDFs affect all measurements and searches and are dominant for several analyses such as the measurement of the W boson mass [49, 50]. The s-quark PDF is particularly interesting and is not well constrained in PDFs derived without including LHC data. Flavor $SU(3)$ symmetry suggests that the three light sea-quarks distributions in the proton are equal. However, s-quarks may be suppressed due to their larger mass. ATLAS measured the s-quark PDF with respect to the d-quark sea PDF in [51, 52, 53, 54]. Chapter 1 presents the ATLAS measurement of the cross section of the production of a W boson with a single c-jet at $\sqrt{s} = 7$ TeV. The interpretation of this measurement in terms of the s-quark PDF is also shown.

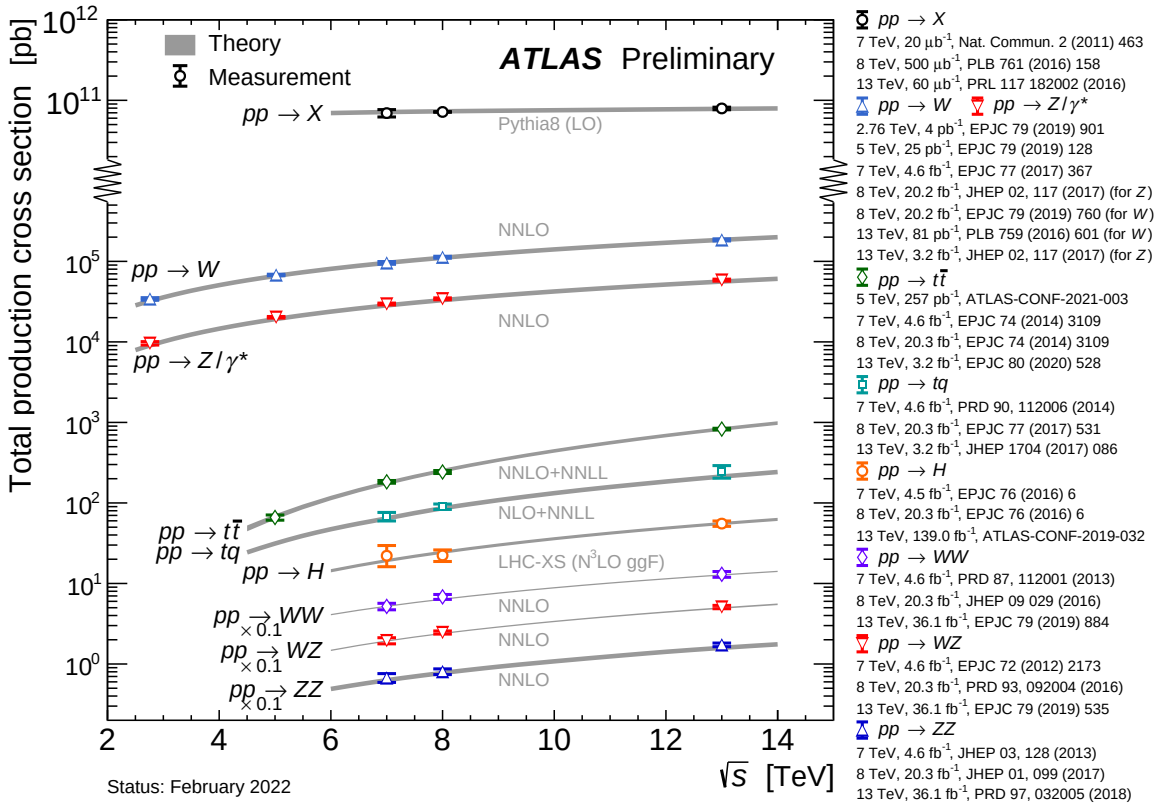

Figure 3: Summary of total production cross-section measurements by ATLAS presented as a function of centre-of-mass energy from 2.76 to 13 TeV for a few selected processes [48].

Higgs Boson Measurements at the LHC

The discovery of the Higgs boson by the ATLAS [28] and CMS [29] collaborations paved the way to precision measurements in the Higgs sector. The run 1 of the LHC allowed to establish the coupling of the Higgs bosons to massive vector bosons and photons. It also allowed to measure the production cross section times branching ratio for various Higgs boson production and decay modes. The measurements are expressed in terms of signal strength μ which measures the deviation from the Standard Model expected value:

$$\mu_i^f = \frac{\sigma_i.\mathrm{B}^f}{\sigma_{i,\mathrm{SM}}.\mathrm{B}^f_{\mathrm{SM}}} \tag{1}$$

where σ_i (i = ggF, VBF, WH, ZH, $t\bar{t}H$) and B^f (f = ZZ, WW, $\gamma\gamma$, $\tau\tau$, bb) are respectively the production cross sections and the decay branching fractions. The subscript "SM" denotes the Standard Model expected values. Figure 4 shows the μ values measured by ATLAS and CMS with the run 1 LHC data [55]. The ggF and VBF production cross sections are relatively well measured while the associated productions with vector bosons and top quarks present large uncertainties. All measurements are compatible with the Standard Model predictions within two standard deviations.

Figure 5 shows the Higgs couplings extracted from a global fit to ATLAS and CMS run 1 measurements. The couplings were measured in the so called κ-framework [56]. In this framework

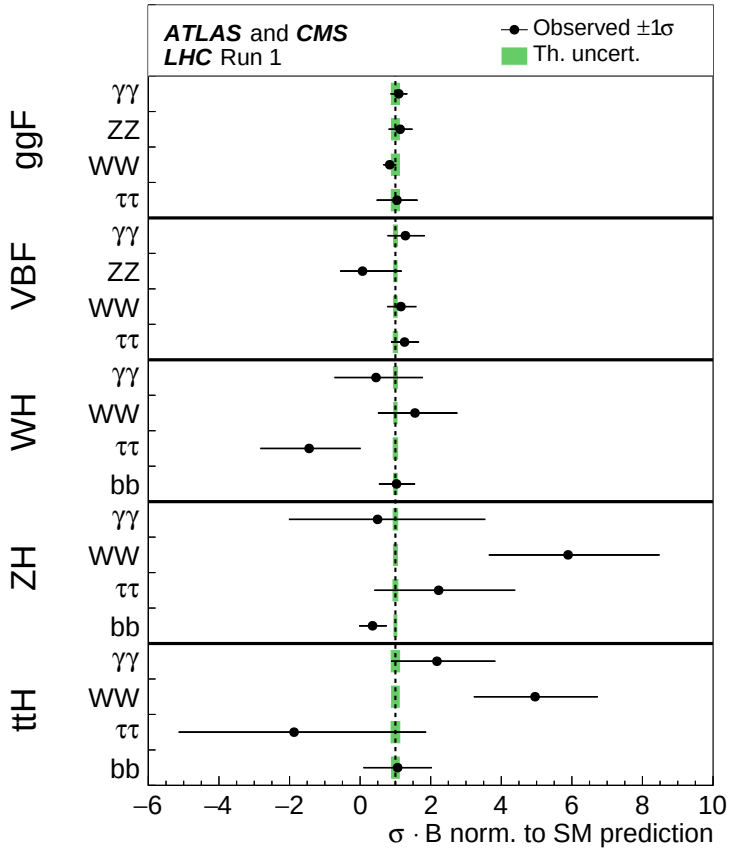

Figure 4: Best fit value of the production cross section times the branching ratio as obtained from a global fit combining ATLAS and CMS run 1 results [55]. The fit results are normalised to the Standard Model predictions. The horizontal bar on each point denotes the 68% confidence interval.

the coupling modifiers (κ_i) for a particle i are defined as:

$$\kappa_i = \sigma_i/\sigma_i^{\mathrm{SM}} = \Gamma_i/\Gamma_i^{\mathrm{SM}} \tag{2}$$

where σ_i is the production cross section through a particle i and Γ_i the partial decay width to a pair of particles i. The couplings to vector bosons and the effective coupling to photons are measured with a precision of about 10%, the effective coupling to gluons and the coupling to τ-leptons are measured with a precision of about 15%, while the couplings to third generation quarks is measured with a precision ranging from 25% to 40%. Beyond the Standard Model (BSM) contributions to the total Higgs boson width are determined to be less than 16%. All measured couplings are compatible with the Standard Model predictions.

The LHC run 2 allowed to establish the coupling of the Higgs boson to third generation fermions, which was one of the main target of ATLAS and CMS during run 2. Chapter 2 presents the search for the Higgs boson in the $t\bar{t}H(H \to b\bar{b})$ channel and its combination with other channels leading to the observation of $t\bar{t}H$ production and $H \to b\bar{b}$ decay by ATLAS. The analyses targeting different Higgs boson channels with full run 2 data are still ongoing and thus the final combination of ATLAS and CMS run 2 results is not yet available. However, an intermediate combination with partial ATLAS results is available in [57]. Figure 6 shows the signal strength for various Higgs

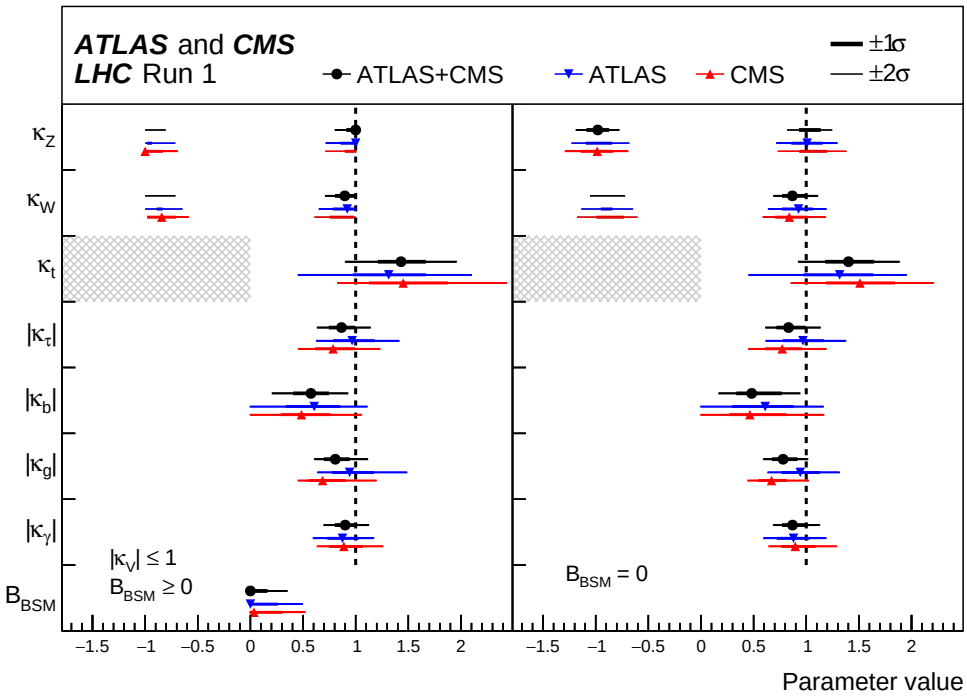

Figure 5: Higgs coupling strength modifiers (κ_i) per particle type with effective photon and gluon couplings measured with ATLAS and CMS run 1 data [55]. The horizontal bars on each point denote the 68% and 95% confidence intervals. The hatched areas show the non-allowed regions in the fit. The modifiers are shown in both cases where BSM particles contribute or not to the total Higgs boson width.

boson production and decay modes from ATLAS run 2 data. Additional channels are available due to the larger luminosity with respect to run 1 data. An excellent agreement with the Standard Model is observed. Figure 7 shows the coupling strength determined in the aforementioned combination. The uncertainties are divided by a factor 2 with respect to the ATLAS/CMS run 1 combination. In addition, the couplings to muons and $Z\gamma$ are added with uncertainties of the order of 30%. The contributions from invisible Higgs boson decay and decays to undetected particles, that can arise from BSM, are below 13% of the total width of the Higgs boson.

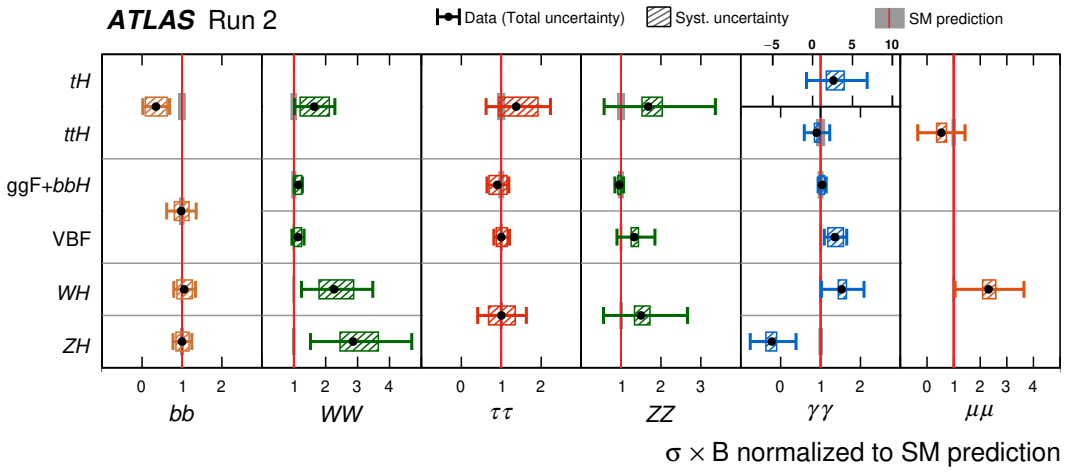

Figure 6: Best fit value of the production cross section times the branching ratio as obtained from a global fit combining ATLAS run 2 results [57]. The fit results are normalised to the Standard Model predictions. The horizontal bar on each point denotes the 68% confidence interval.

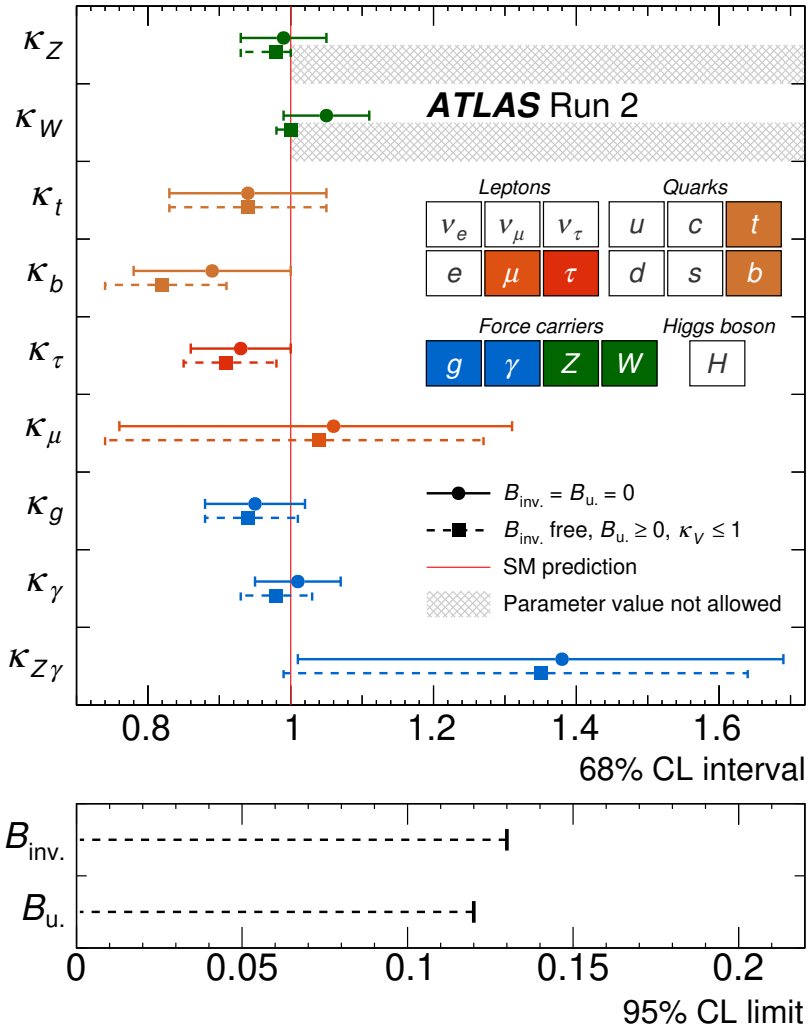

Figure 7: Higgs coupling strength modifiers per particle type with effective photon, $Z\gamma$ and gluon couplings measured with ATLAS run 2 data [57]. The horizontal bar on each point denotes the 68% confidence interval. The hatched areas show the non-allowed regions in the fit. The scenario where no contribution from the decay of the Higgs boson to invisible and undetected particles is allowed ($B_{inv.} = 0, B_u = 0$), is shown in solid lines and circle markers. The scenario with $B_{inv.}$ and B_u are allowed to contribute to the total Higgs boson decay width are shown in dashed lines and square markers. The lower panel shows the 95% CL upper limits on $B_{inv.}$ and B_u.

Chapter 1

Cross section measurement of the production of W bosons with a single c-jet

This chapter presents a cross section measurement of the production of a W boson in association with a single charm quark that is tagged by the presence of a jet of particles containing its semileptonic decay to a muon. The combination with the results from events where the charm quark is tagged by the presence of a charmed hadron reconstructed in the decay modes $D^+ \to K^-\pi^+\pi^+$ and $D^{*+} \to D^0\pi^+$ with $D^0 \to K^-\pi^+$, $D^0 \to K^-\pi^+\pi^0$ or $D^0 \to K^-\pi^+\pi^-\pi^+$, and their charge conjugates (referred to as the $WD^{(*)}$ analysis) is also presented. Finally an interpretation in terms of the strange quark parton density function in protons is discussed. This chapter is mostly based on an ATLAS paper [52] of which I was the co-editor.

1.1 Introduction

The production of a W boson in association with a single charm quark in proton–proton collisions is described at leading order (LO) in perturbative quantum chromodynamics (QCD) by the scattering of a gluon and a down-type quark (d, s, b). The relative contribution from each of the three families in the initial state is determined by the parton distribution functions (PDF) of the proton and by the quark-mixing matrix elements V_{cd}, V_{cs} and V_{cb}. In proton–proton collisions at a centre-of-mass energy of $\sqrt{s} = 7$ TeV, $gs \to W^-c$ and $g\bar{s} \to W^+\bar{c}$ production channels are dominant, while the reaction initiated by a d-quark contributes about 10% [58], being suppressed by the quark mixing matrix element V_{cd}. The contribution of processes that include b quarks is negligible. The next-to-leading-order (NLO) QCD terms [59] are dominated by one-loop corrections to the subprocess $gs \to Wc$ and the tree-level $2 \to 3$ processes $gg \to sWc$ and $qs \to qWc$. Processes with charm quarks in the initial state are not considered for this analysis as explained in section 1.7.3. Since the $gs \to Wc$ process and its higher-order corrections are dominant, the $pp \to WcX$ production is directly sensitive to the s-quark distribution function in the proton at momentum-transfer values on the order of the W-boson mass (m_W).

The s-quark PDF has been determined by neutrino–nucleon deep inelastic scattering (DIS) experiments [60, 61] at momentum transfer squared $Q^2 \sim 10\text{GeV}^2$ and momentum fraction $x \sim 0.1$. However, the interpretation of these data is sensitive to the modelling of c-quark fragmentation and nuclear corrections; some analyses [62, 63, 64] indicate that the s-quark sea is suppressed relative to the d-quark sea at all values of x while others [65] suggest that SU(3) symmetry is restored as

x decreases. A joint analysis of inclusive W and Z production data from ATLAS at $Q^2 \sim m_W^2$ and DIS data from HERA has bolstered the case for an SU(3)-symmetric sea at $x \sim 0.01$ [51]. The main result of that analysis was obtained under the assumption that the s- and $\bar{s}$-quark distributions are equal. However, fits to the neutrino DIS data from NuTeV [61, 62, 66] prefer a small asymmetry between the s and $\bar{s}$ sea.

The possibility of using $W+c$ events as probes of the strange-quark distribution function has been discussed for some time [67, 68]. While the cross section for this process was measured with a precision of 20–30% at the Tevatron [69, 70, 71], the large production rates available at the Large Hadron Collider (LHC) provide the first opportunity for a measurement with sufficient precision to constrain the s-quark PDF at $x \sim 0.01$. A measurement of the $W+c$ production cross section at the LHC was performed by CMS [72] and exploited to constrain the s-quark PDF in ref. [73].

This chapter presents a measurement of the production of a W boson in association with a single charm quark using 4.6 fb^{-1} of pp collision data at $\sqrt{s} = 7$ TeV collected with the ATLAS detector at the LHC in 2011. In events where a W boson decays to an electron or muon, the charm quark is tagged by the presence of a jet of particles containing its semileptonic decay to a muon (hereafter referred to as a soft muon). The results are combined with the $WD^{(*)}$ analysis [52].

The relative sign of the charges of the W boson and the soft muon is exploited to reduce the backgrounds substantially. In $W+c$ production, the final-state W boson is always accompanied by a charm quark with charge of opposite sign, that is $W^+ + \bar{c}$ or $W^- + c$. The soft muon have the same-sign charge as the charm quark and thus a charge opposite to the W boson and its corresponding decay lepton. Requiring the W boson and the soft muon to be of opposite charge therefore selects the $W+c$ signal with very high purity. Most backgrounds are evenly distributed between events with opposite-sign (OS) and same-sign (SS) charge. Therefore, an important strategy used in this analysis is to determine the $W+c$ yields by measuring the difference between the number of opposite-sign and same-sign charge events (OS–SS). Since the kinematics of pair-produced charm and anti-charm quarks are the same, the pair-produced quarks do not contribute to distributions formed from OS–SS events.

The integrated and differential cross sections as a function of the pseudorapidity of the lepton from the W-boson decay are measured for the fiducial region defined by lepton transverse momentum $p_{\mathrm{T}}^{\ell} > 20$ GeV and pseudorapidity $|\eta^{\ell}| < 2.5$, neutrino transverse momentum $p_{\mathrm{T}}^{\nu} > 25$ GeV and W-boson transverse mass $m_{\mathrm{T}}^{W} > 40$ GeV.[1] The fiducial region selection also requires that a soft muon be associated with a jet reconstructed in the calorimeter with a minimum transverse momentum $p_{\mathrm{T}} > 25$ GeV and pseudorapidity $|\eta| < 2.5$. The cross section is evaluated for the production of a W boson in association with a particle-level jet containing a weakly decaying charmed hadron with $p_{\mathrm{T}} > 5$ GeV and within a cone of $\Delta R = \sqrt{(\Delta\phi)^2 + (\Delta\eta)^2} = 0.3$ from the jet axis as described in section 1.5.1. In addition, the cross section is reported in a fiducial region where the above mentioned charmed hadron is required to decay semileptonically to a muon with $p_{\mathrm{T}}^{\mu} > 4$ GeV and pseudorapidity $|\eta^{\mu}| < 2.5$ with $\Delta R < 0.5$ from the jet axis.

The measurements are performed separately for events with a positively and a negatively charged W boson, and the ratio

$$R_c^{\pm} \equiv \sigma(W^+ + \bar{c})/\sigma(W^- + c)$$

is also measured. All measurements are compared to predictions of NLO QCD calculations obtained with various PDF sets and the sensitivity to the choice of PDFs is presented.

[1] m_{T}^{W} is defined as $m_{\mathrm{T}}^{W} = \sqrt{2 p_{\mathrm{T}}^{\ell} E_{\mathrm{T}}^{\mathrm{miss}} (1 - \cos\Delta\phi)}$ where $\Delta\phi$ is the azimuthal separation between the directions of the lepton and the missing momentum in the transverse plane.

1.2 Data and Monte Carlo samples

This analysis is based on data collected with the ATLAS detector in the year 2011 during periods with stable pp collisions at $\sqrt{s} = 7\,\text{TeV}$ in which all relevant detector components are fully operational. The resulting data sample corresponds to an integrated luminosity of 4.6 fb^{-1} with an uncertainty of 1.8% [74].

MC samples are used to compute efficiencies, to model kinematic distributions of signal and background processes and to interpret the results. The signal is defined to be the production of a W boson in association with a single charm quark. Background processes include the production of W+light jets (i.e. light-quark and gluon jets, hereafter referred to as W+light), $W + c\bar{c}$ and $W + b\bar{b}$, while the contribution from $W + b$ production is negligible. Z+jets (including γ^*+jets), top-quark pairs, single top quarks, dibosons and multijet events also contribute to the background.

W bosons produced in association with c-jets, b-jets and light jets are generated separately using ALPGEN 2.13 [75] interfaced to Herwig 6.520 [76] for the parton shower and hadronisation, as well as JIMMY 4.31 [77] for the underlying event. Exclusive samples with zero to four additional partons and an inclusive sample with five or more additional partons are used. Overlaps between different ALPGEN samples with heavy-flavour quarks originating from the matrix element and from the parton shower are removed. In addition, the MLM [78] matching scheme is applied to remove overlaps between events with the same parton multiplicity generated by the matrix element or the parton shower.

A dedicated sample generated with ALPGEN and PYTHIA [79] for the parton shower and hadronisation is used for the W boson plus c-jet signal process. In this sample, the fragmentation fractions are reweighted to those derived from the combination of measurements in e^+e^- and ep collisions [80], the momentum fraction of c-hadrons is reweighted to that given by Herwig++ 2.6.3 [81], the semileptonic branching ratios of c-hadrons are rescaled to the world average values [82] and the distribution of the momentum of outgoing muons in the c-hadron rest frame is reweighted to that provided by EvtGen [83].

Inclusive W production is generated using the POWHEG r1556 [84, 85, 86, 87] generator interfaced to PYTHIA for parton shower, hadronisation and underlying-event modelling. For systematic studies, samples generated using POWHEG or MC@NLO 4.01 [88], where the parton shower and hadronisation are modelled by Herwig and the underlying event by JIMMY, are used. The CT10 [65] PDF is used for the NLO matrix-element calculations, while showering is performed with the CTEQ6L1 PDF [89].

Background from Z+jets events is generated with ALPGEN interfaced to Herwig and JIMMY using the same configuration as for W+jets events. For the diboson backgrounds (WW, WZ and ZZ), MC samples generated with Herwig are used. The $t\bar{t}$ background is obtained from the MC@NLO generator with Herwig used for the parton shower and hadronisation, while single-top production is based on the ACER 3.7 [90] MC generator (interfaced to PYTHIA) in the t-channel, and MC@NLO in the s-channel and for associated production with a W boson. When PYTHIA or Herwig is used, TAUOLA [91] and PHOTOS [92] are employed to model the decay of τ-leptons and the radiation of photons, respectively.

The background processes are normalised to NNLO predictions for inclusive W, Z and $t\bar{t}$ production [93, 94] and to NLO predictions for the other processes [95, 96]. The properties of the multijet background events are determined using data-driven techniques.

Multiple pp collisions per bunch crossing (pileup) are modelled by overlaying minimum-bias events generated using PYTHIA with the hard process.

The MC events are passed through a detailed simulation of the ATLAS detector response [97] based on GEANT4 [98].

1.3 Object reconstruction and selection

Data used for this analysis are triggered either by a single-muon trigger with a requirement on the pseudorapidity of $|\eta^{\mu}| < 2.4$ and on the transverse momentum of $p_{\mathrm{T}}^{\mu} > 18\,\mathrm{GeV}$, or by a single-electron trigger with pseudorapidity coverage of $|\eta^{e}| < 2.47$ and a threshold for the transverse momentum p_{T}^{e} of 20 GeV or 22 GeV, depending on the data-taking period.

Events are required to have at least one vertex. The vertex with the highest sum of the squared transverse momenta of the associated tracks is selected as the primary vertex. Jets are reconstructed with the FastJet package [99] which uses the infrared- and collinear-safe anti-k_t algorithm [100] with radius parameter $R = 0.4$. The input from the calorimeter is based on three-dimensional topological clusters [101] and jet energies are calibrated using the EM+JES scheme [102]. The presence of neutrinos is inferred from the missing transverse momentum. The magnitude ($E_{\mathrm{T}}^{\mathrm{miss}}$) and azimuthal direction are measured from the vector sum of the transverse momenta of calibrated physics objects [103]. Low-p_{T} tracks are used to recover soft particles which are not measured in the calorimeters [104].

Exactly one lepton fulfilling the isolation requirements discussed below is allowed in each event. Events with additional isolated electrons or muons are vetoed to suppress background from Z and $t\bar{t}$ events. The selection applied to veto leptons is looser than the one used for signal leptons to ensure higher background rejection. Trigger and reconstruction scale factors are applied to the MC simulation so that the simulation efficiencies match those measured in data.

1.3.1 $W \to e\nu$

Electrons with transverse momentum $p_{\mathrm{T}}^{e} > 25\,\mathrm{GeV}$ and in the pseudorapidity range $|\eta^{e}| < 2.47$, excluding the calorimeter transition region $1.37 < |\eta| < 1.52$, are selected. Electrons are required to satisfy the "tight" identification criteria described in ref. [105] which are re-optimised for 2011 data-taking conditions. Calorimeter-based isolation requirement is applied to electrons: the sum of transverse energies in the calorimeter cells (including electromagnetic and hadronic sections, and excluding contributions from the electron itself) within a cone of radius $\Delta R = 0.3$ around the electron's direction is required to be less than 3 GeV. The electron must also be separated by $\Delta R > 0.5$ from any jet. A minimum $E_{\mathrm{T}}^{\mathrm{miss}}$ of 25 GeV and a minimum m_{T}^{W} of 40 GeV are required.

1.3.2 $W \to \mu\nu$

Muon candidates are formed from associated tracks in the ID and the MS that are combined using a χ^2-matching procedure [106, 107]. Muons are required to have $p_{\mathrm{T}}^{\mu} > 20\,\mathrm{GeV}$ and a pseudorapidity range $|\eta^{\mu}| < 2.4$. The set of ID hit requirements described in [108] together with an additional condition of at least one hit in the first pixel layer is applied to select high-quality tracks. A combination of track- and calorimeter-based isolation is applied to selected muon: $\Sigma_{\Delta R<0.3} p_{\mathrm{T}}^{\mathrm{track}}$ is required to be less than 2.5 GeV and $\Sigma_{\Delta R<0.2} E_{\mathrm{T}}^{\mathrm{cells}}$ to be less than 4 GeV. Additionally, muons must be separated by $\Delta R > 0.4$ from any jet with $p_{\mathrm{T}} > 25\,\mathrm{GeV}$. A lower $E_{\mathrm{T}}^{\mathrm{miss}}$ threshold of 20 GeV is applied. A stringent minimum m_{T}^{W} requirement of 60 GeV is imposed to improve the suppression of the multijet background.

1.3.3 Charm-jet selection

In addition to the event selection described above events are required to have either one or two jets with $p_{\mathrm{T}} > 25\,\mathrm{GeV}$ and $|\eta| < 2.5$. In order to remove jets reconstructed from energy deposits

from particles produced in pileup events, the p_{T} sum of tracks inside the jet and associated with the primary vertex divided by the p_{T} sum of all tracks inside the jet is required to be larger than 0.75.

Charm-quark production is studied by exploiting the semileptonic decays of charm quarks into muons. In this approach, a charm quark is identified by reconstructing the jet of particles produced by its hadronisation and finding an associated soft muon from its semileptonic decay. One and only one jet is required to contain a soft muon with $p_{\mathrm{T}} > 4\,\mathrm{GeV}$ and $|\eta| < 2.5$. A good match between the ID and MS tracks of the soft muon is required. The same set of ID hit requirements [108] that is used for muon candidates from W-boson decays is applied to soft muons in addition to two impact parameter requirements: $|d_0| < 3$ mm and $|z_0 \cdot \sin\theta| < 3$ mm. Exactly one muon is required to be associated with the jet within a cone of radius $\Delta R = 0.5$; the small fraction of events with jets containing more than one muon is discarded. The soft-muon tagging (SMT) efficiency and mistagging rate are measured in data [109]. The overall c-tagging efficiency is about 4%, due mainly to the low branching ratio of charmed hadrons to muons (approximately 10%). The light-quark mistagging efficiency is around 0.2% depending on the jet kinematics. Scale factors are applied to correct the MC simulation efficiencies to those measured in data. Efficiency scale factors are applied to b- and c-jets. Scale factors for the mistagging rates are applied to light jets. Two additional requirements, with minor impact on the signal, are applied in the muon channel to suppress the Z+jets and the Υ backgrounds. First, the c-jet candidate is required to have either a track multiplicity of at least three or an electromagnetic-to-total energy fraction of less than 0.8. Second, the event is discarded if the invariant mass of the soft muon and the muon from the decay of the W-boson candidate is close to either the Z-boson mass (i.e. 80–100 GeV) or the Υ mass (i.e. 8–11 GeV).

1.4 Event yields for Wc-jet final states

The single-charm yield for each W-boson charge is determined from the OS−SS yields. The analysis is performed on separate samples of events with exactly one and exactly two reconstructed jets as well as on the combined sample of events with one or two jets. The electron and muon decay channels of the W boson are analysed separately and subsequently combined.

1.4.1 Determination of OS–SS yields

Since most backgrounds are nearly OS/SS symmetric, the number of OS−SS events is a good estimator of the signal yield. Nonetheless, residual asymmetries in the backgrounds necessitate an additional subtraction. The signal yields are determined from:

$$N_{Wc\text{-jet}}^{\mathrm{OS-SS}} = N_{\mathrm{data}}^{\mathrm{OS-SS}} - \sum_{\mathrm{bkg}} A_{\mathrm{bkg}} \cdot N_{\mathrm{bkg}}^{\mathrm{OS+SS}}, \tag{1.1}$$

where $N_{\mathrm{bkg}}^{\mathrm{OS+SS}}$ is the sum of the number of background events in the OS ($N_{\mathrm{bkg}}^{\mathrm{OS}}$) and SS ($N_{\mathrm{bkg}}^{\mathrm{SS}}$) samples and the asymmetry A_{bkg} is defined as

$$A_{\mathrm{bkg}} = N_{\mathrm{bkg}}^{\mathrm{OS-SS}} / N_{\mathrm{bkg}}^{\mathrm{OS+SS}}. \tag{1.2}$$

Backgrounds to the Wc-jet candidate sample include the production of W+light, W plus heavy-flavour quark pairs ($c\bar{c}$, $b\bar{b}$), multijet events, Z and, to a lesser extent, single and pair-produced top quarks, and dibosons.

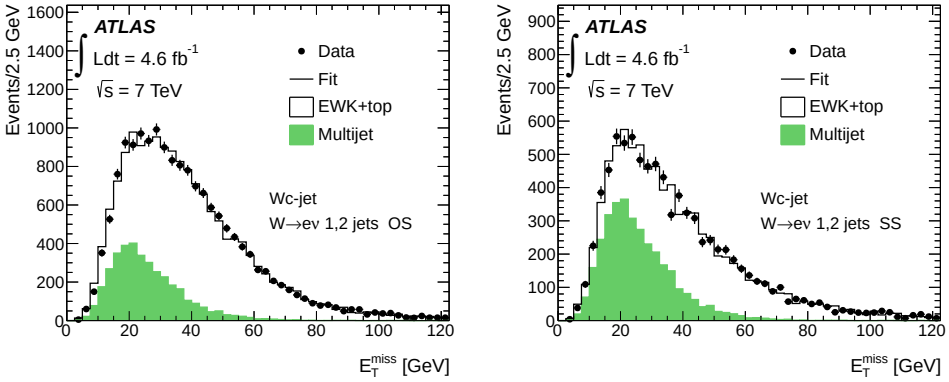

Figure 1.1: Results of the fits to the $E_{\mathrm{T}}^{\mathrm{miss}}$ distribution which are used to determine the multijet background in the electron channel, in the OS (left) and SS (right) samples of W+1,2 jets candidate events. The data are shown by filled markers and the fit result by the solid line. The multijet template, normalised according to the fit result, is shown by the filled histogram. The shape of the distribution for the electroweak and top-quark processes is obtained from simulation. Electroweak processes include W, Z and diboson processes.

The remaining background after the OS−SS subtraction is predominantly W+light and multijet events. W+light events present a relatively large OS/SS asymmetry which is due to the correlation of the charge of the W boson and the associated quark, and to the charge conservation among the fragmentation products of the quark. The background from multijet events is important due to the large production cross section. In the electron channel, multijet events pass the electron selection due to misidentified hadrons, converted photons and semileptonic heavy-flavour decays. In the muon channel, muons from heavy-flavour decays as well as decays in flight of pions and kaons are the dominant sources.

The background from W+light events and multijet events is estimated with data-driven methods. Z events, in which one of the muons from the Z decay radiates a photon that is mistakenly reconstructed as a jet, are a significant background source in the muon channel and are thus determined using a data-driven method. Smaller backgrounds from top-quark and diboson production, and the Z+jets background in the electron channel, are estimated from MC simulations. Backgrounds from $W+b\bar{b}$, $W+c\bar{c}$ are negligible since they are OS/SS symmetric.

1.4.1.1 Backgrounds and yield in the electron channel

The numbers of W+light and multijet background events are obtained from a constrained χ^2 fit to the number of events in the SS sample followed by a propagation to OS−SS using the equation

$$N_{\mathrm{bkg}}^{\mathrm{OS-SS}} = A_{\mathrm{bkg}} \cdot N_{\mathrm{bkg}}^{\mathrm{OS+SS}} = \frac{2 \cdot A_{\mathrm{bkg}}}{1 - A_{\mathrm{bkg}}} N_{\mathrm{bkg}}^{\mathrm{SS}}. \tag{1.3}$$

In the fit, the sum of the multijet and W+light backgrounds plus the remaining backgrounds and a small signal contribution is required to be equal to the total data count in the SS sample. The relative fractions of multijet and W+light events are allowed to vary in the fit, while all other backgrounds and the signal contribution are fixed to the values from simulation.

The OS/SS asymmetry of the multijet background, A_{multijet}, is found by performing a binned maximum-likelihood fit of templates to the $E_{\mathrm{T}}^{\mathrm{miss}}$ distribution in data separately for OS and SS

events. The fit is done in an expanded sample where the $E_{\mathrm{T}}^{\mathrm{miss}}$ selection requirement is removed. Two templates are used: one representing the multijet background and the other representing the contributions from all other sources. The template for the multijet sample is extracted from a data control sample selected by inverting the electron isolation and some of the electron identification requirements. Contamination in the control sample from W/Z and top-quark events is estimated from simulation and subtracted. The template representing all other processes, including the signal, W/Z, diboson and top-quark production, is obtained from MC simulation and built separately for OS and SS samples. Figure 1.1 shows the results for the OS and SS W+1,2 jets samples. A_{multijet} is computed using the fit results in the signal region ($E_{\mathrm{T}}^{\mathrm{miss}} > 25\,\mathrm{GeV}$) and is found to be consistent with zero within uncertainties. The uncertainties are dominated by the statistical component. The systematic uncertainties are estimated by varying the fit range and trying alternative multijet and other background templates. These uncertainties are found to be small.

The OS/SS asymmetry of the W+light background, $A_{W+\mathrm{light}}$, is obtained from MC simulation and corrected using the asymmetry measured in a data control region following the relation:

$$A_{W+\mathrm{light}} = A_{W+\mathrm{light}}^{\mathrm{MC}} \frac{A_{W+\mathrm{light}}^{\mathrm{data,tracks}}}{A_{W+\mathrm{light}}^{\mathrm{MC,tracks}}}. \tag{1.4}$$

$A_{W+\mathrm{light}}^{\mathrm{MC}}$ is the OS/SS asymmetry in the MC simulation for the signal region and $A_{W+\mathrm{light}}^{\mathrm{MC,tracks}}$ ($A_{W+\mathrm{light}}^{\mathrm{data,tracks}}$) is the OS/SS asymmetry in MC (data) events estimated using the charges of the W boson and a generic track that passes the soft-muon kinematic requirements. $A_{W+\mathrm{light}}^{\mathrm{MC,tracks}}$ and $A_{W+\mathrm{light}}^{\mathrm{data,tracks}}$ are computed from an expanded sample selected with no soft-muon requirements (called the pretag sample). $A_{W+\mathrm{light}}$ is found to be approximately 10%. The uncertainty on $A_{W+\mathrm{light}}$ is dominated by the statistical uncertainty on $A_{W+\mathrm{light}}^{\mathrm{MC}}$. The sub-leading systematic uncertainty contains contributions from uncertainties on the background contamination in the pretag sample and the modelling of the track properties.

The estimated numbers of background events are shown in table 1.1. The total number of OS(SS) events in the data SMT samples of W+1 jet and W+2 jets is 7436(3112) and 4187(2593), respectively. The corresponding number of OS−SS events in data is 4320±100 for the W+1 jet and 1590±80 for the W+2 jets sample.

$N^{\mathrm{OS-SS}}$ $(W \to e\nu)$	$W+1$ jet	$W+2$ jets	$W+1,2$ jets
W+light	240±100	100±50	330±130
Multijet	130±140	0±100	160±170
$t\bar{t}$	13±5	79±14	92±16
Single top	62±10	78±12	140±20
Diboson	35±6	35±5	70±9
Z+jets	8±12	15±10	23±15
Total background	490±160	300±120	820±200

Table 1.1: Estimated background in OS−SS events in the W+1 jet, W+2 jets and W+1,2 jets samples for the electron channel. The uncertainties include statistical and systematic contributions. The correlations between the uncertainties for the different background estimates stemming from the constraint in the SS sample is taken into account when computing the total background uncertainties. For backgrounds estimated with data-driven methods the yields in the W+1 jets, W+2 jets, and W+1,2 jets sample are estimated independently.

Figure 1.2 shows the p_{T} distribution of the SMT jet and the soft muon in OS−SS events in the

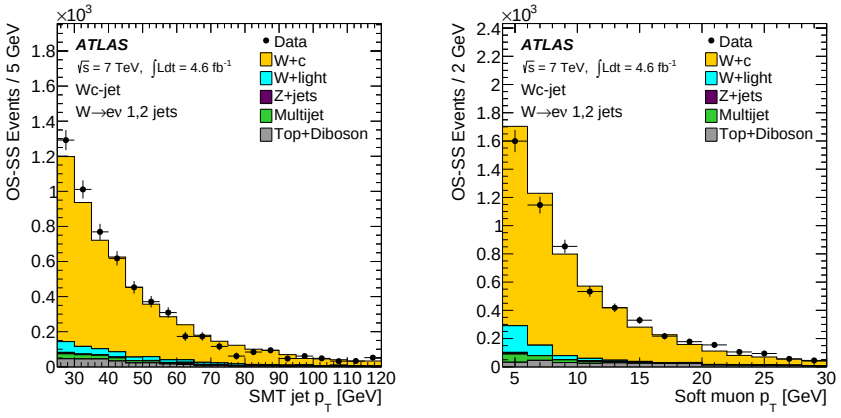

Figure 1.2: Distribution of the SMT jet p_{T} (left) and the soft-muon p_{T} (right) in OS−SS events of the W+1,2 jets sample for the electron channel. The normalisation of the W+light background and the shape and normalisation of the multijet background are obtained with data-driven methods. All other backgrounds are estimated with MC simulations and normalised to their theoretical cross sections. The signal contribution is normalised to the measured yields.

W+1,2 jets sample for the electron channel. The signal contribution is normalised to the measured yields and the background contributions are normalised to the values listed in table 1.1. The MC simulation is in satisfactory agreement with data.

In addition to the inclusive samples, yields and cross sections are measured separately for W^+ and W^- and in 11 bins of $|\eta^\ell|$. The multijet background $|\eta^\ell|$-shape is derived from individual fits to the $E_{\mathrm{T}}^{\mathrm{miss}}$ distribution and normalised to the inclusive total. The remaining backgrounds are taken from simulation.

1.4.1.2 Backgrounds and yield in the muon channel

The multijet background in the muon channel is substantially different from that in the electron channel since it is dominated by heavy-flavour semileptonic decays. The estimation technique is adapted to take this into account. The multijet background in OS+SS events is determined by the equation

$$N_{\mathrm{multijet}}^{\mathrm{OS+SS}} = N_{\mathrm{multijet}}^{\mathrm{pretag}} \cdot R_{\mathrm{multijet}}^{\mathrm{SMT}}, \tag{1.5}$$

where $N_{\mathrm{multijet}}^{\mathrm{pretag}}$ is the multijet event yield in the pretag sample and $R_{\mathrm{multijet}}^{\mathrm{SMT}}$ is the soft-muon tagging rate for events in the multijet sample.

The evaluation of $N_{\mathrm{multijet}}^{\mathrm{pretag}}$ uses a data-driven technique known as the Matrix Method [110]. An expanded sample enriched in multijet events is obtained by applying all selection cuts to the data except for the muon isolation requirements. The efficiencies of the isolation requirements for multijet events and prompt isolated muons are needed to relate the expanded sample to the signal sample. The isolation efficiency for prompt muons is measured in an independent sample of $Z \to \mu\mu$ events. The efficiency in multijet events is measured both in a control sample with inverted missing transverse momentum and W-boson transverse mass requirements, and through a fit to the muon d_0 significance; it is parameterised as a function of the muon and jet kinematics. The average of the results obtained with the two measurements is taken as the final estimate and half the difference is used as the systematic uncertainty.

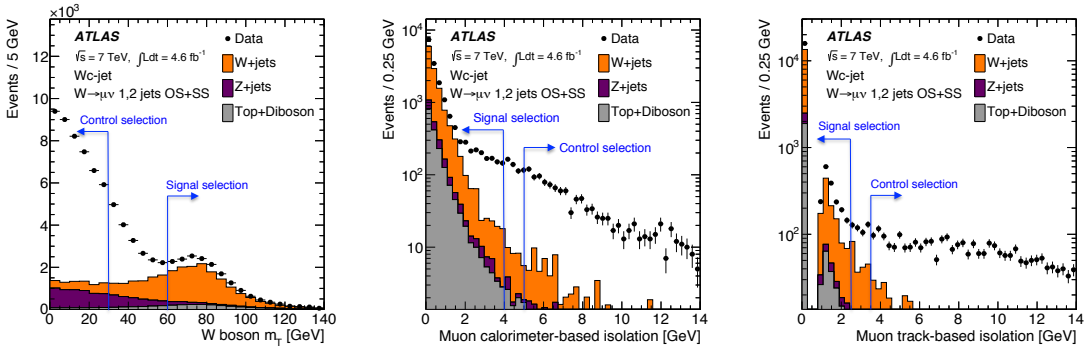

Figure 1.3: Distribution of the W-boson transverse mass (left), muon calorimeter-based isolation (centre) and muon track-based isolation (right) in data and the expectation from W/Z+jets, top-quark and diboson events. Events with low transverse mass and large values of isolation variables are predominantly multijet events. W/Z+jets refers to the production of W/Z bosons in association with light, c or b jets.

$R^{\mathrm{SMT}}_{\mathrm{multijet}}$ and A_{multijet} are independently determined in two control regions enriched in multijet background. The samples are selected by inverting either the muon isolation requirements or the W-boson transverse mass requirement. The distributions of events as a function of the muon isolation variables and the W-boson transverse mass are shown in figure 1.3. The amount of contamination from W/Z+jets events in the multijet control regions is estimated from MC simulation. The contamination from top-quark and diboson production is negligible. The value of $R^{\mathrm{SMT}}_{\mathrm{multijet}}$ is determined by measuring the soft-muon tagging rate as a function of the muon isolation in the multijet control regions and extrapolating it to the signal region assuming a linear dependence. Uncertainties from the W/Z+jets contamination level and from the extrapolation procedure are taken into account. The value of A_{multijet} is deduced from the average of the two control regions and is approximately 20%.

The W+light background in OS+SS events is estimated according to the following equation:

$$N^{\mathrm{OS+SS}}_{W+\mathrm{light}} = N^{\mathrm{pretag}}_{W+\mathrm{jets}} \cdot f_{\mathrm{light}} \cdot R^{\mathrm{SMT}}_{W+\mathrm{light}}, \tag{1.6}$$

where $N^{\mathrm{pretag}}_{W+\mathrm{jets}}$ is the yield of W+jets events in the pretag sample, f_{light} is the fraction of events in which the W boson is produced in association with a light jet and $R^{\mathrm{SMT}}_{W+\mathrm{light}}$ is the soft-muon tagging rate in W+light events. All the terms of equation (1.6) are derived using data-driven methods.

$N^{\mathrm{pretag}}_{W+\mathrm{jets}}$ is calculated as the difference between the number of selected data events and the sum of all other expected background contributions, namely multijet, Z+jets, top-quark, and diboson production in the pretag sample. The multijet background is estimated using the Matrix Method as explained above while all other backgrounds are taken from simulation. The fraction f_{light} is obtained through an analysis of the tagging rate of a lifetime-based tagger in the pretag sample as done in ref. [111]. $R^{\mathrm{SMT}}_{W+\mathrm{light}}$ is determined using a W+light MC simulation corrected by a data-derived scale factor for the soft-muon mistag rate [109]. The asymmetry $A_{W+\mathrm{light}}$ is obtained using equation (1.4), as done in the electron channel.

The Z+jets background is estimated by using a data control sample to normalise the MC simulation. The control sample is defined by requiring the invariant mass of the soft muon and the muon from the decay of the W-boson candidate to be between 80 GeV and 100 GeV. The normalisation is carried out in OS−SS events, which has the advantage of minimising contributions from non-Z events. The Z+jets yield in the control region is estimated from data by subtracting the expected

$N^{\mathrm{OS-SS}}(W \to \mu\nu)$	$W+1$ jet	$W+2$ jets	$W+1,2$ jets
W+light	220±80	40±40	250±90
Multijet	71±27	52±20	120±40
$t\bar{t}$	24±21	129±19	154±21
Single top	58±18	82±21	140±23
Diboson	37±10	39±13	76±20
Z+jets	237±22	207±16	445±34
Total background	650±90	550±60	1190±110

Table 1.2: Estimated background in OS−SS events in the W+1 jet, W+2 jets and W+1,2 jets samples for the muon channel. Uncertainties include statistical and systematic contributions.

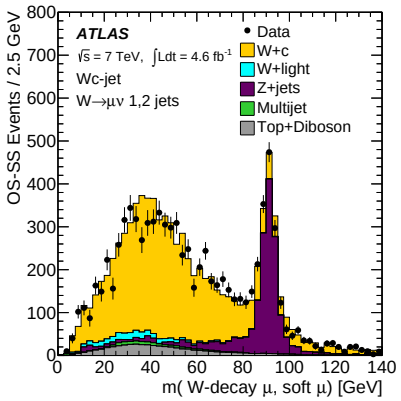

Figure 1.4: Invariant mass constructed using the four-momenta of the soft muon and the muon from the decay of the W-boson candidate.

contamination of $W+c$ signal, W+light and diboson events (the latter two account for less than 1% of the events). The contamination of the control sample by $W+c$ events is estimated initially through MC simulation and then refined by iteratively adjusting the $W+c$, Z+jets and W+jets normalisations to match the data. A normalisation factor for Z+jets of 1.06 ± 0.06 is derived. The invariant mass of the lepton from the decay of the W-boson candidate and the soft muon is shown in figure 1.4 for W+1,2 jets data passing all event selection requirements except for the veto around the invariant masses of the Z boson and the Υ meson. The expected contributions of all processes, normalised as described above, are also shown. The predicted distributions provide a good description of the data.

The total number of OS(SS) events in the data samples of W+1 jet and W+2 jets is 7736(2775) and 4376(2479), respectively. The corresponding number of OS−SS events in data is 4960±100 for the W+1 jet and 1900±80 for the W+2 jets sample. The expected backgrounds are summarised in table 1.2.

Figure 1.5 shows the distribution of the SMT jet p_{T} and the soft-muon p_{T} in OS−SS events in the W+1,2 jets sample for the muon channel. The signal contribution is normalised to the measured yields and the background contributions are normalised to the values listed in table 1.2. The MC simulation is in fair agreement with data.

In addition to the inclusive samples, yields and cross sections are measured in 11 bins of $|\eta^{\ell}|$,

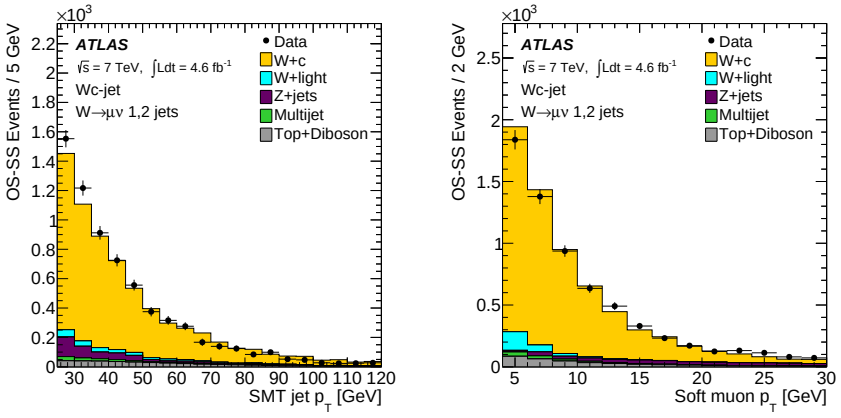

Figure 1.5: Distribution of the SMT jet p_{T} (left) and soft-muon p_{T} (right) in OS−SS events of the W+1,2 jets sample for the muon channel. The normalisations of the W+light and Z+jets backgrounds and the shape and normalisation of the multijet background are obtained with data-driven methods. All other backgrounds are estimated with MC simulations and normalised to their theoretical cross sections. The signal contribution is normalised to the measured yields.

separately for W^+ and W^-, as is done for the electron channel except that the $|\eta^{\ell}|$ distribution of the multijet background is derived from the inverted isolation and low transverse mass control regions.

1.5 Cross-section determination

1.5.1 Definition of the fiducial phase space

The fiducial cross section $\sigma_{\mathrm{fid}}^{\mathrm{OS-SS}}(Wc\text{-jet})$ measure the cross sections times the branching ratio $W \to \ell\nu$ and are determined in a fiducial region defined in MC simulation in terms of the W-boson kinematics as follows:

- $p_{\mathrm{T}}^{\ell} > 20\,\mathrm{GeV}$ and $|\eta^{\ell}| < 2.5$,
- $p_{\mathrm{T}}^{\nu} > 25\,\mathrm{GeV}$,
- $m_{\mathrm{T}}^{W} > 40\,\mathrm{GeV}$,

where ℓ and ν are the charged lepton and the neutrino from the decay $W \to \ell\nu$. The leptons are defined before QED final-state radiation. Particle-level jets are constructed in simulation from stable particles, including muons and neutrinos, using the anti-k_t algorithm with a radius parameter of 0.4. The lepton, all photons within a cone of $\Delta R = 0.1$ around it, and the neutrino originating from the W decay are not used to construct the jets. Particle-level jets are required to pass a $p_{\mathrm{T}}^{\mathrm{jet}} > 25\,\mathrm{GeV}$ and $|\eta^{\mathrm{jet}}| < 2.5$ selection. The particle-level c-jet is defined as the one containing a weakly decaying c-hadron with $p_{\mathrm{T}} > 5\,\mathrm{GeV}$, within $\Delta R < 0.3$. Jets containing c-hadrons originating from b-hadron decays are not counted as c-jets. The signal yield in the fiducial region is defined as the number of events where the c-hadron originates from a c-quark with charge sign opposite to the charge of the W boson, minus the number of events where the c-quark and W boson have the same charge sign.

1.5.2 Cross-section determination

The production cross sections in the fiducial region, σ_{fid}, are calculated using the equation:

$$\sigma_{\text{fid}} = \frac{N - B}{C \cdot \int \text{Ldt}}, \tag{1.7}$$

where N is the number of candidate events observed in data, B is the number of background events and $\int \text{Ldt}$ is the integrated luminosity of the dataset. The correction factor C is determined from MC simulation and accounts for detector efficiency, acceptance and resolution effects.

The ratio between $W^+ + \bar{c}$ and $W^- + c$ production, $R_c^{\pm}$, is computed according to:

$$R_c^{\pm} = \frac{R_{\text{data}}^{\pm}}{C^+/C^-}, \tag{1.8}$$

where $R_{\text{data}}^{\pm}$ is the uncorrected ratio of signal yields in the data, and $C^+(C^-)$ is the correction factor defined in equation (1.7) and calculated separately for $W^+ + \bar{c}$ and $W^- + c$ events, respectively.

The cross sections $\sigma_{\text{fid}}^{\text{OS}-\text{SS}}(Wc\text{-jet})$ are determined by applying equation (1.7) with the correction factors, C, obtained from the ALPGEN+PYTHIA MC simulations and corrected for charm fragmentation and decay as described in section 1.2. The cross sections are evaluated separately in the exclusive 1-jet and 2-jet bins and extrapolated to the fiducial region with one c-jet and any number of additional jets. This constitutes a small extrapolation of the order of 5% and the related systematic uncertainties are discussed in section 1.6. The acceptance times the signal selection efficiency is about 2% owing to the small semileptonic branching ratio.

Differential cross sections are determined in intervals of $|\eta^{\ell}|$ from the same procedure used to determine the total fiducial cross section, but with yields and acceptance corrections determined separately for each $|\eta^{\ell}|$ bin. Since the resolution of $|\eta^{\ell}|$ is much higher than the bin widths chosen, simple bin-by-bin corrections are applied.

In addition, the cross section $\sigma_{\text{fid}}^{\text{OS}-\text{SS}}(Wc\text{-jet}(\text{c} \to \mu))$ is evaluated for a fiducial volume defined in terms of the kinematics of the muon from the c-hadron decay in order to minimise the extrapolation uncertainty. The definition of a particle-level c-jet in section 1.5.1 is extended to require exactly one muon with $p_{\text{T}} > 4\,\text{GeV}$ and $|\eta| < 2.5$ within $\Delta R < 0.5$ of the jet axis and with charge opposite to the charge of the W boson. Muons from decays in flight are explicitly excluded. With this definition, the acceptance times the signal selection efficiency is 35% in the electron channel and 36% in the muon channel.

1.6 Systematic uncertainties

Systematic uncertainties arise from the W reconstruction, the charm tagging, the yield determination and the procedures used to correct for detector effects. The uncertainties on the background yields determination are discussed in section and 1.4. The other systematic uncertainties considered in this analysis are discussed below. The systematic uncertainties for the cross-section measurements are summarised in table 1.3 for $\sigma_{\text{fid}}^{\text{OS}-\text{SS}}(Wc\text{-jet})$. Most of the systematic uncertainties either cancel in the measurement of the ratio $R_c^{\pm}$ or are significantly reduced. The remaining systematic uncertainties are shown in table 1.4 for $\sigma_{\text{fid}}^{\text{OS}-\text{SS}}(W^+\bar{c}\text{-jet})/\sigma_{\text{fid}}^{\text{OS}-\text{SS}}(W^-c\text{-jet})$.

1.6.1 Object reconstruction and selection

The trigger and reconstruction efficiencies for electrons and muons are varied in the simulation within the range of their uncertainties as determined from data, and the Wc-jet cross sections are recalculated. A similar procedure is used to assess the uncertainty due to the lepton momentum scale

Relative systematic uncertainty in %	$W(e\nu)c$-jet	$W(\mu\nu)c$-jet
Lepton trigger and reconstruction*	0.7	0.8
Lepton momentum scale and resolution*	0.5	0.6
Lepton charge misidentification	0.2	-
Jet energy resolution*	0.1	0.1
Jet energy scale	2.4	2.1
$E_{\mathrm{T}}^{\mathrm{miss}}$ reconstruction*	0.8	0.3
Background yields	4.0	1.9
Soft-muon tagging	1.4	1.4
c-quark fragmentation	2.0	1.6
c-hadron decays	2.8	3.0
Signal modelling	0.9	0.2
Statistical uncertainty on response	1.4	1.4
Integrated luminosity*	1.8	1.8
Total	6.5	5.3

Table 1.3: Summary of the systematic uncertainties on the $\sigma_{\mathrm{fid}}^{\mathrm{OS-SS}}(Wc\text{-jet})$ measurement. The uncertainties are given in percent of the measured cross section. Entries marked with an asterisk are correlated between the Wc-jet and the $WD^{(*)}$ measurements. These correlations are taken into account in the combination presented in section 1.7.

and resolution. Lepton charge misidentification effects are also considered. The charge misidentification rates for electrons and muons are given in ref. [105, 30] and are significant only for the electron channel.

The main sources of uncertainty for jets are due to the jet energy scale (JES) and the jet energy resolution (JER). The impact on the cross-section measurements is evaluated by varying each of these in the simulation within their respective uncertainties as determined from data. The JES uncertainty ranges from less than 1% to about 7%, depending on jet p_{T} and η [112], with an additional 2% assigned to charm jets. Together, the JES and JER uncertainties contribute at the few percent level to the Wc-jet cross-section measurement.

Uncertainties on the lepton and jet momentum scale and resolution are propagated to the $E_{\mathrm{T}}^{\mathrm{miss}}$ reconstruction. Additional uncertainties on the $E_{\mathrm{T}}^{\mathrm{miss}}$ from soft jets (those with $7\,\mathrm{GeV} < p_{\mathrm{T}} < 20\,\mathrm{GeV}$) and calorimeter cells not associated with any reconstructed objects are accounted for separately.

The soft-muon tagging efficiency and mistag rates are varied in the simulation within the range allowed by the tagging efficiency ($\leq 1\%$) and mistag (15%) calibrations. The soft-muon reconstruction efficiency is varied in the simulation within the calibration uncertainty ($\simeq 1\%$) and is the dominant contribution to the SMT uncertainties. The uncertainty on the integrated luminosity is 1.8% [74].

1.6.2 c-quark fragmentation

The correction factor for detector effects depends on the modelling of the signal kinematics and its accuracy. In particular, the c-quark fragmentation and c-hadron decay models affect the simulated soft-muon p_{T} spectrum and the number of c-hadrons decaying to muons. In this analysis, the quark fragmentation is simulated with PYTHIA and then corrected for discrepancies in the type and relative population of c-hadrons resulting from the charm fragmentation and the fraction of the c-

Relative systematic uncertainty in %	$W(e\nu)c$-jet	$W(\mu\nu)c$-jet
Lepton trigger and reconstruction	<0.1	<0.1
Lepton momentum scale and resolution	0.2	0.6
Lepton charge misidentification	<0.1	-
Jet energy resolution	0.1	0.1
Jet energy scale	0.2	0.6
$E_{\mathrm{T}}^{\mathrm{miss}}$ reconstruction	0.3	0.3
Background yields	1.4	1.0
Soft-muon tagging	0.2	<0.1
Signal modelling	1.4	1.4
Statistical uncertainty on response	0.5	0.5
Total	2.1	2.0

Table 1.4: Summary of the significant systematic uncertainties on the measurement of the ratio $\sigma_{\mathrm{fid}}^{\mathrm{OS-SS}}(W^+\bar{c}\text{-jet})/\sigma_{\mathrm{fid}}^{\mathrm{OS-SS}}(W^-c\text{-jet})$. The uncertainties are given in percent.

quark energy carried by the c-hadrons. To improve on the PYTHIA modelling, the fragmentation fractions in PYTHIA are reweighted to those derived from the combination of measurements in e^+e^- and ep collisions [80] and the respective uncertainties are taken into account. The modelling of the momentum fraction of c-hadrons ($p_{\mathrm{T}}^{c-\mathrm{hadron}}/p_{\mathrm{T}}^{c-\mathrm{jet}}$) in PYTHIA is reweighted to the fraction given by Herwig++. The modelling of the fragmentation function in Herwig++ is validated by comparing the simulation to e^+e^- data as discussed in section 1.7.3. Based on these studies, a systematic uncertainty of 2% is assigned to the mean value of the fraction of the charm-quark momentum carried by the charmed hadron.

1.6.3 c-hadron decays

Two observables are used to represent the modelling of the decay of c-hadrons inside jets: the branching ratios of c-hadron semileptonic decays to muons, and the momentum of the muon (p^*) in the rest frame of the c-hadron. The latter is important because of the minimum p_{T} requirement of 4 GeV on the soft muon. The semileptonic branching ratios of c-hadrons used in PYTHIA are rescaled to the world average values [82] and the respective uncertainties are taken into account. The distribution of p^* from PYTHIA is reweighted to correspond to the one given by EvtGen and the difference between the two is considered as a systematic uncertainty.

1.6.4 Signal modelling

The impact on the signal acceptance terms stemming from uncertainties on the simulated jet multiplicity is estimated by varying the amount of initial- and final-state radiation in the PYTHIA parton-shower parameterisation. Additionally, the ratio of one-jet events to two-jet events in simulation is reweighted to the ratio measured in data and the acceptance is recomputed. The difference between the derived cross sections is less than 1% and is taken as a systematic uncertainty in the jet multiplicity modelling. Additional uncertainties on the non-perturbative physics modelling (e.g. underlying event, parton shower, color flow) are evaluated by recomputing the acceptance based on a simulation of the Wc-jet signal by ALPGEN + Herwig in which the Herwig charm fragmentation and decay are corrected using the procedure described previously for correcting PYTHIA. The difference between the nominal and the recomputed acceptances is less than 1% and is used as the

systematic uncertainty estimate.

The kinematics of the generated events used to calculate the acceptance is influenced by the PDF set used for the event generation. Thus the choice of PDF set affects the result. To evaluate the magnitude of the effect, the acceptance is recomputed after reweighting the simulated signal sample with four different PDF sets (MSTW2008, NNPDF2.3, HERAPDF1.5 and ATLAS-epWZ12 [51]) using LHAPDF [113]. The maximum difference between the acceptances derived with a single PDF eigenvector set or the different PDF central values is taken as the systematic uncertainty. Finally, the uncertainty on the correction factors due to the limited simulated signal sample size is 1.4%.

1.7 Results and comparison to theoretical predictions

The cross sections as function of the number of jets and the Wc-jet($c \to \mu$) cross section are measured in the Wc-jet analysis and the corresponding results are shown in section 1.7.1. The $WD^{(*)}$ analysis does not require jets nor the decay of c-hadrons to muons and thus no combination for these measurements is carried out. The total fiducial cross section and the cross section as function of the lepton pseudorapidity are combined between the Wc-jet and the $WD^{(*)}$ analysis and the corresponding results are shown in section 1.7.2.

1.7.1 Cross sections $\sigma_{\text{fid}}^{\text{OS}-\text{SS}}(Wc\text{-jet})$ and $\sigma_{\text{fid}}^{\text{OS-SS}}(Wc\text{-jet}(c \to \mu))$ as a function of the jet multiplicity

The cross section is measured with the requirements defined in section 1.5.1, except for requiring either exactly one or exactly two jets only one of which is identified as a c-jet. The results, including the ratio $R_c^{\pm}$, averaged between the electron and muon channels, are shown in table 1.5. Figure 1.6 shows the measured Wc-jet fiducial cross sections for events with exactly one or two jets compared to aMC@NLO [114] predictions with the CT10 NLO PDF set. The aMC@NLO sample used for this prediction is described in details in section 1.7.3. The aMC@NLO central values do not describe the one-to-two-jets ratio well. The ALPGEN predictions normalised to the inclusive W NNLO cross section are also shown for reference. The ALPGEN central values underestimate the data measurements for both the samples with one and two jets; however the one-to-two-jets ratio is well described.

Finally, in order to minimise the systematic uncertainties due to the extrapolation to the fiducial phase space, the cross sections are determined in a phase space as specified in section 1.5.1 but in which the c-hadron decays semileptonically to a muon with $p_{\text{T}} > 4$ GeV, $|\eta| < 2.5$, charge opposite to the W boson and within $\Delta R < 0.5$ from the c-jet axis. The resulting cross sections, for both the exclusive jet multiplicity and inclusive jet multiplicity definitions are also shown in table 1.5, indicating a total systematic uncertainty of 4.7% for the measurement with inclusive jet multiplicity.

	$\sigma_{\text{fid}}^{\text{OS}-\text{SS}}(Wc\text{-jet})$ [pb]
Wc-jet (1 jet)	$52.9 \pm 0.9\,(\text{stat}) \pm 3.0\,(\text{syst})$
Wc-jet (2 jets)	$14.2 \pm 0.6\,(\text{stat}) \pm 1.2\,(\text{syst})$
$R_c^{\pm}$ (1 jet)	$0.91 \pm 0.03\,(\text{stat}) \pm 0.02\,(\text{syst})$
$R_c^{\pm}$ (2 jets)	$0.87 \pm 0.08\,(\text{stat}) \pm 0.02\,(\text{syst})$
	$\sigma_{\text{fid}}^{\text{OS}-\text{SS}}(Wc\text{-jet}(\text{c} \to \mu))$ [pb]
Wc-jet (1 jet)	$2.47 \pm 0.04\,(\text{stat}) \pm 0.13\,(\text{syst})$
Wc-jet (2 jets)	$0.69 \pm 0.03\,(\text{stat}) \pm 0.06\,(\text{syst})$
Wc-jet (inclusive)	$3.36 \pm 0.06\,(\text{stat}) \pm 0.16\,(\text{syst})$

Table 1.5: Measured fiducial cross sections and $R_c^{\pm}$ for exclusive jet multiplicity together with the statistical and systematic uncertainties. The lower part of the table shows the measured fiducial cross section for the production of a W boson together with a soft muon from the charm-quark decay. The branching ratio $W \to \ell\nu$ is included in the fiducial cross section definition.

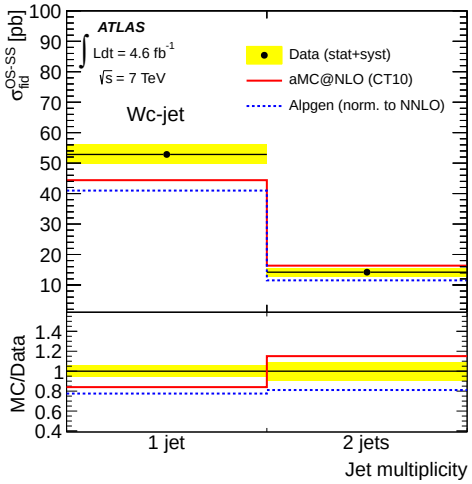

Figure 1.6: Measured cross sections as a function of the jet multiplicity compared to aMC@NLO produced using the CT10 NLO PDF set. The predictions from ALPGEN normalised to the inclusive W NNLO cross section are also shown for reference. In the lower panels, the ratio of the simulated distribution to data is shown.

1.7.2 Data combination of Wc-jet and $WD^{(*)}$

The combination of the cross-section measurements of WD^*, WD and Wc-jet, in the electron and muon channels, is performed using a global fit to simultaneously extract all cross sections in individual channels as well as combined cross sections in relevant regions. The combination procedure is applied to the integrated cross-section measurements as well as to the measurements differential in $|\eta^\ell|$. The Wc-jet measurements entering this combination correspond to the 1-jet inclusive cross sections and do not restrict the number of jets to a maximum of two as done in section 1.7.1. The procedure is based on the averaging method developed in ref. [115], which takes into account statistical uncertainties as well as systematic uncertainties (bin-to-bin correlated and uncorrelated) proportional to the central values of the respective cross sections. The combined cross sections (m^i) in bins i are derived from the individual cross-section measurements (μ_k^i) in channels k by minimising the following χ^2 function:

$$\chi^2 = \sum_{k,i} w_k^i \frac{\left[\mu_k^i - \left(m^i + \sum_j \gamma_{j,k}^i m^i b_j\right)\right]^2}{(\delta_{\text{sta},k}^i)^2 \mu_k^i (m^i - \sum_j \gamma_{j,k}^i m^i b_j) + (\delta_{\text{unc},k}^i m^i)^2} + \sum_j b_j^2. \tag{1.9}$$

where $w_k^i = 1$ if channel k contributes to measurement μ_k^i in bin i, and $w_k^i = 0$ otherwise. The parameters b_j denote the shift introduced by a correlated systematic error source j normalised to its respective standard deviation. The relative statistical and uncorrelated systematic uncertainties on μ_k^i are denoted by $\delta_{\text{sta},k}^i$ and $\delta_{\text{unc},k}^i$ and the variable $\gamma_{j,k}^i$ quantifies the relative influence of the correlated systematic error source j on the measurement μ_k^i.

The sources of systematic uncertainties which are fully correlated between the different measurements and the electron and the muon channels are uncertainties due to the modelling of charm fragmentation and decay, uncertainties on the $E_{\text{T}}^{\text{miss}}$ reconstruction and the luminosity uncertainty. Uncertainties on the lepton reconstruction and identification efficiencies and momentum scale and resolution are correlated among the WD^*, WD and Wc-jet measurements, but uncorrelated between the electron and the muon channel. Uncertainties due to the track and vertex reconstruction are treated as correlated among the WD^* and WD channels, while uncertainties in the c-jet signal reconstruction and identification are correlated for the electron and muon channels in the Wc-jet analysis. Since different methods are used to determine the backgrounds in the individual channels, the corresponding uncertainties are assumed to be uncorrelated among the different channels, but correlated bin-to-bin.

In total there are 58 differential cross-section measurements in 38 independent bins entering the combination with 113 sources of correlated systematic uncertainties. The measured integrated cross sections together with their statistical and systematic uncertainties resulting from the averaging procedure are reported in table 1.6.

The correlation between the total uncertainties of the integrated Wc-jet and WD^* measurements is found to be approximately 10%, while it is about 5% for Wc-jet and WD due to the larger statistical uncertainty of the WD sample. The correlation between WD^* and WD is approximately 20%. Furthermore, the correlations between the uncertainties in the W^+ and the W^- channels are 76%, 58% and 17% for Wc-jet, WD^* and WD, respectively. Different channels use complementary c-hadron decay modes and the statistical overlap between the different selected data samples is of the order of 1%. Therefore the correlations between the statistical uncertainties are neglected.

The averaging procedure described above is also applied to the measurements of the cross-section ratios $\sigma_{\text{fid}}^{\text{OS}-\text{SS}}(W^+\bar{c}\text{-jet})/\sigma_{\text{fid}}^{\text{OS}-\text{SS}}(W^-c\text{-jet})$ and $\sigma_{\text{fid}}^{\text{OS}-\text{SS}}(W^+D^{(*)-})/\sigma_{\text{fid}}^{\text{OS}-\text{SS}}(W^-D^{(*)+})$. The measurements of the ratios are dominated by statistical uncertainties, since most of the systematic uncertainties cancel in the ratio or are significantly reduced. In particular, the systematic uncer-

tainties due to the lepton reconstruction and the luminosity are negligible for the ratio measurements. The measurements in the Wc-jet and $WD^{(*)}$ channels are therefore almost completely uncorrelated. The measurements of the cross-section ratios $\sigma_{\text{fid}}^{\text{OS}-\text{SS}}(W^+D^{*-})/\sigma_{\text{fid}}^{\text{OS}-\text{SS}}(W^-D^{*+})$ and $\sigma_{\text{fid}}^{\text{OS}-\text{SS}}(W^+D^-)/\sigma_{\text{fid}}^{\text{OS}-\text{SS}}(W^-D^+)$ are combined since the measurements are performed in a similar phase space ($p_{\text{T}}^{D^{(*)}} > 8\,\text{GeV}$, $|\eta^{D^{(*)}}| < 2.2$) and residual differences are predicted to be small. The measurement of $\sigma_{\text{fid}}^{\text{OS}-\text{SS}}(W^+\bar{c}\text{-jet})/\sigma_{\text{fid}}^{\text{OS}-\text{SS}}(W^-c\text{-jet})$ on the other hand is sensitive to a different phase space at higher c-jet transverse momentum ($p_{\text{T}}^{\text{jet}} > 25\,\text{GeV}$, $|\eta^{\text{jet}}| < 2.5$). Consequently, the Wc-jet measurement is not combined with the $WD^{(*)}$ measurement, but is subject to the common averaging procedure using equation (1.9).

	$\sigma_{\text{fid}}^{\text{OS}-\text{SS}}$ [pb]
$W^+\bar{c}$-jet	$33.6 \pm 0.9\,(\text{stat}) \pm 1.8\,(\text{syst})$
W^-c-jet	$37.3 \pm 0.8\,(\text{stat}) \pm 1.9\,(\text{syst})$
W^+D^-	$17.8 \pm 1.9\,(\text{stat}) \pm 0.8\,(\text{syst})$
W^-D^+	$22.4 \pm 1.8\,(\text{stat}) \pm 1.0\,(\text{syst})$
W^+D^{*-}	$21.2 \pm 0.9\,(\text{stat}) \pm 1.0\,(\text{syst})$
W^-D^{*+}	$22.1 \pm 0.8\,(\text{stat}) \pm 1.0\,(\text{syst})$

Table 1.6: Measured integrated cross sections times the branching ratio $W \to \ell\nu$ in the fiducial regions together with the statistical and systematic uncertainties.

1.7.3 Theoretical predictions

The theoretical predictions for the cross sections $\sigma_{\text{fid}}^{\text{OS}-\text{SS}}(WD^{(*)})$ and $\sigma_{\text{fid}}^{\text{OS}-\text{SS}}(Wc\text{-jet})$ are obtained from the aMC@NLO MC simulation that incorporates NLO QCD matrix-element calculations into a parton-shower framework. The aMC@NLO event generator is based on the MC@NLO formalism [88] and the MadGraph5 framework [116]. The parton-level cross section obtained with aMC@NLO was found to be in good agreement with the prediction obtained using MCFM [117]. Herwig++ [81] is used to model the parton shower, hadronisation and underlying event of the aMC@NLO simulation. The MC predictions for the charmed-hadron production fractions are corrected to the average of measurements obtained in e^+e^- and ep collisions, as compiled in ref. [80]. The uncertainties on these production fractions are 2.4% for the D^* meson and 3.4% for the D meson and are included in the evaluation of the systematic uncertainty on the prediction.

Events are generated in aMC@NLO using the CT10 NLO PDF set. The dependence of the results on the choice of PDF set is checked by reweighting the aMC@NLO predictions using various NLO and NNLO PDF sets: the CT10, MSTW2008, HERAPDF1.5, NNPDF2.3 and NNPDF2.3COLL [118] NLO PDF sets are used in addition to the ATLAS-epWZ12 NNLO PDF set. Asymmetric uncertainties are calculated following the prescriptions from the PDF sets.

For MSTW2008 and NNPDF2.3 the s-quark sea is suppressed relative to the d-quark sea for all values of x. The ATLAS-epWZ12 PDF set, which is based on the analysis of ATLAS W and Z cross-section measurements [119] together with HERA data [120], has an s-quark PDF that is not suppressed with respect to the d-quark sea at $x \sim 0.01$. The s-quark sea in CT10 is less suppressed than in MSTW2008 or NNPDF2.3. The NNPDF2.3COLL PDF set uses only data from HERA, the Tevatron and the LHC, so that the data from charm production in neutrino–nucleon scattering are excluded. The s-quark sea of this PDF is larger than the d-quark sea at most values of x.

Processes with charm quarks in the initial state such as $dc \to W^-uc$ and $d\bar{c} \to W^-u\bar{c}$ can contribute to the OS-SS $W+c$ signal if there is an asymmetry in the charm and anti-charm PDFs. The

PDF sets studied here do not include a non-perturbative (intrinsic) charm component [121], where significant asymmetries are possible. PDF fits that include phenomenological models of intrinsic charm [122, 62, 123] indicate that for the values of x relevant for this analysis, these contributions are expected to be small.

The dependence of the NLO prediction on the choice of renormalisation and factorisation scales is evaluated by independently halving and doubling their nominal value which is chosen as the sum of the transverse mass of all final-state particles. The largest variation where the scales are varied in opposite directions is taken as the uncertainty and treated as fully correlated. This uncertainty is $+8/-9\%$ for the $WD^{(*)}$ analysis and $+8/-4\%$ for the Wc-jet analysis. To study the modelling of the charm fragmentation function in Herwig++, e^+e^- annihilation events are generated at centre-of-mass energy $\sqrt{s} = 10.6\,\text{GeV}$ and the distribution of $x_p \equiv p/p_{\text{max}}$ for D and D^* is compared to the data from ref. [124]. The evolution of the charm fragmentation function with Q^2 in Herwig++ is validated by generating e^+e^- annihilation events at $\sqrt{s} = 91.2\,\text{GeV}$ and comparing the mean value of $x_E \equiv E/E_{\text{beam}}$ for D^* to that measured in ref. [125]. Based on these studies, a systematic uncertainty of 2% is assigned to the aMC@NLO predictions of $WD^{(*)}$ for the mean value of the fraction of the charm-quark momentum carried by the charmed hadron. The effect of the charm fragmentation uncertainty on the predicted Wc-jet cross section is negligible, while its effect on the acceptance correction is discussed in section 1.6.2.

The effect of the uncertainty in the parton-shower model used in the MC simulation is estimated by comparing the predictions of different MC generators. The corrections for the charm fragmentation and decay discussed in section 1.2 are applied to all MC simulations to avoid a potential double counting of the uncertainties. The comparison of the fiducial cross sections obtained with aMC@NLO+Herwig++, aMC@NLO+Herwig, POWHEG+Herwig and POWHEG+PYTHIA indicates a systematic uncertainty of 3% for $WD^{(*)}$ and 1% for Wc-jet due to the modelling of the parton shower.

1.7.4 Discussion

The measured integrated fiducial cross sections $\sigma_{\text{fid}}^{\text{OS}-\text{SS}}(WD^{(*)})$ and $\sigma_{\text{fid}}^{\text{OS}-\text{SS}}(Wc\text{-jet})$ are compared to the theoretical predictions based on various PDF sets in figure 1.7. The inner error bars on the theoretical predictions are the 68% confidence level (CL) uncertainties obtained from the error sets provided with each PDF set, while the outer error bars show the sum in quadrature of these PDF uncertainties and theoretical uncertainties due to variations in renormalisation and factorisation scale, parton shower and charm-quark fragmentation as discussed previously. The predicted cross sections differ by as much as 25%. The six different measurements give a consistent picture; the predictions obtained with the ATLAS-epWZ12 and NNPDF2.3COLL sets are seen to overlap more with the data but simulations using CT10, HERAPDF1.5 and MSTW2008 also are in agreement with the measurements. The prediction obtained with NNPDF2.3 is less favoured. A quantitative comparison of the various PDF predictions with the measured cross sections is discussed below.

The compatibility of the experimental measurements from different channels is illustrated in figure 1.8, which shows the 68% CL contours for the ratios of the measured cross section with respect to the theoretical prediction obtained from the CT10 PDF. The large overlap of the contours with the diagonal line reflects the good compatibility of the measurements assuming the extrapolation among the different phase spaces as given by aMC@NLO using the CT10 PDF.

Figure 1.9 shows the measured ratio $R_c^{\pm}$ compared to theoretical predictions based on various PDF sets. The predicted production ratio $R_c^{\pm}$ in pp collisions can differ from unity for two reasons [58]. First, because the proton contains valence d-quarks, the Cabbibo-suppressed diagrams involving d-quarks enhance $W^- + c$ production over $W^+ + \bar{c}$, and thereby decrease $R_c^{\pm}$ by about

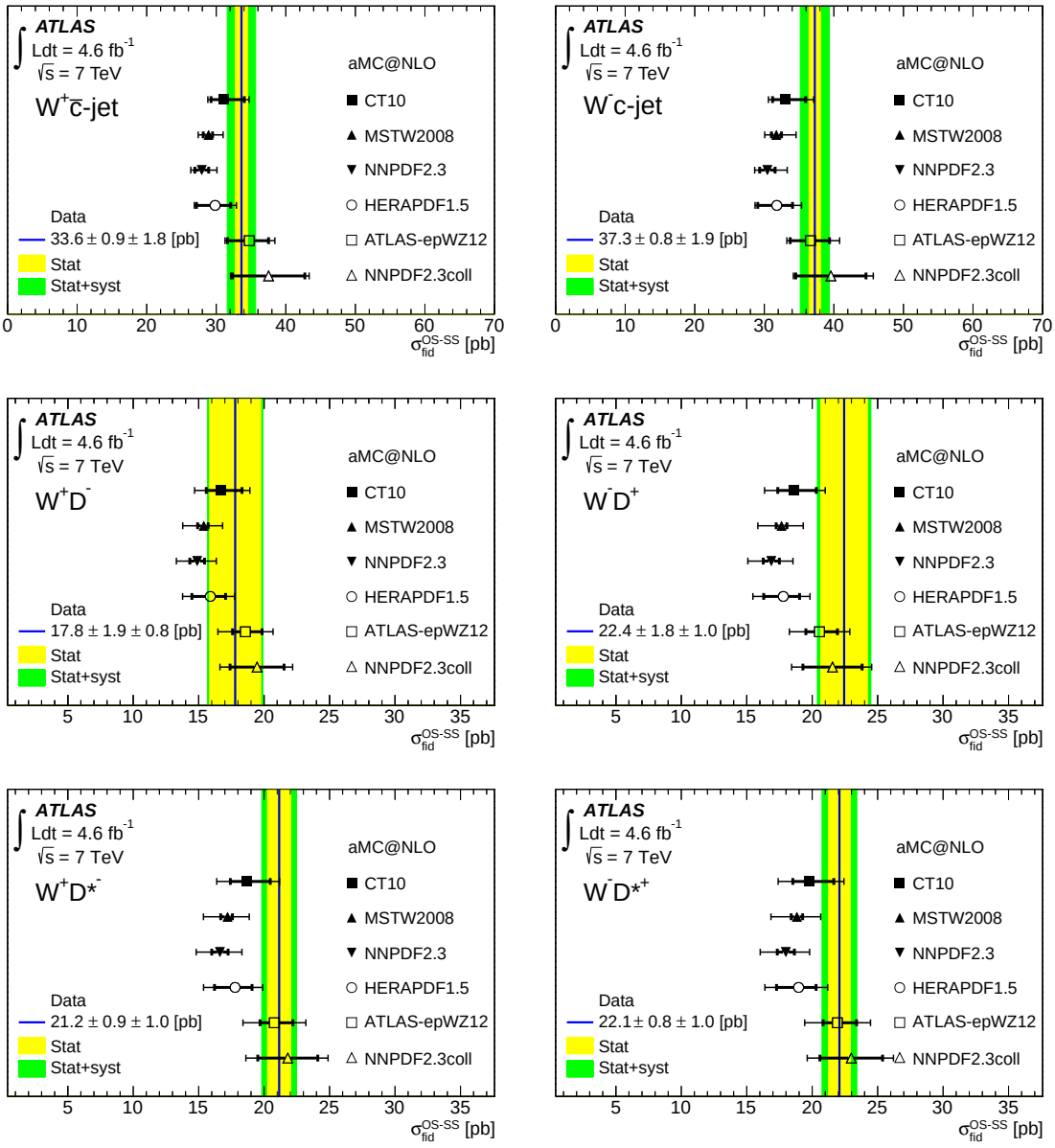

Figure 1.7: Measured fiducial cross sections compared to various PDF predictions based on aMC@NLO. The solid vertical line shows the central value of the measurement, the inner error band corresponds to the statistical uncertainty and the outer error band to the sum in quadrature of the statistical and systematic uncertainties. The PDF predictions are shown by markers. The inner error bars on the theoretical predictions show the 68% confidence level uncertainties obtained from the error sets provided with each PDF set, while the outer error bar represents the total theoretical uncertainty (sum in quadrature of PDF, parton shower, fragmentation and scale uncertainties).

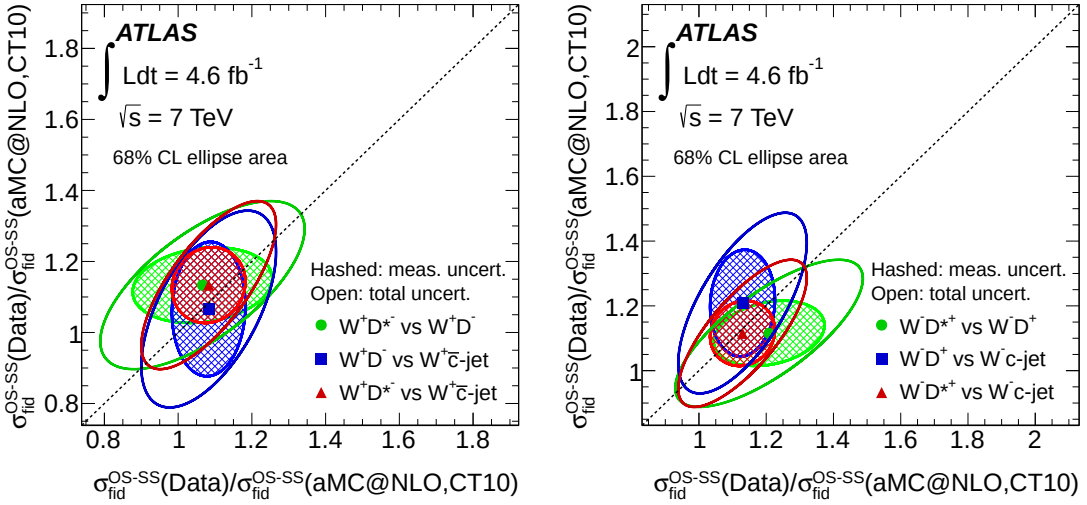

Figure 1.8: 68% CL contours of the measured cross sections normalised to the theoretical prediction obtained from the aMC@NLO simulation using the CT10 PDF. The filled ellipses show the experimental uncertainties, while the open ellipses show the total uncertainties, including the uncertainties on the prediction. The left figure shows the correlations among the W^+D^{*-}, W^+D^- and $W^+\bar{c}$-jet cross sections, while the right figure is for W^-D^{*+}, W^-D^+ and W^-c-jet.

5%. Second, a difference between s and $\bar{s}$ PDFs, as suggested by neutrino data [61], would also influence the value of the ratio: a lower population of $\bar{s}$-quarks relative to s-quarks in the sensitive range of the measurement would push the ratio to a lower value. This effect is implemented in NNPDF2.3 and MSTW2008. The contributions of the strange asymmetry in NNPDF2.3 to $R_c^{\pm}$ are small. For MSTW2008, the strange asymmetry is larger and thus lowers $R_c^{\pm}$ by about 3%. This pattern of predictions is consistent with those obtained from the NLO calculation as implemented in aMC@NLO and shown in figure 1.9. The ratio measurement is consistent (within 1 σ) with all studied PDFs, and the measured uncertainty is comparable to the one obtained with MSTW2008.

For PDFs such as CT10 that require the s and $\bar{s}$ distributions be equal, the Cabibbo-suppressed diagrams are the only mechanism capable of lowering $R_c^{\pm}$. The relative size of strange asymmetry effects using NLO PDFs is studied in ref. [58]; assuming the ratio of d-quark to s-quark densities from CT10 and that the asymmetry which is seen in the measured $R_c^{\pm}$ is mainly due to the d-quark, one can attribute the total difference $R_c^{\pm}(\mathrm{CT10}) - R_c^{\pm}(\mathrm{Data})$ to an effect of a strange asymmetry and thereby estimate the sensitivity of the current measurement. Under these assumptions the relative strange asymmetry ($A_{s\bar{s}}$) can be written as

$$A_{s\bar{s}} = \frac{\langle s(x,Q^2)\rangle - \langle \bar{s}(x,Q^2)\rangle}{\langle s(x,Q^2)\rangle} \approx R_c^{\pm}(\mathrm{CT10}) - R_c^{\pm}(\mathrm{Data}), \tag{1.10}$$

where the s and $\bar{s}$ distributions are averaged over the phase space. A value of $A_{s\bar{s}} = (2 \pm 3)\%$ is obtained for the combination of the Wc-jet and $WD^{(*)}$ analyses. The quoted uncertainty is dominated by statistical uncertainties.

The dependence of the cross section on $|\eta^{\ell}|$, along with predictions of aMC@NLO with various PDFs, is shown in figure 1.10. Similar predictions of the shapes of the $|\eta^{\ell}|$ distributions are obtained with the various PDF sets. The predictions differ mainly in their normalisation. The predicted shapes are in good agreement with the measured distributions.

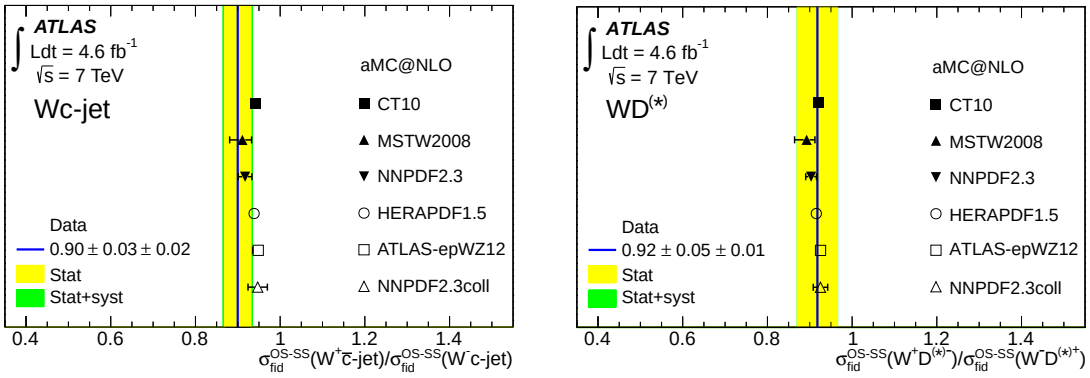

Figure 1.9: Measured ratios $\sigma_{\text{fid}}^{\text{OS}-\text{SS}}(W^+\bar{c}\text{-jet})/\sigma_{\text{fid}}^{\text{OS}-\text{SS}}(W^-c\text{-jet})$ (left) and $\sigma_{\text{fid}}^{\text{OS}-\text{SS}}(W^+D^{(*)-})/\sigma_{\text{fid}}^{\text{OS}-\text{SS}}(W^-D^{(*)+})$ (right) resulting from the averaging procedure compared to various PDF predictions based on aMC@NLO. The blue vertical lines show the central values of the measurements, the inner error bands show the statistical uncertainties and the outer error bands the total experimental uncertainties. The PDF predictions are shown by the black markers. The error bars on the predictions correspond to the 68% CL PDF uncertainties.

In order to perform a quantitative comparison of the measurements and the various PDF predictions, the χ^2 function introduced in equation (1.9) is extended to include the uncertainties on the theoretical predictions:

$$\chi^2 = \sum_{k,i} w_k^i \frac{\left[\mu_k^i - m^i\left(1+\sum_j \gamma_{j,k}^i b_j + \sum_j (\gamma^{\text{theo}})_{j,k}^i b_j^{\text{theo}}\right)\right]^2}{(\delta_{\text{sta},k}^i)^2 \Delta_i^k + (\delta_{\text{unc},k}^i m^i)^2} + \sum_j b_j^2 + \sum_j (b_j^{\text{theo}})^2, \tag{1.11}$$

where

$$\Delta_i^k = \mu_k^i m^i \left(1 - \sum_j \gamma_{j,k}^j b_j - \sum_j (\gamma^{\text{theo}})_{j,k}^i b_j^{\text{theo}}\right). \tag{1.12}$$

The notation follows the one introduced in equation (1.9). The matrix $(\gamma^{\text{theo}})_{j,k}^i$ represents the relative correlated systematic uncertainties on the theory predictions and quantifies the influence of the uncertainty source j on the prediction in bin i and data set k. The parameters b_j^{theo} are defined analogously to the parameters b_j and represent the shifts introduced by a correlated uncertainty source j of the predictions. The χ^2 function is minimised with respect to b_j and b_j^{theo} with the cross-section measurements, μ, fixed to the values determined in section 1.7.2.

Equation (1.11) is further extended to account for asymmetric uncertainties on the predictions. The asymmetric uncertainties are described by parabolic functions

$$f_i(b_j^{\text{theo}}) = \omega_{i,j}(b_j^{\text{theo}})^2 + \gamma_{i,j} b_j^{\text{theo}}, \tag{1.13}$$

which replace the terms $(\gamma^{\text{theo}})_{j,k}^i b_j^{\text{theo}}$ of equation (1.11). The coefficients of $f_i(b_j^{\text{theo}})$ are determined from the values of the cross sections calculated when the parameter corresponding to source j is set to its nominal value $+S_{i,j}^+$ and $-S_{i,j}^-$ where the $S_{i,j}^{\pm}$ are the up and down uncertainties of the respective

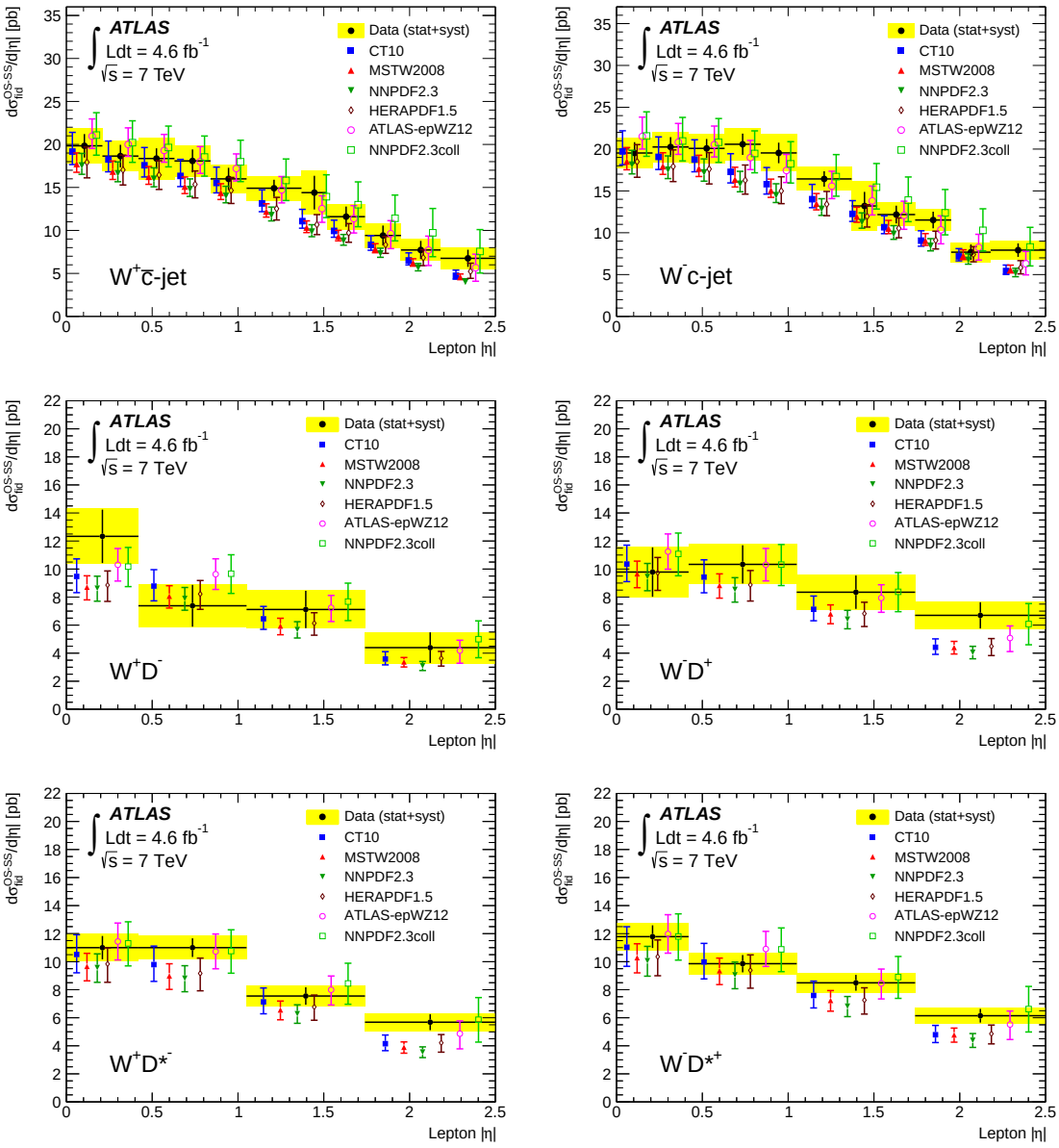

Figure 1.10: Measured differential cross section as a function of lepton $|\eta|$ compared to predictions obtained using various PDF sets: (top left) $W^+\bar{c}$-jet, (top right) W^-c-jet, (middle left) W^+D^-, (middle right) W^-D^+, (bottom left) W^+D^{*-} and (bottom right) W^-D^{*+}. The measurements are shown by the filled circles. The error bars give the statistical uncertainty, while the sum in quadrature of the statistical and systematic uncertainties is shown as an error band. The theory predictions are based on the aMC@NLO simulation. The different markers correspond to the predictions obtained using various PDF sets and the corresponding error bars represent the total theoretical uncertainties (sum in quadrature of PDF, parton shower, fragmentation and scale uncertainties).

	CT10	MSTW2008	HERAPDF1.5	ATLAS-epWZ12	NNPDF2.3	NNPDF2.3COLL
$W^+\bar{c}$-jet (χ^2/ndof)	3.8/11	6.1/11	3.5/11	3.1/11	8.5/11	2.9/11
W^-c-jet (χ^2/ndof)	9.0/11	10.3/11	8.3/11	6.3/11	10.5/11	6.1/11
W^+D^- (χ^2/ndof)	3.6/4	3.7/4	3.7/4	3.4/4	3.8/4	3.4/4
W^-D^+ (χ^2/ndof)	3.7/4	4.6/4	3.3/4	2.0/4	4.7/4	1.6/4
W^+D^{*-} (χ^2/ndof)	2.9/4	6.0/4	2.2/4	1.7/4	8.1/4	1.6/4
W^-D^{*+} (χ^2/ndof)	3.0/4	4.4/4	2.4/4	1.6/4	4.2/4	1.4/4
N_{exp}	114	114	114	114	114	114
N_{theo}	28	22	16	20	40	40
Correlated χ^2 (exp)	0.8	1.8	0.9	1.1	2.2	1.0
Correlated χ^2 (theo)	6.2	1.9	2.6	0.1	7.4	0.2
Correlated χ^2 (scale)	0.6	2.5	1.1	0.0	2.7	0.0
Total χ^2/ndof	33.6/38	41.3/38	28.0/38	19.2/38	52.1/38	18.2/38

Table 1.7: Quantitative comparison of fiducial cross sections to various PDF predictions. The table shows the partial χ^2/ndof for the different cross-section measurements, the number of nuisance parameters for the experimental sources of systematic uncertainties (N_{exp}), the number of nuisance parameters for the uncertainties on the predictions (N_{theo}) as well as the correlated χ^2 corresponding to the experimental uncertainties (χ^2 (exp)), the uncertainties on the predictions excluding the scale uncertainties (χ^2 (theo)) and the scale uncertainty (χ^2 (scale)). The correlations due to the systematic uncertainties of c-quark fragmentation that affect both the measured cross sections and the theoretical predictions are taken into account. To avoid double-counting, these uncertainties are added to N_{exp} and χ^2 (exp) only. Furthermore, the total χ^2/ndof is given.

PDF sets.[2] The coefficients are given by

$$\gamma_{i,j} = \frac{1}{2}\left(S^+_{i,j} - S^-_{i,j}\right) \tag{1.14}$$

$$\omega_{i,j} = \frac{1}{2}\left(S^+_{i,j} + S^-_{i,j}\right). \tag{1.15}$$

The χ^2-minimisation procedure implemented in the HERAFitter framework [120, 126, 127, 128] is used. The cross-section measurements differential in $|\eta^\ell|$ are used to assess the quantitative agreement between the data and the PDF predictions.

The results of the χ^2-minimisation procedure are shown in table 1.7. The measured cross sections are in agreement with all PDF predictions but disfavour NNPDF2.3. In addition to the total χ^2, table 1.7 also shows the individual contributions to the χ^2 from the experimental uncertainties, the uncertainties on the predictions and the scale uncertainty. For the predictions obtained with MSTW2008 and NNPDF2.3 the scale uncertainty is the dominant uncertainty. Improved accuracy in the theory calculation, especially reducing the scale dependence, could enhance the sensitivity of the presented measurements to the PDF significantly.

For values $x \leq 0.1$, the HERAPDF1.5 PDF is constrained mainly by the precise measurement of the proton structure function $F_2(x,Q^2)$ at HERA [120], which fixes the quark-charge-squared weighted sum of quark and anti-quark contributions but has no sensitivity to the flavour composition of the total light-quark sea. In the HERAPDF1.5 PDF set, the strange-quark distribution is expressed as an x-independent fraction, $f_s = \bar{s}/(\bar{d}+\bar{s})$. The central value $f_s = 0.31$ at $Q^2 = 1.9\,\text{GeV}^2$ is chosen to be consistent with determinations of this fraction using the neutrino–nucleon scattering data with an uncertainty spanning the range from 0.23 to 0.38. This model uncertainty is parameterised as a nuisance parameter in the χ^2 minimisation.

[2]The uncertainties for the NNPDF2.3 and NNPDF2.3COLL sets are obtained from the cross-section variations provided with these PDF sets by diagonalising the correlation matrix to determine the corresponding eigenvectors.

The χ^2-minimisation procedure not only gives information about the overall compatibility of the predictions with the data, but also allows constraints on the PDF eigenvectors to be obtained. HERAPDF1.5 is the only publicly available PDF set where the effect of varying the strange-quark density is parameterised by a single parameter (f_s). The χ^2-minimisation procedure discussed above can be used as follows to calculate a value for f_s based solely on the measurements discussed here while ignoring all previous measured or assumed values of f_s. The χ^2 minimisation is repeated for the HERAPDF1.5 PDF set after artificially increasing the uncertainty of the strange-quark fraction f_s. This procedure corresponds to a free fit of the eigenvector representing f_s while all other eigenvectors are constrained within the uncertainties determined in the HERAPDF1.5 fit. A value of

$$r_s \equiv 0.5(s+\bar{s})/\bar{d} = f_s/(1-f_s) = 0.96^{+0.16\,+0.21}_{-0.18\,-0.24}$$

is determined at $Q^2 = 1.9\,\text{GeV}^2$ and is independent of x as implemented in the HERAPDF1.5 PDF. The first uncertainty represents the experimental and theoretical uncertainties and the second uncertainty corresponds to the scale uncertainty of the $W+c$ calculation. Since the scale uncertainty is the dominant uncertainty, its effect is assessed separately by repeating the fit under the assumption of perfect knowledge of the scale. The resulting strange-quark fraction is shown in figure 1.11 as a function of x at $Q^2 = m_W^2$. For the HERAPDF1.5 PDF the s-quark sea density is lower than the d-quark sea density at low values of x and it is further suppressed at higher values of x. The ATLAS Wc-jet/$WD^{(*)}$ data on the other hand favour a symmetric light-quark sea over the whole x range relevant to the presented measurement (10^{-3} to 10^{-1}).

The value of r_s determined in this study is in good agreement with the value of $r_s = 1.00^{+0.25}_{-0.28}$ obtained in the combined analysis of W and Z production at $Q^2 = 1.9\,\text{GeV}^2$ and x = 0.023 by ATLAS [51] and supports the hypothesis of an SU(3)-symmetric light-quark sea. Figure 1.11 also shows that the x-dependence of r_s obtained from the ATLAS-epWZ12 PDF is in good agreement with this study.

1.8 Conclusion

Integrated and differential cross sections for W-boson production in association with a single charm quark are measured as a function of the pseudorapidity of the lepton from the W-boson decay in $4.6\,\text{fb}^{-1}$ of pp collision data at $\sqrt{s} = 7\,\text{TeV}$ collected with the ATLAS detector at the LHC. The charm quarks is identified by the presence of muons from semileptonic charm decays within hadronic jets. The results of this analysis are combined with an analyses where charm quarks are identified by the presence of a charged $D^{(*)}$ (D or D^*) meson. The integrated cross sections for the fiducial region $p_\text{T}^\ell > 20\,\text{GeV}$, $|\eta^\ell| < 2.5$, $p_\text{T}^\nu > 25\,\text{GeV}$, $m_\text{T}^W > 40\,\text{GeV}$ are measured for the Wc-jet events with jets passing the fiducial requirements of $p_\text{T} > 25\,\text{GeV}$, $|\eta| < 2.5$, yielding

$$\begin{aligned}
\sigma_\text{fid}^{\text{OS}-\text{SS}}(W^+\bar{c}\text{-jet}) &= 33.6 \pm 0.9\,(\text{stat}) \pm 1.8\,(\text{syst})\,\text{pb} \\
\sigma_\text{fid}^{\text{OS}-\text{SS}}(W^-c\text{-jet}) &= 37.3 \pm 0.8\,(\text{stat}) \pm 1.9\,(\text{syst})\,\text{pb}
\end{aligned}$$

and for $D^{(*)}$ mesons with $p_\text{T}^{D^{(*)}} > 8\,\text{GeV}$ and $|\eta^{D^{(*)}}| < 2.2$, yielding

$$\begin{aligned}
\sigma_\text{fid}^{\text{OS}-\text{SS}}(W^+D^-) &= 17.8 \pm 1.9\,(\text{stat}) \pm 0.8\,(\text{syst})\,\text{pb} \\
\sigma_\text{fid}^{\text{OS}-\text{SS}}(W^-D^+) &= 22.4 \pm 1.8\,(\text{stat}) \pm 1.0\,(\text{syst})\,\text{pb} \\
\sigma_\text{fid}^{\text{OS}-\text{SS}}(W^+D^{*-}) &= 21.2 \pm 0.9\,(\text{stat}) \pm 1.0\,(\text{syst})\,\text{pb} \\
\sigma_\text{fid}^{\text{OS}-\text{SS}}(W^-D^{*+}) &= 22.1 \pm 0.8\,(\text{stat}) \pm 1.0\,(\text{syst})\,\text{pb}.
\end{aligned}$$

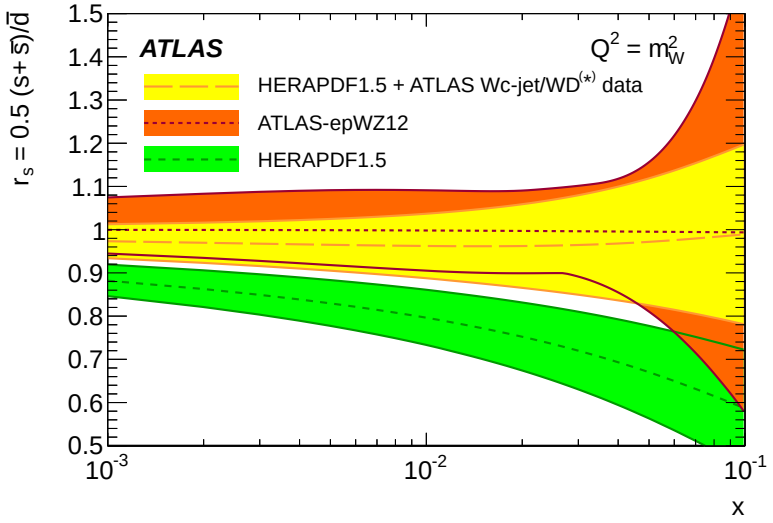

Figure 1.11: Ratio of strange-to-down sea-quark distributions $r_s = 0.5(s+\bar{s})/\bar{d}$ as a function of x as assumed in HERAPDF1.5 PDF compared to the ratio obtained from the fit including the ATLAS Wc-jet/$WD^{(*)}$ data and the ratio obtained from ATLAS-epWZ12. The error band on the ATLAS Wc-jet/$WD^{(*)}$ measurements represents the total uncertainty. The ratio r_s is shown at $Q^2 = m_W^2$.

Furthermore, the cross-section ratios are determined to be

$$R_c^{\pm}(Wc\text{-jet}) = \sigma_{\text{fid}}^{\text{OS-SS}}(W^+\bar{c}\text{-jet})/\sigma_{\text{fid}}^{\text{OS-SS}}(W^-c\text{-jet}) = 0.90 \pm 0.03\,(\text{stat}) \pm 0.02\,(\text{syst})$$
$$R_c^{\pm}(WD^{(*)}) = \sigma_{\text{fid}}^{\text{OS-SS}}(W^+D^{(*)-})/\sigma_{\text{fid}}^{\text{OS-SS}}(W^-D^{(*)+}) = 0.92 \pm 0.05\,(\text{stat}) \pm 0.01\,(\text{syst})$$

and are in agreement with theoretical predictions. In addition to the cross-section measurements differential in lepton pseudorapidity, and the jet multiplicity in Wc-jet events are performed.

The predicted cross sections depend on the choice of PDF set and have uncertainties associated with the choice of renormalisation and factorisation scales. With these uncertainties taken into account, the data are consistent with a wide range of PDFs, but show a preference for PDFs with an SU(3)-symmetric light-quark sea. The ratio of the strange-to-down sea quark distributions is determined to be $r_s = 0.96^{+0.26}_{-0.30}$ at $Q^2 = 1.9\,\text{GeV}^2$.

A recent PDF determination, based on the combination of data from HERA [129] and precision measurements from ATLAS, has been presented in [130]. This PDF set is called the ATLASpdf21 set. The combination uses inclusive and differential cross section measurements of a W or a Z boson production in association with jets, $t\bar{t}$ production, photon production, and multijets production. It does not contain the cross section measurements of the production of a W boson in association with a single charm quark that is presented in this chapter. This combination allows to constrain the up, down, and strange sea PDFs independently and thus test the SU(3) symmetry in the light quark sea. Figure 1.12 shows the value of the strange to up and down quarks sea ratio $R_s = s(s+\bar{s})/x(\bar{u}+\bar{d})$ at $x = 0.023$ and $Q^2 = 1.9\,\text{GeV}^2$ compared to several relatively recent PDF sets. The R_s value is slightly lower than the one determined in previous ATLAS PDF sets but larger than the one in PDF sets that do not include ATLAS data. Assuming a similar contribution from the up and down quarks sea, this recent R_s value is compatible with the r_s value determined from the $W+c$ measurements presented in this chapter. It confirms the enhancement of the strange quark sea contribution with respect to older PDF sets (such as the HERAPDF1.5 PDF set) that have an R_s value of around 0.5.

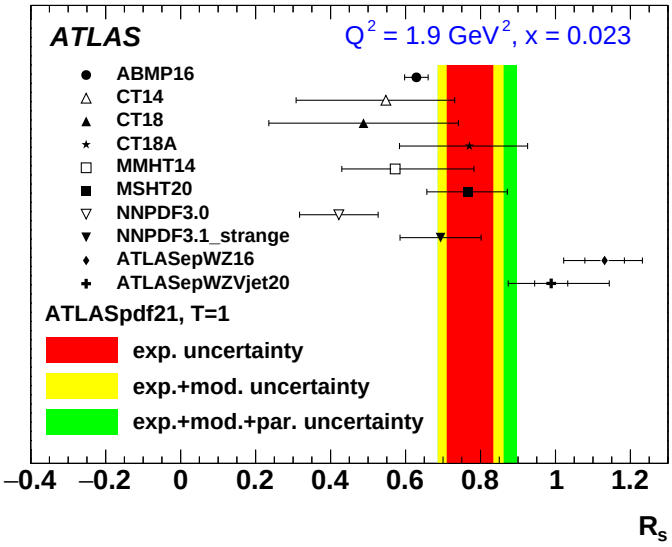

Figure 1.12: $R_s = s(s+\bar{s})/x(\bar{u}+\bar{d})$ at $x = 0.023$ and $Q^2 = 1.9\,\text{GeV}^2$ from the ATLASpdf21 set [130] compared to the ABMP16 [131], CT14 [132], CT18, CT18A [133], MMHT14 [134], MSHT20 [135], NNPDF3.0 [136], NNPDF3.1_strange [137], ATLASepWZ16 [53], and ATLASepWZV-jets20 [138] sets.

Chapter 2

Search for the production of the Higgs boson coupled to top quarks and decaying to b quarks

This chapter presents the search for a Higgs boson produced with a pair of top quarks and decaying to a pair of bottom quarks, $t\bar{t}H(H \to b\bar{b})$, with 36.1 fb^{-1} of pp collision data at $\sqrt{s} = 13$ TeV collected by the ATLAS experiment. This chapter is mostly based on an ATLAS paper [139] of which I was the co-editor. The combinations of this search with other $t\bar{t}H$ channels leading to the observation of the $t\bar{t}H$ process [140], and with other $H \to b\bar{b}$ channels leading to the observation of the $H \to b\bar{b}$ process [141], are also presented.

2.1 Introduction

After the discovery of the Higgs boson [142, 143, 144] in 2012 by the ATLAS [28] and CMS [29] collaborations, attention has turned to more detailed measurements of its properties and couplings as a means of testing the predictions of the Standard Model (SM) [12, 13, 14]. In particular, the coupling to the top quark, the heaviest particle in the SM, could be very sensitive to effects of physics beyond the SM (BSM) [145]. Assuming that no BSM particle couples to the Higgs boson, the ATLAS and CMS experiments measured a value of the top-quark's Yukawa coupling equal to 0.87 ± 0.15 times the SM prediction by combining [55] their respective Higgs-boson measurements from the Run 1 dataset collected at center-of-mass energies of 7 TeV and 8 TeV at the Large Hadron Collider (LHC). This measurement relies largely on the gluon–gluon fusion production mode and on the decay mode to photons, which both depend on loop contributions with a top quark. If no assumption is made about the particle content of such loop contributions, then the top-quark coupling is only determined through tree-level processes, and a value of 1.4 ± 0.2 times the SM prediction is obtained.

Higgs-boson production in association with a pair of top quarks, $t\bar{t}H$, is the most favorable production mode for a direct measurement of the top-quark's Yukawa coupling [146, 147, 148, 149]. Although this production mode only contributes around 1% of the total Higgs-boson production cross-section [150], the top quarks in the final state offer a distinctive signature and allow many Higgs-boson decay modes to be accessed. Of these, the decay to two b-quarks is predicted to have a branching fraction of about 58% [150], the largest Higgs-boson decay mode. This decay mode is sensitive to the b-quark's Yukawa coupling, the second largest in the SM. In order to select events at the trigger level and reduce the backgrounds, the analysis targets events in which one or both top

quarks decay semi-leptonically, producing an electron or a muon.[1] The main experimental challenges for this channel are the low combined efficiency to reconstruct and identify all final-state particles, the combinatorial ambiguity from the many jets containing b-hadrons in the final state which makes it difficult to reconstruct the Higgs boson, and the large backgrounds from the production of $t\bar{t}$ + jets especially when the associated jets stem from b- or c-quarks. Some representative Feynman diagrams for the $t\bar{t}H$ signal are shown in Figure 2.1, together with the dominant $t\bar{t}+b\bar{b}$ background.

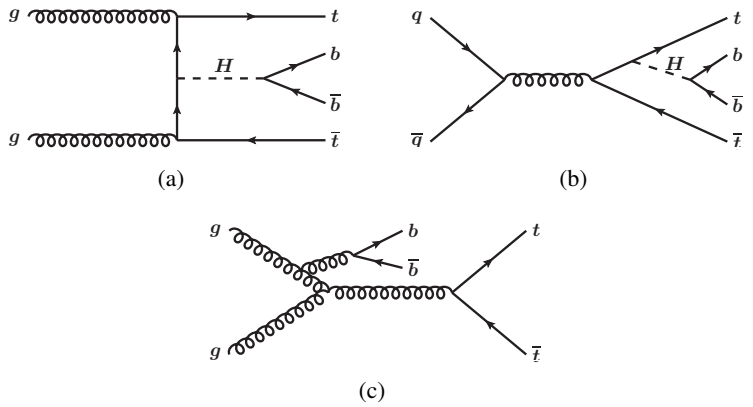

Figure 2.1: Representative tree-level Feynman diagrams for (a) t-channel and (b) s-channel production of the Higgs boson in association with a top-quark pair ($t\bar{t}H$) and the subsequent decay of the Higgs boson to $b\bar{b}$, and (c) for the main background, $t\bar{t}+b\bar{b}$.

The ATLAS collaboration searched for $t\bar{t}H$ production with Higgs-boson decays to $b\bar{b}$ at $\sqrt{s}=$ 8 TeV, using $t\bar{t}$ decays with at least one lepton [151] or no leptons [152]. A combined signal strength $\mu=\sigma/\sigma_{\text{SM}}$ of 1.4 ± 1.0 was measured. The CMS collaboration searched for the same process at $\sqrt{s}=7$ TeV and $\sqrt{s}=8$ TeV using $t\bar{t}$ decays with a single-lepton or dilepton in the final state, obtaining a signal strength of 0.7 ± 1.9 [153]. These results were combined with each other, and with results for Higgs boson decay to vector bosons, to τ-leptons or to photons [154, 155, 153], resulting in an observed (expected) significance of 4.4 (2.0) standard deviations for $t\bar{t}H$ production [55]. The measured signal strength is $2.3^{+0.7}_{-0.6}$.

In this chapter, a search for $t\bar{t}H$ production with 36.1 fb^{-1} of pp collision data at $\sqrt{s}=13$ TeV is presented. The analysis targets Higgs-boson decays to b-quarks, but all the decay modes are considered and may contribute to the signal. Events with either one or two leptons are taken into account, and exclusive analysis categories are defined according to the number of leptons, the number of jets, and the value of a b-tagging discriminant which provides a measure of how likely a jet is to contain a b-hadron. In the single-lepton channel, a specific category, referred to as 'boosted' in the following, is designed to select events containing a Higgs boson and with at least one of the two top quarks produced at high transverse momentum. In the analysis categories with the largest signal contributions, multivariate discriminants are used to classify events as more or less signal-like. The signal-rich categories are analyzed together with the signal-depleted ones in a combined profile likelihood fit that simultaneously determines the event yields for the signal and for the most important background components, while constraining the overall background model within the assigned systematic uncertainties.

[1] Throughout this chapter, 'lepton' refers to electron or muon, unless otherwise specified. Electrons and muons from the decay of a τ itself originating from a W boson are included.

The chapter is organized as follows. Section 2.2 summarizes the selection criteria applied to events and physics objects. The signal and background modeling are presented in Section 2.3. Section 2.4 describes the event categorization while Section 2.5 presents the multivariate analysis techniques. The systematic uncertainties are summarized in Section 2.6. Section 2.7 presents the results. The combination of the results from the $t\bar{t}H(H \to b\bar{b})$ channel with the results from other analyses targeting $t\bar{t}H$ production with different final states is reported in section 2.8 and the combination of all $H \to b\bar{b}$ channels is reported in section 2.9. Section 2.10 gives the conclusions.

2.2 Event selection

Events are selected from pp collisions at $\sqrt{s} = 13$ TeV recorded by the ATLAS detector in 2015 and 2016. Only events for which all relevant subsystems were operational are considered. Events are required to have at least one vertex with two or more tracks with transverse momentum $p_{\mathrm{T}} > 0.4$ GeV. The vertex with the largest sum of the squares of the transverse momenta of associated tracks is taken as the primary vertex. The event reconstruction is affected by multiple pp collisions in a single bunch crossing and by collisions in neighboring bunch crossings, referred to as 'pileup'. The number of interactions per bunch crossing in this dataset ranges from about 8 to 45 interactions. The dataset corresponds to an integrated luminosity of 3.2 ± 0.1 fb^{-1} recorded in 2015 and 32.9 ± 0.7 fb^{-1} recorded in 2016, for a total of 36.1 ± 0.8 fb^{-1} [156].

Events in both the single-lepton and dilepton channels were recorded using single-lepton triggers. Events are required to fire triggers with either low lepton p_{T} thresholds and a lepton isolation requirement, or with higher thresholds but with a looser identification criterion and without any isolation requirement. The lowest p_{T} threshold used for muons is 20 (26) GeV in 2015 (2016), while for electrons the threshold is 24 (26) GeV.

Electrons are reconstructed from energy deposits (clusters) in the electromagnetic calorimeter matched to tracks reconstructed in the ID [157, 158] and are required to have $p_{\mathrm{T}} > 10$ GeV and $|\eta| < 2.47$. Candidates in the calorimeter barrel–endcap transition region ($1.37 < |\eta| < 1.52$) are excluded. Electrons must satisfy the *loose* identification criterion described in Ref. [158], based on a likelihood discriminant combining observables related to the shower shape in the calorimeter and to the track matching the electromagnetic cluster. Muons are reconstructed from either track segments or full tracks in the MS which are matched to tracks in the ID [159]. Tracks are then re-fitted using information from both detector systems. Muons are required to have $p_{\mathrm{T}} > 10$ GeV and $|\eta| < 2.5$. To reduce the contribution of leptons from hadronic decays (non-prompt leptons), both electrons and muons must satisfy isolation criteria based on information from both the tracker and the calorimeter. The *loose* lepton isolation working point [158, 159] is used. Finally, lepton tracks must match the primary vertex of the event: the longitudinal impact parameter $\mathrm{IP_z}$ is required to satisfy $|\mathrm{IP_z}| < 0.5$ mm, while the transverse impact parameter significance, $|\mathrm{IP}_{r\phi}|/\sigma_{\mathrm{IP}_{r\phi}}$, must be less than 5 for electrons and 3 for muons.

Jets are reconstructed from three-dimensional topological energy clusters [160] in the calorimeter using the anti-k_t jet algorithm [100] implemented in the FastJet package [161] with a radius parameter of 0.4. Each topological cluster is calibrated to the electromagnetic scale response prior to jet reconstruction. The reconstructed jets are then calibrated to the jet energy scale derived from simulation and in situ corrections based on 13 TeV data [162]. After energy calibration, jets are required to have $p_{\mathrm{T}} > 25$ GeV and $|\eta| < 2.5$. Quality criteria are imposed to identify jets arising from non-collision sources or detector noise, and any event containing such a jet is removed [163]. Finally, to reduce the effect of pileup, an additional requirement is made using an algorithm that matches jets with $p_{\mathrm{T}} < 60$ GeV and $|\eta| < 2.4$ to tracks with $p_{\mathrm{T}} > 0.4$ GeV to identify jets consistent

with the primary vertex. This algorithm is known as jet vertex tagger [164], referred to as JVT in the remainder of this chapter.

Jets are tagged as containing b-hadrons through a multivariate b-tagging algorithm (MV2c10) that combines information from an impact-parameter-based algorithm, from the explicit reconstruction of an inclusive secondary vertex and from a multi-vertex fitter that attempts to reconstruct the b- to c-hadron decay chain [165, 166]. This algorithm is optimized to efficiently select jets containing b-hadrons (b-jets) and separate them from jets containing c-hadrons (c-jets), jets containing hadronically decaying τ-leptons (τ-jets) and from other jets (light jets). Four working points are defined by different MV2c10 discriminant output thresholds and are referred to in the following as *loose*, *medium*, *tight* and *very tight*. The efficiency for b-jets with $p_{\mathrm{T}} > 20$ GeV in simulated $t\bar{t}$ events to pass the different working points are 85%, 77%, 70% and 60%, respectively, corresponding to rejection factors[2] of c-jets in the range 3–35 and of light jets in the range 30–1500. A b-tagging discriminant value is assigned to each jet according to the tightest working point it satisfies, ranging from 1 for a jet that does not satisfy any of the b-tagging criteria defined by the considered working points up to 5 for jets satisfying the *very tight* criteria. This b-tagging discriminant is used to categorize selected events as discussed in Section 2.4 and as an input to multivariate analysis techniques described in Section 2.5.

Hadronically decaying τ leptons (τ_{had}) are distinguished from jets using the track multiplicity and a multivariate discriminant based on the track collimation, further jet substructure, and kinematic information [167]. These τ_{had} candidates are required to have $p_{\mathrm{T}} > 25$ GeV, $|\eta| < 2.5$ and pass the *Medium* τ-identification working point.

To avoid counting a single detector response as more than one lepton or jet, an overlap removal procedure is adopted. To prevent double-counting of electron energy deposits as jets, the closest jet within $\Delta R_y = \sqrt{(\Delta y)^2 + (\Delta\phi)^2} = 0.2$ of a selected electron is removed.[3] If the nearest jet surviving that selection is within $\Delta R_y = 0.4$ of the electron, the electron is discarded. Muons are removed if they are separated from the nearest jet by $\Delta R_y < 0.4$, which reduces the background from heavy-flavor decays inside jets. However, if this jet has fewer than three associated tracks, the muon is kept and the jet is removed instead; this avoids an inefficiency for high-energy muons undergoing significant energy loss in the calorimeter. A τ_{had} candidate is rejected if it is separated by $\Delta R_y < 0.2$ from any selected electron or muon.

The missing transverse momentum in the event is defined as the negative vector sum of the p_{T} of all the selected electrons, muons and jets described above, with an extra term added to account for energy in the event which is not associated with any of these. This extra term, referred to as the 'soft term' in the following, is calculated from ID tracks matched to the primary vertex to make it resilient to pileup contamination [168, 169]. The missing transverse momentum is not used for event selection but it is included in the inputs to the multivariate discriminants that are built in the most sensitive analysis categories.

For the boosted category, the selected jets are used as inputs for further jet reclustering [170] through an anti-k_t algorithm with a radius parameter of $R = 1.0$, resulting in a collection of large-R jets. Large-R jets with a reconstructed invariant mass lower than 50 GeV are removed. The resulting large-R jets are used to identify top quarks and Higgs bosons in signal events when these have high transverse momenta (boosted) and decay into collimated hadronic final states. Boosted Higgs-boson candidates are required to have $p_{\mathrm{T}} > 200$ GeV and contain at least two constituent jets, among which at least two are b-tagged at the *loose* working point. If more than one boosted Higgs-boson

[2] The rejection factor is defined as the inverse of the efficiency to pass a given b-tagging working point.

[3] The rapidity is defined as $y = \frac{1}{2}\ln\frac{E+p_z}{E-p_z}$ where E is the energy and p_z is the longitudinal component of the momentum along the beam pipe.

candidate is identified, the one with the highest sum of constituent-jet b-tagging discriminants is selected. Additional large-R jets are considered as potential boosted top-quark candidates. Boosted top-quark candidates are required to have $p_{\mathrm{T}} > 250$ GeV, exactly one constituent jet satisfying the *loose* b-tagging working point plus at least one additional constituent jet which is not b-tagged. If more than one boosted top-quark candidate is identified, the one with the highest mass is selected.

Events are required to have at least one reconstructed lepton with $p_{\mathrm{T}} > 27$ GeV matching a lepton with the same flavor reconstructed by the trigger algorithm within $\Delta R < 0.15$. Events in the dilepton channel must have exactly two leptons with opposite electric charge. The subleading lepton p_{T} must be above 15 GeV in the ee channel or above 10 GeV in the $e\mu$ and $\mu\mu$ channels. In the ee and $\mu\mu$ channels, the dilepton invariant mass must be above 15 GeV and outside of the Z-boson mass window 83–99 GeV. To maintain orthogonality with other $t\bar{t}H$ search channels [171], dilepton events are vetoed if they contain one or more τ_{had} candidates. Events enter the single-lepton channel if they contain exactly one lepton with $p_{\mathrm{T}} > 27$ GeV and no other selected leptons with $p_{\mathrm{T}} > 10$ GeV. In the single-lepton channel, events are removed if they contain two or more τ_{had} candidates.

To improve the purity in events passing the above selection, selected leptons are further required to satisfy additional identification and isolation criteria, otherwise the corresponding events are removed. For electrons, the *tight* identification criterion based on a likelihood discriminant [158] is used, while for muons the *medium* identification criterion [159] is used. Both the electrons and muons are required to satisfy the Gradient isolation criteria [158, 159], which become more stringent as the p_{T} of the leptons considered drops.

Finally, events in the dilepton channel must have at least three jets, of which at least two must be b-tagged at the *medium* working point. Single-lepton events containing at least one boosted Higgs-boson candidate, at least one boosted top-quark candidate and at least one additional jet b-tagged at the *loose* working point enter the boosted category. Events that do not enter the boosted category and have at least five jets, with at least two of them b-tagged at the *very tight* working point or three of them b-tagged at the *medium* working point, are classified as 'resolved' single-lepton events. The fraction of simulated $t\bar{t}H(H \to b\bar{b})$ events passing the dilepton event selection is 2.5%. These fractions are 8.7% for the resolved single-lepton channel and 0.1% for the boosted category.

2.3 Signal and background modeling

This section describes the simulation and data-driven techniques used to model the $t\bar{t}H$ signal and the background processes, to train the multivariate discriminants and to define the templates for the signal extraction fit. In this analysis, most Monte Carlo (MC) samples were produced using the full ATLAS detector simulation [97] based on GEANT4 [98]. A faster simulation, where the full GEANT 4 simulation of the calorimeter response is replaced by a detailed parameterization of the shower shapes [172], was adopted for some of the samples used to estimate modeling systematic uncertainties. To simulate the effects of pileup, additional interactions were generated using PYTHIA 8.186 [173] and overlaid onto the simulated hard-scatter event. Simulated events are reweighted to match the pileup conditions observed in the data. All simulated events are processed through the same reconstruction algorithms and analysis chain as the data. In the simulation, the top-quark mass is assumed to be $m_t = 172.5$ GeV. Decays of b- and c-hadrons were performed by EVTGEN v1.2.0 [83], except in samples simulated by the SHERPA event generator.

2.3.1 Signal modeling

The $t\bar{t}H$ signal process was modeled using MADGRAPH5_aMC@NLO [174] (referred to in the following as MG5_aMC@NLO) version 2.3.2 for the matrix element (ME) calculation at next-to-leading-order (NLO) accuracy in quantum chromodynamics (QCD), interfaced to the PYTHIA 8.210 parton shower (PS) and hadronization model using the A14 set of tuned parameters [175]. The NNPDF3.0NLO parton distribution function (PDF) set [136] was used, and the factorization and renormalization scales were set to $\mu_F = \mu_R = H_T/2$, with H_T defined as the scalar sum of the transverse masses $\sqrt{p_T^2 + m^2}$ of all final-state particles. The top quarks were decayed using MADSPIN [176], preserving all spin correlations. The Higgs-boson mass was set to 125 GeV and all decay modes were considered. The $t\bar{t}H$ cross-section of 507^{+35}_{-50} fb was computed [177, 178, 179, 180, 181, 150] at NLO accuracy in QCD and includes NLO electroweak corrections. The branching fractions were calculated using HDECAY [182, 150].

2.3.2 $t\bar{t}$ + jets background

The nominal sample used to model the $t\bar{t}$ background was generated using the POWHEG-BOX v2 NLO event generator [84, 85, 86, 183], referred to as POWHEG in the following, with the NNPDF3.0NLO PDF set. The h_{damp} parameter, which controls the transverse momentum of the first gluon emission beyond the Born configuration, was set to 1.5 times the top-quark mass [184]. The parton shower and the hadronization were modeled by PYTHIA 8.210 with the A14 set of tuned parameters. The renormalization and factorization scales were set to the transverse mass of the top quark, defined as $m_{T,t} = \sqrt{m_t^2 + p_{T,t}^2}$, where $p_{T,t}$ is the transverse momentum of the top quark in the $t\bar{t}$ center-of-mass reference frame. The sample is normalized using the predicted cross-section of 832^{+46}_{-51} pb, calculated with the Top++2.0 program [185] at next-to-next-to-leading order (NNLO) in perturbative QCD including resummation of next-to-next-to-leading logarithmic (NNLL) soft gluon terms [94, 94, 186, 187, 188]. Alternative $t\bar{t}$ samples used to derive systematic uncertainties are described in Section 2.6.

The $t\bar{t}$ + jets background is categorized according to the flavor of additional jets in the event, using the same procedure as described in Ref. [151]. Generator-level particle jets are reconstructed from stable particles (mean lifetime $\tau > 3 \times 10^{-11}$ seconds) using the anti-k_t algorithm with a radius parameter $R = 0.4$, and are required to have $p_T > 15$ GeV and $|\eta| < 2.5$. This categorization employs a jet flavor-labeling procedure that is more refined than the one described in Section 2.2. The flavor of a jet is determined by counting the number of b- or c-hadrons within $\Delta R < 0.4$ of the jet axis. Jets matched to exactly one weakly decaying b-hadron, with p_T above 5 GeV, are labeled single-b-jets, while those matched to two or more b-hadrons are labeled B-jets (with no p_T requirement on the second hadron); single-c- and C-jets are defined analogously, only considering jets not already defined as single-b- or B-jets. Events that have at least one single-b- or B-jet, not counting heavy-flavor jets from top-quark or W-boson decays, are labeled as $t\bar{t} + \geq 1b$; those with no single-b- or B-jet but at least one single-c- or C-jet are labeled as $t\bar{t} + \geq 1c$. Finally, events not containing any heavy-flavor jets aside from those from top-quark or W-boson decays are labeled as $t\bar{t}$ + light. This classification is used to define the background categories in the likelihood fit. A finer classification is then used to assign correction factors and estimate uncertainties: events with exactly two single-b-jets are labeled as $t\bar{t} + b\bar{b}$, those with only one single-b-jet are labeled as $t\bar{t} + b$, and those with only one B-jet are labeled as $t\bar{t} + B$, the rest of the $t\bar{t} + \geq 1b$ events being labeled as $t\bar{t} + \geq 3b$. Events with additional b-jets entirely originating from multi-parton interactions (MPI) or b-jets from final-state radiation (FSR), i.e. originating from gluon radiation from the top-quark decay products, are considered separately in the $t\bar{t} + b$ (MPI/FSR) subcategory. Background events from $t\bar{t}$ containing

extra c-jets are divided analogously.

To model the dominant $t\bar{t}+\geq 1b$ background with the highest available precision, the relative contributions of the different subcategories, $t\bar{t}+\geq 3b$, $t\bar{t}+b\bar{b}$, $t\bar{t}+B$ and $t\bar{t}+b$, in the POWHEG+PYTHIA 8 sample described above are scaled to match those predicted by an NLO $t\bar{t}b\bar{b}$ sample including parton showering and hadronization [189], generated with SHERPA+OPENLOOPS [190, 191]. The sample was produced with SHERPA version 2.1.1 and the CT10 four-flavor (4F) scheme PDF set [192, 193]. The renormalization scale for this sample was set to the CMMPS value, $\mu_{\text{CMMPS}} = \prod_{i=t,\bar{t},b,\bar{b}} E_{\text{T},i}^{1/4}$ [189], while the factorization scale was set to $H_{\text{T}}/2 = \frac{1}{2}\sum_{i=t,\bar{t},b,\bar{b}} E_{\text{T},i}$. The resummation scale μ_{Q}, which sets an upper bound for the hardness of the parton-shower emissions, was also set to $H_{\text{T}}/2$. This sample, referred to as 'SHERPA4F' in the remainder of this article, employs a description of the kinematics of the two additional b-jets with NLO precision in QCD, taking into account the b-quark mass, and is therefore the most precise MC prediction for the $t\bar{t}+\geq 1b$ process available at present. Topologies that are not included in this NLO calculation but are labeled as $t\bar{t}+\geq 1b$, i.e. events in the $t\bar{t}+b$ (MPI/FSR) subcategory, are not scaled.

Figure 2.2 shows the predicted fractions for each of the $t\bar{t}+\geq 1b$ subcategories, with the POWHEG+PYTHIA 8 inclusive $t\bar{t}$ sample compared to the $t\bar{t}+b\bar{b}$ SHERPA4F sample. The $t\bar{t}+b$ (MPI/FSR) subcategory is not present in the $t\bar{t}+b\bar{b}$ SHERPA4F sample and accounts for 10% of the events in the POWHEG+PYTHIA 8 $t\bar{t}+\geq 1b$ sample.

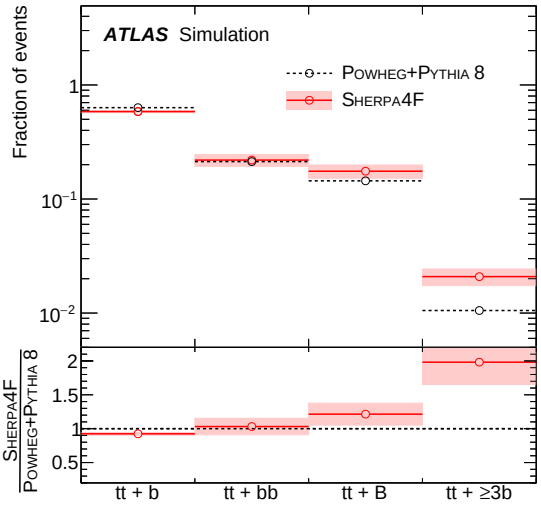

Figure 2.2: The relative predicted fractions of the $t\bar{t}+b$, $t\bar{t}+b\bar{b}$, $t\bar{t}+B$ and $t\bar{t}+\geq 3b$ subcategories before any event selection. The prediction from the inclusive POWHEG+PYTHIA 8 sample is compared to the four-flavor $t\bar{t}b\bar{b}$ calculation from SHERPA4F, with its uncertainties (from a combination of the sources discussed in Section 2.6) shown as the shaded area. The fractions are normalized to the sum of the four contributions shown here, without considering the $t\bar{t}+b$ (MPI/FSR) subcategory as part of the total.

2.3.3 Other backgrounds

Samples of $t\bar{t}W$ and $t\bar{t}Z$ ($t\bar{t}V$) events were generated with an NLO matrix element using MG5_aMC@NLO interfaced to PYTHIA 8.210 with the NNPDF3.0NLO PDF and the A14 parameter set.

Samples of Wt and s-channel single-top-quark backgrounds were generated with POWHEG-BOX v1 at NLO accuracy using the CT10 PDF set. Overlap between the $t\bar{t}$ and Wt final states was handled using the 'diagram removal' scheme [194]. The t-channel single-top-quark events were generated using the POWHEG-BOX v1 event generator at NLO accuracy with the four-flavor PDF set CT10 4F. For this process, the top quarks were decayed using MADSPIN. All single-top-quark samples were interfaced to PYTHIA 6.428 [79] with the Perugia 2012 set of tuned parameters [195]. The single-top-quark Wt, t- and s-channel samples are normalized using the approximate NNLO theoretical cross-sections [196, 197, 198].

Samples of W/Z production in association with jets were generated using SHERPA 2.2.1. The matrix elements were calculated for up to two partons at NLO and four partons at leading order (LO) using COMIX [199] and OPENLOOPS, and merged with the SHERPA parton shower [200] using the ME+PS@NLO prescription [201]. The NNPDF3.0NNLO PDF set was used in conjunction with dedicated parton-shower tuning. The W/Z + jet events are normalized using the NNLO cross-sections [202]. For Z + jet events, the normalization of the heavy-flavor component is corrected by a factor 1.3, extracted from dedicated control regions in data, defined by requiring two opposite-charge same-flavor leptons (e^+e^- or $\mu^+\mu^-$) with an invariant mass, $m_{\ell\ell}$, inside the Z-boson mass window 83–99 GeV. The diboson + jet samples were generated using SHERPA 2.1.1 as described in Ref. [203].

Higgs-boson production in association with a single top quark is rare in the SM, but is included in the analysis and treated as background. Samples of single top quarks produced in association with a W boson and with a Higgs boson, tWH, were produced with MG5_aMC@NLO interfaced to HERWIG++ [81] with the CTEQ6L1 PDF set. Samples of single top quarks plus Higgs boson plus jets, $tHqb$, were produced at LO with MG5_aMC@NLO interfaced to PYTHIA 8, using the CT10 4F scheme PDF set. The other Higgs-boson production modes were found to be negligible and are not considered. Four-top production ($t\bar{t}t\bar{t}$) as well as $t\bar{t}WW$ events were generated with MG5_aMC@NLO with LO accuracy and interfaced with PYTHIA 8. Events from tZ production were also generated with MG5_aMC@NLO with LO accuracy, but interfaced with PYTHIA 6. The process tZW was also generated with MG5_aMC@NLO interfaced with PYTHIA 8, but with NLO accuracy.

In the single-lepton channel, the background from events with a jet or a photon misidentified as a lepton (hereafter referred to as fake lepton) or non-prompt lepton is estimated directly from data using a matrix method [204]. A data sample enhanced in fake and non-prompt leptons is selected by removing the lepton isolation requirements and, for electrons, loosening the identification criteria. Next, the efficiency for these 'loose' leptons to satisfy the nominal selection ('tight') criteria is measured in data, separately for real prompt leptons and for fake or non-prompt leptons. For real prompt leptons the efficiency is measured in Z-boson events, while for fake and non-prompt leptons it is estimated from events with low missing transverse momentum and low values of the reconstructed leptonic W-boson transverse mass.[4] With this information, the number of fake or non-prompt leptons satisfying the tight criteria can be calculated by inverting the matrix defined by the two equations:

$$N^{\mathrm{l}} = N^{\mathrm{l}}_{\mathrm{r}} + N^{\mathrm{l}}_{\mathrm{f}}, \qquad N^{\mathrm{t}} = \varepsilon_{\mathrm{r}} N^{\mathrm{l}}_{\mathrm{r}} + \varepsilon_{\mathrm{f}} N^{\mathrm{l}}_{\mathrm{f}},$$

where N^{l} (N^{t}) is the number of events observed in data passing the loose (tight) lepton selection, $N^{\mathrm{l}}_{\mathrm{r}}$ ($N^{\mathrm{l}}_{\mathrm{f}}$) is the number of events with a real prompt (fake or non-prompt) lepton in the loose lepton sample, and ε_{r} (ε_{f}) is the efficiency for these events to pass the tight lepton selection. By generalizing

[4] The reconstructed leptonic W-boson transverse mass is defined as $\sqrt{2p_{\mathrm{T}}^{\mathrm{lepton}} E_{\mathrm{T}}^{\mathrm{miss}} (1-\cos\Delta\phi)}$, where $p_{\mathrm{T}}^{\mathrm{lepton}}$ is the transverse momentum of the selected lepton, $E_{\mathrm{T}}^{\mathrm{miss}}$ is the magnitude of the missing transverse momentum and $\Delta\phi$ is the azimuthal angle between the lepton and the missing transverse momentum.

the resulting formula to extract $\varepsilon_{\mathrm{f}} N_{\mathrm{f}}^{\mathrm{l}}$, a weight is assigned to each event selected in the loose lepton data sample, providing a prediction for both the yields and the kinematic distribution shapes for the fake and non-prompt lepton background. In the three most sensitive single-lepton signal regions, $\mathrm{SR}_1^{\geq 6\mathrm{j}}$, $\mathrm{SR}_2^{\geq 6\mathrm{j}}$ and $\mathrm{SR}_1^{5\mathrm{j}}$ (see Section 2.4), the contribution from events with a fake or non-prompt lepton is found to be very small, consistent with zero, and is neglected. In the dilepton channel, this background is estimated from simulation and is normalized to data in a control region with two same-sign leptons.

All background samples described in this section, apart from the $t\bar{t}V$ samples, are referred to as 'non-$t\bar{t}$' and grouped together in the figures and tables. The contribution to the total background prediction from non-$t\bar{t}$ varies between 4% and 15% depending on the considered signal or control region.

2.4 Event categorization

After the selection, the data sample is dominated by background from $t\bar{t}$ events. In order to take advantage of the higher jet and b-jet multiplicities of the $t\bar{t}H$ signal process, events are classified into non-overlapping analysis categories based on the total number of jets, as well as the number of b-tagged jets at the four working points. Events in the boosted single-lepton category are not further categorized due to the small number of selected events in this category. Events in the dilepton (resolved single-lepton) channel are first classified according to whether the number of jets is exactly three (five) or at least four (six). These events are then further subdivided into analysis categories, depending on the number of jets tagged at the four b-tagging working points, or, equivalently, on the values of the b-tagging discriminant for the jets. The b-tagging requirements are optimized in order to obtain categories enriched in one of the relevant sample components: $t\bar{t}H$ plus $t\bar{t}+b\bar{b}$, $t\bar{t}+b$, $t\bar{t}+\geq 1c$ and $t\bar{t}+$light. The analysis categories where $t\bar{t}H$ and $t\bar{t}+b\bar{b}$ are enhanced relative to the other backgrounds are referred to as 'signal regions'; in these, multivariate techniques are used to further separate the $t\bar{t}H$ signal from the background events. The remaining analysis categories are referred to as 'control regions'; no attempt is made to separate the signal from the background in these analysis categories, but they provide stringent constraints on backgrounds and systematic uncertainties in a combined fit with the signal regions.

In the dilepton channel, three signal regions are defined, with different levels of purity for the $t\bar{t}H$ and $t\bar{t}+b\bar{b}$ components. The signal region with the highest $t\bar{t}H$ signal purity, referred to as $\mathrm{SR}_1^{\geq 4\mathrm{j}}$, is defined by requiring at least four jets of which three are b-tagged at the *very tight* working point and another one is b-tagged at the *tight* working point. The other two signal regions, $\mathrm{SR}_2^{\geq 4\mathrm{j}}$ and $\mathrm{SR}_3^{\geq 4\mathrm{j}}$, are defined with looser b-tagging requirements. The remaining dilepton events with at least four jets are divided into two control regions, one enriched in $t\bar{t}+$light, $\mathrm{CR}_{t\bar{t}+\mathrm{light}}^{\geq 4\mathrm{j}}$, and one in $t\bar{t}+\geq 1c$, $\mathrm{CR}_{t\bar{t}+\geq 1c}^{\geq 4\mathrm{j}}$. Dilepton events with three jets are split into two control regions, $\mathrm{CR}_{t\bar{t}+\mathrm{light}}^{3\mathrm{j}}$ and $\mathrm{CR}_{t\bar{t}+\geq 1b}^{3\mathrm{j}}$, enriched in $t\bar{t}+$light and $t\bar{t}+\geq 1b$, respectively. The detailed definition of the signal and control regions for the dilepton channel is presented in Figure 2.3.

In the single-lepton channel, five signal regions are formed from events passing the resolved selection, three requiring at least six jets, and the other two requiring exactly five jets. They are referred to as $\mathrm{SR}_1^{\geq 6\mathrm{j}}$, $\mathrm{SR}_2^{\geq 6\mathrm{j}}$, $\mathrm{SR}_3^{\geq 6\mathrm{j}}$, $\mathrm{SR}_1^{5\mathrm{j}}$ and $\mathrm{SR}_2^{5\mathrm{j}}$. The two purest signal regions, $\mathrm{SR}_1^{\geq 6\mathrm{j}}$ and $\mathrm{SR}_1^{5\mathrm{j}}$, require four b-tagged jets at the *very tight* working point, while looser requirements are applied in the other signal regions. Events passing the boosted single-lepton selection form a sixth signal region, $\mathrm{SR}^{\mathrm{boosted}}$. The remaining events with at least six jets are then categorized into three control regions enriched in $t\bar{t}+$light, $t\bar{t}+\geq 1c$ and $t\bar{t}+b$, referred to as $\mathrm{CR}_{t\bar{t}+\mathrm{light}}^{\geq 6\mathrm{j}}$, $\mathrm{CR}_{t\bar{t}+\geq 1c}^{\geq 6\mathrm{j}}$, $\mathrm{CR}_{t\bar{t}+b}^{\geq 6\mathrm{j}}$,

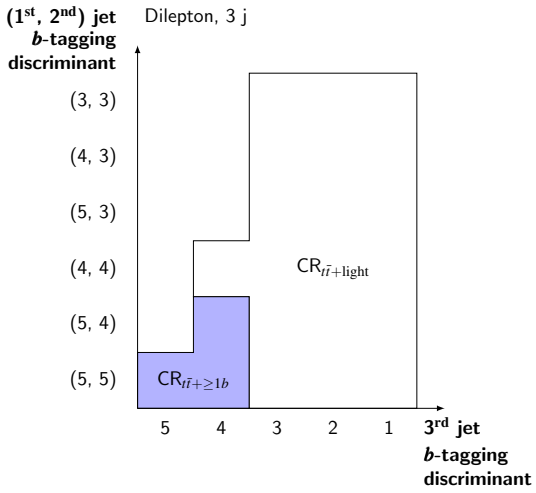

(a)

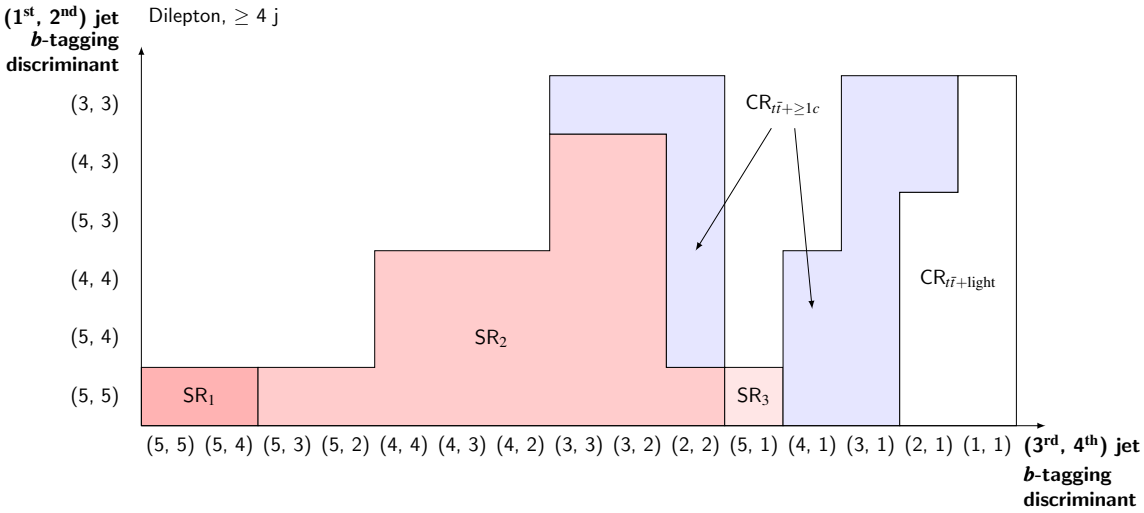

(b)

Figure 2.3: Definition of the (a) three-jet and (b) four-jet signal and control regions in the dilepton channel, as a function of the b-tagging discriminant defined in Section 2.2. The vertical axis shows the values of the b-tagging discriminant for the first two jets, while the horizontal axis shows these values for (a) the third jet or (b) the third and fourth jets. The jets are ordered according to their value of the b-tagging discriminant in descending order.

respectively. Analogously, remaining events with exactly five jets are categorized into other three control regions, referred to as $\text{CR}^{5\text{j}}_{t\bar{t}+\text{light}}$, $\text{CR}^{5\text{j}}_{t\bar{t}+\geq 1c}$ and $\text{CR}^{5\text{j}}_{t\bar{t}+b}$. The detailed definition of the signal and control regions for the resolved single-lepton channel is presented in Figure 2.4.

Figures 2.5 and 2.6 show, respectively, the fraction of the different background components as well as the $t\bar{t}H$ signal purity for each of the signal and control regions in the dilepton and single-lepton channels. The $H \to b\bar{b}$ decay represents 89% of the $t\bar{t}H$ signal events in the signal regions of the dilepton channel, 96% in the signal regions of the resolved single-lepton channel and 86% in the boosted signal region. The predicted event yields in each of the analysis categories, broken down into the different signal and background contributions and compared to the observed yields

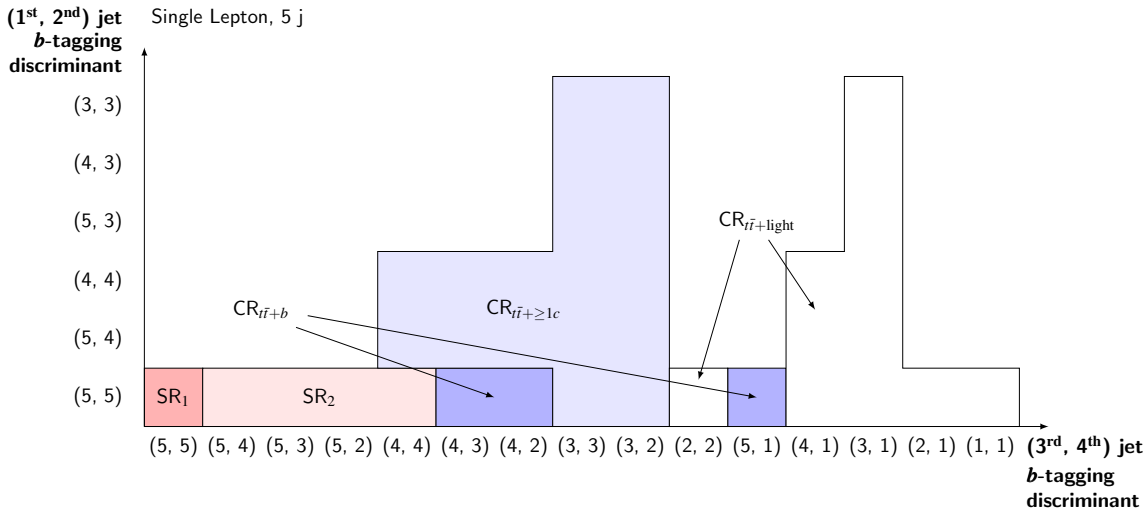

(a)

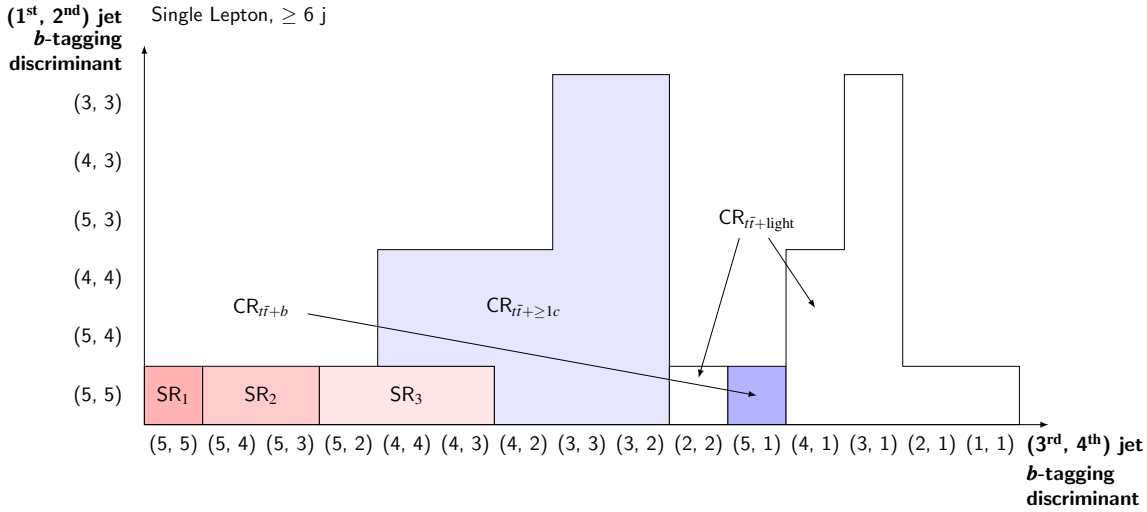

(b)

Figure 2.4: Definition of the (a) five-jet and (b) six-jet signal and control regions in the single-lepton resolved channel, as a function of the b-tagging discriminant defined in Section 2.2. The vertical axis shows the values of the b-tagging discriminant for the first two jets, while the horizontal axis shows these values for the third and fourth jets. The jets are ordered according to their value of the b-tagging discriminant in descending order.

in data, are reported in Tables 2.1, 2.2 and 2.3. Both the pre-fit and post-fit predictions are shown, where post-fit refers to the combined fit to the dilepton and single-lepton channels with the signal-plus-background hypothesis, reported in Section 2.7. The total uncertainties of each of the signal and background components, and of the total prediction are also reported.

Table 2.1: Event yields in the dilepton channel (top) control regions and (bottom) signal regions. Post-fit yields are after the combined fit in all channels to data. The uncertainties are the sum in quadrature of statistical and systematic uncertainties in the yields. In the post-fit case, these uncertainties are computed taking into account correlations among nuisance parameters and among the normalization of different processes. The uncertainty in the $t\bar{t}+\geq 1b$ and $t\bar{t}+\geq 1c$ normalization is not defined pre-fit and therefore only included in the post-fit uncertainties; the reported prefit uncertainties on the $t\bar{t}+\geq 1b$ and $t\bar{t}+\geq 1c$ components arise only from acceptance effects. For the $t\bar{t}H$ signal, the pre-fit yield values correspond to the theoretical prediction and corresponding uncertainties, while the post-fit yield and uncertainties correspond to those in the signal-strength measurement.

Sample	$\mathrm{CR}^{3\mathrm{j}}_{t\bar{t}+\mathrm{light}}$		$\mathrm{CR}^{3\mathrm{j}}_{t\bar{t}+\geq 1b}$		$\mathrm{CR}^{\geq 4\mathrm{j}}_{t\bar{t}+\mathrm{light}}$		$\mathrm{CR}^{\geq 4\mathrm{j}}_{t\bar{t}+\geq 1c}$	
	Pre-fit	Post-fit	Pre-fit	Post-fit	Pre-fit	Post-fit	Pre-fit	Post-fit
$t\bar{t}H$	32.2 ± 3.8	27 ± 20	8.7 ± 1.1	7.3 ± 5.4	114 ± 11	95 ± 70	35.3 ± 3.6	29 ± 22
$t\bar{t}$ + light	$63\,100 \pm 5500$	$59\,100 \pm 1400$	290 ± 110	255 ± 44	$42\,500 \pm 9700$	$37\,100 \pm 1300$	1730 ± 730	1410 ± 180
$t\bar{t}+\geq 1c$	4800 ± 2100	7700 ± 1100	360 ± 160	536 ± 89	6300 ± 2800	$10\,300 \pm 1400$	1410 ± 590	2160 ± 290
$t\bar{t}+\geq 1b$	2130 ± 230	2620 ± 240	710 ± 140	848 ± 75	2510 ± 280	2850 ± 290	1080 ± 120	1240 ± 110
$t\bar{t}+V$	113 ± 31	112 ± 29	7 ± 27	7 ± 30	350 ± 180	330 ± 170	52 ± 41	50 ± 39
Non-$t\bar{t}$	6300 ± 1500	6500 ± 1200	110 ± 29	112 ± 23	4700 ± 1100	4930 ± 910	420 ± 120	460 ± 100
Total	$76\,400 \pm 6500$	$76\,010 \pm 390$	1500 ± 260	1765 ± 60	$56\,000 \pm 11\,000$	$55\,650 \pm 420$	4700 ± 1100	5350 ± 120
Data	76 025		1744		55 627		5389	

Sample	$\mathrm{SR}^{\geq 4\mathrm{j}}_{3}$		$\mathrm{SR}^{\geq 4\mathrm{j}}_{2}$		$\mathrm{SR}^{\geq 4\mathrm{j}}_{1}$	
	Pre-fit	Post-fit	Pre-fit	Post-fit	Pre-fit	Post-fit
$t\bar{t}H$	21.9 ± 2.5	18 ± 13	29.1 ± 4.2	25 ± 18	15.6 ± 2.5	12.9 ± 9.5
$t\bar{t}$ + light	83 ± 41	95 ± 30	250 ± 110	215 ± 43	6.4 ± 9.9	11.1 ± 9.3
$t\bar{t}+\geq 1c$	235 ± 61	313 ± 53	340 ± 210	427 ± 89	12.6 ± 9.4	25.8 ± 7.8
$t\bar{t}+\geq 1b$	819 ± 85	917 ± 71	590 ± 96	669 ± 59	247 ± 61	263 ± 20
$t\bar{t}+V$	15 ± 35	15 ± 34	22 ± 38	22 ± 39	7 ± 56	7 ± 57
Non-$t\bar{t}$	75 ± 17	78 ± 16	115 ± 36	121 ± 29	13.6 ± 3.8	14.6 ± 3.8
Total	1250 ± 140	1436 ± 55	1350 ± 320	1479 ± 66	302 ± 85	334 ± 59
Data	1467		1444		319	

Table 2.2: Event yields in the single-lepton channel five-jet (top) control regions and (bottom) signal regions, including the boosted signal region. Post-fit yields are after the combined fit in all channels to data. The uncertainties are the sum in quadrature of statistical and systematic uncertainties in the yields. In the post-fit case, these uncertainties are computed taking into account correlations among nuisance parameters and among the normalization of different processes. The uncertainty in the $t\bar{t}+\geq 1b$ and $t\bar{t}+\geq 1c$ normalization is not defined pre-fit and therefore only included in the post-fit uncertainties; the reported prefit uncertainties on the $t\bar{t}+\geq 1b$ and $t\bar{t}+\geq 1c$ components arise only from acceptance effects. For the $t\bar{t}H$ signal, the pre-fit yield values correspond to the theoretical prediction and corresponding uncertainties, while the post-fit yield and uncertainties correspond to those in the signal-strength measurement.

Sample	$\mathrm{CR}^{5\mathrm{j}}_{t\bar{t}+\mathrm{light}}$		$\mathrm{CR}^{5\mathrm{j}}_{t\bar{t}+\geq 1c}$		$\mathrm{CR}^{5\mathrm{j}}_{t\bar{t}+b}$	
	Pre-fit	Post-fit	Pre-fit	Post-fit	Pre-fit	Post-fit
$t\bar{t}H$	224 ± 22	190 ± 140	18.7 ± 2.5	15 ± 12	68.0 ± 7.6	57 ± 42
$t\bar{t}$ + light	$197\,000 \pm 26\,000$	$179\,900 \pm 4900$	2580 ± 720	2300 ± 210	4250 ± 920	3560 ± 240
$t\bar{t}+\geq 1c$	$27\,500 \pm 4300$	$44\,100 \pm 5500$	1280 ± 500	1840 ± 250	1770 ± 270	2590 ± 390
$t\bar{t}+\geq 1b$	$11\,300 \pm 1100$	$13\,500 \pm 1300$	790 ± 130	944 ± 94	3400 ± 440	4030 ± 320
$t\bar{t}+V$	589 ± 55	584 ± 54	23.2 ± 4.1	21.3 ± 2.9	48.1 ± 5.9	46.6 ± 5.4
Non-$t\bar{t}$	$21\,300 \pm 4100$	$20\,900 \pm 3200$	520 ± 180	440 ± 100	960 ± 190	860 ± 160
Total	$258\,000 \pm 29\,000$	$259\,320 \pm 910$	5200 ± 1100	5560 ± 160	$10\,400 \pm 1300$	$11\,140 \pm 290$
Data	$259\,320$		5465		$11\,095$	

Sample	$\mathrm{SR}^{5\mathrm{j}}_{2}$		$\mathrm{SR}^{5\mathrm{j}}_{1}$		$\mathrm{SR}^{\mathrm{boosted}}$	
	Pre-fit	Post-fit	Pre-fit	Post-fit	Pre-fit	Post-fit
$t\bar{t}H$	40.1 ± 5.1	34 ± 25	15.9 ± 2.1	13.3 ± 9.8	16.9 ± 1.9	14 ± 10
$t\bar{t}$ + light	500 ± 210	393 ± 67	15 ± 33	12.5 ± 9.3	180 ± 120	112 ± 32
$t\bar{t}+\geq 1c$	436 ± 92	610 ± 100	30 ± 17	28 ± 14	168 ± 70	235 ± 39
$t\bar{t}+\geq 1b$	1230 ± 200	1450 ± 110	273 ± 53	335 ± 25	236 ± 89	229 ± 33
$t\bar{t}+V$	19.9 ± 2.9	19.7 ± 2.4	6.4 ± 1.3	6.4 ± 1.2	16.1 ± 2.9	16.6 ± 2.4
Non-$t\bar{t}$	269 ± 64	220 ± 52	54 ± 11	28.1 ± 8.4	104 ± 30	101 ± 26
Total	2440 ± 390	2724 ± 70	371 ± 68	423 ± 23	710 ± 200	708 ± 40
Data	2798		426		740	

Table 2.3: Event yields in the single-lepton channel six-jet (top) control regions and (bottom) signal regions. Post-fit yields are after the combined fit in all channels to data. The uncertainties are the sum in quadrature of statistical and systematic uncertainties in the yields. In the post-fit case, these uncertainties are computed taking into account correlations among nuisance parameters and among the normalization of different processes. The uncertainty in the $t\bar{t}+\geq 1b$ and $t\bar{t}+\geq 1c$ normalization is not defined pre-fit and therefore only included in the post-fit uncertainties; the reported prefit uncertainties on the $t\bar{t}+\geq 1b$ and $t\bar{t}+\geq 1c$ components arise only from acceptance effects. For the $t\bar{t}H$ signal, the pre-fit yield values correspond to the theoretical prediction and corresponding uncertainties, while the post-fit yield and uncertainties correspond to those in the signal-strength measurement.

Sample	$\mathrm{CR}^{\geq 6\mathrm{j}}_{t\bar{t}+\mathrm{light}}$		$\mathrm{CR}^{\geq 6\mathrm{j}}_{t\bar{t}+\geq 1c}$		$\mathrm{CR}^{\geq 6\mathrm{j}}_{t\bar{t}+b}$	
	Pre-fit	Post-fit	Pre-fit	Post-fit	Pre-fit	Post-fit
$t\bar{t}H$	450 ± 48	370 ± 280	102 ± 13	87 ± 64	100 ± 12	83 ± 61
$t\bar{t}$ + light	$125\,000 \pm 34\,000$	$108\,200 \pm 4300$	4300 ± 2000	3350 ± 430	2220 ± 520	1820 ± 170
$t\bar{t}+\geq 1c$	$28\,400 \pm 7200$	$45\,700 \pm 5100$	3600 ± 1300	5300 ± 680	1460 ± 330	2080 ± 300
$t\bar{t}+\geq 1b$	$13\,100 \pm 1800$	$14\,600 \pm 1400$	2660 ± 540	2950 ± 280	3670 ± 500	4080 ± 320
$t\bar{t}+V$	1010 ± 120	996 ± 91	118 ± 21	118 ± 14	70.5 ± 8.5	67.9 ± 7.2
Non-$t\bar{t}$	$12\,600 \pm 3000$	$11\,800 \pm 2000$	1060 ± 340	1000 ± 210	710 ± 160	600 ± 110
Total	$181\,000 \pm 39\,000$	$181\,690 \pm 860$	$11\,800 \pm 3200$	$12\,810 \pm 260$	8200 ± 1100	8730 ± 230
Data	181 706		12 778		8576	

Sample	$\mathrm{SR}_3^{\geq 6\mathrm{j}}$		$\mathrm{SR}_2^{\geq 6\mathrm{j}}$		$\mathrm{SR}_1^{\geq 6\mathrm{j}}$	
	Pre-fit	Post-fit	Pre-fit	Post-fit	Pre-fit	Post-fit
$t\bar{t}H$	85 ± 10	71 ± 52	81 ± 10	68 ± 50	62 ± 11	51 ± 38
$t\bar{t}$ + light	750 ± 370	586 ± 98	210 ± 210	96 ± 33	14 ± 10	12.1 ± 5.8
$t\bar{t}+\geq 1c$	880 ± 350	1330 ± 190	350 ± 100	473 ± 99	53 ± 33	44 ± 20
$t\bar{t}+\geq 1b$	2100 ± 420	2290 ± 170	1750 ± 370	1850 ± 130	1010 ± 240	1032 ± 59
$t\bar{t}+V$	51.2 ± 7.4	50.8 ± 5.9	40.8 ± 5.7	40.3 ± 4.8	25.8 ± 3.7	25.3 ± 3.2
Non-$t\bar{t}$	303 ± 82	267 ± 63	155 ± 52	134 ± 46	75 ± 20	58 ± 17
Total	4140 ± 850	4590 ± 110	2550 ± 510	2657 ± 82	1220 ± 250	1223 ± 42
Data	4698		2641		1222	

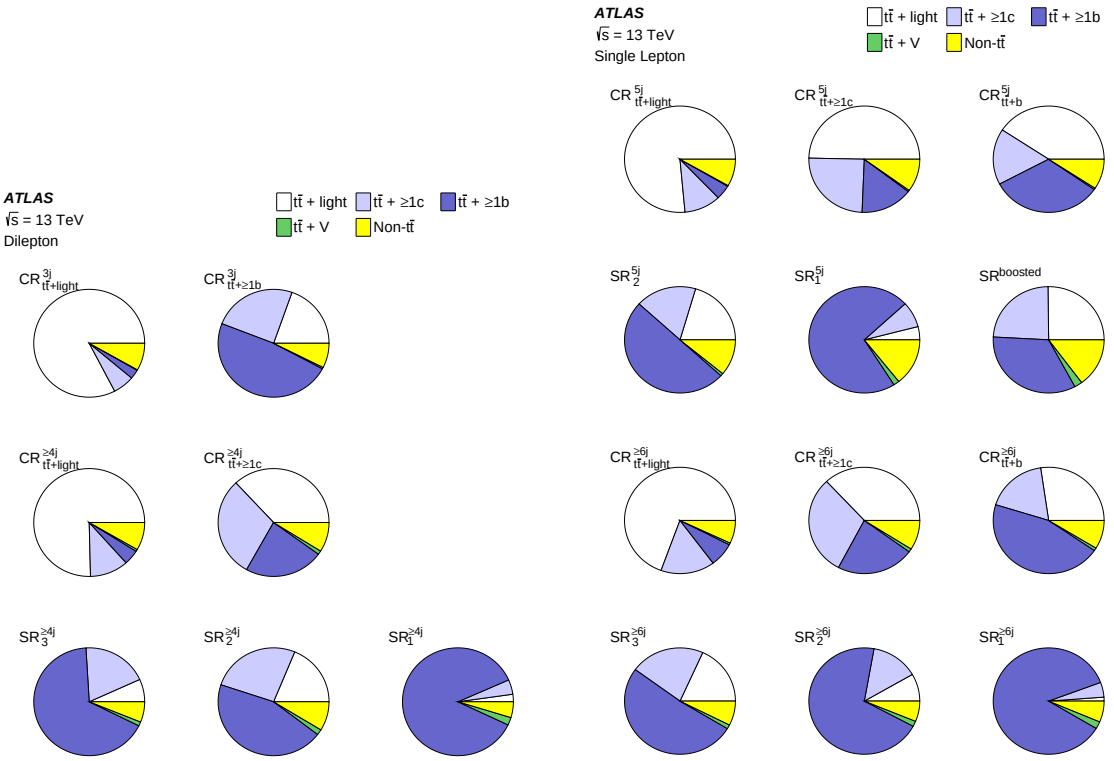

(a) (b)

Figure 2.5: Fractional contributions of the various backgrounds to the total background prediction in each analysis category (a) in the dilepton channel and (b) in the single-lepton channel. The predictions for the various background contributions are obtained through the simulation and the data-driven estimates described in Section 2.3. The $t\bar{t}$ background is divided as described in Section 2.3. The predicted event yields in each of the analysis categories, broken down into the different signal and background contributions, are reported in Tables 2.1, 2.2 and 2.3.

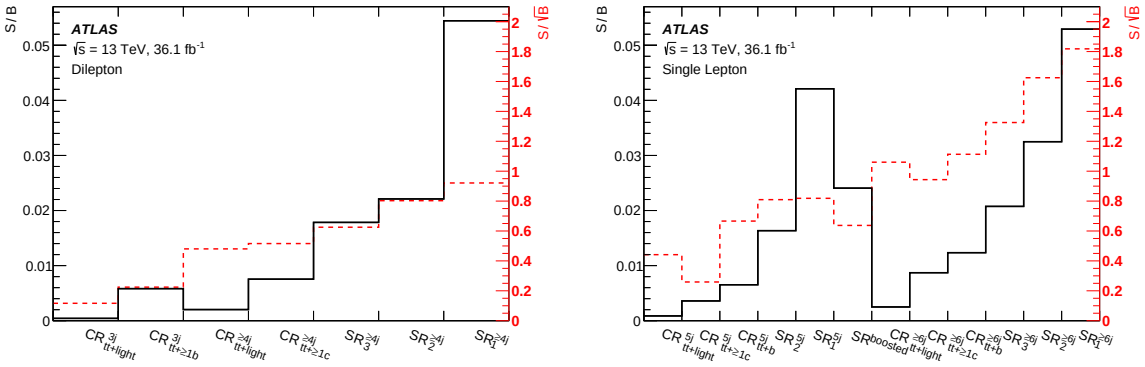

(a) (b)

Figure 2.6: The ratios S/B (black solid line, referring to the vertical axis on the left) and $S/\sqrt{B}$ (red dashed line, referring to the vertical axis on the right) for each of the analysis categories (a) in the dilepton channel and (b) in the single-lepton channel, where S (B) is the number of selected signal (background) events predicted by the simulation or through the data-driven estimates as described in Section 2.3.

2.5 Multivariate analysis techniques

In each of the signal regions, a boosted decision tree (BDT) is exploited to discriminate between the $t\bar{t}H$ signal and the backgrounds. This BDT is referred to as the 'classification BDT' in the following. The distributions of the classification BDTs in the signal regions are used as the final discriminants for the profile likelihood fit described in Section 2.7. In the control regions, the overall event yield is used as input to the fit, except in those enriched in $t\bar{t}+\geq 1c$ in the single-lepton channel, $\mathrm{CR}^{5\mathrm{j}}_{t\bar{t}+\geq 1c}$ and $\mathrm{CR}^{\geq 6\mathrm{j}}_{t\bar{t}+\geq 1c}$; in these two control regions, the distribution of the scalar sum of the p_{T} of the jets, $H_{\mathrm{T}}^{\mathrm{had}}$, is used to further control the $t\bar{t}+\geq 1c$ background.

The final state of the $t\bar{t}H(H\to b\bar{b})$ process is composed of many jets stemming from the Higgs-boson and top-quark decay products, as well as from additional radiation. Many combinations of these jets are possible when reconstructing the Higgs-boson and top-quark candidates to explore their properties and the signal event topology. To enhance the signal separation, three intermediate multivariate techniques are implemented prior to the classification BDT: (a) the 'reconstruction BDT' used to select the best combination of jet–parton assignments in each event and to build the Higgs-boson and top-quark candidates, (b) a likelihood discriminant (LHD) method that combines the signal and background probabilities of all possible combinations in each event, (c) a matrix element method (MEM) that exploits the full matrix element calculation to separate the signal from the background. The outputs of the three intermediate multivariate methods are used as input variables to the classification BDT in one or more of the signal regions. The properties of the Higgs-boson and top-quark candidates from the reconstruction BDT are used to define additional input variables to the classification BDT. Although the intermediate techniques exploit similar information, they make use of this information from different perspectives and based on different assumptions, so that their combination further improves the separation power of the classification BDT. Details of the implementation of these multivariate techniques are described in Sections 2.5.1–2.5.4.

2.5.1 Classification BDT

The classification BDT is trained to separate the signal from the $t\bar{t}$ background on a sample that is statistically independent of the sample used for the evaluation. The toolkit for multivariate analysis (TMVA) [205] is used to train both this and the reconstruction BDT. The classification BDT is built by combining several input variables that exploit the different kinematics of signal and background events, as well as the b-tagging information. General kinematic variables, such as invariant masses and angular separations of pairs of reconstructed jets and leptons, are combined with outputs of the intermediate multivariate discriminants and the b-tagging discriminants of the selected jets. In the case of the boosted single-lepton signal region, kinematic variables are built from the properties of the large-R jets and their jet constituents. The input variables are selected to maximize the performance of the classification BDT; however, only variables with good modeling of data by simulation are considered.

The input variables to the classification BDT are listed in Table 2.4 for the dilepton channel, in Table 2.5 for the resolved single-lepton channel and in Table 2.6 for the boosted category. Variables are grouped according to the type of information that is exploited. The variables from the reconstruction BDT exploit the chosen jet–parton assignments described in Section 2.5.2. The b-tagging discriminant assigned to each jet is defined in Section 2.2. Some kinematic and topological variables are built considering only b-tagged-jets in the event. The b-tagging requirements for these jets are optimized separately for each variable in each region to improve the classification BDT performance. In the resolved single-lepton channel, b-tagged-jets are defined as the four jets with the largest value of the b-tagging discriminant. If two jets have the same b-tagging discriminant value,

they are ordered by decreasing jet p_{T} value. In the dilepton channel, the b-tagging requirements depend on the signal region: in $\mathrm{SR}_1^{\geq 4\mathrm{j}}$ the *tight* working point is used, in $\mathrm{SR}_3^{\geq 4\mathrm{j}}$ the *very tight* working point is used and in $\mathrm{SR}_2^{\geq 4\mathrm{j}}$ the *loose* working point is used with the exception of $N_{bb}^{\text{Higgs }30}$, which uses the *medium* working point, and $\text{Aplanarity}_{b\text{-jet}}$, which uses the *tight* working point. The *loose* working point is used in the boosted signal region. The most powerful variables in the classification BDT are the reconstruction BDT output, the LHD (Section 2.5.3) and the MEM_{D1} (Section 2.5.4).

2.5.2 Reconstruction BDT

The reconstruction BDT is employed in all dilepton and resolved single-lepton signal regions. It is trained to match reconstructed jets to the partons emitted from top-quark and Higgs-boson decays. For this purpose, W-boson, top-quark and Higgs-boson candidates are built from combinations of jets and leptons. The b-tagging information is used to discard combinations containing jet–parton assignments inconsistent with the correct parton candidate flavor.

In the single-lepton channel, leptonically decaying W-boson candidates are assembled from the lepton four-momentum (p_ℓ) and the neutrino four-momentum (p_ν); the latter is built from the missing transverse momentum, its z component being inferred by solving the equation $m_W^2 = (p_\ell + p_\nu)^2$, where m_W represents the W-boson mass. Both solutions of this quadratic equation are used in separate combinations. If no real solutions exist, the discriminant of the quadratic equation is set to zero, giving a unique solution. The hadronically decaying W-boson and the Higgs-boson candidates are each formed from a pair of jets. The top-quark candidates are formed from one W-boson candidate and one jet. The top-quark candidate containing the hadronically (leptonically) decaying W boson is referred to as the hadronically (leptonically) decaying top-quark candidate. In the single-lepton signal regions with exactly five selected jets, more than 70% of the events do not contain both jets from the hadronically decaying W boson. Therefore, the hadronically decaying top-quark candidate is assembled from two jets, one of which is b-tagged. In the dilepton channel, no attempt to build leptonically decaying W-boson candidates is made and the top-quark candidates are formed by one lepton and one jet.

Simulated $t\bar{t}H$ events are used to iterate over all allowed combinations. The reconstruction BDT is trained to distinguish between correct and incorrect jet assignments, using invariant masses and angular separations in addition to other kinematic variables as inputs. In each event a specific combination of jet–parton assignments, corresponding to the best BDT output, is chosen in order to compute kinematic and topological information of the top-quark and Higgs-boson candidates to be input to the classification BDT. However, although the best possible reconstruction performance can be obtained by including information related to the Higgs boson, such as the candidate Higgs-boson invariant mass, in the reconstruction BDT, this biases the background distributions of these Higgs-boson-related observables in the chosen jet–parton assignment towards the signal expectation, reducing their ability to separate signal from background. For this reason, two versions of the reconstruction BDT are used, one with and one without the Higgs-boson information and the resulting jet–parton assignments from one, the other or both are considered when computing input variables for the classification BDT.

The Higgs boson is correctly reconstructed in 48% (32%) of the selected $t\bar{t}H$ events in the single-lepton channel $\mathrm{SR}_1^{\geq 6\mathrm{j}}$ using the reconstruction BDT with (without) information about the Higgs-boson kinematics included. For the dilepton channel, the corresponding reconstruction efficiencies are 49% (32%) in $\mathrm{SR}_1^{\geq 4\mathrm{j}}$. The reconstruction techniques are not needed in the signal region $\mathrm{SR}^{\text{boosted}}$, as the Higgs-boson and the top-quark candidates are chosen as the selected large-R jets described in Section 2.2. The large-R jet selected as a Higgs-boson candidate contains two b-tagged jets stemming from the decay of a Higgs boson in 47% of the selected $t\bar{t}H$ events.

2.5.3 Likelihood discriminant

In the resolved single-lepton signal regions, the output from a likelihood discriminant is included as an additional input variable for the classification BDT. The LHD is computed analogously to Ref. [208] as a product of one-dimensional probability density functions, pdfs, for the signal and the background hypotheses. The pdfs are built for various invariant masses and angular distributions from reconstructed jets and leptons and from the missing transverse momentum, in a similar way to those used in the reconstruction BDT.

Two background hypotheses are considered, corresponding to the production of $t\bar{t}$ + ≥ 2 b-jets and $t\bar{t}$ + exactly one b-jet, respectively. The likelihoods for both hypotheses are averaged, weighted by their relative fractions in simulated $t\bar{t}$ + jets events. In a significant fraction of both the $t\bar{t}H$ and $t\bar{t}$ simulated events with at least six selected jets, only one jet stemming from the hadronically decaying W boson is selected. An additional hypothesis, for both the signal and the background, is considered to account for this topology. In events with exactly five selected jets, variables including the hadronically decaying top-quark candidate are built similarly to those for the reconstruction BDT.

The probabilities p^{sig} and p^{bkg}, for signal and background hypotheses, respectively, are obtained as the product of the pdfs for the different kinematic distributions, averaged among all possible jet–parton matching combinations. Combinations are weighted using the b-tagging information to suppress the impact from parton–jet assignments that are inconsistent with the correct parton candidates flavor. For each event, the discriminant is defined as the ratio of the probability p^{sig} to the sum of p^{sig} and p^{bkg}, and added as an input variable to the classification BDT. As opposed to the reconstruction BDT method, the LHD method takes advantage of all possible combinations in the event, but it does not fully account for correlations between variables in one combination, as it uses a product of one-dimensional pdfs.

2.5.4 Matrix element method

A discriminant (MEM_{D1}) based on the MEM is computed following a method similar to the one described in Ref. [151] and is included as another input to the classification BDT. The MEM consumes a significant amount of computation time and thus is implemented only in the most sensitive single-lepton signal region, $\text{SR}_{1}^{\geq 6\text{j}}$. The degree to which each event is consistent with the signal and background hypotheses is expressed via signal and background likelihoods, referred to as L_S and L_B, respectively. These are computed using matrix element calculations at the parton level rather than using simulated MC samples as for the LHD method. The matrix element evaluation is performed with MG5_aMC@NLO at the LO accuracy. The $t\bar{t}H(H \to b\bar{b})$ process is used as a signal hypothesis, while $t\bar{t}+b\bar{b}$ is used as a background hypothesis. To reduce the computation time, only diagrams representing gluon-induced processes are considered. The parton distribution functions are modeled with the CT10 PDF set, interfaced via the LHAPDF package [209]. Transfer functions, that map the detector quantities to the parton level quantities, are derived from a $t\bar{t}$ sample generated with POWHEG+PYTHIA 6 and validated with the nominal POWHEG+PYTHIA 8 $t\bar{t}$ sample. The directions in η and ϕ of all visible final-state objects are assumed to be well measured, and their transfer functions are thus represented by δ-functions. The neutrino momentum is constrained by imposing transverse momentum conservation in each event, while its p_z is integrated over. The integration is performed using VEGAS [210], following the implementation described in Ref. [211]. As in the reconstruction BDT, b-tagging information is used to reduce the number of jet–parton assignments considered in the calculation. The discriminating variable, MEM_{D1}, is defined as the difference between the logarithms of the signal and background likelihoods: $\text{MEM}_{D1} = \log_{10}(L_S) - \log_{10}(L_B)$.

Table 2.4: Variables used in the classification BDTs in the dilepton signal regions. For variables from the reconstruction BDT, those with a * are from the BDT using Higgs-boson information, those with no * are from the BDT without Higgs-boson information while for those with a ** both versions are used. These two versions of the reconstruction BDT are described in Section 2.5.2.

Variable	Definition	$SR_1^{\geq 4j}$	$SR_2^{\geq 4j}$	$SR_3^{\geq 4j}$
General kinematic variables				
m_{bb}^{min}	Minimum invariant mass of a b-tagged jet pair	✓	✓	-
m_{bb}^{max}	Maximum invariant mass of a b-tagged jet pair	-	-	✓
$m_{bb}^{\text{min }\Delta R}$	Invariant mass of the b-tagged jet pair with minimum ΔR	✓	-	✓
$m_{\text{jj}}^{\text{max }p_{\text{T}}}$	Invariant mass of the jet pair with maximum p_{T}	✓	-	-
$m_{bb}^{\text{max }p_{\text{T}}}$	Invariant mass of the b-tagged jet pair with maximum p_{T}	✓	-	✓
$\Delta\eta_{bb}^{\text{avg}}$	Average $\Delta\eta$ for all b-tagged jet pairs	✓	✓	✓
$\Delta\eta_{\ell,\text{j}}^{\text{max}}$	Maximum $\Delta\eta$ between a jet and a lepton	-	✓	✓
$\Delta R_{bb}^{\text{max }p_{\text{T}}}$	ΔR between the b-tagged jet pair with maximum p_{T}	-	✓	✓
$N_{bb}^{\text{Higgs 30}}$	Number of b-tagged jet pairs with invariant mass within 30 GeV of the Higgs-boson mass	✓	✓	-
$n_{\text{jets}}^{p_{\text{T}}>40}$	Number of jets with $p_{\text{T}} > 40$ GeV	-	✓	✓
$\text{Aplanarity}_{b\text{-jet}}$	$1.5\lambda_2$, where λ_2 is the second eigenvalue of the momentum tensor [206] built with all b-tagged jets	-	✓	-
$H_{\text{T}}^{\text{all}}$	Scalar sum of p_{T} of all jets and leptons	-	-	✓
Variables from reconstruction BDT				
BDT output	Output of the reconstruction BDT	✓**	✓**	✓
m_{bb}^{Higgs}	Higgs candidate mass	✓	-	✓
$\Delta R_{H,t\bar{t}}$	ΔR between Higgs candidate and $t\bar{t}$ candidate system	✓*	-	-
$\Delta R_{H,\ell}^{\text{min}}$	Minimum ΔR between Higgs candidate and lepton	✓	✓	✓
$\Delta R_{H,b}^{\text{min}}$	Minimum ΔR between Higgs candidate and b-jet from top	✓	✓	-
$\Delta R_{H,b}^{\text{max}}$	Maximum ΔR between Higgs candidate and b-jet from top	-	✓	-
$\Delta R_{bb}^{\text{Higgs}}$	ΔR between the two jets matched to the Higgs candidate	-	✓	-
Variables from b-tagging				
$w_{b\text{-tag}}^{\text{Higgs}}$	Sum of b-tagging discriminants of jets from best Higgs candidate from the reconstruction BDT	-	✓	-

Table 2.5: Input variables to the classification BDTs in the single-lepton signal regions. For variables from the reconstruction BDT, those with a * are from the BDT using Higgs-boson information, those with no * are from the BDT without Higgs-boson information. These two versions of the reconstruction BDT are described in Section 2.5.2. The MEM_{D1} variable is only used in $\text{SR}_1^{\geq 6j}$, while variables based on the b-tagging discriminant are not used in this region.

Variable	Definition	$\text{SR}_{1,2,3}^{\geq 6j}$	$\text{SR}_{1,2}^{5j}$
General kinematic variables			
$\Delta R_{bb}^{\text{avg}}$	Average ΔR for all b-tagged jet pairs	✓	✓
$\Delta R_{bb}^{\text{max } p_{\text{T}}}$	ΔR between the two b-tagged jets with the largest vector sum p_{T}	✓	–
$\Delta\eta_{\text{jj}}^{\text{max}}$	Maximum $\Delta\eta$ between any two jets	✓	✓
$m_{bb}^{\text{min } \Delta R}$	Mass of the combination of two b-tagged jets with the smallest ΔR	✓	–
$m_{\text{jj}}^{\text{min } \Delta R}$	Mass of the combination of any two jets with the smallest ΔR	–	✓
$N_{bb}^{\text{Higgs 30}}$	Number of b-tagged jet pairs with invariant mass within 30 GeV of the Higgs-boson mass	✓	✓
$H_{\text{T}}^{\text{had}}$	Scalar sum of jet p_{T}	–	✓
$\Delta R_{\ell,bb}^{\text{min}}$	ΔR between the lepton and the combination of the two b-tagged jets with the smallest ΔR	–	✓
Aplanarity	$1.5\lambda_2$, where λ_2 is the second eigenvalue of the momentum tensor [206] built with all jets	✓	✓
H_1	Second Fox–Wolfram moment computed using all jets and the lepton	✓	✓
Variables from reconstruction BDT			
BDT output	Output of the reconstruction BDT	✓*	✓*
m_{bb}^{Higgs}	Higgs candidate mass	✓	✓
$m_{H,b_{\text{lep top}}}$	Mass of Higgs candidate and b-jet from leptonic top candidate	✓	–
$\Delta R_{bb}^{\text{Higgs}}$	ΔR between b-jets from the Higgs candidate	✓	✓
$\Delta R_{H,t\bar{t}}$	ΔR between Higgs candidate and $t\bar{t}$ candidate system	✓*	✓*
$\Delta R_{H,\text{lep top}}$	ΔR between Higgs candidate and leptonic top candidate	✓	–
$\Delta R_{H,b_{\text{had top}}}$	ΔR between Higgs candidate and b-jet from hadronic top candidate	–	✓*
Variables from likelihood and matrix element method calculations			
LHD	Likelihood discriminant	✓	✓
MEM_{D1}	Matrix element discriminant (in $\text{SR}_1^{\geq 6j}$ only)	✓	–
Variables from b-tagging (not in $\text{SR}_1^{\geq 6j}$)			
$w_{b\text{-tag}}^{\text{Higgs}}$	Sum of b-tagging discriminants of jets from best Higgs candidate from the reconstruction BDT	✓	✓
B_{jet}^3	3rd largest jet b-tagging discriminant	✓	✓
B_{jet}^4	4th largest jet b-tagging discriminant	✓	✓
B_{jet}^5	5th largest jet b-tagging discriminant	✓	✓

Table 2.6: Input variables to the classification BDT in the boosted single-lepton signal region. Additional b-jets are b-jets not contained in the Higgs-boson and top-quark candidates.

Variable	Definition
Variables from jet reclustering	
$\Delta R_{H,t}$	ΔR between the Higgs-boson and top-quark candidates
$\Delta R_{t,b^{\text{add}}}$	ΔR between the top-quark candidate and additional b-jet
$\Delta R_{H,b^{\text{add}}}$	ΔR between the Higgs-boson candidate and additional b-jet
$\Delta R_{H,\ell}$	ΔR between the Higgs-boson candidate and lepton
$m_{\text{Higgs candidate}}$	Higgs-boson candidate mass
$\sqrt{d_{12}}$	Top-quark candidate first splitting scale [207]
Variables from b-tagging	
$w_{b\text{-tag}}$	Sum of b-tagging discriminants of all b-jets
$w^{\text{add}}_{b\text{-tag}}/w_{b\text{-tag}}$	Ratio of sum of b-tagging discriminants of additional b-jets to all b-jets

2.6 Systematic uncertainties

Many sources of systematic uncertainty affect the search, including those related to the luminosity, the reconstruction and identification of leptons and jets, and the theory modeling of signal and background processes. Different uncertainties may affect only the overall normalization of the samples, or also the shapes of the distributions used to categorize the events and to build the final discriminants. All the sources of experimental uncertainty considered, with the exception of the uncertainty in the luminosity, affect both the normalizations and the shapes of distributions in all the simulated samples. Uncertainties related to modeling of the signal and the backgrounds affect both the normalizations and the shapes of the distributions for the processes involved, with the exception of cross-section and normalization uncertainties that affect only the normalization of the considered sample. Nonetheless, the normalization uncertainties modify the relative fractions of the different samples leading to a shape uncertainty in the distribution of the final discriminant for the total prediction in the different analysis categories.

A single independent nuisance parameter is assigned to each source of systematic uncertainty, as described in Section 2.7. Some of the systematic uncertainties, in particular most of the experimental uncertainties, are decomposed into several independent sources, as specified in the following. Each individual source then has a correlated effect across all the channels, analysis categories, signal and background samples. For modeling uncertainties, especially $t\bar{t}$ modeling, additional nuisance parameters are included to split some uncertainties into several sources independently affecting different subcomponents of a particular process.

2.6.1 Experimental uncertainties

The uncertainty of the combined 2015+2016 integrated luminosity is 2.1%. It is derived, following a methodology similar to that detailed in Ref. [156], from a calibration of the luminosity scale using x–y beam-separation scans performed in August 2015 and May 2016. A variation in the pileup reweighting of MC events is included to cover the uncertainty in the ratio of the predicted and measured inelastic cross-sections in the fiducial volume defined by $M_X > 13$ GeV where M_X is the mass of the hadronic system [212].

The jet energy scale and its uncertainty are derived by combining information from test-beam data, LHC collision data and simulation [162]. The uncertainties from these measurements are factorized into eight independent sources. Additional uncertainties are considered, related to jet flavor, pileup corrections, η dependence, and high-p_{T} jets, yielding a total of 20 independent sources. Although the uncertainties are not large, totaling 1%–6% per jet (depending on the jet p_{T}), the effects are amplified by the large number of jets in the final state. Uncertainties in the jet energy resolution and in the efficiency to pass the JVT requirement that is meant to remove jets from pileup are also considered. The jet energy resolution is divided into two independent components.

The efficiency to correctly tag b-jets is measured in data using dileptonic $t\bar{t}$ events. The mis-tag rate for c-jets is also measured in $t\bar{t}$ events, identifying hadronic decays of W bosons including c-jets, while for light jets it is measured in multi-jet events using jets containing secondary vertices and tracks with impact parameters consistent with a negative lifetime [165]. The b-tagging efficiencies and mis-tag rates are first extracted for each of the four working points used in the analysis as a function of jet kinematics, and then combined into a calibration of the b-tagging discriminant distribution, with corresponding uncertainties that correctly describe correlations across multiple working points. The uncertainty associated with the b-tagging efficiency, whose size ranges between 2% and 10% depending on the working point and on the jet p_{T}, is factorized into 30 independent sources. The size of the uncertainties associated with the mis-tag rates is 5%–20% for c-jets depending on

the working point and on the jet p_{T}, and 10%–50% for light jets depending on the working point and on the jet p_{T} and η. These uncertainties are factorized into 15 (80) independent sources for c-jets (light jets). Jets from τ_{had} candidates are treated as c-jets for the mis-tag rate corrections and systematic uncertainties. An additional source of systematic uncertainty is considered on the extrapolation between c-jets and these τ-jets.

Uncertainties associated with leptons arise from the trigger, reconstruction, identification, and isolation efficiencies, as well as the lepton momentum scale and resolution. These are measured in data using leptons in $Z \to \ell^+\ell^-$, $J/\psi \to \ell^+\ell^-$ and $W \to e\nu$ events [158, 159]. Uncertainties of these measurements account for a total of 24 independent sources, but have only a small impact on the result.

All uncertainties in energy scales or resolutions are propagated to the missing transverse momentum. Additional uncertainties in the scale and resolution of the soft term are considered, for a total of three additional sources of systematic uncertainty.

2.6.2 Modeling uncertainties

The predicted $t\bar{t}H$ signal cross-section uncertainty is $^{+5.8\%}_{-9.2\%}$(scale) $\pm$ 3.6%(PDF), the first component representing the QCD scale uncertainty and the second the PDF+α_{S} uncertainty [150, 177, 178, 179, 180, 181]. These two components are treated as uncorrelated in the fit. The effect of QCD scale and PDF variations on the shape of the distributions considered in this analysis is found to be negligible. Uncertainties in the Higgs-boson branching fractions are also considered; these amount to 2.2% for the $b\bar{b}$ decay mode [150]. An additional uncertainty associated with the choice of parton shower and hadronization model is derived by comparing the nominal prediction from MG5_aMC@NLO+PYTHIA 8 to the one from MG5_aMC@NLO interfaced to HERWIG++.

The systematic uncertainties affecting the modeling of the $t\bar{t}$ +jets background are summarized in Table 2.7. An uncertainty of $\pm$6% is assumed for the inclusive $t\bar{t}$ NNLO+NNLL production cross-section [185], including effects from varying the factorization and renormalization scales, the PDF, α_{S}, and the top-quark mass. The $t\bar{t}+\geq 1b$, $t\bar{t}+\geq 1c$ and $t\bar{t}+$light processes are affected by different types of uncertainties: $t\bar{t}+$light has additional diagrams and profits from relatively precise measurements in data; $t\bar{t}+\geq 1b$ and $t\bar{t}+\geq 1c$ can have similar or different diagrams depending on the flavor scheme used for the PDF, and the mass differences between c- and b-quarks contribute to additional differences between these two processes. For these reasons, all uncertainties in $t\bar{t}$ + jets background modeling, except the uncertainty in the inclusive cross-section, are assigned independent nuisance parameters for the $t\bar{t}+\geq 1b$, $t\bar{t}+\geq 1c$ and $t\bar{t}+$light processes. The normalizations of $t\bar{t}+\geq 1b$ and $t\bar{t}+\geq 1c$ are allowed to float freely in the fit. Systematic uncertainties in the shapes are extracted from the comparison between the nominal sample and various alternative samples. For all these uncertainties, alternative samples are reweighted in such a way that they have the same fractions of $t\bar{t}+\geq 1c$ and $t\bar{t}+\geq 1b$ as the nominal sample. In the case of the $t\bar{t}+\geq 1b$ background, separate uncertainties are applied to the relative normalization of the $t\bar{t}+\geq 1b$ subcomponents as described later. Therefore, for all the alternative samples used to derive uncertainties that are not specifically associated with these fractions, the relative contributions of the $t\bar{t}+\geq 1b$ subcategories are scaled to match the predictions of SHERPA4F, in the same way as for the nominal sample. This scaling is not applied to the $t\bar{t}+b$ (MPI/FSR) subcategory, as explained in Section 2.3.

Uncertainties associated with the choice of $t\bar{t}$ inclusive NLO event generator as well as the choice of parton shower and hadronization model are derived by comparing the prediction from POWHEG+PYTHIA 8 with the SHERPA predictions (hence varying simultaneously the NLO event generator and the parton shower and hadronization model) and with the predictions from POWHEG interfaced with HERWIG 7 [213] (varying just the parton shower and hadronization model). The

Table 2.7: Summary of the sources of systematic uncertainty for $t\bar{t}$ + jets modeling. The systematic uncertainties listed in the second section of the table are evaluated in such a way as to have no impact on the relative fractions of $t\bar{t}+\geq 1b$, $t\bar{t}+\geq 1c$ and $t\bar{t}+$ light events, as well as on the relative fractions of the $t\bar{t}+b$, $t\bar{t}+b\bar{b}$, $t\bar{t}+B$ and $t\bar{t}+\geq 3b$ subcategories, which are all kept at their nominal values. The systematic uncertainties listed in the third section of the table affect only the fractions of the various $t\bar{t}+\geq 1b$ subcategories. The last column of the table indicates the $t\bar{t}$ category to which a systematic uncertainty is assigned. In the case where all three categories ($t\bar{t}+$ light, $t\bar{t}+\geq 1c$ and $t\bar{t}+\geq 1b$) are involved (marked with 'all'), the last column also specifies whether the uncertainty is considered as correlated or uncorrelated across them.

Systematic source	Description	$t\bar{t}$ categories
$t\bar{t}$ cross-section	Up or down by 6%	All, correlated
$k(t\bar{t}+\geq 1c)$	Free-floating $t\bar{t}+\geq 1c$ normalization	$t\bar{t}+\geq 1c$
$k(t\bar{t}+\geq 1b)$	Free-floating $t\bar{t}+\geq 1b$ normalization	$t\bar{t}+\geq 1b$
SHERPA5F vs. nominal	Related to the choice of NLO event generator	All, uncorrelated
PS & hadronization	POWHEG+HERWIG 7 vs. POWHEG+PYTHIA 8	All, uncorrelated
ISR / FSR	Variations of μ_{R}, μ_{F}, h_{damp} and A14 Var3c parameters	All, uncorrelated
$t\bar{t}+\geq 1c$ ME vs. inclusive	MG5_aMC@NLO+HERWIG++: ME prediction (3F) vs. incl. (5F)	$t\bar{t}+\geq 1c$
$t\bar{t}+\geq 1b$ SHERPA4F vs. nominal	Comparison of $t\bar{t}+b\bar{b}$ NLO (4F) vs. POWHEG+PYTHIA 8 (5F)	$t\bar{t}+\geq 1b$
$t\bar{t}+\geq 1b$ renorm. scale	Up or down by a factor of two	$t\bar{t}+\geq 1b$
$t\bar{t}+\geq 1b$ resumm. scale	Vary μ_{Q} from $H_{\mathrm{T}}/2$ to μ_{CMMPS}	$t\bar{t}+\geq 1b$
$t\bar{t}+\geq 1b$ global scales	Set μ_{Q}, μ_{R}, and μ_{F} to μ_{CMMPS}	$t\bar{t}+\geq 1b$
$t\bar{t}+\geq 1b$ shower recoil scheme	Alternative model scheme	$t\bar{t}+\geq 1b$
$t\bar{t}+\geq 1b$ PDF (MSTW)	MSTW vs. CT10	$t\bar{t}+\geq 1b$
$t\bar{t}+\geq 1b$ PDF (NNPDF)	NNPDF vs. CT10	$t\bar{t}+\geq 1b$
$t\bar{t}+\geq 1b$ UE	Alternative set of tuned parameters for the underlying event	$t\bar{t}+\geq 1b$
$t\bar{t}+\geq 1b$ MPI	Up or down by 50%	$t\bar{t}+\geq 1b$
$t\bar{t}+\geq 3b$ normalization	Up or down by 50%	$t\bar{t}+\geq 1b$

former alternative sample was generated using SHERPA version 2.2.1 with the ME+PS@NLO setup, interfaced with OPENLOOPS, providing NLO accuracy for up to one additional parton and LO accuracy for up to four additional partons. The NNPDF3.0NNLO PDF set was used and both the renormalization and factorization scales were set to $\sqrt{0.5 \times (m^2_{\mathrm{T},t} + m^2_{\mathrm{T},\bar{t}})}$. This sample is referred to as 'SHERPA5F' in the remainder of this article, which should not be confused with the SHERPA4F sample defined in Section 2.3. The comparison with the latter alternative sample is considered as an independent source of uncertainty, related to the parton shower and hadronization model choice. This sample was generated with the same settings for POWHEG as the nominal $t\bar{t}$ sample in terms of h_{damp}, PDF and renormalization and factorization scales, but it was interfaced with HERWIG 7 version 7.0.1, with the H7-UE-MMHT set of tuned parameters for the underlying event. Additionally, the uncertainty in the modeling of initial- and final-state radiation (ISR / FSR) is assessed with two alternative POWHEG+PYTHIA 8 samples [214]. One sample with the amount of radiation increased has the renormalization and factorization scales decreased by a factor of two, the h_{damp} parameter doubled, and uses the Var3c upward variation of the A14 parameter set. A second sample with the amount of radiation decreased has the scales increased by a factor of two and uses the Var3c downward variation of the A14 set. The uncertainties described in this paragraph correspond to three independent sources for each of the $t\bar{t}+$light, $t\bar{t}+\geq 1c$ and $t\bar{t}+\geq 1b$ components.

For the background from $t\bar{t}+\geq 1c$, there is little guidance from theory or experiment to determine whether the nominal approach of using charm jets produced primarily in the parton shower is more or less accurate than a prediction with $t\bar{t}+c\bar{c}$ calculated at NLO in the matrix element. For this reason, an NLO prediction with $t\bar{t}+c\bar{c}$ in the matrix element, including massive c-quarks and therefore using the 3F scheme for the PDFs, is produced with MG5_aMC@NLO interfaced to HERWIG++, as described in Ref. [215]. The difference between this sample and an inclusive $t\bar{t}$ sample produced with the same event generator and a 5F scheme PDF set, in which the $t\bar{t}+\geq 1c$ process originates through the parton shower only, is taken as an additional uncertainty in the $t\bar{t}+\geq 1c$ prediction. This uncertainty is related to the choice between the $t\bar{t}+c\bar{c}$ ME calculation and the prediction from the inclusive $t\bar{t}$ production with c-jets via parton shower and is applied as one additional independent source to the $t\bar{t}+\geq 1c$ background.

For the $t\bar{t}+\geq 1b$ process, the difference between the predictions from POWHEG+PYTHIA 8 and SHERPA4F is considered as one additional source of uncertainty. This uncertainty accounts for the difference between the description of the $t\bar{t}+\geq 1b$ process by the NLO $t\bar{t}$ inclusive MC sample with a 5F scheme and a description at NLO of $t\bar{t}+b\bar{b}$ in the ME with a 4F scheme. This uncertainty is not applied to the $t\bar{t}+b$ (MPI/FSR) subcategory since it is not included in the 4F calculation.

The uncertainties described above do not affect the relative fractions of the $t\bar{t}+b$, $t\bar{t}+b\bar{b}$, $t\bar{t}+B$ and $t\bar{t}+\geq 3b$ subcomponents as these fractions are fixed to the prediction of SHERPA4F. The uncertainties in these fractions in SHERPA4F are assessed separately and are divided into seven independent sources. Three of these sources are evaluated by varying the renormalization scale up and down by a factor of two, changing the functional form of the resummation scale to μ_{CMMPS}, and adopting a global scale choice, $\mu_{\mathrm{Q}} = \mu_{\mathrm{R}} = \mu_{\mathrm{F}} = \mu_{\mathrm{CMMPS}}$. Additionally, two alternative PDF sets, MSTW2008NLO [62] and NNPDF2.3NLO, are considered, as well as an alternative shower recoil scheme and an alternative set of tuned parameters for the underlying event. These sources of uncertainty contribute to the uncertainty band shown in Figure 2.2 for the SHERPA4F prediction. Given the large difference between the 4F prediction and the various 5F predictions for the $t\bar{t}+\geq 3b$ process, which is not covered by the uncertainties described above, this sub-process is given an extra 50% normalization uncertainty.

The relative fraction of the $t\bar{t}+b$ (MPI/FSR) subcategory is not fixed in the alternative samples used to derive the systematic uncertainties related to the choice of NLO event generator, parton

shower and hadronization model and to ISR/FSR. These sources already incorporate variations related to the fraction and shape of the $t\bar{t}+b$ (MPI/FSR) subcategory. In addition, a 50% normalization uncertainty is assumed for the contribution from MPI, based on studies of different underlying event sets of tuned parameters.

In total, thirteen independent sources of modeling uncertainties are assigned to the $t\bar{t}+\geq 1b$ component, four to the $t\bar{t}+\geq 1c$ component and three to the $t\bar{t}+$light component in addition to the one source that corresponds to the inclusive $t\bar{t}$ production cross-section uncertainty.

An uncertainty of 40% is assumed for the W + jets cross-section, with an additional 30% normalization uncertainty used for W + heavy-flavor jets, taken as uncorrelated between events with two and more than two heavy-flavor jets. These uncertainties are based on variations of the factorization and renormalization scales and of the matching parameters in the SHERPA simulation. An uncertainty of 35% is then applied to the Z + jets normalization, uncorrelated across jet bins, to account for both the variations of the scales and matching parameters in SHERPA simulation and the uncertainty in the extraction from data of the correction factor for the heavy-flavor component.

An uncertainty of $^{+5\%}_{-4\%}$ is considered for each of the three single-top production mode cross-sections [198, 196, 197]. For the Wt and t-channel production modes, uncertainties associated with the choice of parton shower and hadronization model and with initial- and final-state radiation are evaluated according to a set of alternative samples analogous to those used for the $t\bar{t}$ process: the nominal prediction is compared with samples generated with POWHEG interfaced with HERWIG++ and with alternative POWHEG-BOX v1 + PYTHIA 6 samples with factorization and renormalization scale variations and appropriate variations of the Perugia 2012 set of tuned parameters. The uncertainty in the amount of interference between Wt and $t\bar{t}$ production at NLO [194] is assessed by comparing the default 'diagram removal' scheme to the alternative 'diagram subtraction' scheme.

A 50% normalization uncertainty in the diboson background is assumed, which includes uncertainties in the inclusive cross-section and additional jet production [203]. The uncertainty of the $t\bar{t}V$ NLO cross-section prediction is 15% [216], split into PDF and scale uncertainties as for $t\bar{t}H$. An additional $t\bar{t}V$ modeling uncertainty, related to the choice of event generator, parton shower and hadronization model, is assessed by comparing the nominal sample with alternative ones generated with SHERPA. Uncertainties in $t\bar{t}V$ production are all treated as uncorrelated between $t\bar{t}Z$ and $t\bar{t}W$. A total 50% normalization uncertainty is considered for the $t\bar{t}t\bar{t}$ background. The small backgrounds from tZ, $t\bar{t}WW$, $tHjb$ and WtH are each assigned two cross-section uncertainties, split into PDF and scale uncertainties, while tWZ is assigned one cross-section uncertainty that accounts for both the scale and PDF effects.

Finally, a 50% uncertainty is assigned to the overall estimated yield of non-prompt lepton events in the single-lepton channel, taken as uncorrelated between electron-plus-jet and muon-plus-jet events, between boosted and resolved analysis categories, and between the resolved analysis categories with exactly five jets and those with six or more jets. In the dilepton channel, the non-prompt lepton background is assigned a 25% uncertainty, correlated across lepton flavors and all analysis categories.

2.7 Results

The distributions of the discriminants from each of the analysis categories are combined in a profile likelihood fit to test for the presence of a signal, while simultaneously determining the normalization and constraining the differential distributions of the most important background components. As described in Section 2.5, in the signal regions, the output of the classification BDT is used as the discriminant while only the total event yield is used in the control regions, with the exception of

$\mathrm{CR}^{5\mathrm{j}}_{t\bar{t}+\geq 1c}$ and $\mathrm{CR}^{\geq 6\mathrm{j}}_{t\bar{t}+\geq 1c}$, where the $H_{\mathrm{T}}^{\mathrm{had}}$ distribution is used. No distinction is made in the fit between signal and control regions, other than a different choice of discriminant variables. The binning of the classification BDT is optimized to maximize the analysis sensitivity while keeping the total MC statistical uncertainty in each bin to a level adjusted to avoid biases due to fluctuations in the predicted number of events.

The likelihood function, $\mathscr{L}(\mu,\theta)$, is constructed as a product of Poisson probability terms over all bins in each distribution. The Poisson probability depends on the predicted number of events in each bin, which in turn is a function of the signal-strength parameter $\mu = \sigma/\sigma_{\mathrm{SM}}$ and θ, where θ is the set of nuisance parameters that encode the effects of systematic uncertainties, and of the two free floating normalization factors $k(t\bar{t}+\geq 1b)$ and $k(t\bar{t}+\geq 1c)$ for the $t\bar{t}+\geq 1b$ and $t\bar{t}+\geq 1c$ backgrounds, respectively. The nuisance parameters are implemented in the likelihood function as Gaussian, log-normal or Poisson priors, with the exception of the normalization factors $k(t\bar{t}+\geq 1b)$ and $k(t\bar{t}+\geq 1c)$, for which no prior knowledge from theory or subsidiary measurements is assumed and hence which are only constrained by the profile likelihood fit to the data. The statistical uncertainty of the prediction, that incorporates the statistical uncertainty of the MC events and of the data-driven fake and non-prompt lepton estimate, is included in the likelihood in the form of additional nuisance parameters, one for each of the included bins. The test statistic t_μ is defined as the profile likelihood ratio: $t_\mu = -2\ln(\mathscr{L}(\mu,\hat{\hat{\theta}}_\mu)/\mathscr{L}(\hat{\mu},\hat{\theta}))$, where $\hat{\mu}$ and $\hat{\theta}$ are the values of the parameters which maximize the likelihood function, and $\hat{\hat{\theta}}_\mu$ are the values of the nuisance parameters which maximize the likelihood function for a given value of μ. This test statistic is used to measure the probability that the observed data is compatible with the background-only hypothesis, and to perform statistical inferences about μ, such as upper limits using the $\mathrm{CL_s}$ method [217, 218, 219]. The uncertainty of the best-fit value of the signal strength, $\hat{\mu}$, is obtained varying t_μ by one unit.

Figure 2.7 shows the observed event yield compared to the prediction in each control and signal region, both before the fit to data ('pre-fit') and after the fit to data ('post-fit'), performed in all the analysis categories in the two channels and with the signal-plus-background hypothesis. For the pre-fit prediction, the normalization factors for the $t\bar{t}+\geq 1b$ and $t\bar{t}+\geq 1c$ processes are set to 1, which corresponds to considering the prediction from POWHEG + PYTHIA 8 for the fraction of each of these components relative to the total $t\bar{t}$ prediction. Figure 2.8 shows the $H_{\mathrm{T}}^{\mathrm{had}}$ distributions in the $t\bar{t}+\geq 1c$-enriched control regions of the single-lepton channel, while Figures 2.9, 2.10 and 2.11 show the distributions of the classification BDTs in the dilepton and single-lepton signal regions, both before and after the fit. All these distributions are reasonably well modeled pre-fit within the assigned uncertainties. The level of agreement is improved post-fit due to the nuisance parameters being adjusted by the fit. In particular, the best-fit values of $k(t\bar{t}+\geq 1b)$ and $k(t\bar{t}+\geq 1c)$ are 1.24 ± 0.10 and 1.63 ± 0.23, respectively. The uncertainties in these measured normalization factors do not include the theory uncertainty of the corresponding $t\bar{t}+\geq 1b$ and $t\bar{t}+\geq 1c$ cross-sections. The post-fit uncertainty is also significantly reduced, as a result of the nuisance-parameter constraints and the correlations generated by the fit.

In addition to the distributions that are given as input to the fit, all the distributions of the input variables to the classification BDTs in the signal regions are checked post-fit, and no significant deviations of the predictions from data are found. Figure 2.12 shows the data compared to the post-fit prediction for three of these distributions, namely the Higgs-boson candidate mass distributions in the most sensitive signal regions in the dilepton channel and the single-lepton resolved channels as well as in the single-lepton boosted signal region.

The best-fit μ value is:

$$\mu = 0.84 \pm 0.29\ (\mathrm{stat.})\ ^{+0.57}_{-0.54}\ (\mathrm{syst.}) = 0.84^{+0.64}_{-0.61},$$

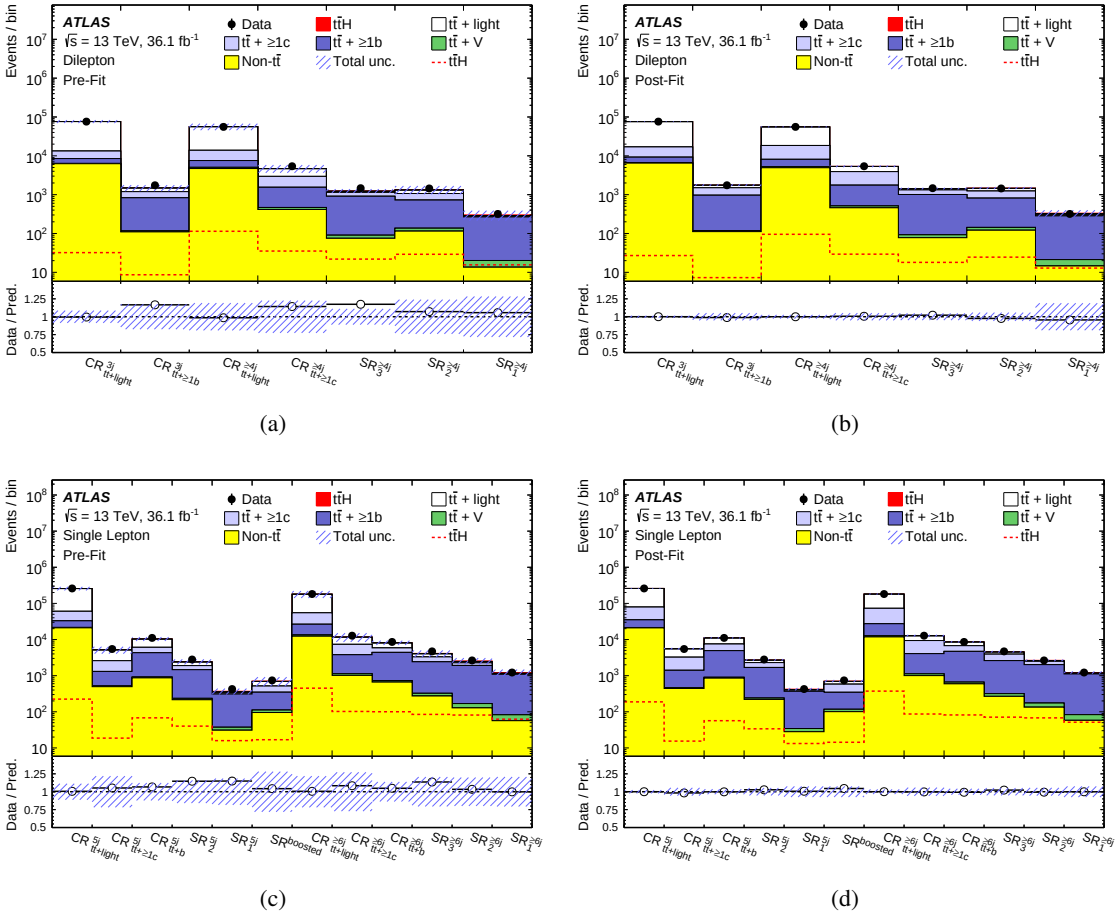

(a) (b)

(c) (d)

Figure 2.7: Comparison of predicted and observed event yields in each of the control and signal regions, in the dilepton channel (a) before and (b) after the fit to the data, and in the single-lepton channel (c) before and (d) after the fit to the data. The $t\bar{t}H$ signal is shown both as a filled red area stacked on the backgrounds and separately for visibility as a dashed red line, normalized to the SM cross-section before the fit and to the fitted μ after the fit. The hatched area corresponds to the fitted uncertainty in the total prediction. The pre-fit plots do not include an uncertainty for the $t\bar{t}+\geq 1b$ or $t\bar{t}+\geq 1c$ normalization.

determined by the combined fit in all signal and control regions in the two channels. The expected uncertainty of the signal strength is identical to the measured one. An alternative combined fit is also performed in which the dilepton and single-lepton channels are assigned two independent signal strengths. The corresponding fitted values of μ are $-0.24^{+1.02}_{-1.05}$ in the dilepton channel and $0.95^{+0.65}_{-0.62}$ in the single-lepton channel. The probability of obtaining a discrepancy between these two signal-strength parameters equal to or larger than the one observed is 19%. Figure 2.13 shows the comparison between the combined μ and the two independent signal-strength parameters from the combined fit, with their uncertainties split into the statistical and systematic components. The statistical uncertainty is obtained by redoing the fit to data after fixing all the nuisance parameters to their post-fit values, with the exception of the free normalization factors in the fit: $k(t\bar{t}+\geq 1c)$, $k(t\bar{t}+\geq 1b)$ and μ. The total systematic uncertainty is obtained from the subtraction in quadrature of the statistical uncertainty from the total uncertainty. The statistical uncertainty contributes significantly

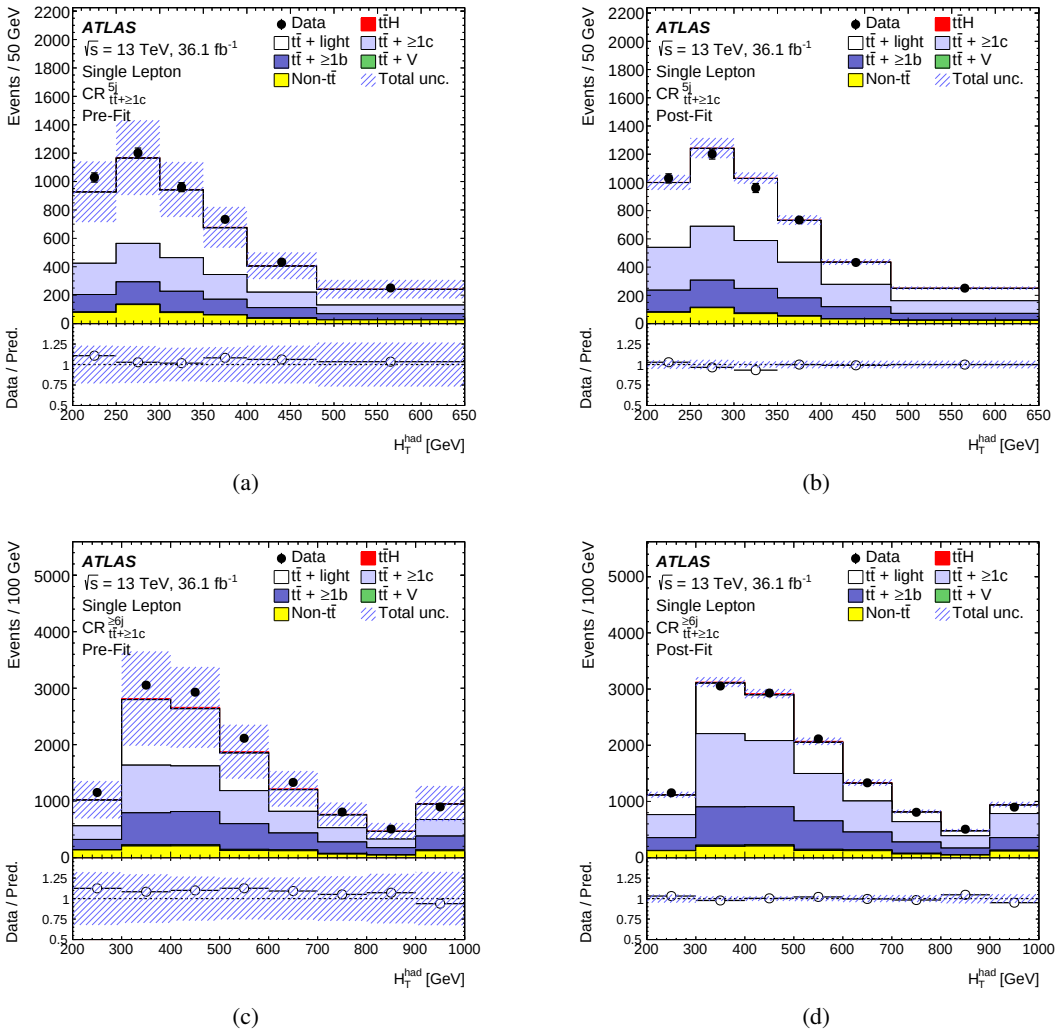

Figure 2.8: Comparison between data and prediction for the $H_{\mathrm{T}}^{\mathrm{had}}$ distributions in the single-lepton $t\bar{t}+\geq 1c$-enriched control regions (a, c) before, and (b, d) after the combined dilepton and single-lepton fit to the data. Despite its small contribution in these control regions, the $t\bar{t}H$ signal prediction is shown stacked at the top of the background prediction, normalized to the SM cross-section before the fit and to the fitted μ after the fit. The pre-fit plots do not include an uncertainty for the $t\bar{t}+\geq 1b$ or $t\bar{t}+\geq 1c$ normalization.

less than the systematic component to the overall uncertainty of the measurement. When fitting the dilepton and single-lepton data separately, the observed signal strengths are $0.11^{+1.36}_{-1.41}$ and $0.67^{+0.71}_{-0.69}$, respectively. These two signal-strength values are both lower than the combined measured μ due to the large correlations in the systematic uncertainties of the background prediction between the two channels.

The contributions from the different sources of uncertainty in the combined fit to μ are reported in Table 2.8. The total systematic uncertainty is dominated by the uncertainties in the modeling of the $t\bar{t}+\geq 1b$ background, the second-largest source being the limited number of events in the simulated samples, followed by the uncertainties in the b-tagging efficiency, the jet energy scale and

resolution, and the signal process modeling. The 20 nuisance parameters describing the independent sources of systematic uncertainty with the largest contribution to the total uncertainty of the measured signal strength are reported in Figure 2.14, ranked by decreasing contribution. For each of these nuisance parameters, the best-fit value and the post-fit uncertainty are shown. The uncertainty coming from the comparison between the SHERPA5F and the nominal prediction for the $t\bar{t}+\geq 1b$ process, related to the choice of the NLO event generator for this background component, has the largest impact on the signal strength, followed by three uncertainties also related to the modeling of the $t\bar{t}+\geq 1b$ background. Systematic uncertainties related to the $t\bar{t}H$ signal modeling, the modeling of the $t\bar{t}+\geq 1c$ and $t\bar{t}+$light backgrounds, and to experimental sources such as b-tagging, jet energy scale and resolution, also appear in Figure 2.14; however, their contributions are significantly smaller than the ones from the $t\bar{t}+\geq 1b$ background. The total uncertainty of the signal strength is reduced by 5% if the fit is performed excluding the systematic uncertainties not shown in this figure.

The theoretical predictions for the $t\bar{t}+\geq 1b$ process suffer from large uncertainties as reflected in the size of the difference between alternative simulated samples used to model this background. The corresponding systematic uncertainties are therefore large and are a crucial limiting factor for this search. The choice of nuisance parameters for systematic uncertainties related to the $t\bar{t}+\geq 1b$ background is studied carefully to ensure sufficient flexibility in the fit to correct for possible mis-modeling of this background and avoid any bias in the measured signal strength. In total, 13 independent nuisance parameters are assigned to $t\bar{t}+\geq 1b$ background modeling uncertainties. The capability of the fit to correct for mis-modeling effects, beyond the ones present in the distributions used in the fit, is confirmed by comparing the predictions of all input variables of the classification BDT obtained post-fit to data. As mentioned before, no significant deviations of the predictions from data are found and the agreement is improved post-fit. Alternative approaches to model the $t\bar{t}+\geq 1b$ background, to define the associated uncertainties and to correlate them are also tested, and the corresponding results are found to be compatible with the nominal result.

To further validate the robustness of the fit, a pseudo-data set was built from simulated events by replacing the nominal $t\bar{t}$ background by an alternative sample that is not used in the definition of any uncertainty. This alternative sample was generated with POWHEG+PYTHIA 6 and is similar to the sample used for the $t\bar{t}H(H\rightarrow b\bar{b})$ analysis [151] in Run 1 of the LHC. The fit to this pseudo-data sample did not reveal any bias in the signal extraction.

Figure 2.14 shows that some nuisance parameters are shifted in the fit from their nominal values. To understand the origin of these shifts, the corresponding nuisance parameters are switched to be uncorrelated between analysis categories and samples and the fit is repeated. These shifts are found to correct mainly the predictions of the $t\bar{t}$ background to the observed data in various regions. Similar shifts are observed when a background-only fit is performed after removing the bins with the most significant signal contributions. Moreover, the variations induced in the signal strength by these shifts are quantified by fixing the corresponding nuisance parameters to their pre-fit values, repeating the fit, and comparing the obtained μ-value with the one from the nominal fit. These variations were found to be smaller than the uncertainty in the signal strength. Independent signal-strength values extracted from different sets of analysis categories and from the two channels are also found to be compatible.

Figure 2.14 also shows that the uncertainties corresponding to some nuisance parameters are reduced by the fit. When performing the profile likelihood fit, nuisance parameters associated with uncertainties affecting the discriminant distributions by variations that would result in large deviations from to data are significantly constrained. The capability of the fit to constrain systematic uncertainties is validated on the pseudo-data sample described above, and on the pseudo-data sample produced from the nominal predictions, the Asimov dataset [217].

An excess of events over the expected SM background is found with an observed (expected)

significance of 1.4 (1.6) standard deviations. A signal strength larger than 2.0 is excluded at the 95% confidence level, as shown in Figure 2.15. The expected significance and exclusion limits are calculated using the background estimate after the fit to the data. Figure 2.16 shows the event yield in data compared to the post-fit prediction for all events entering the analysis selection, grouped and ordered by the signal-to-background ratio of the corresponding final-discriminant bins. The predictions are shown for both the fit with the background-only hypothesis and with the signal-plus-background hypothesis, where the signal is scaled to either the measured μ or the value of the upper limit on μ.

Table 2.8: Breakdown of the contributions to the uncertainties in μ. The line 'background-model stat. unc.' refers to the statistical uncertainties in the MC events and in the data-driven determination of the non-prompt and fake lepton background component in the single-lepton channel. The contribution of the different sources of uncertainty is evaluated after the fit described in Section 2.7. The total statistical uncertainty is evaluated, as described in the text, by fixing all the nuisance parameters in the fit except for the free-floating normalization factors for the $t\bar{t}+\geq 1b$ and $t\bar{t}+\geq 1c$ background components. The contribution from the uncertainty in the normalization of both $t\bar{t}+\geq 1b$ and $t\bar{t}+\geq 1c$ is then included in the quoted total statistical uncertainty rather than in the systematic uncertainty component. The statistical uncertainty evaluated after also fixing the normalization of $t\bar{t}+\geq 1b$ and $t\bar{t}+\geq 1c$ is then indicated as 'intrinsic statistical uncertainty'. The other quoted numbers are obtained by repeating the fit after having fixed a certain set of nuisance parameters corresponding to a group of systematic uncertainty sources, and subtracting in quadrature the resulting total uncertainty of μ from the uncertainty from the full fit. The same procedure is followed for quoting the individual effects of the $t\bar{t}+\geq 1b$ and the $t\bar{t}+\geq 1c$ normalization. The total uncertainty is different from the sum in quadrature of the different components due to correlations between nuisance parameters built by the fit.

Uncertainty source	$\Delta\mu$	
$t\bar{t}+\geq 1b$ modeling	$+0.46$	-0.46
Background-model stat. unc.	$+0.29$	-0.31
b-tagging efficiency and mis-tag rates	$+0.16$	-0.16
Jet energy scale and resolution	$+0.14$	-0.14
$t\bar{t}H$ modeling	$+0.22$	-0.05
$t\bar{t}+\geq 1c$ modeling	$+0.09$	-0.11
JVT, pileup modeling	$+0.03$	-0.05
Other background modeling	$+0.08$	-0.08
$t\bar{t}+$ light modeling	$+0.06$	-0.03
Luminosity	$+0.03$	-0.02
Light lepton (e,μ) id., isolation, trigger	$+0.03$	-0.04
Total systematic uncertainty	$+0.57$	-0.54
$t\bar{t}+\geq 1b$ normalization	$+0.09$	-0.10
$t\bar{t}+\geq 1c$ normalization	$+0.02$	-0.03
Intrinsic statistical uncertainty	$+0.21$	-0.20
Total statistical uncertainty	$+0.29$	-0.29
Total uncertainty	$+0.64$	-0.61

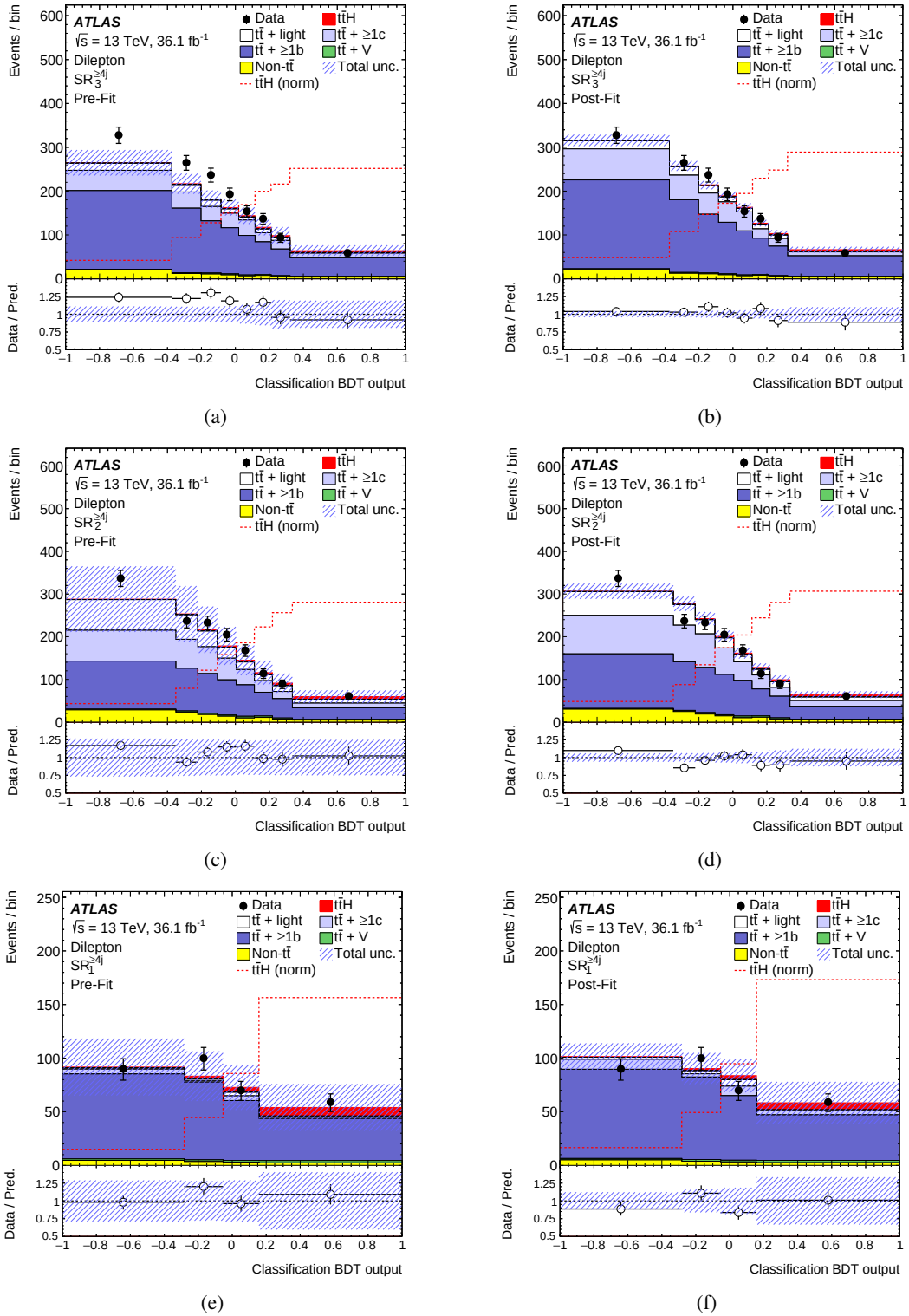

Figure 2.9: Comparison between data and prediction for the BDT discriminant in the dilepton signal regions (a, c, e) before, and (b, d, f) after the combined dilepton and single-lepton fit to the data. The $t\bar{t}H$ signal yield (solid red) is normalized to the SM cross-section before the fit and to the fitted μ after the fit. The dashed line shows the $t\bar{t}H$ signal distribution normalized to the total background prediction. The pre-fit plots do not include an uncertainty for the $t\bar{t}+\geq 1b$ or $t\bar{t}+\geq 1c$ normalization.

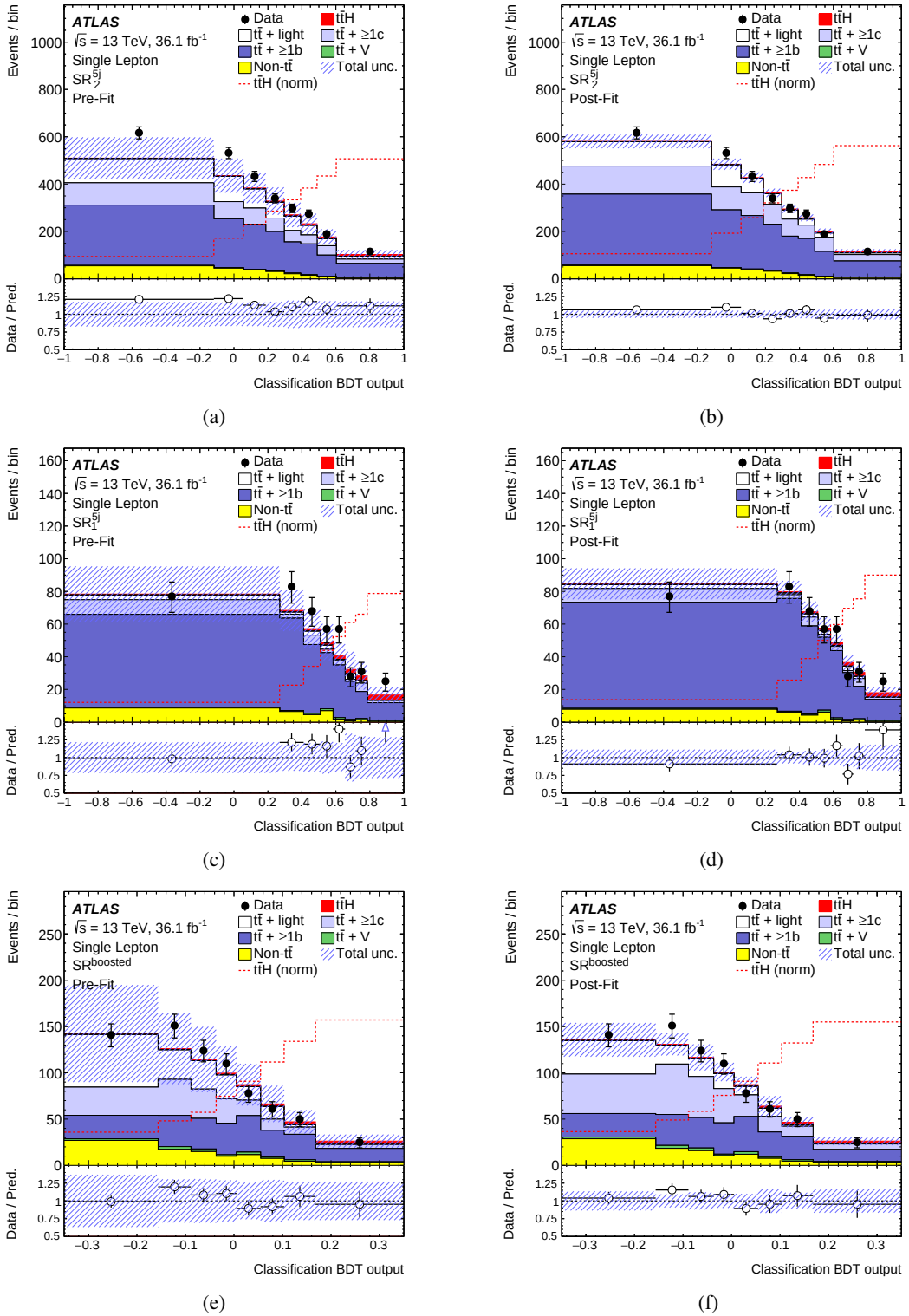

Figure 2.10: Comparison between data and prediction for the BDT discriminant in the single-lepton channel five-jet and boosted signal regions (a, c, e) before, and (b, d, f) after the combined dilepton and single-lepton fit to the data. The $t\bar{t}H$ signal yield (solid red) is normalized to the SM cross-section before the fit and to the fitted μ after the fit. The dashed line shows the $t\bar{t}H$ signal distribution normalized to the total background prediction. The pre-fit plots do not include an uncertainty for the $t\bar{t}+\geq 1b$ or $t\bar{t}+\geq 1c$ normalization.

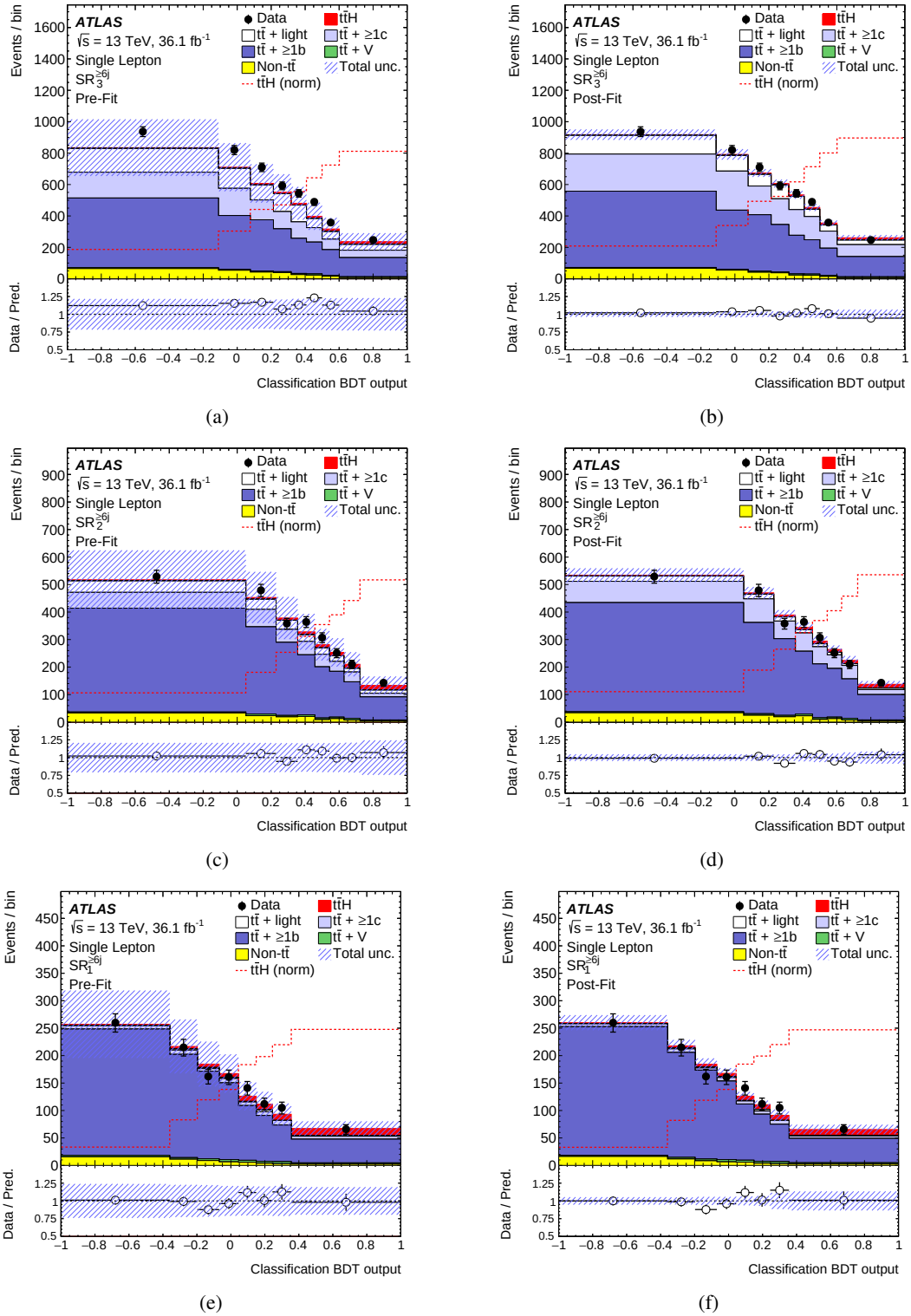

Figure 2.11: Comparison between data and prediction for the BDT discriminant in the single-lepton channel six-jet signal regions (a, c, e) before, and (b, d, f) after the combined dilepton and single-lepton fit to the data. The $t\bar{t}H$ signal yield (solid red) is normalized to the SM cross-section before the fit and to the fitted μ after the fit. The dashed line shows the $t\bar{t}H$ signal distribution normalized to the total background prediction. The pre-fit plots do not include an uncertainty for the $t\bar{t}+\geq 1b$ or $t\bar{t}+\geq 1c$ normalization.

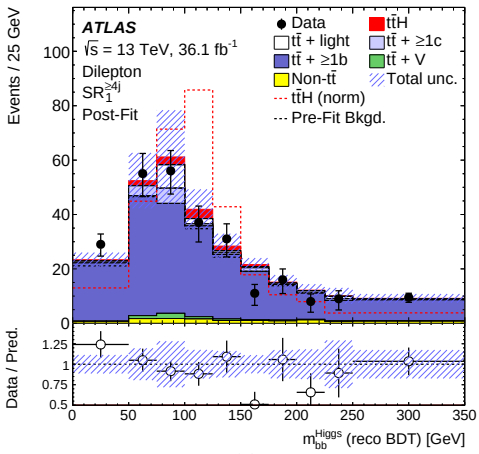

(a)

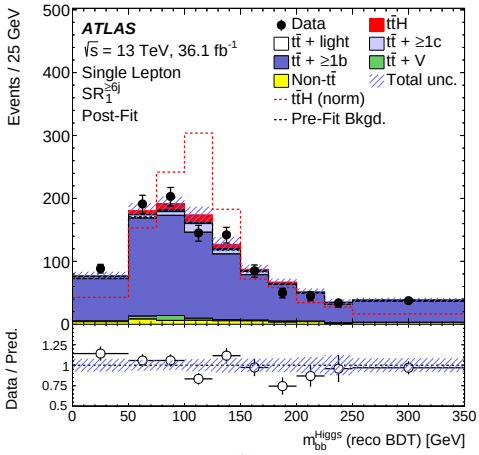

(b)

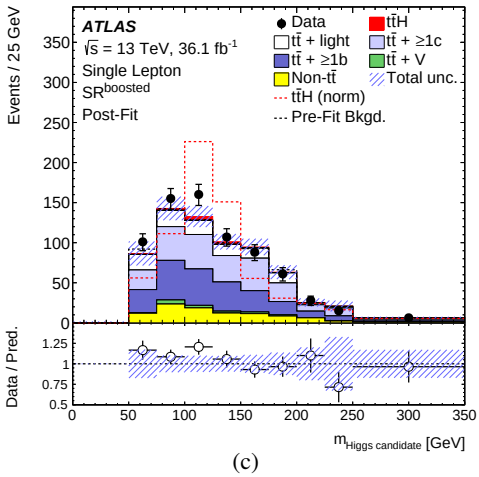

(c)

Figure 2.12: Comparison between data and prediction for the Higgs-boson candidate mass from the reconstruction BDT trained without variables involving the Higgs-boson candidate (a) in the dilepton $SR_1^{\geq 4j}$ and (b) in the single-lepton $SR_1^{\geq 6j}$, and (c) for the boosted Higgs-boson candidate in $SR^{boosted}$, after the combined dilepton and single-lepton fit to the data. The $t\bar{t}H$ signal yield (solid red) is normalized to the fitted μ after the fit. The dashed red line shows the $t\bar{t}H$ signal distribution normalized to the total background yield. The dashed black line shows the pre-fit total background prediction.

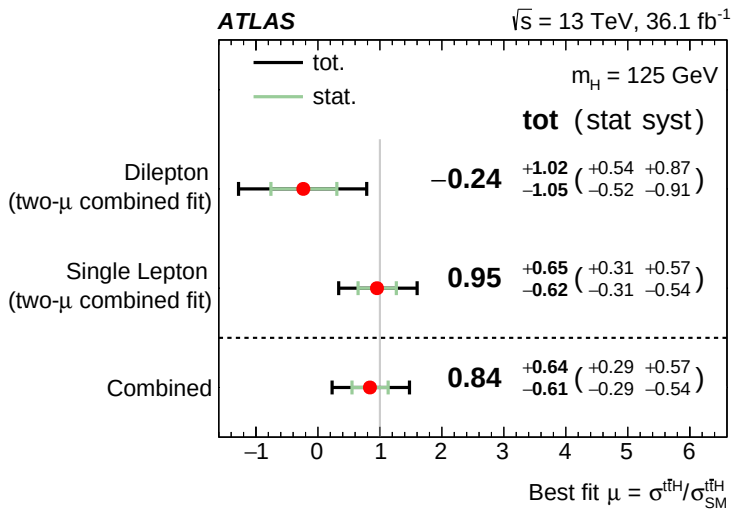

Figure 2.13: Summary of the signal-strength measurements in the individual channels and for the combination. All the numbers are obtained from a simultaneous fit in the two channels, but the measurements in the two channels separately are obtained keeping the signal strengths uncorrelated, while all the nuisance parameters are kept correlated across channels.

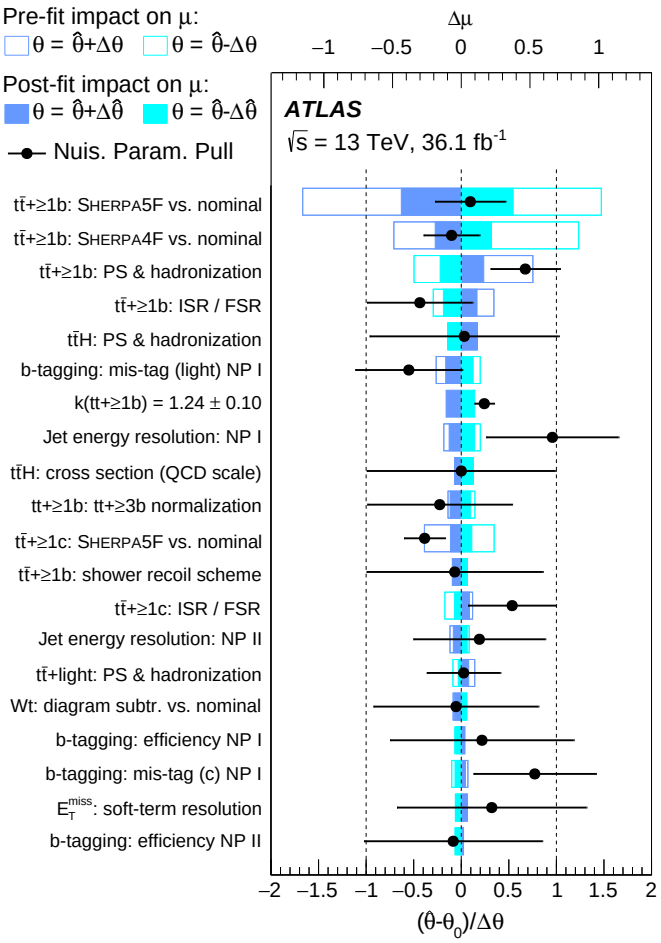

Figure 2.14: Ranking of the nuisance parameters included in the fit according to their impact on the measured signal strength μ. Only the 20 most highly ranked parameters are shown. Nuisance parameters corresponding to MC statistical uncertainties are not included here. The empty blue rectangles correspond to the pre-fit impact on μ and the filled blue ones to the post-fit impact on μ, both referring to the upper scale. The impact of each nuisance parameter, $\Delta\mu$, is computed by comparing the nominal best-fit value of μ with the result of the fit when fixing the considered nuisance parameter to its best-fit value, $\hat{\theta}$, shifted by its pre-fit (post-fit) uncertainties $\pm\Delta\theta$ ($\pm\Delta\hat{\theta}$). The black points show the pulls of the nuisance parameters relative to their nominal values, θ_0. These pulls and their relative post-fit errors, $\Delta\hat{\theta}/\Delta\theta$, refer to the scale on the bottom axis. The parameter $k(t\bar{t}+\geq 1b)$ refers to the floating normalization of the $t\bar{t}+\geq 1b$ background, for which the pre-fit impact on μ is not defined, and for which both θ_0 and $\Delta\theta$ are set to 1. For experimental uncertainties that are decomposed into several independent sources, NP I and NP II correspond to the first and second nuisance parameters, ordered by their impact on μ, respectively.

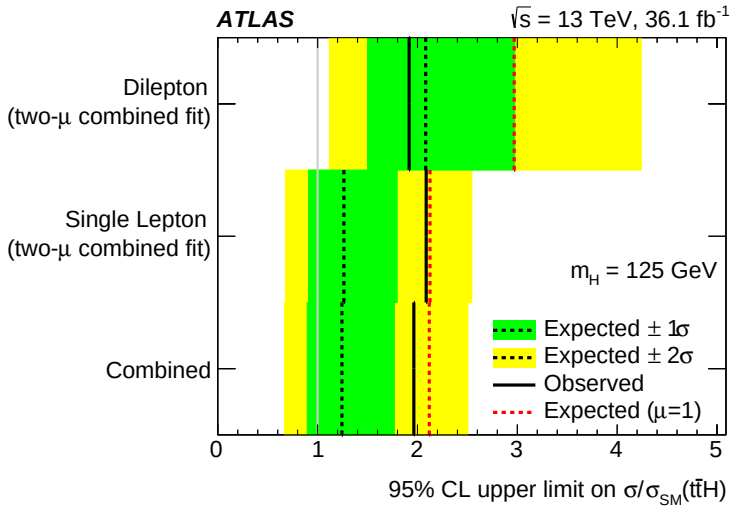

Figure 2.15: Summary of the 95% confidence level (CL) upper limits on $\sigma(t\bar{t}H)$ relative to the SM prediction in the individual channels and for the combination. The observed limits are shown, together with the expected limits both in the background-only hypothesis (dotted black lines) and in the SM hypothesis (dotted red lines). In the case of the expected limits in the background-only hypothesis, one- and two-standard-deviation uncertainty bands are also shown. The limits for the two individual channels are derived consistently with Figure 2.13, both extracted from the profile likelihood including the data in both channels, but with independent signal strengths in the two channels.

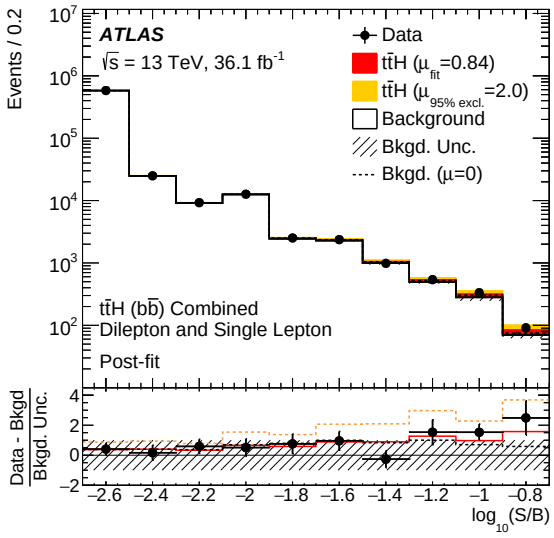

Figure 2.16: Post-fit yields of signal (S) and total background (B) as a function of $\log(S/B)$, compared to data. Final-discriminant bins in all dilepton and single-lepton analysis categories are combined into bins of $\log(S/B)$, with the signal normalized to the SM prediction used for the computation of $\log(S/B)$. The signal is then shown normalized to the best-fit value and to the value excluded at the 95% CL, in both cases summed to the background prediction from the fit. The lower frame reports for each bin the pull (residual divided by its uncertainty) of the data relative to the background prediction from the fit. These data pulls are compared to the pulls of the signal-plus-background prediction from the fit, assuming a signal strength equal to the best-fit value (solid red line) and equal to the exclusion limit (dashed orange line). The background and its pull are also shown after the fit to data assuming zero signal contribution (dashed black line, obscured by solid line in the upper frame). The first bin includes the underflow.

2.8 Combination with other $t\bar{t}H$ channels

The results presented in this chapter are combined with results from other $t\bar{t}H$ channels with the Higgs boson decaying to multileptons in the final state [171], to a pair of photons [140], and to 4 leptons through a pair of Z bosons [140]. The combined results are published in [140]. The $H \to b\bar{b}$ and multilepton results correspond to a dataset with an integrated luminosity of 36.1 fb^{-1} at $\sqrt{s} = 13$ TeV, while the $H \to \gamma\gamma$ and $H \to 4\ell$ results correspond to a dataset with an integrated luminosity of 79.8 fb^{-1} at $\sqrt{s} = 13$ TeV.

The combination is performed using a simultaneous profile likelihood fit to the signal and control regions of the individual analyses. The different analyses cuts are designed to reduce the overlap between the corresponding regions. This overlap was found to be negligible and does not affect the combination results. The systematic uncertainties are added to the profile likelihood fit as nuisance parameters. The theoretical uncertainties on the signal and the backgrounds that are common to two or more channels are treated as correlated in the fit. The only exception is the theoretical uncertainties on the $t\bar{t}$ background in the $H \to b\bar{b}$ analysis which has a special treatment and is kept uncorrelated in this channel. The experimental uncertainties are treated as correlated between the $H \to b\bar{b}$ and the multilepton channels with the exception of the uncertainty on the quark/gluon fraction that enters the jet energy scale. This fraction is different in the two analyses regions which justifies keeping it uncorrelated between these two channels. The experimental uncertainties are also treated as correlated between the $H \to \gamma\gamma$ and $H \to 4\ell$ channels. However the $H \to \gamma\gamma$ and $H \to 4\ell$ analyses use a more recent dataset with improved software for the reconstruction of physics objects. Thus only some components of the experimental uncertainties, that are not affected by the reconstruction updated, are correlated between all four channels.

The combined fit results in an observed (expected) excess of 5.8 (4.9) standard deviations relative to the background only hypothesis. The measured total cross section for $t\bar{t}H$ production is 670 ± 90 (stat.) $^{+110}_{-100}$ (syst.) fb, in agreement with the SM prediction of 507^{+35}_{-50} fb [177, 220, 149, 178, 221, 179, 180, 222, 181, 150], which is calculated to next-to-leading-order accuracy (both QCD and electroweak). A breakdown of the systematic uncertainties in the $t\bar{t}H$ production cross section measurement is shown in table 2.9. The dominant uncertainties arise from the modelling of the $t\bar{t}$ + heavy flavour background in the $H \to b\bar{b}$ channel followed by the uncertainty from the $t\bar{t}H$ signal modelling. The measured $t\bar{t}H$ cross section and the significance relative to the background only hypothesis in individual channels is shown in table 2.10. The ratio of the individual and combined measured cross sections with respect to the SM prediction is shown in figure 2.17. The measurements are compatible with the SM predictions in all channels.

A combination is also performed with the $t\bar{t}H$ searches based on datasets corresponding to integrated luminosities of 4.5 fb^{-1} at $\sqrt{s} = 7$ TeV and 20.3 fb^{-1} at $\sqrt{s} = 8$ TeV [223]. The corresponding observed (expected) significance is 6.3 (5.1) standard deviations relative to the background only hypothesis.

Table 2.9: Summary of the systematic uncertainties affecting the combined $t\bar{t}H$ cross-section measurement at 13 TeV. Only systematic uncertainty sources with at least 1% impact are listed. The fake-lepton uncertainty is due to the estimate of leptons from heavy-flavour decay, conversions or misidentified hadronic jets. The jet, electron, and photon uncertainties, as well as the uncertainties associated with hadronically decaying τ-leptons, include those in reconstruction and identification efficiencies, as well as in the energy scale and resolution. The Monte Carlo (MC) statistical uncertainty is due to limited numbers of simulated events. More detailed descriptions of the sources of the systematic uncertainties are given in Refs. [139, 171, 140].

Uncertainty source	$\Delta\sigma_{t\bar{t}H}/\sigma_{t\bar{t}H}$ [%]
Theory uncertainties (modelling)	11.9
$t\bar{t}$ + heavy flavour	9.9
$t\bar{t}H$	6.0
Non-$t\bar{t}H$ Higgs boson production	1.5
Other background processes	2.2
Experimental uncertainties	9.3
Fake leptons	5.2
Jets, $E_{\mathrm{T}}^{\mathrm{miss}}$	4.9
Electrons, photons	3.2
Luminosity	3.0
τ-leptons	2.5
Flavour tagging	1.8
MC statistical uncertainties	4.4

Table 2.10: Measured total $t\bar{t}H$ production cross sections at 13 TeV, as well as observed (Obs.) and expected (Exp.) significances (sign.) relative to the background-only hypothesis. The results of the individual analyses, as well as the combined results are shown. Since no event is observed in the $H \to ZZ^* \to 4\ell$ decay channel, an observed upper limit is set at 68% confidence level on the $t\bar{t}H$ production cross section in that channel using pseudo-experiments.

Analysis	Integrated luminosity [fb^{-1}]	$t\bar{t}H$ cross section [fb]	Obs. sign.	Exp. sign.
$H \to \gamma\gamma$	79.8	$710\ ^{+210}_{-190}$ (stat.) $^{+120}_{-90}$ (syst.)	4.1σ	3.7σ
$H \to$ multilepton	36.1	790 ± 150 (stat.) $^{+150}_{-140}$ (syst.)	4.1σ	2.8σ
$H \to b\bar{b}$	36.1	$400\ ^{+150}_{-140}$ (stat.) $\pm$ 270 (syst.)	1.4σ	1.6σ
$H \to ZZ^* \to 4\ell$	79.8	<900 (68% CL)	0σ	1.2σ
Combined (13 TeV)	36.1$-$79.8	670 ± 90 (stat.) $^{+110}_{-100}$ (syst.)	5.8σ	4.9σ

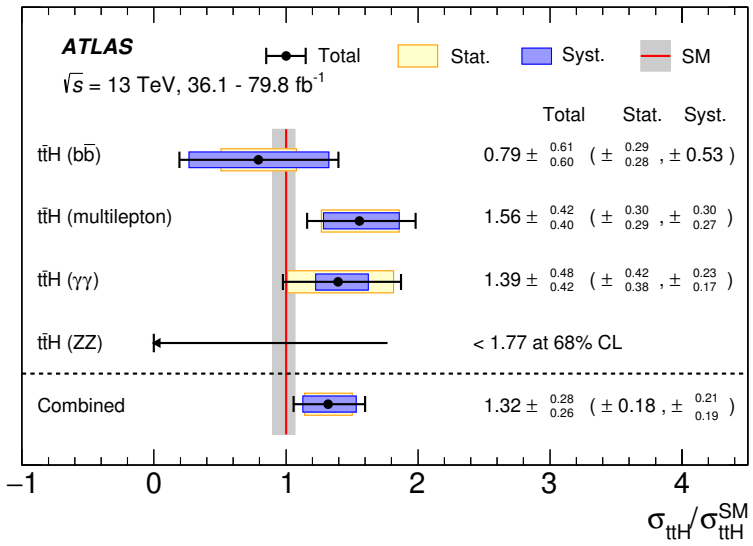

Figure 2.17: Combined $t\bar{t}H$ production cross section, as well as cross sections measured in the individual analyses, divided by the SM prediction. The $\gamma\gamma$ and $ZZ^* \to 4\ell$ analyses use 13 TeV data corresponding to an integrated luminosity of 79.8 fb^{-1}, and the multilepton and $b\bar{b}$ analyses use data corresponding to an integrated luminosity of 36.1 fb^{-1}. The black lines show the total uncertainties, and the bands indicate the statistical and systematic uncertainties. The red vertical line indicates the SM cross-section prediction, and the grey band represents the PDF+α_S uncertainties and the uncertainties due to missing higher-order corrections.

2.9 Combination with other $H \to b\bar{b}$ channels

The $t\bar{t}H(H \to b\bar{b})$ results shown in this chapter are combined with $H \to b\bar{b}$ results in the VH production mode at 13 TeV [141] and at 7 TeV and 8 TeV [224], the VBF production mode at 13 TeV [225] and at 8 TeV [226], and the $t\bar{t}H(H \to b\bar{b})$ production mode at 8 TeV [151]. The results of this combination is published in [141]. The analysis targeting the VBF production mode has a significant contribution from gluon–gluon fusion events; thus it is referred to as the VBF+ggF analysis in the following.

The observed (expected) combined significance for the $H \to b\bar{b}$ decay is 5.4 (5.5) standard deviations relative to the background only hypothesis. Table 2.11 shows the significance values independently for each of the considered production channels. Assuming the production cross sections are those predicted by the SM, the combined measured $H \to b\bar{b}$ branching ratio divided by the SM predicted branching ratio is $\mu_{H\to bb} = 1.01 \pm 0.12(\text{stat.})^{+0.16}_{-0.15}(\text{syst.})$. The $\mu_{H\to bb}$ values obtained from a fit where individual $\mu_{H\to bb}$ are fitted simultaneously for the three production modes are displayed in Figure 2.18. All fitted values are compatible with the SM prediction. The probability of compatibility of the individual $\mu_{H\to bb}$ in the three production channels is 83%.

Table 2.11: Expected and observed significance values (in standard deviations) for the $H \to b\bar{b}$ channels fitted independently and their combination using the 7 TeV, 8 TeV and 13 TeV data.

Channel	Significance	
	Exp.	Obs.
VBF+ggF	0.9	1.5
$t\bar{t}H$	1.9	1.9
VH	5.1	4.9
$H \to b\bar{b}$ combination	5.5	5.4

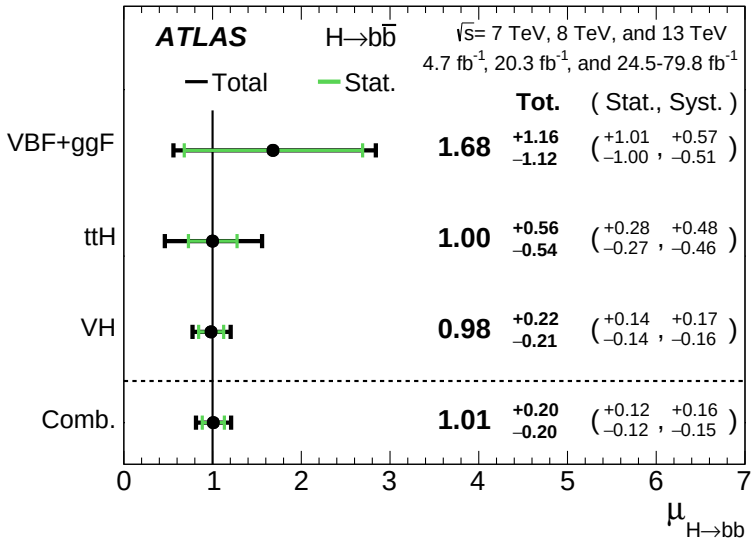

Figure 2.18: The fitted values of the Higgs boson signal strength $\mu_{H\to bb}$ for $m_h = 125$ GeV separately for the VH, $t\bar{t}H$ and VBF+ggF analyses along with their combination, using the 7 TeV, 8 TeV and 13 TeV data. The individual $\mu_{H\to bb}$ values for the different production modes are obtained from a simultaneous fit with the signal strengths for each of the processes floating independently.

2.10 Conclusion

A search for the associated production of the Standard Model Higgs boson with a pair of top quarks is presented, based on 36.1 fb^{-1} of pp collision data at $\sqrt{s} = 13$ TeV, collected with the ATLAS detector at the Large Hadron Collider in 2015 and 2016. The search focuses on decays of the Higgs boson to $b\bar{b}$ and decays of the top quark pair to a final state containing one or two leptons. Multivariate techniques are used to discriminate between signal and background events, the latter being dominated by $t\bar{t}$ + jets production. The observed data are consistent with both the background-only hypothesis and with the Standard Model $t\bar{t}H$ prediction. A 1.4 σ excess above the expected background is observed, while an excess of 1.6 σ is expected in the presence of a Standard Model Higgs boson. The signal strength is measured to be $0.84^{+0.64}_{-0.61}$, consistent with the expectation from the Standard Model. A value higher than 2.0 is excluded at the 95% confidence level, compared to an expected exclusion limit of 1.2 in the absence of signal. The measurement uncertainty is presently dominated by systematic uncertainties, and more specifically by the uncertainty in the theoretical knowledge of the $t\bar{t} + \geq 1b$ production process. An improved understanding of this background will be important for future efforts to observe the $t\bar{t}H(H \to b\bar{b})$ process.

The combination of the $t\bar{t}H(H \to b\bar{b})$ results with other $t\bar{t}H$ channels leads to the observation of the $t\bar{t}H$ process with a significance of 5.8 standard deviations. The combination of the $t\bar{t}H(H \to b\bar{b})$ results with other $H \to b\bar{b}$ channels leads to the observation of the $H \to b\bar{b}$ process with a significance of 5.5 standard deviations. Both the measured $t\bar{t}H$ production cross section at $\sqrt{s} = 13$ TeV and the $H \to b\bar{b}$ branching ratio are found to be compatible with the SM predictions.

Chapter 3

Upgrade of the ATLAS liquid argon calorimeter

This chapter presents the upgrades of the electronics of the liquid argon (LAr) calorimeter of the ATLAS experiment. The upgrade Phase-I was finalised in 2022 and the corresponding results are published in [227]. The section of this chapter covering the Phase-I upgrade is mostly based on this Phase-I paper for which I was part of the editorial team. The preparations for the upgrade Phase-II are ongoing and this chapter will focus on development of embedded neural networks on FPGAs to compute the energy deposited in the calorimeter during the HL-LHC phase. This section of the chapter is mostly based on two papers [228, 229] that I published with a team of engineers and scientists from the CPPM laboratory and the university of Dresden.

3.1 The ATLAS LAr calorimeter

The LAr calorimeter is a sampling calorimeter formed of lead, copper, or tungsten absorber immersed in a liquid argon active material. It provides electronic calorimetry over the full η range, hadronic calorimetry in the range $1.5 < |\eta| < 3.2$, extended by forward calorimetry in the range $3.1 < |\eta| < 4.9$. A schematic view of the LAr calorimeter is shown in figure 3.1. Details about the LAr calorimeter can be found in [30].

The electromagnetic (EM) calorimeter is formed of lead absorbers with copper and kapton electrodes. The accordion geometry of the electrodes leads to a full ϕ coverage with high hermicity. The electromagnetic calorimeter is divided into three parts each housed in a different cryostat. The centre part (called barrel or EMB) is composed of two identical halves separated by a small gap at η=0 and covers the region $|\eta| <$1.475. The EMB is extended by two endcaps (called EMEC) each formed of two wheels. The outer wheel covers the region 1.375$< |\eta| <$2.5 and the inner wheel completes the coverage till $|\eta|$=3.2. The EMB and the EMEC inner wheels are longitudinally segmented into three layers. This ensures a precise measurement in the region also covered by the inner tracker ($|\eta| <$2.5). The first layer has fine granularity in η direction and thus give the best calorimeter η measurement. The second and third layers provide a better granularity in the ϕ direction. The region with $|\eta| <$1.8 is covered by a presampler situated in front of the electromagnetic calorimeter. This presampler helps to estimate the energy loss due to the material in front of the calorimeter. A schematic view of the three longitudinal layers and the presampler is represented in figure 3.2. The EMEC outer wheels are segmented into two layers with a coarser granularity in both directions.

The hadronic endcaps (HEC) are liquid argon calorimeters with copper plates as absorber material. They share the same cryostat as the EMEC. The HEC is segmented into four layers constructed

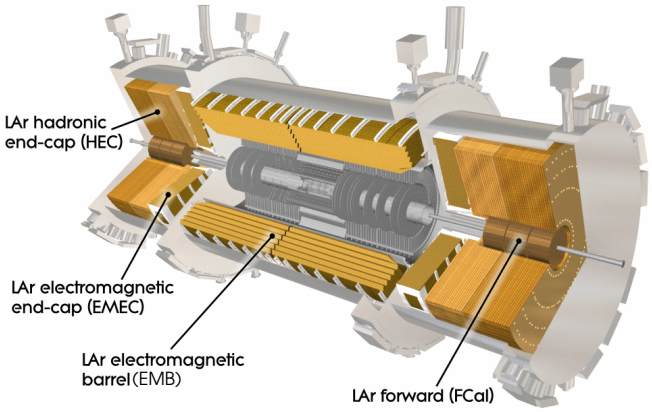

Figure 3.1: Cut-away view of the LAr calorimeter showing the different subsystems.

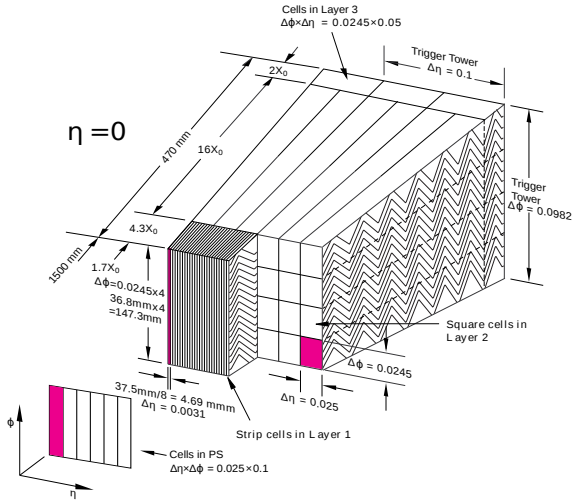

Figure 3.2: Sketch of an EMB module where the different layers are shown. The granularity in η and ϕ is also show.

in parallel-plate geometry. It has copper absorbers and copper and kapton electrodes.

To allow a measurement of forward jets and a better estimation of the missing energy, two forward calorimeters (FCal) were set at each side of the ATLAS detector. These calorimeters also help limiting the background in the muon chambers. The forward calorimeters are divided longitudinally into 3 modules. The first module, closer to the interaction point, uses copper as absorber and is optimised for electromagnetic detection. The two other modules use tungsten as absorber and are optimised for hadronic detection. All three modules share the same liquid argon cryostat with the EMEC and HEC.

The LAr calorimeter contains 182418 channels otherwise known as calorimeter cells. The cells η and ϕ segmentation in each layer of the central barrel region is shown in figure 3.2. The cell signals are readout at the level 1 trigger frequency of 100 kHz. The corresponding data path is called the main readout path. The LAr calorimeter also provides trigger capabilities. The trigger

readout path has coarser segmentation to allow for fast readout and processing at 40 MHz. In this path up to 60 cells are summed together to form Trigger Towers of $\eta \times \phi = 0.1 \times 0.1$ over most of the calorimeter coverage.

3.1.1 LAr readout electronics

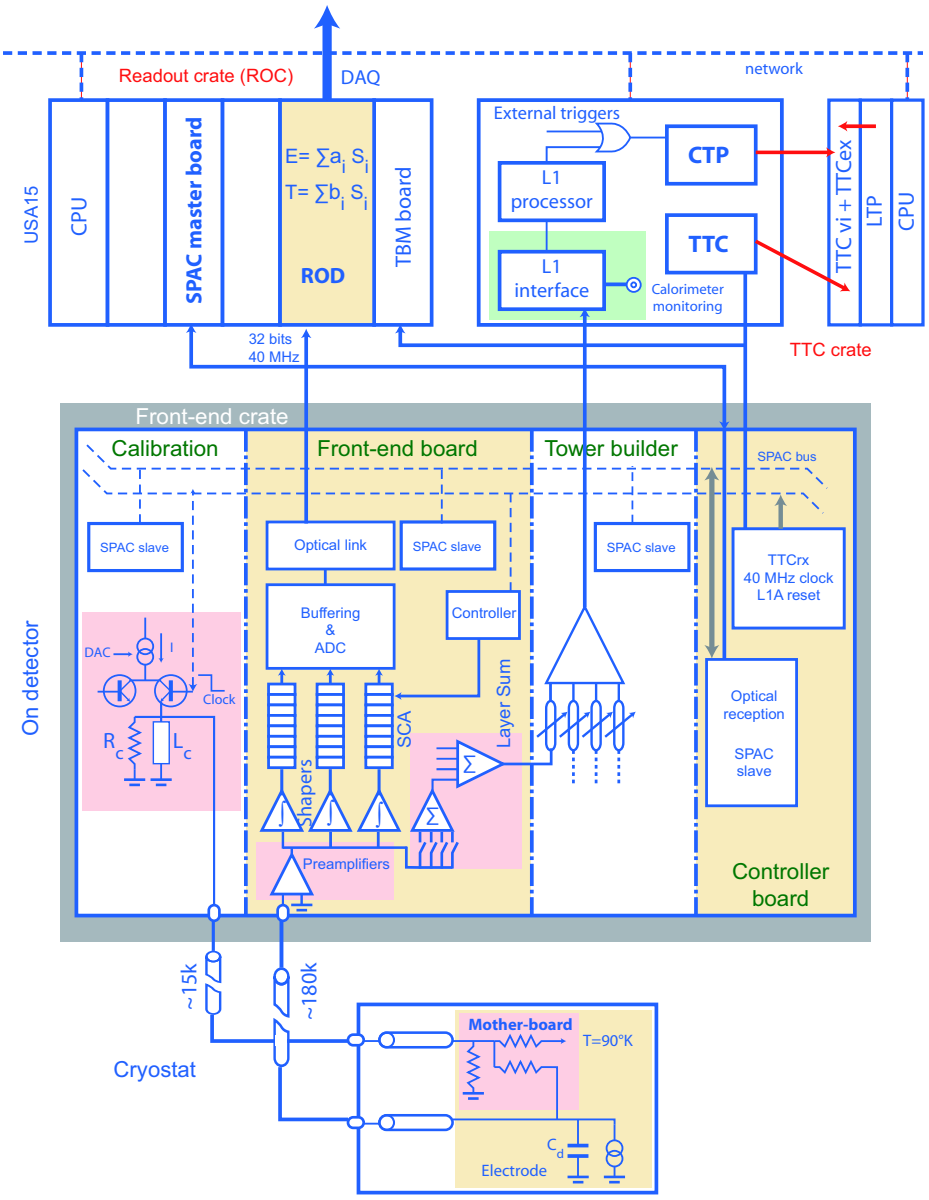

Figure 3.3: The LAr readout electronic chain before the Phase-I upgrade. This diagram depicts the EM calorimeters; HEC and FCal electronics are slightly different [227].

The readout electronics of the LAr system before the Phase-I upgrade (referred too as the legacy system in the rest of this chapter) is shown in figure 3.3. The electrodes inside the cryostat connect to the frontend electronics by means of feedthroughs [230]. In total 114 feedthroughs are present in the 3 cryostats of the LAr calorimeter. The frontend electronic boards are organised in 58 frontend

crates (FECs). The FECs are divided into two halves; each halve[1] contains the readout electronics corresponding to the signals from one feedthrough. A baseplane is installed at the bottom of each halve crate. Flex ribbon cables from the feedthrough connect to the backside of the baseplanes. Several types of boards are plugged into the front side of the baseplanes:

- The frontend board (FEB) amplifies and shapes the signals from up to 128 calorimeter channels before storing them in switched capacitor arrays. Upon the reception of a level 1 trigger signal the FEBs digitise the cell signals before sending them to the backend electronics. The layer sum board (LSB) is a mezzanine board that is plugged into the FEB. It sums the individual cell analogue signals corresponding to each of the layers in a Trigger Tower.
- The tower builder board (TBB) receives summed signals from the LSBs and further adds them to form the Trigger Tower. The Trigger Tower analogue signals are sent to the trigger system where they are digitised at 40 MHz.
- The control board receives the configuration and monitoring commands, and the timing, trigger and control (TTC) signals from the backend electronics and distributes them to other boards in the FEC.
- The calibration board injects calibration pulses with known current which allows to calibrate the energy and the time of the signals in the calorimeter.

The backend electronics is formed of two main systems:

- The readout drivers (RODs) hosted in the readout crates (ROCs) collect and process the signals sent by the FEBs. They compute the energy and the time of the deposits in the calorimeter before sending these values to the ATLAS data acquisition (DAQ) system. The ROCs also contain boards that configure and monitor the frontend boards.
- The TTC crates receive the trigger and timing information from the ATLAS TTC system and send it to the RODs and the FECs.

In addition to the LAr backend boards, the trigger receiver boards which are part of the trigger system, receive the analogue signals corresponding to Trigger Towers before sending them to additional trigger components in order to compute the trigger decision.

Energy deposits in the calorimeter produces a triangular pulse that is shaped to a bipolar pulse as shown in figure 3.4. The area of the positive and negative parts of the bipolar signal are equal allowing to cancel the electronic pulses from pileup energy deposits which are randomly distributed in time. The energy and the time of deposit are computed from the sampled pulse using an optimal filtering [231] algorithm as explained in [232].

[1] For the two FCAL crates, only one half of the crates is used.

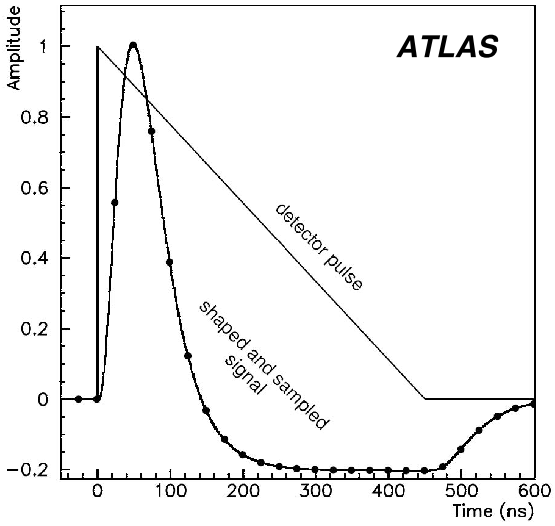

Figure 3.4: Shapes of the LAr calorimeter pulse in the detector and of the signal output after bipolar shaping. The dots represent the samples seperated by 25 ns [227].

3.2 Phase I upgrade of the LAr calorimeter

During the run 3 of the LHC the instantaneous luminosity was originally expected to increase up to $3 \times 10^{34}\,\mathrm{cm}^{-2}\mathrm{s}^{-1}$ with an average pileup of $\langle\mu\rangle = 80$ while the average pileup in run 2 was $\langle\mu\rangle = 33$. These changes will result in an overall detector occupancy increase, while the first level trigger rate remains at 100 kHz which leads to a degradation of the calorimeter trigger performance. An increase of the trigger thresholds would be needed with the legacy trigger system to maintain the trigger rates, leading to a decrease in trigger efficiency for several physics processes. To avoid this efficiency loss and enhance the physics reach, a new trigger system is designed to increase the readout granularity by up to a factor of ten. New longitudinal and lateral segmentations replace the Trigger Towers by smaller clusters called Super Cells. The finer segmentation of the Super Cells provide access to the longitudinal and lateral shower shapes allowing increased separation between electromagnetic and hadronic showers, increased energy resolution, and enhanced calculation of the isolation of the reconstructed objects. Figure 3.5 shows an electron with $E_\mathrm{T} = 70$ GeV as seen by the legacy and the new trigger systems.

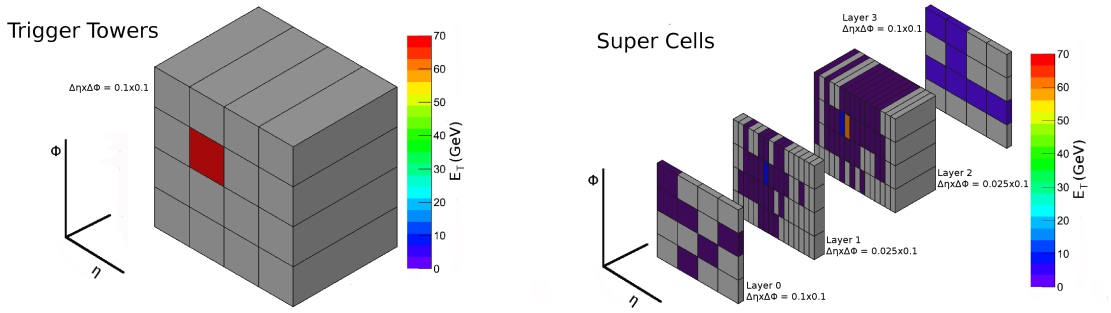

Figure 3.5: An electron with $E_\mathrm{T} = 70$ GeV as seen by (left) the legacy trigger system and (right) the new trigger system [227].

3.2.1 The digital trigger system electronics

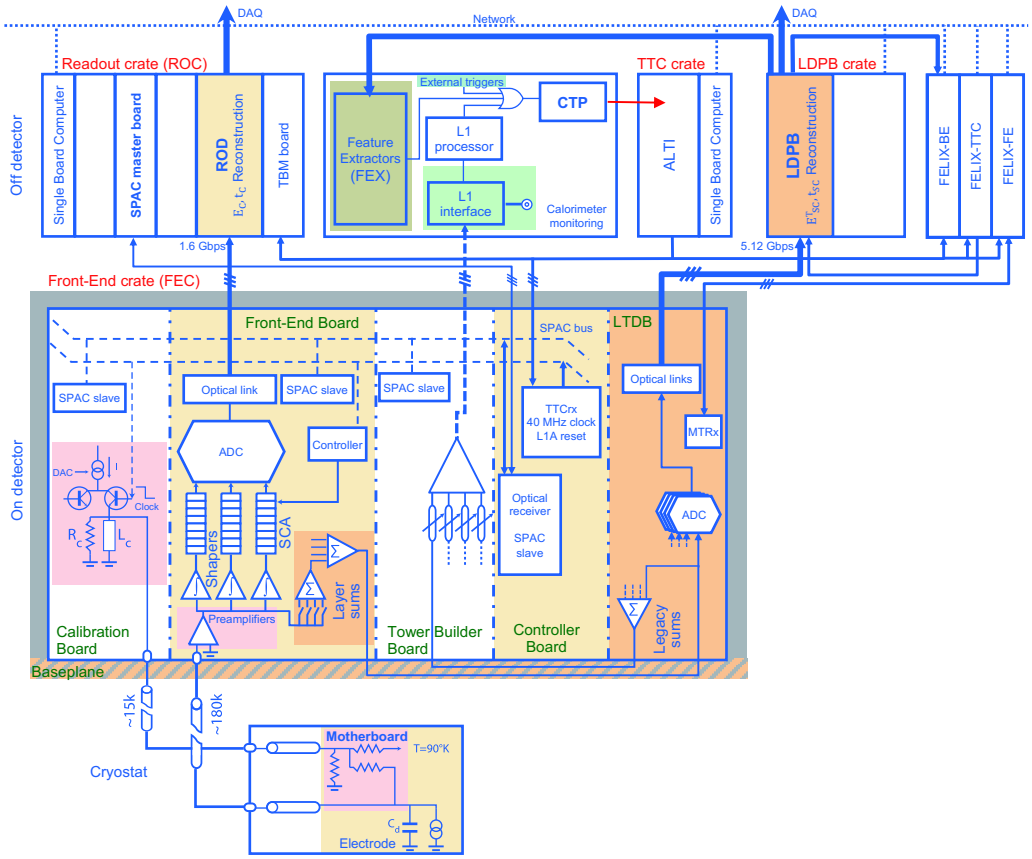

Figure 3.6: The LAr readout electronic chain after the Phase-I upgrade. The new LAr boards are highlighted in orange. This diagram depicts the EM calorimeters; HEC and FCal electronics are slightly different [227].

The phase I upgrade of the LAr calorimeter is described in details in [37] and [227]. In the new trigger system the Super Cell signals are digitised on the frontend electronics before being sent to the backend while the Trigger Tower signals of the legacy system are sent as analogue signals to the backend. That is why the new trigger system is referred to as the digital trigger system for the rest of this chapter. The legacy trigger is kept operational in parallel to the digital trigger to ensure the trigger operation during the commissioning of the new system at the beginning of the data taking period.

The readout electronics of the LAr calorimeter after the Phase-I upgrade is represented in figure 3.6. Several components had to be replaced or added to install the digital trigger system. On the frontend, the LSBs are replaced to account for the new sums needed for the Super Cells. For this all FEBs are removed, refurbished, and reinstalled on the detector. The LAr trigger digitiser boards (LTDBs) are added to the FECs. These boards receive the Super Cell signals from the LSBs, digitise it using an ADC with a dynamic range of approximately 12 bits, and send it to the backend through optical fibers. The LTDBs also add the analogue signals from Super Cells corresponding to one layer in a Trigger Tower to reproduce the legacy signals from the old LSBs and then send these signals to the TBBs. This functionality insures that the legacy trigger system is maintained operational. All baseplanes are replaced to be able to route the new Super Cell signals from the

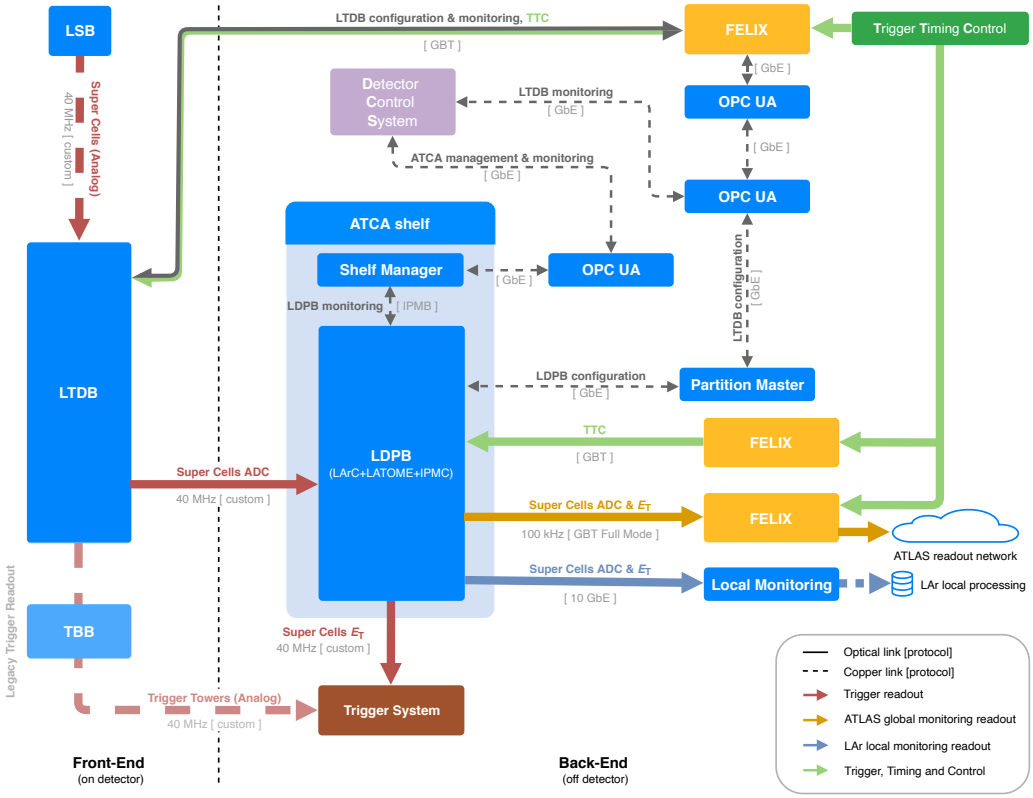

Figure 3.7: Schematics representing the different components of the LAr digital trigger system with the various communication links between these components.

LSBs to the LTDBs and the legacy signals from the LTDBs to the TBBs. On the backend side, the LAr digital processing system (LDPS) is added. This system is formed of 30 LAr digital processing boards (LDPBs) housed in 3 advanced telecommunications computing architecture (ATCA) crates. Each LDPB is formed of one carrier board (LArC) and 4 mezzanine boards (LATOME). The LArC provides the LDPB interface to the DAQ and TTC systems while the LATOME receives the signals from the LTDBs and computes the energies deposited in the calorimeter before sending them to the trigger system.

The communication between the different systems on the frontend and the backend is sketched in figure 3.7. The configuration and monitoring of the LTDBs is performed through the frontend link exchange (FELIX) system [233] by means of open platform communications unified architecture (OPC-UA) servers. The FELIX system also distributes the TTC signals to the LTDBs and the LDPBs. The configuration of the LDPBs is done through a GbE connection while its monitoring is done using the ATCA shelf manager through an OPC-UA server.

The LATOME boards are the core of the digital trigger backend system. The main component of these boards is the Intel® Arria® 10 field-programmable gate arrays (FPGA), part number 10AX115R3F40E2SG. This FPGA is responsible of processing the data received from the LTDBs. The block diagram of the LATOME firmware is shown in figure 3.8. The firmware is built around the Low-Level Interface (LLI) which controls the hardware components of the LATOME. The main data path links the LTDBs to the trigger system and is formed of four blocks:

- The Input Stage receives, decode and align in time the data transmitted by the LTDBs.

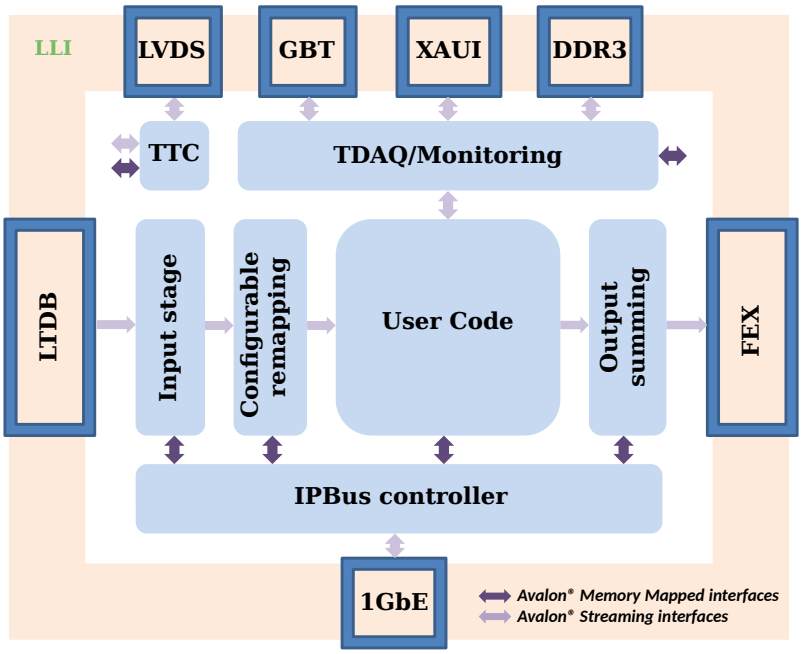

Figure 3.8: LATOME firmware block diagram. The pale brown frame corresponds to the interface with the hardware while the blue boxes correspond to the higher level functional blocks.

- The Configurable Remapping organises the signals from different channels following geometrical considerations to ease the subsequent processing at the trigger level.
- The User Code computes the energy deposited in the detector using the samples sent by the LTDBs.
- The Output Summing transmits the energies computed by the user code to the trigger system. It also creates sums of energies in predefined clusters that are needed by the trigger system.

The samples and the energies computed by the User Code are buffered in the TDAQ/Monitoring block and transmitted to the DAQ system if a trigger level 1 accept signal is received. The TTC block receives the TTC signals from the LArC and distributes them to other firmware blocks while the IPBus Controller block receives the firmware configuration sent on a 1 GbE link and transmits it to the other blocks.

Important efforts are made to insure that the digital trigger system (especially the LATOME firmware) fits the total allowed latency which is unchanged during the Phase-I upgrade. Table 3.1 details the measured digital trigger latency starting from the proton-proton collision time to the reception of the computed energy by the trigger system. The latency is given in bunch crossing (BC) units which correspond to 25 ns. The total latency amounts to 43.8 BCs which is well within the 51 BCs required by the trigger system [227].

Table 3.1: Latency measurements for the Phase-I upgrade of the LAr trigger readout electronics. BCs correspond to 25 ns time intervals.

	Latency [ns]	Latency [BCs]	Sub-total [BCs]	Total [BCs]
Time-of-flight at $\eta = 2$	15.0	0.6		
Cable to pulse preamplifier	30.0	1.2		
Preamplifier, shaper, and linear mixer	21.6	0.9	**2.7**	**2.7**
LTDB	153.7	6.1	**6.1**	**8.8**
Optical fiber cable (77 m) LTDB to LDPB	385.0	15.4	**15.4**	**24.2**
Deserializing and descrambling	81.1	3.2		
BCID aligning	28.2	1.1		
Channel remapping	67.7	2.7		
Optimal filtering	108.2	4.3		
Encoding and summing	94.6	3.8		
Serializing	35.7	1.4	**16.6**	**40.8**
Optical fiber cable (15 m) LDPB to FEX	75.0	3.0	**3.0**	**43.8**

3.2.2 Commissioning of the digital trigger system with calibration data

Each component of the digital trigger system was tested as described in [227] and only the boards that pass a set of requirements are installed in ATLAS. In addition the full chain of the LAr trigger and data acquisition electronics including the frontend and the backend electronics is tested in situ after the installation in the ATLAS cavern. A set of scans is designed to validate the new system: mapping scans to check the connectivity of all channels; timing scans to align various components in time; and calibration scans to validate the pedestal values, the shape of the pulse and the value and linearity of the gains.

Due to the installation of the new baseplanes and the LTDBs, the electronic path for some of the input channels to the legacy Trigger Towers were modified. Moreover, the FEBs were removed from the old baseplanes, refurbished with new LSBs and installed on the new baseplanes. These operations might have affected the legacy main readout. The legacy trigger system is required to run in parallel to the new digital trigger system during Run 3. For these reasons, both main and trigger legacy readout paths are validated after the installation of the new frontend electronics. The noise levels for the different cells and Trigger Towers before and after the installation of the new baseplanes and LTDBs can be seen in Figure 3.9 and 3.10 respectively. No significant change in the level of the electronic noise is observed due to the installation of the new electronic boards. The jump at $\eta = 0.8$ observed in both figures is due to a change in the barrel calorimeter sampling fraction, that affects the conversion of the signal in μA to a signal in MeV.

The timing of the different Trigger Tower channels is adjusted on the TBBs to take into account the new signal path due to the new boards. The time difference relative to the middle layer channels in the different layers before and after the LTDB installation and before and after the correction is shown in Figure 3.11.

To validate the new digital trigger path, data from the LTDBs are received, time-aligned and processed on the LATOME boards and then sent to a local monitoring path to be collected by a

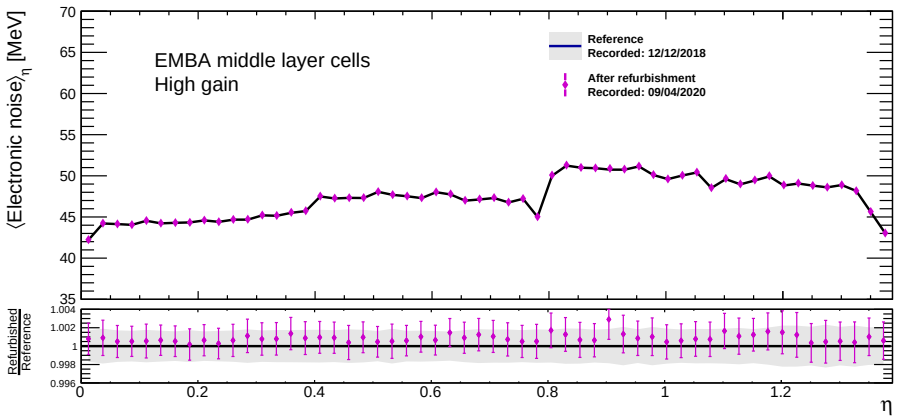

Figure 3.9: Noise level as function of the pseudorapidity for cells before and after the installation of the new frontend electronics. The noise level corresponds to the mean value of the readout electronic noise in MeV over the cells in a given pseudorapidity (η) range. Only the cells of the middle layer of the EMB on side A are included. The black line and the gray uncertainty band show the values measured at the end of Run 2. The purple dots show the values measured after the refurbishment of the FECs and FEBs during the LS2. The displayed uncertainties are computed as $\sigma_{\text{noise, cells}}/\sqrt{N_{\text{cells}}}$, where $\sigma_{\text{noise, cells}}$ are the standard deviations over the cells in the given η range and N_{cells} is the number of cells in the given η range. The systematic increase of approximately one per mil over the whole η range will have a negligible impact on data analyses.

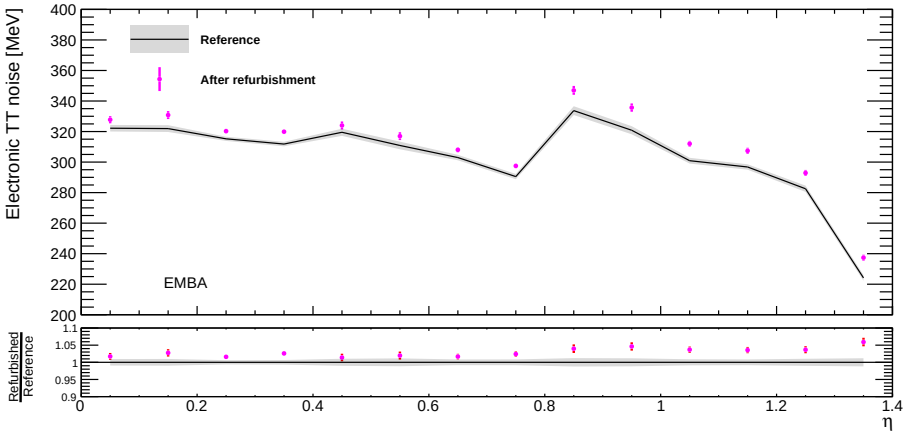

Figure 3.10: Noise level as function of the pseudorapidity for Trigger Towers (TTs) before and after the installation of the new trigger readout electronics. The noise level corresponds to the mean value of the readout electronic noise in MeV over the TTs in the same pseudorapidity (η) position. Only the TTs of the EMB on side A are included. The black line and the gray uncertainty band show the values measured at the end of Run 2. The purple dots show the values measured after the refurbishment of the FECs and FEBs and the installation of the LTDBs during the LS2. The displayed uncertainties are computed as $\sigma_{\text{noise, TT}}/\sqrt{N_{\text{TT}}}$, where $\sigma_{\text{noise, TT}}$ are the standard deviations over the TTs in the given η position and N_{TT} is the number of TTs in the given η position. The systematic increase of approximately 2 to 5% over the whole η range is due to a more complex analog signal path and has a negligible impact on trigger performance.

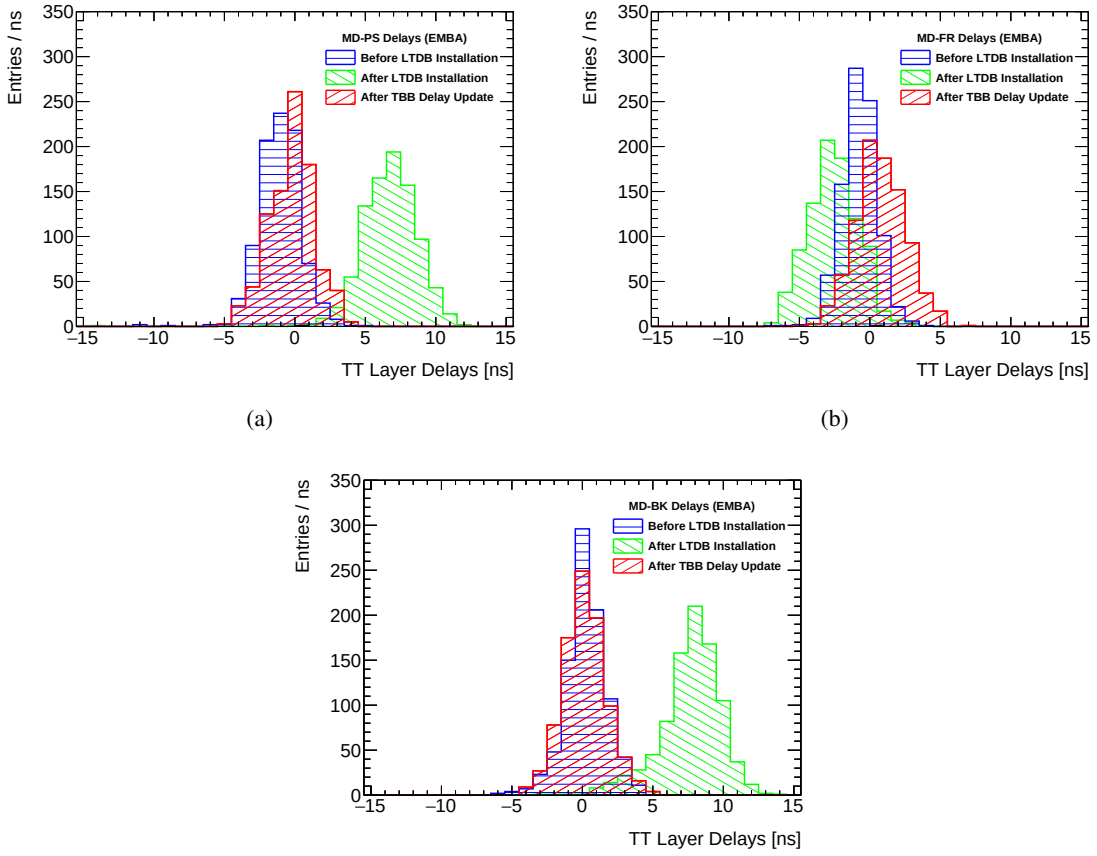

Figure 3.11: Time difference between (a) middle (MD) layer and presampler (PS) channels, (b) between middle and front (FR) layer channels, and (c) between middle and back (BK) layer channels before and after the baseplane replacement and the LTDB insertion. After the corrections applied to the TBB delays to take into account the new hardware, the distributions match well. Only EMB side A is considered here.

UDP server running on a dedicated machine. More precisely, a calibration pulse is injected in the frontend electronics synchronously to a delayed L1A signal. The LTDB data, corresponding to 32 ADC samples, are received at 40 MHz and buffered on the LATOME boards, which send the data to the local monitoring path when the L1A is received. To be able to retrieve the 32 ADC samples that correspond to the injected pulse the LATOME boards are time-aligned. With this procedure the shape of the pulse collected by the LATOME can be verified for different energy regimes, as illustrated for one Super Cell in Figure 3.12. To obtain this shape with a fine granularity from a 32 ADC sample readout, a series of twenty four consecutive calibration pulses is used, each one with an incremental delay of about 1.04 ns. Distortion in the pulse shape can be seen at high energy due to saturation effects which will be discussed in the following.

In order to compute the Super Cell energy from a pulse, the pedestal value must be measured beforehand. Pedestal data are collected without injecting any pulse in the frontend electronics. From this data, the electronic noise can also be studied since it corresponds to the root mean square of the pedestal value. In Figure 3.13 the pedestal value and its root mean square can be seen as function of the η position of the Super Cells, in the EMB and EMEC areas and for the different calorimeter

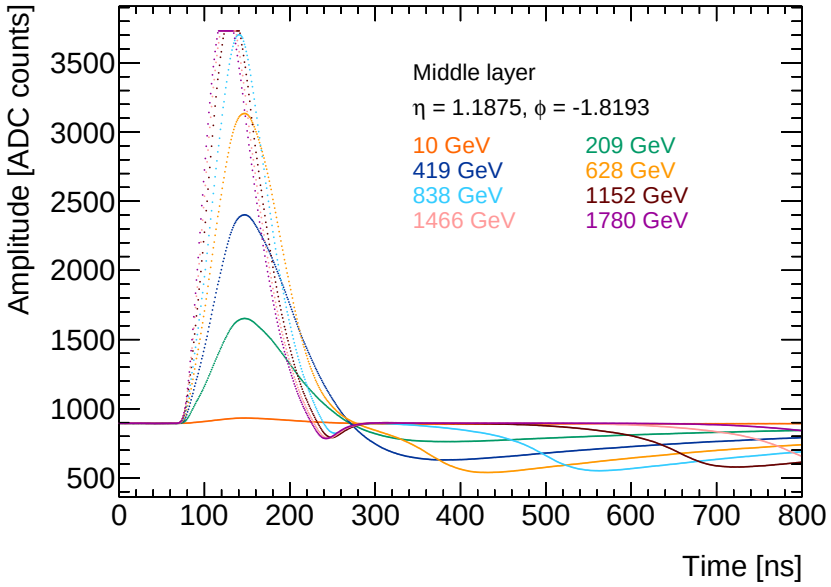

Figure 3.12: Pulse shape collected by a LATOME board for one Super Cell in the barrel part of the detector at $\eta = 1.1875$ and $\phi = -1.8193$ in the middle layer for several injected current pulses corresponding to different E_{T} values.

layers. They are found to be consistent with the expectation from the design of the LTDB boards, with the electronic noise is always smaller than one ADC count.

Ramp runs are used to measure the linearity of each channel, using a series of 16 LAr signals injected with different amplitudes ranging from the baseline to the maximum signal close to ADC saturation. The peak ADC value with respect to the pedestal as function of the E_{T} corresponding to the injected pulse as seen by four channels on a LATOME board is presented in Figure 3.14. The peak ADC value is extracted with an optimal filtering algorithm. The ADC values are linearly increasing with the deposited E_{T} up to about 800 GeV, where saturation of the Super Cell pulse occurs. This saturation is mainly due to the analog electronics (Linear Mixer), however digital saturation can occur for some channels in addition to the analog one at very high energies.

The E_{T} per ADC count is computed from the ramp runs. This value is shown in Figure 3.15 as function of the pseudorapidity in the EMB and EMEC areas. The jump at $\eta = 0.8$ is due to a change in the EMB sampling fraction, the one at $\eta = 1.5$ corresponds to the EMB-EMEC transition and the one at $\eta = 2.5$ to the boundary between the EMEC inner and outer wheels. The values are consistent with the ones expected from the design of the LTDB boards.

The main readout system, which reads individual cells of the LAr calorimeter, is well understood and calibrated based on years of ATLAS operation. To fully validate the trigger system, the E_{T} values computed by the LATOME for certain Super Cells are compared to the sum of E_{T} values computed for the corresponding cells using data collected with the main readout. The data are collected simultaneously by both readout paths after injecting an electronic pulse in the frontend electronics. In both cases the E_{T} values are computed with an optimal filtering algorithm. Figure 3.16 shows good agreement between the Super Cell E_{T} and the sum of the E_{T} values in the corresponding cells for the middle layer of the calorimeter in the barrel region. At high energy the Super Cell pulse shape is saturated and the energy computed using the LATOME data does not increase anymore with the deposited energy.

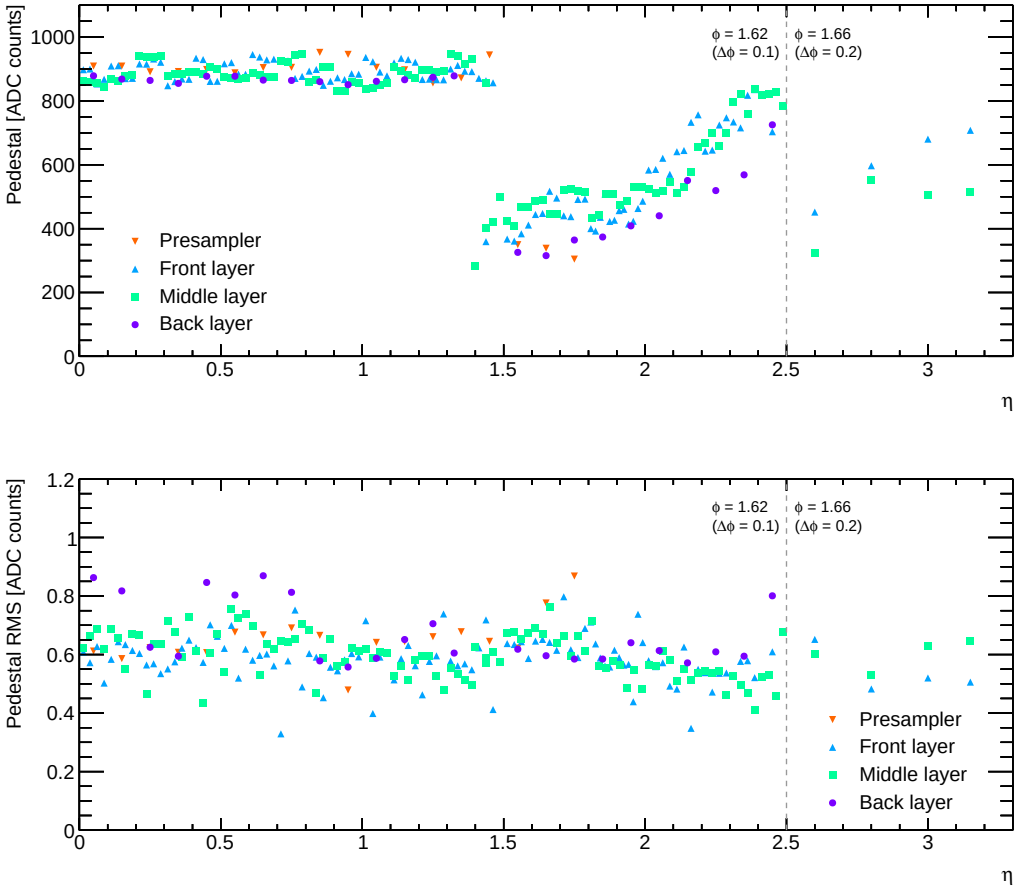

Figure 3.13: The pedestal value (top) and its root mean square (bottom) as function of the η position of the Super Cells at $\phi = 1.62$ ($\phi = 1.66$) and $0 < \eta < 2.5$ ($2.5 < \eta < 3.2$), corresponding to a $\Delta\phi$ granularity of 0.1 (0.2) and for the different calorimeter layers.

A similar comparison is performed between the Trigger Tower E_{T} computed by the legacy trigger system and the sum of the E_{T} values in the corresponding cells. Figure 3.16 shows good agreement between the two E_{T} measurements, with a Trigger Tower saturation that occurs earlier in energy than with the Super Cell readout.

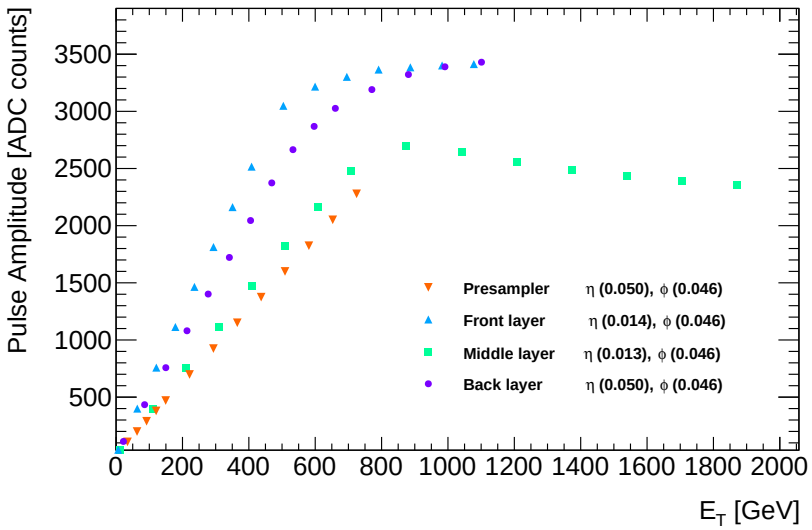

Figure 3.14: Peak ADC value with respect to the pedestal as function of the E_{T} corresponding to the injected pulse as seen on a LATOME board by four channels of the different calorimeter layers.

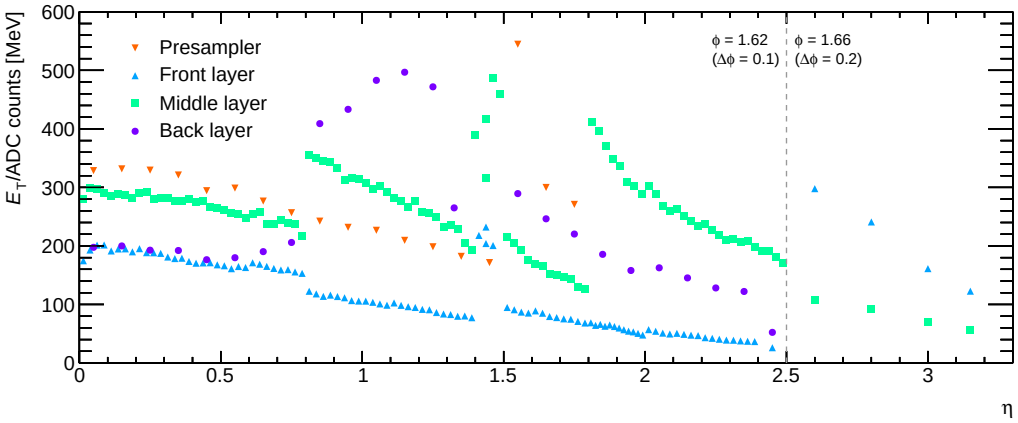

Figure 3.15: Measured E_{T} per ADC count as function of the η position of the Super Cells at $\phi = 1.62$ ($\phi = 1.66$) and $0 < \eta < 2.5$ ($2.5 < \eta < 3.2$), corresponding to a $\Delta\phi$ granularity of 0.1 (0.2) and for the different calorimeter layers.

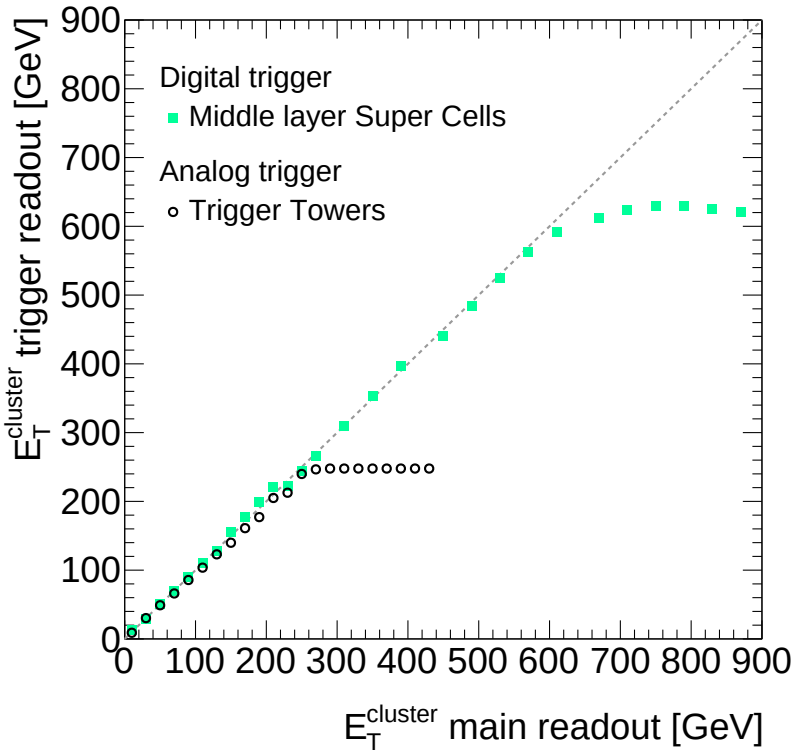

Figure 3.16: Comparison between the E_T in middle layer Super Cells or Trigger Towers and the sum of the E_T in the corresponding cells of the LAr barrel calorimeter. The Super Cell data are collected by the LATOME boards while the energy deposited in the cells and the Trigger Towers is collected by the legacy main and trigger readout systems for injected signals. The deposited energy measured by the LATOME or the legacy trigger system corresponds well to the one measured by the main readout system up to the level where the signal on the Super Cells or the legacy Trigger Towers is saturated.

3.2.3 Commissioning of the digital trigger system with LHC data

The run 3 of the LHC started in 2023 following a pilot run in November 2022. Proton-proton collision runs are preceded by splash events where the collimators on both sides of ATLAS are closed and intercept the proton beam. Splashes lead to a jet of particles that hits ATLAS depositing a large amount of energy in all parts of the detector. Splash events are interesting since they are isolated events with energy deposits in all channels in the calorimeter. They allow to verify that all channels are working properly. They also allow a first crude time alignment of the trigger and readout systems. The LAr digital trigger system was fully ready to collect data during the pilot run and at the beginning of run 3. To validate the energy computed by the digital trigger system, the Super Cell energy is compared to the sum of energies deposited in the corresponding cells computed by the well known legacy system. Such a comparison for a splash event during the pilot run is shown in figure 3.17 for the electromagnetic part of the calorimeter. The Super Cell energy is computed with preliminary calibration constants obtained from the calibration system. A good agreement between the cell and Super Cell energy is observed over almost all channels.

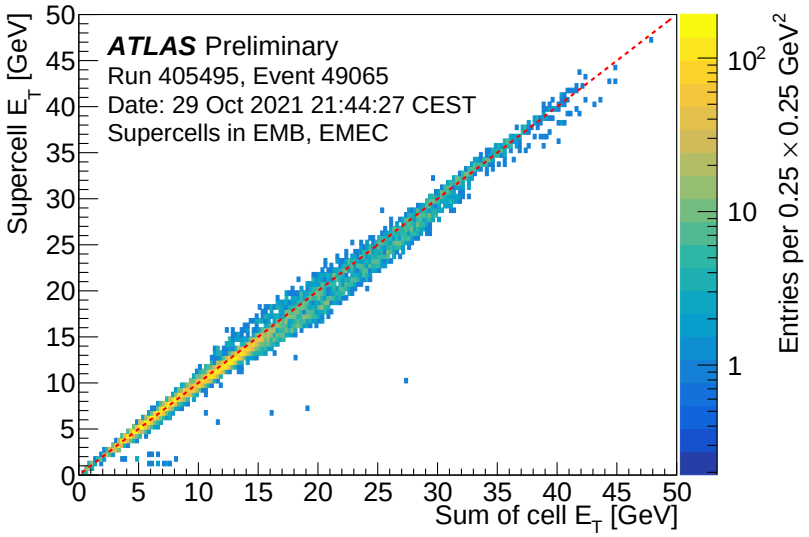

Figure 3.17: The measured supercell (SC) transverse energies (E_{T}) from all layers of the LAr Electromagnetic Barrel (EMB) and Electromagnetic Endcaps (EMEC) are compared to the summed transverse energies from their constituent calorimeter cells, obtained through the main readout path. The data are from a single event of a beam splash run, where energy calculations are performed offline using optimal filtering with preliminary calibration constants. A good agreement is observed between the two readouts, as indicated by the y=x diagonal red line.

The first splash events are used to adjust the timing of the digital trigger system. The recorded data is scanned over 32 BCs to find the pulse peaks corresponding to the energy deposits and the timing delays are adjusted in the LATOME firmware such that the pulse peaks are centred at the expected BC. This procedure allows to tune the timing of the Super Cells to precision of the order of one BC (25 ns). Figure 3.18 shows the spread of Super Cells timing with respect to the collision time as function of η. Most Super Cells time is within the ± 1 BC range as expected after the timing adjustment described above. Further adjustment is ongoing with proton-proton collisions with a target spread of the order of 1 ns.

Figure 3.19 shows the Super Cell energies compared to the corresponding cells energy sum in

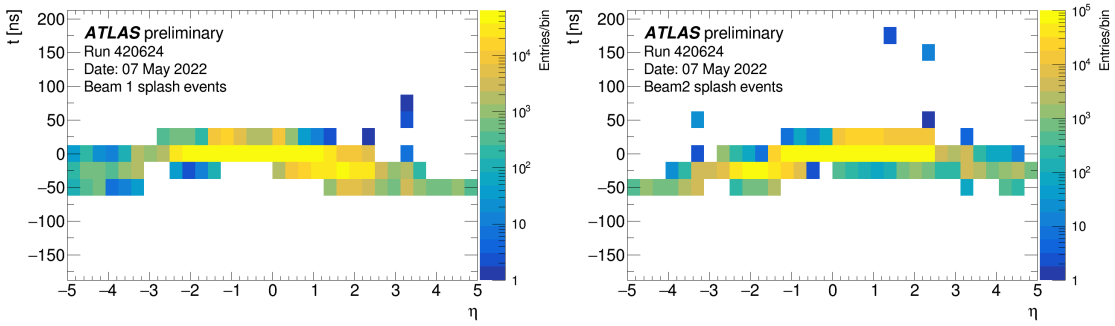

Figure 3.18: The super cell timing uniformity, tuned at the BC level, for the LAr detectors as a function of η. The data are from events of the beam splash ATLAS Run 420624 with the particles delivered by (left) LHC Beam 1 and entered from the positive η (A) side or (right) LHC Beam 2 and entered from the negative η (C) side. Only super cells which are not saturated are selected. The timing is not corrected to account for the time of flight of particles.

proton-proton collisions at $\sqrt{s}$ = 13.6 TeV. The calibration constants used are further adjusted with respect to the ones used for splash events but are still preliminary since they do not account for time shifts in the pulses nor for the difference between calibration and physics pulse shapes. A good agreement is observed validating the full electronic chain of the digital trigger system including the LATOME firmware.

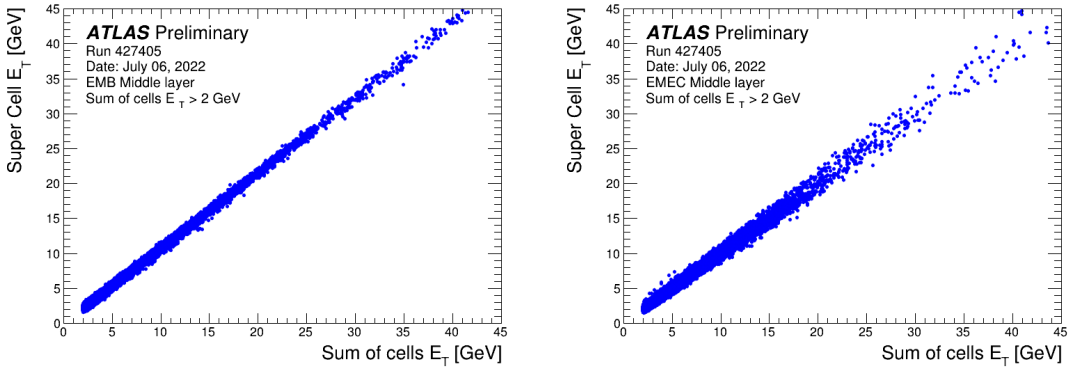

Figure 3.19: The measured Super Cells (SC) transverse energies (E_{T}) using data collected with the first stable beam proton-proton collision at $\sqrt{s}$ = 13.6 TeV from Run 427405, computed on LATOME boards in real time from the middle layer of the LAr (left) EMB and (right) EMEC, excluding not well calibrated SCs, compared to the summed transverse momentum from their constituent calorimeter cells, obtained through the main readout path. Preliminary calibration constants are used without adjusting the phase of the pulse. A reasonable agreement is observed between the two readouts.

3.3 Phase II upgrade of the LAr calorimeter

In the years 2026-2029 the LHC will undergo a major upgrade to increase its instantaneous luminosity by a factor of 5-7 leading to the High luminosity LHC (HL-LHC). The increased luminosity

will lead to 140 to 200 simultaneous proton-proton interactions. During the same period the ATLAS detector will be upgraded to cope with the increased luminosity of the HL-LHC. This upgrade is called the phase-II upgrade. The readout electronics of the ATLAS LAr calorimeter will be replaced as part of the phase-II upgrade [44]. The new frontend boards will shape, sample, and digitise at 40 MHz the electronic signals from the calorimeter before sending the samples to the backend electronics through optical fibers. The new backend boards employ FPGAs to compute the energy deposited in the calorimeter out of the samples received from the frontend boards. The computed energy is then sent to the trigger system at 40 MHz, and to the readout system at 1 MHz in case of a level 1 trigger accept decision. For the trigger data path, a latency of about 125 ns is allocated to the reconstruction of the energy, based on a preliminary analysis of the full data processing chain [43, 44].

FPGA technology has been chosen for the backend boards in favour of other processing devices because of the large input data bandwidth of about 250 Tbps required for the full system and the possibility to directly capture the detector data transmitted by serial links with 36,000 optical fibers. The system shall be installed in an underground area which has a limited floor space, so that compact solutions with high integration factor, like custom FPGA boards, are needed. Most importantly, the FPGA technology allows a custom configuration which permits an evolution of the data processing scheme during the expected lifetime of the system of more than 10 years. In the current design options, 384 LAr calorimeter cells shall be processed by one Intel® Agilex® FPGA. The Agilex® device was chosen for several reasons: experience of the firmware development group with Intel® design tools, a high number of multi-Gbps serial links per device, as well as the available memory and the number of logic modules. A demonstrator board is already produced with Stratix® 10 FPGAs while waiting for the Agilex® FPGAs to be available. In this section we consider the implementation of energy reconstruction algorithms in a Stratix® 10 FPGA (part number 1SG280HU1F50E2VG).

Currently, the energy is computed using optimal filtering algorithms [231] that assume a nominal pulse shape of the electronic signal. Calorimeter electronic signals of up to 25 subsequent collisions overlap and create distortions to the pulse shape. This increases the difficulty of energy reconstruction and identification of the corresponding proton-proton bunch crossing. Up to 200 simultaneous proton-proton collisions are expected at the HL-LHC, which will lead to a high rate of overlapping signals in a given calorimeter channel. This will result in a significant energy degradation [44] especially for low time-gap between two consecutive pulses. To meet the challenging task of real-time energy reconstruction new machine learning methods are explored. Artificial neural networks (ANNs) implemented in FPGAs have demonstrated enhanced object reconstruction and identification at trigger level in LHC experiments [234, 235, 236, 237, 238]. The application of ANNs on FPGAs, however, is constrained by the limited digital signal processing (DSP) resources, logic, and memory available in the FPGA devices. This, in turn, limits the number and type of mathematical operations that can be used by the machine learning application. In the following, first results and experience aiming at real-time reconstruction of LAr calorimeter energies with ANNs are presented.

3.3.1 LAr cell energy reconstruction by artificial neural networks

3.3.1.1 Simulation of LAr pulse sequences and legacy energy reconstruction

The first step in the development of the FPGA-based ANNs is the training of the networks on simulated data sequences. The AREUS [239] tool is used to convert the series of true energy deposits in the LAr calorimeter cells into a sequence of overlaid and digitized pulses taking into account ana-

logue and digital electronics noise. The true energy spectrum corresponds to the one expected for HL-LHC operation and is dominated by low-energy deposits in the range up to approximately 1 GeV from particles produced in inelastic proton-proton collisions. In order to emulate hard-scattering events, a uniform transverse energy spectrum is overlaid randomly, with maximum energy deposits of 5 GeV. The mean time interval of the additionally injected signals is 30 BC with a standard deviation of 10 BC, so that both overlapping and non-overlapping high energy pulses are generated. An example sequence for one cell in the EMB, which is selected for the study presented here, is displayed in figure 3.20 for a mean number of pileup events, $\langle\mu\rangle$, of 140.

The current readout electronics of the LAr calorimeters applies an optimal filter [231] (OF) to determine the energy in each cell. By linear combination of up to five digitized pulse samples, electronic noise and signal pileup are suppressed. The coefficients of the OF are determined using the analogue pulse shape and the total noise auto-correlation. In order to further identify true energy deposits and assign them to a certain BC, a peak finder is applied to the output sequence of the OF by selecting the maximum value in each group of three consecutive BCs. The OF results combined with the maximum finder are used to compare with the ANN solutions described in the following.

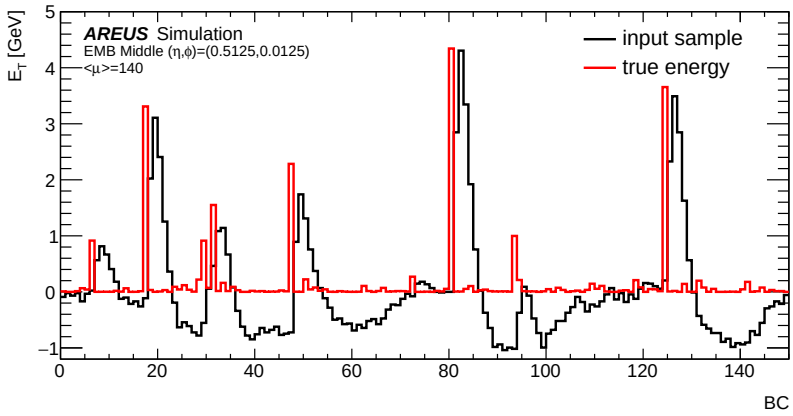

Figure 3.20: Sample sequence (black) of an EMB middle-layer cell located at a pseudorapidity η=0.5125 and an azimuthal angle ϕ=0.0125 within the ATLAS coordinate system, simulated by AREUS, together with the true transverse energy (E_T) deposits (red), at an average pileup μ of 140 as a function of the bunch crossing (BC) counter. The samples amplitude is normalized to the value of the deposited energy in GeV.

3.3.1.2 Recurrent neural networks

Recurrent neural network (RNN) algorithms are designed for the inference of time series data and extraction of the underlying parameters. They are natural candidates for the inference of deposited energies from time-ordered digitised LAr signals. Two RNN architectures are considered: vanilla RNN [240] and long short-term memory (LSTM) [241]. Supervised learning is applied during the network training. The true deposited energies in specific bunch-crossings, which are indicated in figure 3.20, serve as target values. The network training utilizes the Keras [242] API to the TensorFlow [243] platform. The mean squared error (MSE) loss function is used to train all RNNs. The energy reconstruction using RNNs will be compared with the OF algorithm and with the convolutional neural networks (CNN) that are described in [228].

LSTM based algorithms: LSTM based networks demonstrate utmost management of information through long sequences, allowing the use of long-term correlations in data. LSTM cells are composed of four internal neural networks, three learn to open and close access to the data flow through time, the last acting directly on the data to extract the desired features at a given time. However, their complexity scales rapidly with the dimension of the internal networks, while the application of intelligent algorithms in the LAr calorimeter read-out system sets tight limits on the network size. In order to limit the parameter count to a few hundred, only one layer of LSTM cells, with 10 internal dimensions, is used. Fewer internal dimensions significantly degrade the energy resolution. Improvements compared to the LSTM configuration chosen here, are only seen when increasing the parameter count to a few thousands. A decoder, consisting of a network with a single neuron and ReLU activation, is placed after the LSTM layer to concatenate the output in a single energy measurement. Architectures with additional RNN or dense layers did not show improvements which would justify the additional resource consumption.

Two LSTM based networks for real-time energy measurements are presented. The single-cell design derives from a many-to-many RNN evaluation, and is illustrated in figure 3.21. At each BC, an LSTM cell analyses the LAr signal amplitude and the output of the previous cell to predict an energy. The same operation with the same LSTM object is repeated until the end of data. To allow the RNN to accumulate enough information a delay of five BCs is imposed in the training process. This delay also avoids the RNN to learn from yet to happen collisions in the training phase. The second design uses a sliding-window algorithm and is illustrated in figure 3.22. At each BC an LSTM network is instantiated. This network is trained as a many-to-one RNN targeting an energy prediction with five ADC samples as input. The target energy corresponds to potential pulses starting on the second BC, allowing the network to read one BC before the deposit, and four on the pulse. This is found to be the best compromise between the correction for past events, the energy inference on the pulse, and short sequences meeting FPGA constraints. The sliding-window algorithm applies the network to subsequent BCs allowing a prediction in real time. The final dense operation corresponds to the single neuron decoder which reads the LSTM output and calculates the energy.

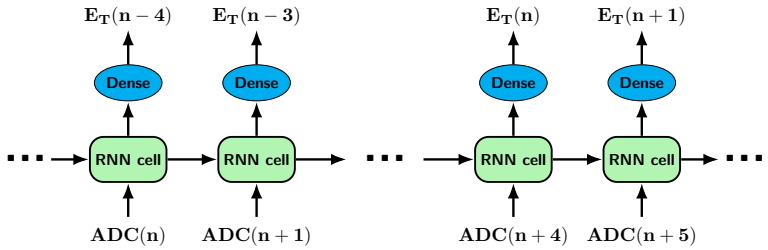

Figure 3.21: Single-cell application of LSTM based recurrent networks. The LSTM cell and its dense decoder are computed at every BC. They analyse the present signal amplitude and output of the past cell, accumulating long range information through a recurrent application.

Vanilla RNN based algorithm: The vanilla RNN cell is the most compact RNN architecture. It is composed of a single internal neural network trained both to forward the relevant information in time, and to infer the energy at a given BC. In order to fulfill constraints from the LAr calorimeter system, the size of the vanilla RNN internal network is reduced as much as possible. Only 8 internal dimensions are used. To avoid the use of look-up tables in the FPGA, a ReLU activation is used.

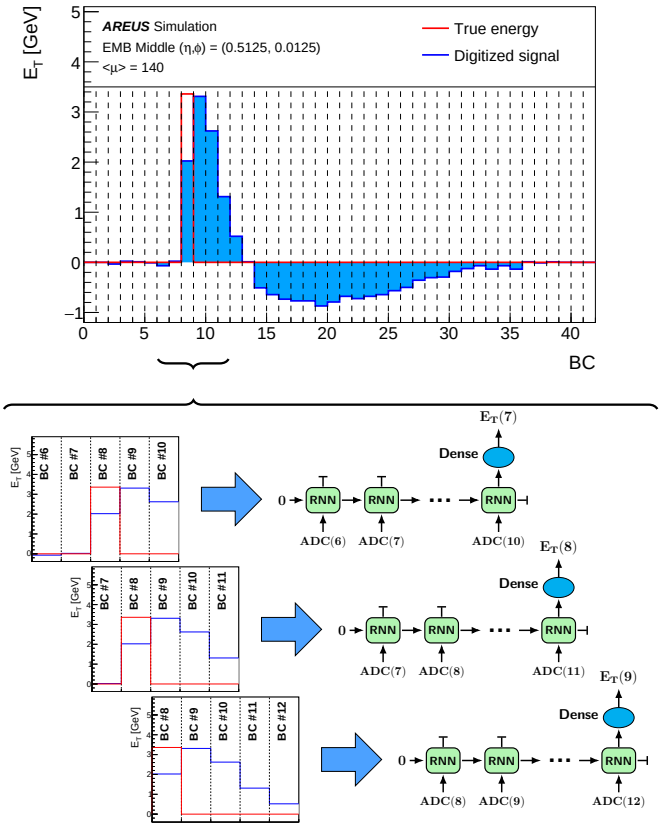

Figure 3.22: Sliding window application of LSTM based recurrent networks. At each instant, the signal amplitude of the four past and present bunch crossings are input into an LSTM layer. The last cell output is concatenated with a dense operation consisting of a single neuron and providing the transverse energy prediction.

As for LSTM networks, a single neuron decoder with ReLU activation concatenates the output in a single energy measurement. In total, the network comprises 89 parameters and 368 MACs.

With limited internal capabilities, vanilla RNN networks are not capable of managing the information over long periods of time. Therefore, only a sliding window application is considered. It is defined in the same way as for the LSTM networks.

Discussion: The final structure and parameter choices of the three RNN networks are shown in table 3.2. For the same number of parameters, the single-cell and sliding-window applications are expected to provide different insights into the features of the data. In particular, the sliding-window algorithm focuses only on a few inputs around the BC of interest: four on the pulse and one in the past which is immediately before the energy deposit. It is thus expected to be more robust when regressing the energy value of isolated data pulses. On the other hand, the single-cell design concatenates the present data with all past measurements. While this could limit the robustness of the measurement in consecutive but isolated pulses, it better alleviates remnants of past events. Out-of-time pileup and recurrent LHC bunch patterns are typically expected to impact measurements in tens of subsequent BCs. High performance in these cases requires a correction of long-lived patterns that can only be achieved with efficient management of the information through time. The

single-cell design is particularly robust in situations where subsequent pulses overlap as described in section 3.3.1.3. The vanilla RNN network demonstrates performance competitive with LSTM networks. This, added to its compact design, makes the vanilla RNN network the most suited among the RNN based algorithms for treating individual channels of the ATLAS LAr calorimeter system.

Table 3.2: Configurable key parameters of the single-cell and sliding-window algorithms.

		Single-cell	Sliding-window	
		LSTM	LSTM	Vanilla RNN
Time inference	Receptive Field	∞	5	5
	Samples after deposit	5	4	4
RNN layer	Dimension	10	10	8
	Activation	tanh	tanh	ReLU
	Recurrent Activation	sigmoid	sigmoid	N/A
Dense layer	Dimension	1	1	1
	Activation	ReLU	ReLU	ReLU
Number of Parameters		491	491	89
MAC units		480	2360	368

3.3.1.3 Results

Performance of the aforementioned RNN methods and the OF mith maximum finder are estimated in an AREUS simulation of energy deposits in one selected calorimeter cell at ($\eta = 0.5125$, $\phi = 0.0125$) in the middle layer of the barrel (labelled EMB middle) and for long BC sequences. An average pileup $\langle\mu\rangle = 140$ is assumed. Furthermore, only energy deposits 3σ above the noise threshold (corresponding to $E_{\mathrm{T}}^{\mathrm{true}} > 240\,\mathrm{MeV}$) are retained in what follows. Figure 3.23 shows a comparison of the energy resolution between the legacy OF, the three RNN algorithms, and two CNN algorithms described in [228]. The CNNs and RNNs outperform the OF both in terms of bias in the mean and of resolution. The smallest range that contains 98% of the entries is also shown to exhibit non-Gaussian behaviour present in the far tails of the resolution, and particularly at low energies. The single-cell implementation of the LSTM network has the best performance although it has the same number of parameters as the sliding-window implementation. Even though the vanilla RNN has fewer parameters than the LSTM, its performance is similar in the sliding-window implementation. The CNN networks have between 88 and 94 parameters depending on the architecture. The 3-Conv architecture outperforms the 4-Conv architecture and the Vanilla RNN. Overall, the LSTM networks achieve a better performance than the CNNs and the vanilla RNN. However, the LSTM implementations require 5 times more parameters than the compact CNNs and the vanilla RNN.

One of the challenges of the energy reconstruction algorithms is to correctly predict two subsequent deposited energies with overlapping pulses. Figure 3.24 show the energy resolution as a function of the time-gap between two deposited energies. Only deposited energies above 240 MeV are considered. This ensures that the pulse amplitude is large enough to distort the pulse shape of the subsequent event. With a time-gap smaller than 20 BCs the computed energy is underestimated by the OF algorithm and the resolution is significantly degraded. The RNN algorithms are robust against pulse shape distortion by overlapping events and allow for an improved energy reconstruc-

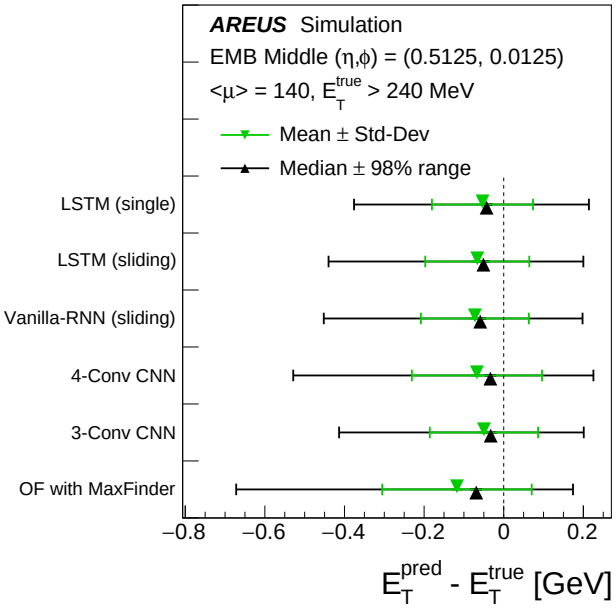

Figure 3.23: Transverse energy reconstruction performance for the optimal filtering and the various ANN algorithms. The performance is assessed by comparing the true transverse energy deposited in an EMB middle LAr cell ($\eta = 0.5125$ and $\phi = 0.0125$) to the ANN prediction after simulating the sampled pulse with AREUS assuming $\langle\mu\rangle = 140$. Only energies 3σ above the noise threshold are considered. The mean, the median, the standard deviation, and the smallest range that contains 98% of the events are shown.

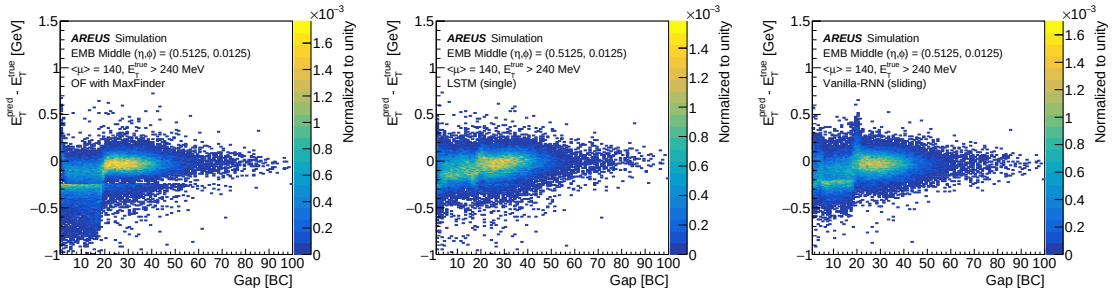

Figure 3.24: Resolution of the transverse energy reconstruction as a function of the gap, i.e. the distance in units of BC, between two consecutive energy deposits for the (left) OF algorithm and a subsequent maximum finder, (middle) the LSTM single-cell algorithm, and (right) the vanilla RNN sliding-window algorithm.

tion also at small time gaps. LSTM based algorithms in the single-cell application are particularly stable along the time gap as they can access as many BC in the past as found necessary in the training phase. On the other hand, the sliding-window vanilla RNN is only using one BC prior to the deposit. Therefore, it is the least capable of correcting for overlapping pulses at short gaps.

3.3.2 Neural networks implementation on FPGAs

3.3.2.1 Firmware implementation for one channel in HLS

In a first stage, the neural networks were implemented for a single data input channel to assess the feasibility of a firmware implementation that fits the requirements in terms of latency and FPGA occupancy for each of the networks. The RNN algorithms are initially implemented in Intel® high-level synthesis (HLS). The HLS is a design process that takes as input a behavioural specification of a digital system and convert it to a register-transfer level (RTL) realising the described functions. The HLS permits a flexible design automatically optimised to a given hardware target. The Intel® HLS takes a C++ code as input and produces RTL optimised for Intel® FPGAs. It provides several macros which are inlined in the C++ code that allow control over the RTL implementation. The Intel® HLS implements the standard C++ types but also defines several other types, in particular arbitrary precision fixed-point representations.

The RNN HLS implementation is based on two different functions, the first being the implementation of a single RNN cell, the second one handling the recursive aspect of the network architecture. The LSTM or vanilla RNN cells are coded as template functions. The template is used to pass on the weights and the internal architecture of the cell. The weights and architecture parameters are automatically generated by Python scripts from the Keras model. The precision of the fixed-point value is a configurable parameter. The activation functions and the recurrent activation functions other than the ReLU are implemented as LUT. The LUTs are generated with Python scripts. A configurable parameter allows using full precision mathematical functions instead of LUTs.

Two variants of the recurrent functions are implemented to support the single-cell and the sliding-window architectures. The single-cell function uses one instance of the LSTM cell implementation and allows linking the output of this cell at a given BC to its input at the subsequent BC. A continuous output flow is achieved with data entering through recursive calls of the logic, however requiring an input frequency no larger than the cell computation time. In the sliding-window, the function invokes for each window five instances of either the LSTM cell or the vanilla RNN cell, one for each BC. The output of each cell serves as an input to the next. The algorithm requires one such chain of five RNN cells for each BC in order to predict the deposited energy. To be able to process data in real time without using multiple RNN chains for multiple BCs, a fully pipelined design is needed. The implemented design ensures that the initiation interval, i.e. the number of clock cycles between two inputs in HLS, is equal to one. Every loop is fully unrolled: each of the loop iterations has its own logic resources. The memory needed is implemented as registers to optimize the latency.

A comparison of the energy computation in software, as given by Keras, and in firmware simulation with Quartus® 21.1 and Questa Sim 10.7c is shown in figure 3.25. The fixed point values are chosen to ensure a resolution of the order of 1%. For the sliding-window LSTM 18 bits are used including 13 bits for the decimal points. For the single-cell 22 bits are used including 14 bits for the decimal part. For the sliding-window vanilla RNN, data paths in the cell and RNN weights use different representations. Data paths use 19 bits with 16 bits for the decimal part. Weights are implemented using 16 bits out of which 13 are for the decimal part. The LUT implementation is optimized using logic to account for symmetries in the sigmoid and tanh functions. The LUT size is reduced by a factor 4 compared to the naive linear range. Their granularity is also optimized and 1024 words are found to be sufficient.

Performance results of these implementations on a Stratix® 10 FPGA are shown in table 3.3, comparing maximum execution frequency, F_{max}, latency, initiation interval and resource usage in terms of number of DSPs and adaptive logic modules (ALM). The maximum achievable processing

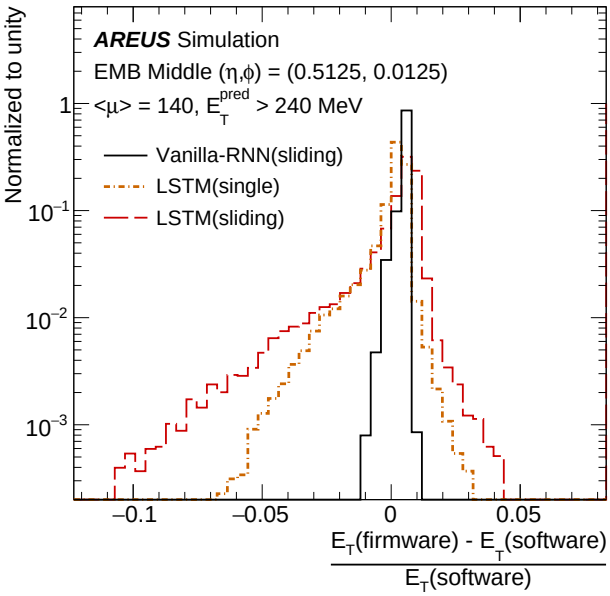

Figure 3.25: Relative deviation of the firmware implementations from the software results for the different transverse energy reconstruction RNNs. Only bunch crossings with predicted transverse energies larger than 240 MeV are considered. Inputs to the RNNs are sampled pulses obtained from the simulation of an EMB middle LAr cell ($\eta = 0.5125$ and $\phi = 0.0125$) with AREUS assuming $\langle\mu\rangle = 140$.

frequency for all implementations is in the range of 500–600 MHz. In this way up to fifteen-fold multiplexing of the input data, which is received at the LHC BC frequency of 40 MHz, is possible. In the baseline scenario imposed by the ATLAS trigger system, about 125 ns can be allocated to the energy reconstruction with the optimal filtering algorithm. Further optimisations are needed for the RNNs to meet this requirement. The sliding-window algorithms have an initiation interval of one by construction. The single-cell LSTM, however, has to wait for the output of the previous calculation leading to an initiation interval equal to the latency. In the present case, the single-cell LSTM can only process continuous streams of data at 2.5 MHz or less. This design is therefore more adapted to measurements which use events already selected by the ATLAS trigger system.

One FPGA should process 384 channels and therefore 384 instances of the RNNs should be implemented in the FPGA if no time-domain multiplexing is used. This is not possible for any of the RNNs within the Stratix® 10 FPGA resource limits. However the Vanilla RNN resource usage is small enough to consider an optimised implementation with multiplexing that can reach the target number of channels. This optimised implementation is described in what follows. The LSTM resource usage is too large to fit within the FPGA resources even with multiplexing.

3.3.2.2 Improved HLS implementation with multiple channels

All mathematical operations inside the Vanilla RNN are inspected and their firmware implementation is optimised to achieve the best possible latency and resource usage.

Table 3.3: Performance of the HLS implementation of RNNs compiled with Quartus® 20.4 for a Stratix® 10 FPGA (reference 1SG280HU1F50E2VG) and a single data input channel.

	Vanilla RNN	LSTM (single)	LSTM (sliding)
Frequency F_{max} [MHz]	641	560	517
Latency clk_{core} cycles	206	220	363
Initiation interval clk_{core} cycles	1	220	1
Resource Usage			
DSPs	34 0.6%	176 3.1%	738 12.8%
ALMs	13115 1.4%	18079 1.9%	69892 7.5%

Detailed inspection of Vanilla RNN operations The network implementation is composed of five consecutive RNN cells followed by a dense layer as shown in figure 3.26. Each cell process the input from one sample corresponding to one bunch crossing. Each of the cells is composed of 5 blocks of computation as shown in figure 3.27: two addition blocks, one multiplication of a scalar with a vector, one multiplication of a vector with a matrix, and one activation function. The weights of the network obtained from the training are stored in memory and are given as input to the RNN cells along with the electronic pulse samples. The same weights are used for each of the five network cells. The ReLU, described in equation 3.1, is used as the activation function for its simple implementation in FPGAs.

$$f(x) = \begin{cases} 0 & \text{if } x \leq 0 \\ x & \text{otherwise} \end{cases} \tag{3.1}$$

Implementation of multiplications Inside the Vanilla RNN cell there is one vector multiplication and one matrix multiplication which reduces to several vector multiplications which in turn reduce to several scalar multiplications and scalar additions. There is a dedicated component inside the FPGA to perform scalar multiplications called the Digital Signal Processing (DSP). The DSP can be used in three possible modes. The first mode performs one 32×32 bits multiplication in the floating-point representation. The second mode performs one 27×27 bits multiplication in the fixed-point representation. The third mode can perform two independent 19×18 bits multiplications in the fixed-point representation. As explained in the following paragraph, the number of multiplications of the FPGA limits the number of calorimeter cells that can be handled by one FPGA. The third mode is thus chosen since it allows doubling the available dedicated multiplication resources on the FPGA.

Multiplexing The number of multiplications inside the neural network depends on the size of the state vector (n) and the number of network cells (c) following equation 3.2 :

$$n^2 \times (c-1) + n \times (c+1) \tag{3.2}$$

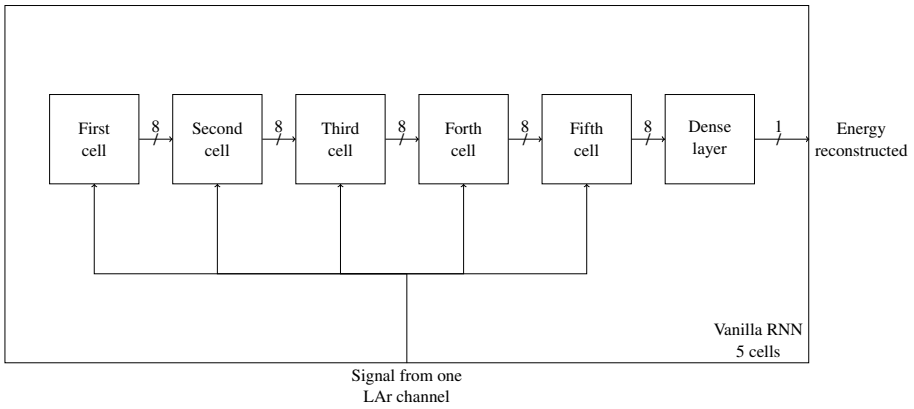

Figure 3.26: Schematics of a Vanilla RNN with 5 cells and 8 internal dimensions (size of the state vector) followed by a dense layer. Each cell calculates a new state using the input data and the state of the previous cell. As the first cell does not have a previous cell, the calculation is only based on the input data. The dense layer computes the transverse energy using the state of the last cell.

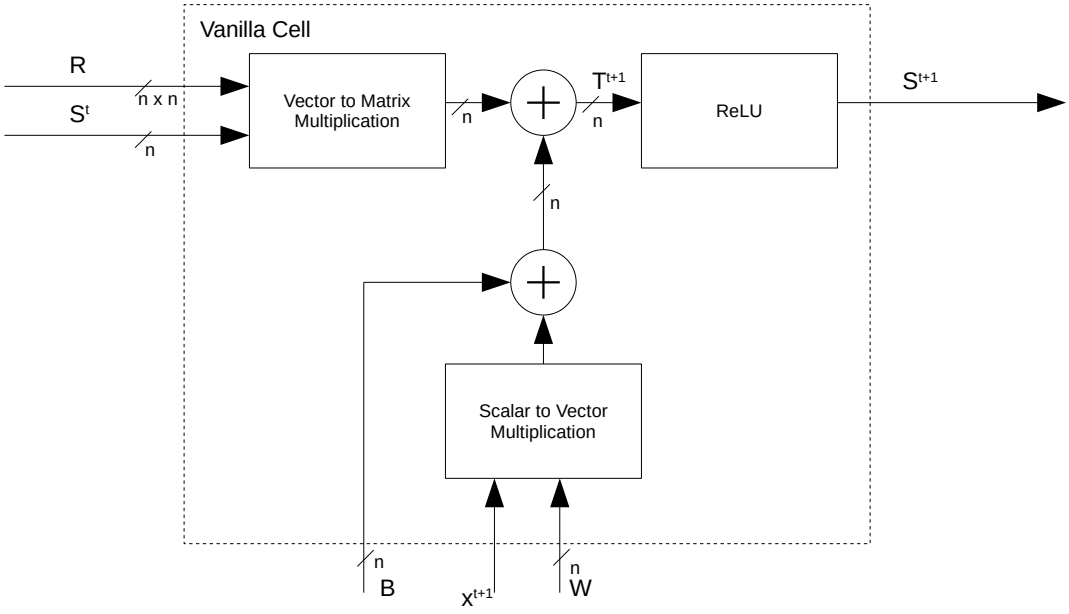

Figure 3.27: Schematics of the operations performed inside each of the RNN cells. The recurrent weight multiplication multiplies the state vector from the previous cell (S^t) with the recurrent kernel weight matrix (R). Simultaneously, the LAr cell input (X^{t+1}) is multiplied by the kernel weight vector (W) and added to the bias weight (B). The results from the two above operations are added to create the internal vector T^{t+1}. The ReLU activation function is applied on the elements of T^{t+1} to create the state vector S^{t+1}. The state vector size (n) is equal to 8.

where $n = 8$ and $c = 5$. Therefore, 304 multiplications are needed for the vanilla RNN used in this study. This leads to 116,736 multiplications that are needed to handle the 384 channels processed in one FPGA. The Stratix® 10 FPGA possesses only 11,520 multiplication blocks. Therefore, each

neural network instance in the FPGA must be utilised for several channels. The easiest way to do so is to increase the DSP block computation frequency as a multiple of the input frequency (40MHz). Several channels are then multiplexed using the same block. This multiplexing is limited by the maximum frequency of the computation block. In what follows we will target the maximum achievable frequency to increase the multiplexing for a given implementation of the neural network.

Implementation of arithmetic operations Intel® HLS implements two binary representations of numbers: a fixed point representation and a floating point representation. The implementation of floating point representation is relatively complex and uses more arithmetic and logic blocks for the addition operations. Furthermore, the DSP blocks of the Stratix® 10 FPGA allows only one floating point multiplication instead of two simultaneous fixed point multiplications as explained above. The fixed point representation is chosen in order to minimise the resource usage in the FPGA.

The fixed point representation implemented in Intel® HLS follows the Algorithmic C (AC) Data-types defined by Mentor® Graphics. Four parameters define this representation: the total number of bits, the number of bits of the integer part, the quantisation type, and the treatment of the overflow. Three different data categories are defined for the vanilla RNN implementation: the input and output data, the neural network weights, and the intermediate data which are the results of the internal computation inside the neural network blocks. 19 bits are used for the width of the internal and input/output categories, while 16 bits are used for the weights. This ensures an efficient use of the DSP resources inside the FPGA while providing a very good compatibility between the firmware computation and the one performed in the Keras software with floating points arithmetic operations. The firmware resolution, which is defined as the relative difference between the firmware and the Keras computed energies, is less than 0.1 % with this choice of number of bits.

The overflow defines how the bits to the left of the most significant bit (MSB) are lost due to saturation. The number of bits and the position of the radix point are chosen to be able to represent the maximum value that could occur in the network. Thus, no saturation detection is needed and a simple drop of bits implementation is used.

The quantisation defines how the bits to the right of the least significant bit (LSB) are lost. The loss of bits can occur during the conversion of the floating points representing the inputs and weights. The inputs to the neural network are given by the AREUS simulation while the weights are provided by Keras. These two use 32-bit signed floating point representations that need to be converted to a fixed point representation in order to be used in the firmware. The loss of bits can also occur inside the neural network internal computations. The 37-bit output of the DSP is reduced to the number of bits internally used. Two types of quantisation are implemented in the Intel® HLS compilation: truncation and rounding. Each of these types possess different subtypes which are explained in [244].

Figure 3.28 shows a comparison of the resource usage, in terms of DSPs, arithmetic lookup tables (ALUT), Flip Flops (FF), and random access memory (RAM), and the latency of the firmware for different implementations of the quantisation. The same quantisation is applied for all categories of data of the network. Two modes are interesting, the default truncation (TRN) and the default rounding (RND) which use lower resources and lower latency compared to other quantisation modes. Figure 3.29 shows a comparison of the transverse energy computed in firmware and the one computed in software, with a full floating point implementation, for the different quantisation modes. All quantisation modes show similar resolution with the exception of the TRN quantisation modes which have large tails. The RND mode gives a good compromise among resource usage, latency, and resolution.

To further optimise the firmware implementation, a mix of quantisation procedures are used

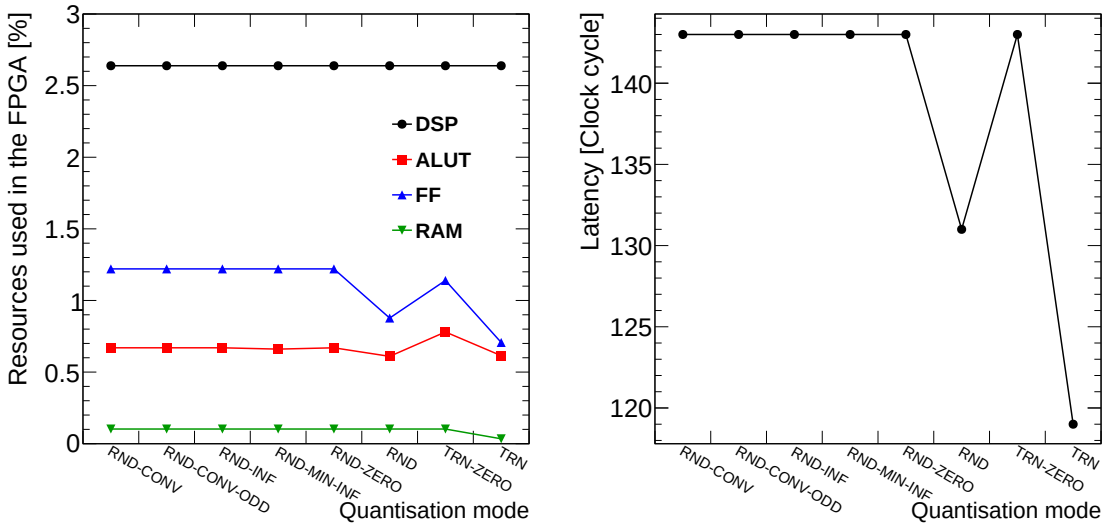

Figure 3.28: Comparison of the resource usage (left) and the latency (right) of the vanilla RNN firmware with different implementation of the quantisation in Intel® HLS. For each mode, the same quantisation is applied for all categories of the data of the network. The different quantisation modes are described in [244].

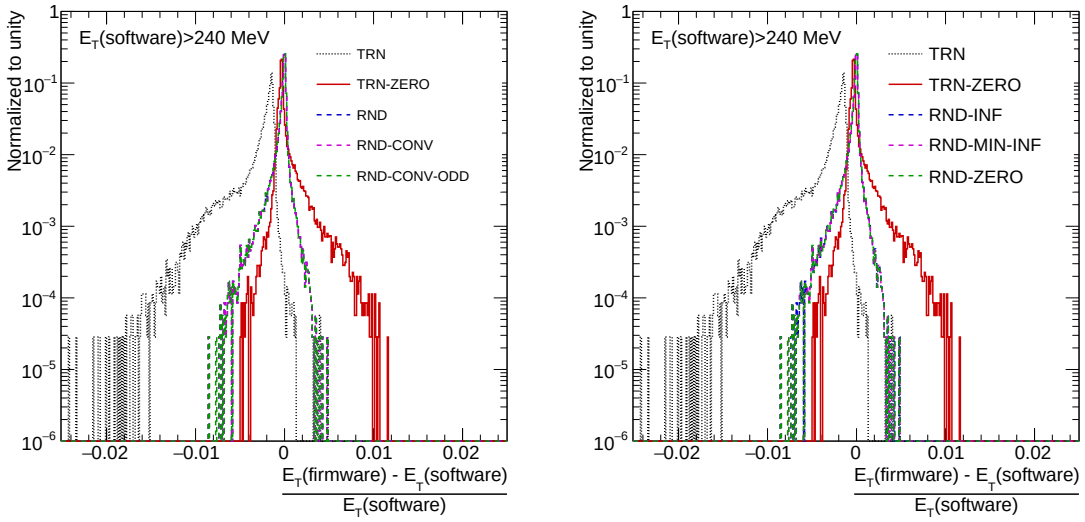

Figure 3.29: Resolution of the transverse energy (E_T) computed in firmware with respect to the one computed in software. The E_T(firmware) is computed with different implementations of the quantisation in Intel® HLS. In each mode, the same quantisation is applied for all categories of the data of the network. The different quantisation modes are described in [244]. The different RND modes give very similar results and their corresponding curves overlap. A lower cut of 240 MeV is applied on E_T(software) to remove low energies below the 3σ noise level.

for different data categories. Figure 3.30 shows the resource usage and the latency while applying the TRN and RND quantisations on different data categories. The rounding of the weights does not require any additional resources in the FPGA since it can be done in software before loading

these weights into the FPGA. The input data will be digitised and quantised in the frontend boards and does not require additional resources for rounding in the FPGA. The Rounding of the simulated input data is thus also done offline before loading it into the FPGA. Rounding the output data induces a slight increase in the latency. Rounding the internal data categories increases the needed resources and the latency significantly. Figure 3.31 shows a comparison of the transverse energy computed in firmware and the one computed in software depending on which of the data categories is rounded. One can see that it is important to round the weights and input/output categories, while rounding the internal data category does not have any significant impact on the resolution. The root mean square (RMS) of the TRN distribution is 0.2%. It decreases to 0.07% if all categories are rounded (RND_IWD). The RMS becomes slightly worse (0.09%) if only the weights and the input/output are rounded (RND_WD). Therefore, the TRN mode is used for the internal data computation while the RND is used for the other data categories. These optimisations allow significant improvement of the resolution of the firmware at a low resource and latency cost.

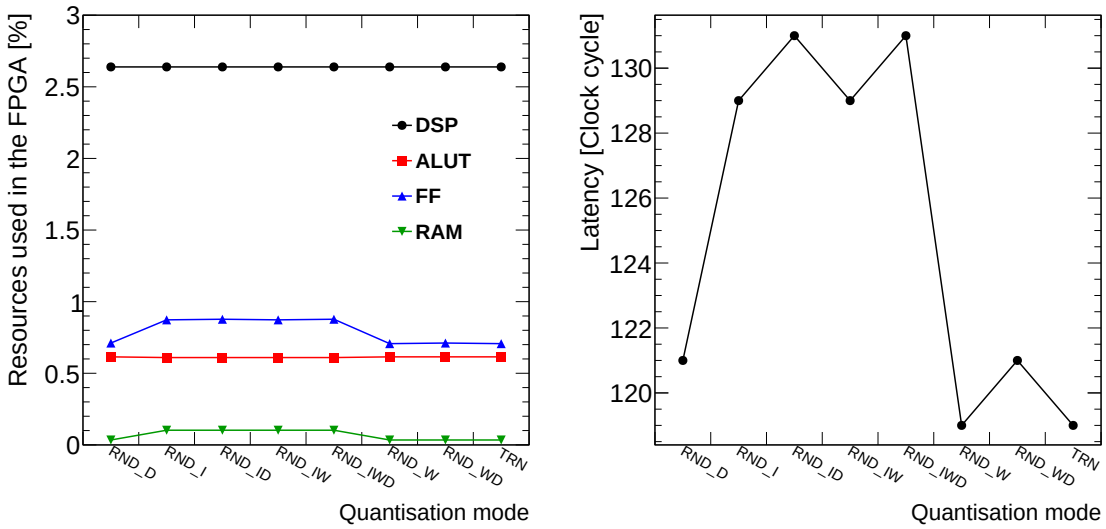

Figure 3.30: Comparison of the resource usage (left) and the latency (right) of the vanilla RNN firmware with different implementation of the quantisation for the three data categories of the network computation. For each test, the letters I, W, and D indicate that the RND is applied for the internal data category, the weights, and the input/output data, respectively, while the TRN mode is applied by default in all other categories.

Implementation of the neural network The computation inside the neural network requires 304 multiplications and 303 additions. The multiplications are implemented inside the DSPs, and the additions are initially implemented using ALUTs and FFs. The DSP allows summing the output of the two multiplications internally. The usage of such functionality reduces the number of additions implemented in the ALUTs and FFs from 303 to 131. Furthermore, the DSP component contains an additional adder that can take an external input. It is possible to chain two DSPs to sum their outputs by using the output of the first DSP in the additional adder of the second DSP. By doing this, it is necessary to synchronise the DSPs so that their results arrive at the same time to the additional adder of the second DSP. Therefore, the second DSP in the chain should be shifted by 1 clock cycle. The same procedure is applied to more DSPs to build a full chain. In such case, all additions can be implemented in DSPs.

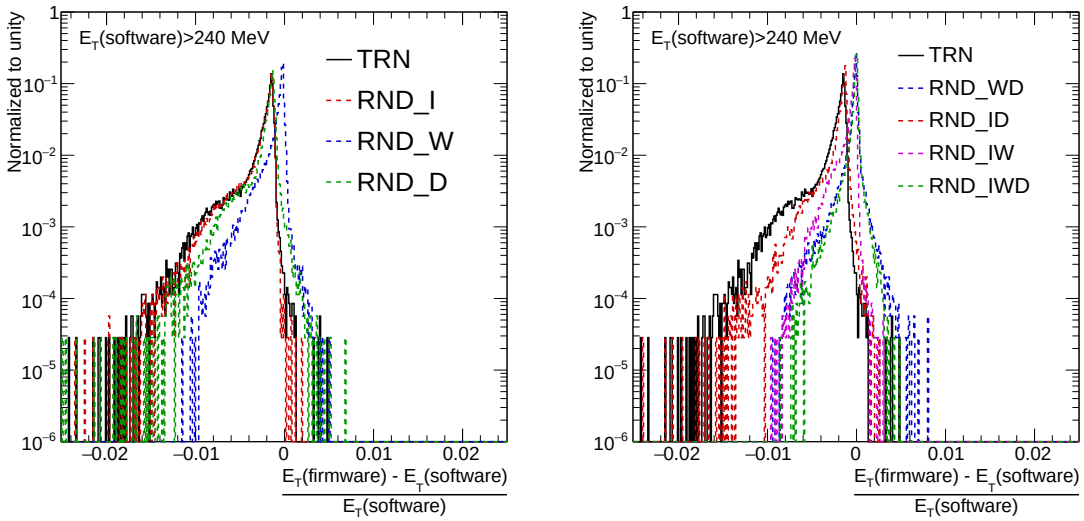

Figure 3.31: Resolution of the transverse energy (E_T) computed in firmware with respect to the one computed in software. The E_T(firmware) is computed with different implementations of the quantisation for the three data categories of the network. For each test, the letters I, W, and D indicate that the RND is applied for the internal data category, the weights, and the input/output data, respectively, while the TRN mode is applied by default in all other categories. A lower cut of 240 MeV is applied on E_T(software) to remove low energies below the 3σ noise level.

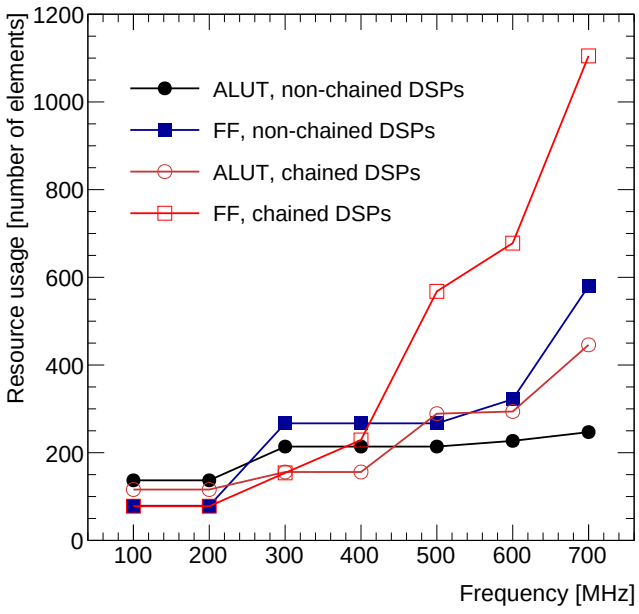

Figure 3.32: Resource usage for ALUTs and FFs depending on the frequency for two implementations of a matrix multiplication with and without chained DSPs. The maximum frequency of an MLAB is 450 MHz. Above this frequency, there is a significant increase of the logic resource usage for the chained DSP implementation.

To perform the timing shift, each input of the DSPs needs an additional level of registers to delay the results. This is done by combining several ALUTs to create a memory logic array block (MLAB) to implement a first in first out (FIFO) memory. However, the MLAB frequency is limited to 450 MHz in read-during-write mode needed for FIFO implementation. At higher frequencies the synchronisation cannot be implemented in MLAB, in such case the delays are implemented in basic ALUTs and FFs which increase the number of needed logic elements significantly. At high frequency, more ALUTs and FFs are needed to synchronise the DSPs in chained mode than to implement the additions in a non-chained mode. Figure 3.32 shows the FPGA resource usage as function of the frequency for DSPs used in chained or non-chained mode for one matrix multiplication. The chained mode is advantageous below 450 MHz. Above this frequency, it is more advantageous to use logic elements to do the additions than to chain DSPs. This will be the option retained for the implemented RNN since we seek higher frequencies to increase the multiplexing and thus reduce the overall resource usage.

Results of the HLS Implementation The designed RNN HLS code is compiled in Intel® HLS and Quartus®. The results of these two compilations are given in table 3.4. For one implemented network the design can run at 455 MHz which a priory allows multiplexing up to 11 channels per network for a data input rate of 40 MHz. However, with a multiplexing of 10 the maximum frequency reached is 393 MHz while the needed frequency is 400 MHz for the firmware to run without timing violations. The maximum frequency is reduced when applying multiplexing due to the additional weights that are needed by the network to perform the computation for several channels. Up to 37 networks can fit in the FPGA which leads to the usage of 100% of the available DSP resources and most of the logic resources. The logic resources are given in terms of ALUTs and FFs in the HLS report and adaptive logic modules (ALM) for the Quartus® report. The ALMs are the actual physical resources in the FPGA and each ALM can be configured to be used as two ALUTs or 4 FFs. The HLS design does not allow reaching the required 384 channels processed in one FPGA, even with full utilisation of resources in the FPGA. In practice only part of these resources will be available for the transverse energy computation as discussed in section 3.3.2.3. Additional optimisations are needed to fulfil the requirements of the LAr calorimeter. Furthermore, the latency of this HLS firmware is 277.5 ns which is significantly larger than the required 125 ns. The HLS design was optimised for the maximum possible frequency which leads to additional registers added by the compiler to meet the required timing constraints. This in turn increases the latency of the design.

Table 3.4: Resource usage and the maximum frequency (Fmax) given by the Intel® HLS and Quartus® compiler reports for one and 37 implemented networks in the FPGA. The multiplexing is set to 10 so that each network instance can process 10 independent channels.

	Networks	Multiplexing	Channels	ALUTs	FFs	ALMs	DSPs	Memory	Fmax
HLS	1	10	10	0,6%	0.7%	-	3%	0,3%	-
	37	10	370	22.9%	25.9%	-	100%	11%	-
Quartus®	1	10	10	-	-	2,4%	3%	0,3%	455 MHz
	37	10	370	-	-	90%	100%	11%	393 MHz

3.3.2.3 VHDL Implementation

The HLS implementation adds an additional level of abstraction that allows fast and efficient optimisation of the network parameters and firmware implementation. However, this additional level of

abstraction prevents some finer optimisations that are possible in VHDL. These finer optimisations allow to meet the specifications, which is not possible for the HLS implementation. That is why VHDL is used for the final optimisation and placement of the RNN firmware implementation.

Reuse of common computations between RNN cells As shown in figure 3.27, the Kernel Weight Multiplication and the Bias Addition depend only on the input of the neural network and do not depend on the past network state. However, these two computations done in the second cell at a given time t are identical to the computations in the first cell at time $t-1$. More generally, these computations in cell n at time t are identical to the computations in the first cell at time $t-n-1$. One can do these two computations one time at the first cell and propagate the output to the other four cells at the proper time. Moreover, the first cell does not need the Recurrent Weight Matrix Multiplication since there is no previous RNN state at this level. Therefore, this computation is removed from the first cell. These two optimisations allow a reduction in the number of used DSPs by 10%. The ALM usage is also reduced by 21% due to the removal of the duplicated Bias Additions.

Placement constraints Several instances of the neural network are needed to process all 384 channels. In a given compilation each instance have a different placement shape. Moreover, these shapes change between compilations due to the randomisation in Quartus®. This complicates the optimisation of the timing critical paths that is needed to reach higher frequencies and thus higher multiplexing.

Placement constraints are used to force the same placement shape of the implemented neural network. Thus, all instances of the neural network have the same shape which simplifies the optimisation of the critical paths. Moreover, the placement of the 5 network cells is optimised to minimise the distance between connected cells. The shape of the neural network is shown in figure 3.33. The first cell is placed in the middle since it is connected to all other four cells as described in the previous paragraph. The other cells are placed around the first cell and ordered to reduce the distance between consecutive cells. The dense layer is placed next to the fifth cell.

All cells use the same set of recurrent weights except for the first cell that does not have a recurrent block. These weights are stored in memory (M20K blocks) and are directly connected to the DSPs to make the matrix multiplications. To reduce the mean distance between the M20k block and each DSP the recurrent weights are duplicated. Each set of weights is used for two cells instead of four.

These placement constraints allow increasing the maximum frequency from 434 MHz to 492 MHz if 28 instances of the RNN implemented in the FPGA.

Incremental compilation Quartus® compilation is composed of three parts: Analysis and Synthesis, Fitting, and Timing Analysis. The Analysis and Synthesis will translate the VHDL code into RTL. The RTL code creates a high-level representation of a circuit. The Fitter will place and route the design into the FPGA. It will determine the required resources and the wiring between the different components. The Timing Analysis will determine the maximum frequency that the FPGA can reach with a given design.

Quartus® can divide a firmware design into multiple partitions. It also provides the possibility to preserve the results of a given compilation at different steps of the process for each partition. To further increase the maximum frequency the firmware design is partitioned in a way that each partition corresponds to one neural network instance. A sequence of compilations are performed and each partition that reaches the target frequency is preserved while the others are recompiled.

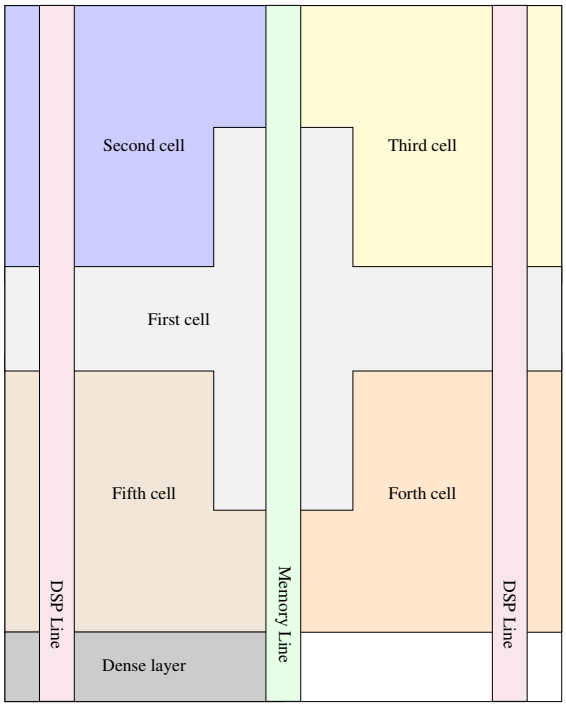

Figure 3.33: Schematic view of the optimised placement of the Vanilla RNN showing the 5 cells and the dense layer with respect to the memory and DSP lines inside the FPGA.

Several combinations of target frequencies and numbers of neural networks instances are tested. We converged on a configuration with a target frequency of 560 MHz and 28 instances of the RNN. This allows to run the RNN with a multiplexing of 14 and reach the required number of channels to be processed in one FPGA. Four compilations are needed to reach the target frequency in this configuration, while 18 out of the 28 instances reach the target frequency at the first compilation.

Results of the VHDL implementation The final firmware implemented in VHDL contains 28 instances of the vanilla RNN each with a multiplexing of 14 which allows covering 392 channels. The results from this firmware are summarised in table 3.5. This firmware can run at 561 MHz while the required frequency for a multiplexing of 14 is 560 MHz. The final requirements on the resource usage are not available since the full final phase-II firmware is not yet available. However, we require a resource usage of the neural network block similar to the transverse energy computation block used for the Phase-I upgrade [37] of the LAr calorimeter which is currently in operation. This block uses about 70% of the DSPs and 30% of the logic. The optimised RNN resource usage is within these requirements as shown in table 3.5. The latency of the firmware is 65 clock cycles corresponding to 116 ns which is within the 125 ns required latency. The optimisations done in VHDL do not affect the results of the energy computation; therefore, the firmware resolution stays below 0.1 % as it was for the HLS implementation.

Table 3.5: Resource usage and the maximum frequency (Fmax) given by the Quartus® compiler report for 28 implemented networks in the FPGA. The multiplexing is set to 14 so that each network can process 14 independent channels.

Type	Networks	Multiplexing	Channels	ALM	DSP	Memory	Fmax
Specification	-	-	384	30%	70%	30%	560 MHz
Quartus®	28	14	392	18%	66%	16%	561 MHz

3.4 conclusion

The ATLAS liquid argon calorimeter provides electromagnetic calorimetry over the full η range and hadronic calorimetry for $|\eta| > 1.5$. It also provides trigger capabilities to the ATLAS detector. The Phase-I upgrade of the LAr calorimeter was achieved in 2022. The newly installed digital trigger provides an increased granularity up to a factor of 10 with respect to the legacy trigger. All digital trigger components are installed and operational. The commissioning of this new system and its integration with the ATLAS trigger system is being finalised with the first data of the run 3 of the LHC. Preparation for the Phase-II upgrade that will take place in 2026-2028 is ongoing. The new backend boards of the Phase-II system will use state-of-the-art FPGAs which allows the unique opportunity to implement neural networks in order to improve the computation of the transverse energy deposited in the calorimeter. RNNs targeting an FPGA implementation have been successfully trained to reconstruct LAr calorimeter cell energies. All tested RNNs outperform the legacy optimal filter algorithm. The Vanilla RNN is successfully implemented in firmware and meets the tight requirements in terms of FPGA resource constraints and latency.

Appendix

A Research activity after my PhD

After I obtained my PhD in 2009, my research activities are centred around three subjects:

- Measurements of the production cross sections of several Standard Model processes;
- Search for the Higgs boson in channels where it couples to third generation quarks;
- Upgrade of the ATLAS liquid argon calorimeter (LAr) readout electronics.

In what follows I will summarise my contribution to physics analyses within the ATLAS experiment (section A.1) and to the upgrade of the ATLAS LAr calorimeter (section A.2).

A.1 Physics analyses

Since I obtained my PhD, I have participated to two searches for the Higgs boson in the $t\bar{t}H(H \to b\bar{b})$ and the $VH(H \to b\bar{b})$ channels, and to four measurements of inelastic proton-proton collisions through charged particles multiplicity, Wbb cross section, Wc cross section, and the cross section of $t\bar{t} + b\bar{b}$.

A.1.1 Search for the Higgs boson produced with a top quark pair and decaying to a pair of b-quarks

The discovery of the Higgs boson by the ATLAS and CMS collaborations in 2012 is one of the most important achievement of LHC experiments. Establishing the coupling between the Higgs boson and the third generation quarks is of great importance to demonstrate the Standard Model (SM) nature of the newly discovered boson. The top Yukawa coupling is the largest in the SM and the decay of the Higgs boson to a pair of b-quarks is largely dominant in the SM.

The production of a Higgs boson in association with a pair of top quarks ($t\bar{t}H$) provides the only possibility at the LHC to measure the top Yukawa coupling in a direct way. The subsequent decay of the Higgs boson to a pair of b-quarks in the $t\bar{t}H$ channel ($t\bar{t}H(H \to b\bar{b})$) provides also an access to the bottom Yukawa coupling. The $t\bar{t}H(H \to b\bar{b})$ channel is very challenging due to the presence of the $t\bar{t} + b\bar{b}$ irreducible background with large uncertainties. In addition, the presence of 4 b-quarks in the final state makes the reconstruction of this channel challenging due to a large combinatorial background in the signal itself. I led the first $t\bar{t}H(H \to b\bar{b})$ analysis performed by ATLAS with a fraction of LHC run 2 data at $\sqrt{s} = 13$ TeV. The $t\bar{t}H(H \to b\bar{b})$ group was formed of about 100 members from several institutes with different contributions to the analysis. I fully developed the analysis software framework for the group. I also developed the multivariate analyses techniques (based on Boosted Decision Trees (BDTs)) that were retained for the final analysis; they outperformed other techniques developed by other groups. The BDTs where used for signal/background

classification but also for solving the signal combinatorics and reconstructing the top quarks and the Higgs boson. This was the first time a multivariate technique is used for the reconstruction of $t\bar{t}H$ at ATLAS and CMS. I also worked on the analysis selection mainly the identification of b-jets (b-tagging) which is very important for $t\bar{t}H(H \to b\bar{b})$ due to the presence of four b-jets in the final state.

The $t\bar{t}H(H \to b\bar{b})$ analysis is very sensitive to systematic uncertainties on the background processes due to its very low signal to background event ratio. I led the effort to understand the major systematics coming from the top-pair production modelling. In this context I worked on comparing state-of-the-art Monte Carlo (MC) generators for the production of a pair of top quarks with additional jets (especially additional b-jets). This work was done with wide interaction with theorists and contributed to new developments on the generators side.

The $t\bar{t}H(H \to b\bar{b})$ search requires a complex fit containing the signal, the background, and the respective uncertainties included as nuisance parameters. The fit is composed of O(100) data points and O(200) nuisance parameters. Understanding such a fit is one of the biggest challenges of this analysis. I supervised the student that was in charge of this fit and took over this responsibility after he finished his thesis. I also worked on the combination of the $t\bar{t}H(H \to b\bar{b})$ channel with various other $t\bar{t}H$ and $H \to b\bar{b}$ channels. This led to ATLAS publishing the evidence of $t\bar{t}H$ production and later the discovery of $t\bar{t}H$ and $H \to b\bar{b}$. These two discoveries are one of the most important accomplishments of ATLAS during the LHC run 2.

The $t\bar{t}H(H \to b\bar{b})$ analysis was an important challenge that mobilised large effort from ATLAS. The first analysis lasted 2 years with a large group. I had a leading role in all aspects of this analysis. I put a lot of effort to lead this analysis to completion despite important difficulties. At the end of this analysis I was appointed as one of the two editors of the corresponding paper which was published in 2018 [139]. The results of this work is presented in chapter 2.

With the increased luminosity collected in run 2, the $t\bar{t}H(H \to b\bar{b})$ channel sensitivity is not anymore competitive with other "cleaner" $t\bar{t}H$ channels such as the channel where the Higgs boson decays to two photons. However this analysis is still important in order to measure some properties of the Higgs boson produced with top quarks. Due to the large $H \to b\bar{b}$ branching ratio, this analysis provides enough data to probe the high-p_{T} spectrum of the Higgs boson. This phase space region is particularly interesting to constrain BSM models with modified top-Higgs coupling. That is why I continued my involvement in the $t\bar{t}H(H \to b\bar{b})$ analysis with the full run 2 data collected by ATLAS.

After the first publication, my involvement decreased gradually due to increased involvement in the upgrade of the LAr calorimeter. However I continued working on this analysis mainly to implement the improvements that I didn't have the chance to add in the first publication. The main improvement was related to a modification of the method to estimate the $t\bar{t}+b\bar{b}$ background and its uncertainties. I supervised the work of a student that performed a detailed study of various available MC generators. We also developed a new method to correct the $t\bar{t}+b\bar{b}$ background estimation with a data driven method and constrain its large MC uncertainties. This work was very valuable for the ATLAS $t\bar{t}H(H \to b\bar{b})$ analysis with the full run 2 data that was published in [245]. This paper measures the $t\bar{t}H(H \to b\bar{b})$ cross section in several bins of the transverse momentum of the Higgs boson in the so called simplified template cross section (STXS) formalism [150].

A.1.2 Search for the Higgs boson produced with W/Z boson and decaying to pair of b-quarks

During the run 1 of the LHC, I worked on the search for the Higgs boson in the $VH(H \to b\bar{b})$ channel where V stands for a W or a Z boson. This channel is the most sensitivity to $H \to b\bar{b}$. At the time the ATLAS search for $VH(H \to b\bar{b})$ was using a cut-based analysis without employing any multivariate techniques. I introduced the usage of BDTs to separate the signal and background in

this analysis and I was appointed the responsible of the group in charge of developing multivariate techniques for the search for $VH(H \to b\bar{b})$. I also worked on the estimation of the main background which is the production of vector bosons with b-jets. The analysis relying on BDTs outperformed the cut-based analysis and was used for the final run 1 publication [224]. I supervised the work of a master and then PhD student on this subject.

A.1.3 Measurement of the cross section of a top quark pair produced with a b-jet pair

The $t\bar{t}+b\bar{b}$ process is very poorly modelled in current MC generators due to the presence of two different natural scales ($t\bar{t}$ and $b\bar{b}$) for the QCD calculation. This process is an important background to many searches in particular the search for $t\bar{t}H(H \to b\bar{b})$ discussed above. In addition this process allows a better understanding of the effect of the scale choice in QCD computations especially the ones involving multiple jets in the final state. In parallel to the work on $t\bar{t}H(H \to b\bar{b})$, I contributed to the analysis focusing on the differential cross section measurements of many observables of the $t\bar{t}+b\bar{b}$ process. I participated to the definition of the variables to measure and the unfolding procedure. I supervised the work of a student on these two subjects. This analysis was published in 2019 [246].

The work on $t\bar{t}H(H \to b\bar{b})$ and $t\bar{t}+b\bar{b}$ was supported by an ANR[2] grant (Hbb+ttH@LHC) that involved 4 institutes. I participated to this grant as a member.

A.1.4 Measurement of the cross section of W bosons produced with a single c-jet

The measurement of the cross section of a W boson produced with a single c-jet is interesting in proton-proton collisions. This production is mainly initiated by an s-quark. As such, it allows to constrain the Parton Density Function (PDF) of this quark. ATLAS results [51] using the cross sections of W and Z boson production to constrain the proton PDFs show a density of $s(\bar{s})$ quarks similar to the $d(\bar{d})$ quarks produced in the proton sea. No effect due to the larger mass of the s quark is observed. The measured density is twice as large as that commonly used in different PDFs. Measuring the cross section of Wc production presents a direct way to constrain the s-quark PDF.

The analysis with ATLAS data collected in 2011 allowed the measurement of the Wc cross section with an accuracy better than 10%. This analysis is based on the identification of c-jets by the presence of a muon in the jet. The muon from the c-quark carries an opposite electric charge to the lepton from the W boson. Most of the backgrounds show no such charge correlation. These backgrounds are greatly reduced after subtracting events with two leptons of the same charge from those with an opposite charge. I have performed the complete analysis in the channel where the W boson decays to an electron and part of the analysis in the muon channel. This includes selection, extraction of the main background noise (W+jets and multijet) from the data, and correction of the detector effects (unfolding). I have developed new methods to be able to constrain the W+jets and multijet backgrounds using data-driven techniques. In addition, I have performed several studies involving special MC simulations to be able to understand theoretical uncertainties due to the c-quark fragmentation and semi-leptonic decay of c-hadrons. Finally I performed the comparison of the measured cross section with theoretical estimates with different PDF sets which led to constraining the s-quark PDF. I supervised the work of a master student on this subject.

The cross section of a W boson production with a single c-jet is measured as a function of the pseudorapidity of the lepton from the decay of the W boson to have better sensitivity to different PDFs. It is also measured for the W^+ and W^- bosons separately to constrain the asymmetry between

[2] Agence Nationale de la Recherche.

the s-quark and the $\bar{s}$-quark in the proton. This work is shown in chapter 1 and was published in [52]. I was one of the two editors of the corresponding paper.

A.1.5 Measurement of the cross section of W bosons produced with b-jet pair

The measurement of the cross section of W boson production in association with a pair of heavy jets (b,c) is important at the LHC. These processes represent the main background for several analyses including the search for the Higgs boson in the $VH(H \to b\bar{b})$ channel. At the beginning of the run 1 of the LHC, I participated in the measurement of the cross section of the W boson production in association with b-jets using data collected in 2010 at $\sqrt{s} = 7$ TeV. My contribution was mainly focused around b-jets: difference between several methods to define a jet as initiated by a b-quark (labelling) and the effect of b-jets from multiple parton interactions (MPI) in the proton. This analysis was published in [247].

A.1.6 Charged-particle multiplicities measurements

Analysis of minimum bias data is crucial at the LHC due to the large pileup that is increasing with the luminosity of the LHC. Describing inelastic interactions is of great importance especially for analyses using missing energy and jets. I participated in the minimum bias analysis including the first 7 TeV data collected by ATLAS. I worked on different aspects of this analysis in particular on the reconstruction efficiency and properties of tracks, the reconstruction efficiency of the primary vertex, unfolding of the different differential cross sections, and the determination of various systematic uncertainties. It should be noted that this analysis pushes the ATLAS detector towards the limits of its performance by measuring tracks in a very wide p_T range starting at 100 MeV and going up to 50 GeV. During this analysis I developed several new techniques to control the efficiency and systematic uncertainties related to very small and very large p_T tracks. This analysis was published in [248].

A.1.7 b-tagging

The identification of jets from the fragmentation of b-quarks is essential for the search for the Higgs boson in the $H \to b\bar{b}$ channels as well as for the Wbb and Wc analyses to which I participated. I have accumulated an important experience after working for several years in the b-tagging ATLAS group. I have performed several performance studies for several b-tagging algorithms. I have also developed a new algorithm whose goal is to identify jets containing two b-hadrons. It is based on the reconstruction of two vertices in a single jet. I was responsible of the b-tagging software in 2010 and 2011 and continued to maintain this software until 2014.

The Wc analysis that I performed allows to have access to a c-jets sample with high purity (85%). I used this fact to develop a new method to measure the b-tagging efficiency of c-jets in Wc events. I supervised the work of one PhD student on this subject. My work on b-tagging was published as part of a global ATLAS b-tagging paper that can be found in [165].

A.2 LAr calorimeter upgrade

The ATLAS detector will undergo two upgrade phases to prepare to the increased LHC luminosity and to expand its physics reach. The first phase (Phase-I) started in 2019 and was finalised in 2022. It consists of upgrading the trigger readout pass of the LAr calorimeter and exchanging the muon detector small wheel. The second phase (Phase-II) will take place in the years 2026-2028 to cope with an increase by a factor 5 to 7 of the instantaneous luminosity expected at the HL-LHC. During

Phase-II ATLAS will undergo a major upgrade with a complete exchange of the inner detector and the readout electronics of all detectors.

A.2.1 The Phase-I upgrade of the LAr calorimeter

The Phase-I upgrade of the ATLAS LAr calorimeter consists of exchanging the trigger readout electronics to increase the granularity by a factor up to 10. This increase allows to improve the background rejection at the first trigger level and maintain (even outperform) the performance of the legacy ATLAS trigger system despite the increased pileup expected in run 3. A new frontend board (LTDB) dedicated to the trigger system is installed on the detector. For that the full legacy frontend boards are extracted, refurbished to allow the installation of the LTDB, and reinstalled. A new backend board is also installed to collect the data from the LTDBs. This board is based on an ATCA mother board with 4 mezzanine boards (LATOME), each containing an ALTERA (now INTEL) ARRIA 10 FPGA. These FPGAs compute the energy deposited in the calorimeter and send it to the new level 1 trigger system. They also buffer the computed energy and send it to the data acquisition (DAQ) system upon reception of a level 1 accept (L1A) trigger signal. The data is sent to the DAQ system through the FELIX system which consists of PCIe boards that receive the data from the LATOME boards and transfer it to computer memory using the PCIe protocol.

My involvement in the Phase-I upgrade of the LAr calorimeter gradually increased since 2016. From 2016 to 2018 I mainly worked on various developments needed for the new backend electronics. The connections between the LTDBs and the LATOMEs consists of 6000 optical fibers. A similar number of fibers goes out from the LATOMEs to the trigger system. To optimise the number of fibers and thus the number of required boards a complex mapping was designed where several LTDBs are connected to several LATOMEs. The same optimisation is required for the connections between the LATOME and the trigger system. The LAr collaboration also decided to develop one unique firmware for all 116 LATOME FPGAs. This firmware is required to be configurable to account for various types of mapping and exceptions in the detector. I was in charge of designing this optimal mapping in collaboration with the trigger group. Due to the complexity of this mapping, I developed a tool that generates the best mapping configuration and insures its consistency. This tool also produces the configurations for the firmware of the 116 LATOMEs. During the commissioning period I developed tools to validate this mapping for the new installed hardware. By the end of the installation period all 34048 channels of the new system were validated. I was also responsible of determining the firmware interface with the trigger and DAQ system. I worked on designing the communication protocols, the data content and its encoding, and the corresponding validation tests on the installed hardware. Between 2016 and 2022, I coordinated the LATOME firmware group with an engineer from LAPP. I worked on determining the firmware specifications, the needed functionalities, and the needed in-situ tests. I managed a group of 10 engineers from 7 institutes that participate to this firmware.

In October 2018, I moved to CERN as a project associate and became the convener of the operation and commissioning group of the LAr calorimeter (50 persons). I had the important responsibility of leading the commissioning of the new trigger readout system. I took active parts in all aspects of this commissioning including hardware and firmware validation, online and offline software development, data acquisition and processing, and the coordination of the work of the full group. I supervised a PhD student that was in charge of developing the detector control and monitoring system of the LTDB boards. In addition, I took the important responsibility of maintaining, updating and installing the LAr online software. I also developed the DAQ software package of the Phase-I system. This software allows to collect LATOME data through the FELIX system. Finally, I developed the code that allows to read and decode this data in the ATLAS offline software (Athena)

and several analyses packages to analyse this data. These tools were used to validate the hardware and the firmware. They were also used to produce the calibration constants needed to compute the energies in the LATOME boards and to time-align the system.

During 4 years at CERN, I organised 14 integration weeks to boost the commissioning of the Phase-I system. About 30 persons (engineers, physicists, postdocs, and students) participated in these weeks and worked on different areas including hardware validation, firmware, detector control system (DCS), online and offline software, monitoring and data analysis. This was a huge amount of work since I had to understand (and in many occasions actually do the work) all areas of the system. These weeks took place even during the COVID pandemic. This was hard to organise with people in different time zones. However these weeks were mandatory to successfully commission the system. The LAr group published a paper dedicated to the installation and the commissioning of the Phase-I system [227]. I was the editor of the system integration section and contributed to many of the results presented in this paper.

At the end of 2021, the LHC performed a pilot run with collisions at 900 GeV (officially called frictions). We managed to collect data for the full detector including the Phase-I system. All installed boards operated correctly. Although the LHC produced collision data during only few days, we were able to quickly time-align the system to adjust the readout window for the vast majority of the channels in the detector. The collected data was of good quality to study the deposited energy in the calorimeter. I had the leading role in this work that consisted of preparing the system for data acquisition, aligning the system, and analysing the data to produce the final results. This work continued in 2022 with the first LHC collisions at $\sqrt{s} = 13.6$ TeV. We managed to quickly commission the new trigger path with the first data and carry on the integration with the new trigger system. The commissioning with the trigger system continued until the end of 2022. Beginning of 2023, the trigger group started phasing out part of the items of the legacy trigger system which were outperformed by the new trigger system.

Finally, during my presence at CERN I had two management positions in the LAr collaboration: from 2018 to 2022 I was part of the LAr executive board and acted as scientific secretary, and between 2020 and 2022 I was a member (chair in 2022) of the LAr speakers committee responsible of handling LAr contributions to conferences.

A.2.2 The Phase-II upgrade of the LAr calorimeter

The Phase-II upgrade of the LAr calorimeter consists of exchanging the full readout chain to cope with the increased pileup and the higher trigger rate which is planned during the HL-LHC era. All legacy frontend and backend boards have to be exchanged. I am mainly involved in the upgrade of the backend system. The new backend boards have to handle the calorimeter data with full granularity at the collision rate of 40 MHz while the legacy system received data only at the level 1 trigger rate of 100 KHz. It has also to send this data to the Phase-II trigger system at 40 MHz and to the DAQ system at 1 MHz. This puts stringent requirements of the bandwidth (320 Tb/s) and the latency (few micro seconds) of the system. The new backend board (LASP) uses the ATCA technology (to allow a compact system) and is based on stat-of-the-art FPGAs from INTEL (AGILEX). The CPPM ATLAS group is designing these boards and will be responsible of their production. The first demonstrator board was produced in 2021. Preliminary tests done at the end of 2021 show that all needed functionalities are working correctly on this board. With the CPPM team, I contributed to the discussions and studies that were needed for the choice of the board design and its main functionalities. This effort led the LAr collaboration to entrust the design of the LASP board to the CPPM group. I manage the group of engineers working on this activity as the scientific responsible of the LAr upgrade group at CPPM.

The increased pileup at the HL-LHC significantly reduces the performance of the optimal filtering algorithm that is currently used to compute the energy deposited in the LAr calorimeter. Machine learning techniques can significantly improve the energy resolution and the identification of the time of the deposited energy. The substantial processing power of the FPGAs of the LASP boards is a unique opportunity to implement machine learning techniques to improve the performance of the LAr calorimeter at the HL-LHC. For this I initiated a project (AIDAQ[3]) aiming to implement neural networks to compute the energies on the LASP FPGAs. I obtained 3 grants (ANR and AMIDEX[4]) to support this project that started in 2019. I lead a group of one postdoc, 3 students and one engineer working on this project in collaboration with a group from the University of Dresden. The CPPM group concentrated on recursive neural network (RNN) architectures which are adapted for the treatment of time ordered series. We managed to develop RNNs that are able to outperform the optimal filtering algorithm while being small enough to fit on FPGAs. We also ported these networks to firmware. The firmware was highly optimised to fit the FPGA occupancy and latency requirements of the LASP board. The work on this subject led to two publications [228, 229].

B Supervision work

B.1 Supervised postdocs

I have supervised 3 postdocs since I joined CPPM/CNRS as a junior researcher:

Grigore Tarna (2021-2023): Electron/photon identification efficiency measurements with LHC run 3 data.

- Funded by CNRS in 2021.
- Grigore started his postdoc in December 2021. He is mainly focusing on electron/photon identification efficiency measurements and he is appointed as the convener of the ATLAS group in charge of these measurements. He also contributes to the Phase-II upgrade of the LAr calorimeter in particular the reconstruction of the energy deposited in the calorimeter using neural networks.
- This postdoc is for 2 years and will end in 2023.

Nairit Sur (2021-2024): Development of artificial intelligence algorithms embedded in FPGAs to compute the energy deposited in the ATLAS LAr calorimeter.

- Funded by an ANR grant that I obtained in 2020.
- Nairit took over the work of Thomas (see below) related to the AIDAQ project which aims to use embedded neural networks on FPGAs to improve the energy resolution and trigger capabilities of the LAr calorimeter at the HL-LHC. He works mainly on neural network development and simulations with HL-LHC conditions.
- This postdoc is for 3 years and will end in 2024.

[3] Artificial Intelligence on FPGAs: a breakthrough for Data AcQuisition in high energy physics experiments and beyond.

[4] Excellence Initiative of Aix-Marseille University.

Thomas Calvet (2020-2021): Development of artificial intelligence algorithms embedded in FPGAs to compute the energy deposited in the ATLAS LAr calorimeter.

- Funded by an AMIDEX grant that I obtained in 2019.
- As part of the AIDAQ project, Thomas developed neural networks capable of improving the energy resolution of the LAr calorimeter in HL-LHC conditions. He also worked on adapting these neural networks for embedded firmware implementation.
- Thomas finished his postdoc in 2021 and is now working as a data scientist in industry.

B.2 Supervised PhD students

Since I obtained my PhD in 2009, I have officially co-supervised 5 PhD students (in addition to 3 PhD students that I supervised without official mandate):

Nemer Chiedde (2020-2023): Implementation of embedded artificial intelligence algorithms on the backend readout boards of the ATLAS LAr calorimeter.

- Co-supervised with Emmanuel Monnier.
- Nemer is an electronics engineer that decided to continue with a PhD. He is developing firmware adapted for embedded neural networks that can run on FPGAs. This thesis is part of the AIDAQ project.
- Nemer finished his thesis in October 2023.

Lauri Laatu (2020-2023): Development of artificial intelligence algorithms adapted to big data processing in embedded trigger and data acquisition systems at the LHC.

- Co-supervised with Emmanuel Monnier.
- Lauri is a software engineer that decided to continue with a PhD. He is developing neural networks capable to improve the energy computation in the LAr calorimeter in the high pileup conditions at the HL-LHC. Lauri is funded by a joint AMIDEX/ANR grant that I obtained for the AIDAQ project.
- Lauri finished his thesis in September 2023.

Fortin Etienne (2018-2022): Commissioning and performance of the trigger and readout system of the liquid argon calorimeter of the ATLAS experiment.

- Co-supervised with Emmanuel Monnier.
- Etienne is an electronics engineer that decided to continue with a PhD. He developed the full monitoring, control and configuration software of the new frontend boards (LTDB) of the Phase-I upgrade of the LAr calorimeter. He also designed a firmware containing neural networks that are capable of reconstructing the energy deposited in the LAr calorimeter. This firmware can run on the state-of-the-art FPGAs from INTEL.
- Etienne finished his thesis in 2022 and is now a fellow at CERN.

Nihal Brahimi (2016-2019): Search for the Higgs boson in the $t\bar{t}H(H \to b\bar{b})$ channel and measurement of the production cross-section of $t\bar{t} + b\bar{b}$ with the ATLAS detector at the LHC.

- Co-supervised with Laurent Vacavant.
- Nihal focused mainly on the search for the Higgs boson in the $t\bar{t}H(H \to b\bar{b})$ channel more particularly on the $t\bar{t} + b\bar{b}$ background modelling. She also worked on b-tagging performance studies to help defining the design of the new inner tracker (ITK) that will be installed during the Phase-II upgrade of the ATLAS detector.
- Nihal continued as a postdoc in ATLAS after her thesis.

Thomas Calvet (2014-2017): Search for the associated production of a Higgs boson with a pair of top quarks and decaying to a b-quark pair and b-jet identification with the ATLAS experiment at LHC.

- Co-supervised with Arnaud Duperrin.
- This thesis focused on the search for the Higgs boson in the $t\bar{t}H(H \to b\bar{b})$ channel. The CPPM group and Thomas in particular had the main contribution to this analysis that led to the first ATLAS $t\bar{t}H(H \to b\bar{b})$ publication with the LHC run 2 data, and to the combination of channels that resulted in the evidence and later the discovery of $t\bar{t}H$. Thomas also worked on b-tagging and Monte Carlo generator studies for the $t\bar{t} + b\bar{b}$ process.
- Thomas did 2 postdocs in ATLAS after his thesis and he is now working as a data scientist in industry.

Bibliography

[1] Paul A. M. Dirac, *The Quantum theory of electron*, Proc. Roy. Soc. Lond. **A117** (1928) 610 (cit. on p. 3).

[2] E. Fermi, *Trends to a Theory of beta Radiation*, Nuovo Cim. **11** (1934) 1 (cit. on p. 3).

[3] D. J. Gross and Frank Wilczek, *Ultraviolet behavior of non-abelian gauge theories*, Phys. Rev. Lett. **30** (1973) 1343 (cit. on p. 3).

[4] D. J. Gross and Frank Wilczek, *Asymptotically Free Gauge Theories. 1*, Phys. Rev. **D8** (1973) 3633 (cit. on p. 3).

[5] H. David Politzer, *Reliable perturbative results for strong interactions?*, Phys. Rev. Lett. **30** (1973) 1346 (cit. on p. 3).

[6] Murray Gell-Mann, *A Schematic Model of Baryons and Mesons*, Phys. Lett. **8** (1964) 214 (cit. on p. 3).

[7] G. Zweig, *An SU(3) model for strong interaction symmetry and its breaking*, (1964), CERN-TH-412 (cit. on p. 3).

[8] M. Y. Han and Yoichiro Nambu, *Three-triplet model with double SU(3) symmetry*, Phys. Rev. **139** (1965) B1006 (cit. on p. 3).

[9] F. Englert and R. Brout, *Broken Symmetry and the Mass of Gauge Vector Mesons*, Phys. Rev. Lett. **13** (1964) 321 (cit. on p. 3).

[10] Peter W. Higgs, *Broken symmetries, massless particles and gauge fields*, Phys. Lett. **12** (1964) 132 (cit. on p. 3).

[11] Peter W. Higgs, *Broken Symmetries and the Masses of Gauge Bosons*, Phys. Rev. Lett. **13** (1964) 508 (cit. on p. 3).

[12] S. L. Glashow, *Partial Symmetries of Weak Interactions*, Nucl. Phys. **22** (1961) 579 (cit. on pp. 3, 39).

[13] Steven Weinberg, *A Model of Leptons*, Phys. Rev. Lett. **19** (1967) 1264 (cit. on pp. 3, 39).

[14] Abdus Salam, *Weak and Electromagnetic Interactions*, Conf. Proc. **C680519** (1968) 367 (cit. on pp. 3, 39).

[15] Nicola Cabibbo, *Unitary Symmetry and Leptonic Decays*, Phys. Rev. Lett. **10** (1963) 531 (cit. on p. 3).

[16] Makoto Kobayashi and Toshihide Maskawa, *CP Violation in the Renormalizable Theory of Weak Interaction*, Prog. Theor. Phys. **49** (1973) 652 (cit. on p. 3).

[17] Gerard 't Hooft and M. J. G. Veltman, *Regularization and Renormalization of Gauge Fields*, Nucl. Phys. **B44** (1972) 189 (cit. on p. 3).

[18] F. J. Hasert et al., *Search for Elastic ν_μ Electron Scattering*, Phys. Lett. B **46** (1973) 121 (cit. on p. 3).

[19] F. J. Hasert et al., *Observation of Neutrino Like Interactions without Muon or Electron in the Gargamelle Neutrino Experiment*, Nucl. Phys. B **73** (1974) 1 (cit. on p. 3).

[20] G. Arnison et al., *Experimental Observation of Isolated Large Transverse Energy Electrons with Associated Missing Energy at $\sqrt{s} = 540$ GeV*, Phys. Lett. B **122** (1983) 103 (cit. on p. 3).

[21] M. Banner et al., *Observation of Single Isolated Electrons of High Transverse Momentum in Events with Missing Transverse Energy at the CERN anti-p p Collider*, Phys. Lett. B **122** (1983) 476 (cit. on p. 3).

[22] G. Arnison et al., *Experimental Observation of Lepton Pairs of Invariant Mass Around 95-GeV/c**2 at the CERN SPS Collider*, Phys. Lett. B **126** (1983) 398 (cit. on p. 3).

[23] P. Bagnaia et al., *Evidence for $Z^0 \to e^+e^-$ at the CERN $\bar{p}p$ Collider*, Phys. Lett. B **129** (1983) 130 (cit. on p. 3).

[24] Elliott D. Bloom et al., *High-Energy Inelastic e p Scattering at 6-Degrees and 10-Degrees*, Phys. Rev. Lett. **23** (1969) 930 (cit. on p. 3).

[25] G. Miller et al., *Inelastic Electron-Proton Scattering at Large Momentum Transfers and the Inelastic Structure Functions of the Proton*, Phys. Rev. D **5** (3 1972) 528 (cit. on p. 3).

[26] F. Abe et al., *Observation of top quark production in $\bar{p}p$ collisions*, Phys. Rev. Lett. **74** (1995) 2626, arXiv: hep-ex/9503002 (cit. on p. 3).

[27] S. Abachi et al., *Observation of the top quark*, Phys. Rev. Lett. **74** (1995) 2632, arXiv: hep-ex/9503003 (cit. on p. 3).

[28] ATLAS Collaboration, *Observation of a new particle in the search for the Standard Model Higgs boson with the ATLAS detector at the LHC*, Phys. Lett. B **716** (2012) 1, arXiv: 1207.7214 [hep-ex] (cit. on pp. 3, 7, 39).

[29] CMS Collaboration, *Observation of a new boson at a mass of 125 GeV with the CMS experiment at the LHC*, Phys. Lett. B **716** (2012) 30, arXiv: 1207.7235 [hep-ex] (cit. on pp. 3, 7, 39).

[30] ATLAS Collaboration, *The ATLAS Experiment at the CERN Large Hadron Collider*, JINST **3** (2008) S08003 (cit. on pp. 4, 24, 84).

[31] Lyndon Evans and Philip Bryant, *LHC Machine*, JINST **3** (2008) S08001 (cit. on p. 4).

[32] ATLAS Collaboration, *Performance of the ATLAS trigger system in 2015*, Eur. Phys. J. C **77** (2017) 317, arXiv: 1611.09661 [hep-ex] (cit. on p. 4).

[33] ATLAS Collaboration, *The ATLAS Collaboration Software and Firmware*, ATL-SOFT-PUB-2021-001, 2021, URL: https://cds.cern.ch/record/2767187 (cit. on p. 4).

[34] LHC collaboration, *High Luminosity LHC Project*, 2022, URL: https://hilumilhc.web.cern.ch/content/hl-lhc-project (cit. on pp. 4, 5).

[35] ATLAS Collaboration, *ATLAS Insertable B-Layer: Technical Design Report*, ATLAS-TDR-19; CERN-LHCC-2010-013, 2010, URL: https://cds.cern.ch/record/1291633 (cit. on p. 5), Addendum: ATLAS-TDR-19-ADD-1; CERN-LHCC-2012-009, 2012, URL: https://cds.cern.ch/record/1451888.

[36] B. Abbott et al., *Production and integration of the ATLAS Insertable B-Layer*, JINST **13** (2018) T05008, arXiv: 1803.00844 [physics.ins-det] (cit. on p. 5).

[37] ATLAS Collaboration, *ATLAS Liquid Argon Calorimeter Phase-I Upgrade: Technical Design Report*, ATLAS-TDR-022; CERN-LHCC-2013-017, 2013, URL: https://cds.cern.ch/record/1602230 (cit. on pp. 5, 89, 117).

[38] ATLAS Collaboration, *ATLAS TDAQ System Phase-I Upgrade: Technical Design Report*, ATLAS-TDR-023; CERN-LHCC-2013-018, 2013, URL: https://cds.cern.ch/record/1602235 (cit. on p. 5).

[39] ATLAS Collaboration, *ATLAS New Small Wheel: Technical Design Report*, ATLAS-TDR-020; CERN-LHCC-2013-006, 2013, URL: https://cds.cern.ch/record/1552862 (cit. on p. 5).

[40] CMS Collaboration, *CMS Physics Technical Design Report, Volume II: Physics Performance*, J. Phys. G **34** (2007) 995 (cit. on p. 5).

[41] ATLAS Collaboration, *ATLAS Inner Tracker Pixel Detector: Technical Design Report*, ATLAS-TDR-030; CERN-LHCC-2017-021, 2017, URL: https://cds.cern.ch/record/2285585 (cit. on p. 5).

[42] ATLAS Collaboration, *ATLAS Muon Spectrometer Phase-II Upgrade: Technical Design Report*, ATLAS-TDR-026; CERN-LHCC-2017-017, 2017, URL: https://cds.cern.ch/record/2285580 (cit. on p. 5).

[43] ATLAS Collaboration, *ATLAS TDAQ Phase-II Upgrade: Technical Design Report*, ATLAS-TDR-029; CERN-LHCC-2017-020, 2017, URL: https://cds.cern.ch/record/2285584 (cit. on pp. 5, 101).

[44] ATLAS Collaboration, *ATLAS LAr Calorimeter Phase-II Upgrade: Technical Design Report*, ATLAS-TDR-027; CERN-LHCC-2017-018, 2017, URL: https://cds.cern.ch/record/2285582 (cit. on pp. 5, 101).

[45] ATLAS Collaboration, *ATLAS Tile Calorimeter Phase-II Upgrade: Technical Design Report*, ATLAS-TDR-028; CERN-LHCC-2017-019, 2017, URL: https://cds.cern.ch/record/2285583 (cit. on p. 5).

[46] ATLAS Collaboration, *A High-Granularity Timing Detector for the ATLAS Phase-II Upgrade: Technical Design Report*, ATLAS-TDR-031; CERN-LHCC-2020-007, 2020, URL: https://cds.cern.ch/record/2719855 (cit. on p. 5).

[47] ATLAS Collaboration, *Observation of WWW Production in pp Collisions at* $\sqrt{s} = 13\,TeV$ *with the ATLAS Detector*, Phys. Rev. Lett. **129** (2022) 061803, arXiv: 2201.13045 [hep-ex] (cit. on p. 6).

[48] ATLAS Collaboration, *Standard Model Summary Plots February 2022*, ATL-PHYS-PUB-2022-009, 2022, URL: https://cds.cern.ch/record/2804061 (cit. on pp. 6, 7).

[49] ATLAS Collaboration, *Measurement of the W-boson mass in pp collisions at $\sqrt{s} = 7$ TeV with the ATLAS detector*, Eur. Phys. J. C **78** (2018) 110, arXiv: 1701.07240 [hep-ex] (cit. on p. 6), Erratum: Eur. Phys. J. C **78** (2018) 898.

[50] ATLAS Collaboration, *Improved W boson Mass Measurement using $\sqrt{s} = 7$ TeV Proton-Proton Collisions with the ATLAS Detector*, ATLAS-CONF-2023-004, 2023, URL: https://cds.cern.ch/record/2853290/ (cit. on p. 6).

[51] ATLAS Collaboration, *Determination of the Strange-Quark Density of the Proton from ATLAS Measurements of the $W \to \ell\nu$ and $Z \to \ell\ell$ Cross Sections*, Phys. Rev. Lett. **109** (2012) 012001, arXiv: 1203.4051 [hep-ex] (cit. on pp. 6, 13, 26, 36, 121).

[52] ATLAS Collaboration, *Measurement of the production of a W boson in association with a charm quark in pp collisions at $\sqrt{s} = 7$ TeV with the ATLAS detector*, JHEP **05** (2014) 068, arXiv: 1402.6263 [hep-ex] (cit. on pp. 6, 12, 13, 122).

[53] ATLAS Collaboration, *Precision measurement and interpretation of inclusive W^+, W^- and Z/γ^* production cross sections with the ATLAS detector*, Eur. Phys. J. C **77** (2017) 367, arXiv: 1612.03016 [hep-ex] (cit. on pp. 6, 38).

[54] ATLAS Collaboration, *Determination of the parton distribution functions of the proton from ATLAS measurements of differential W and Z/γ^* boson and $t\bar{t}$ cross sections*, ATL-PHYS-PUB-2018-017, 2018, URL: https://cds.cern.ch/record/2633819 (cit. on p. 6).

[55] ATLAS and CMS Collaborations, *Measurements of the Higgs boson production and decay rates and constraints on its couplings from a combined ATLAS and CMS analysis of the LHC pp collision data at $\sqrt{s} = 7$ and 8 TeV*, JHEP **08** (2016) 045, arXiv: 1606.02266 [hep-ex] (cit. on pp. 7–9, 39, 40).

[56] S Heinemeyer et al., *Handbook of LHC Higgs Cross Sections: 3. Higgs Properties*, arXiv: 1307.1347 [hep-ph] (cit. on p. 7).

[57] ATLAS Collaboration, *A detailed map of Higgs boson interactions by the ATLAS experiment ten years after the discovery*, Nature **607** (2022) 52, arXiv: 2207.00092 [hep-ex] (cit. on pp. 8, 10, 11).

[58] W. J. Stirling and E. Vryonidou, *Charm production in association with an electroweak gauge boson at the LHC*, Phys. Rev. Lett. **109** (2012) 082002, arXiv: 1203.6781 [hep-ph] (cit. on pp. 12, 30, 32).

[59] P. B. Arnold and M. H. Reno, *The Complete Computation of High p(t) W and Z Production in 2nd Order QCD*, Nucl. Phys. **B 319** (1989) 37 (cit. on p. 12).

[60] D. Mason et al., *Measurement of the Nucleon Strange-Antistrange Asymmetry at Next-to-Leading Order in QCD from NuTeV Dimuon Data*, Phys. Rev. Lett. **99** (2007) 192001 (cit. on p. 12).

[61] M. Goncharov et al., *Precise measurement of dimuon production cross-sections in muon neutrino Fe and muon anti-neutrino Fe deep inelastic scattering at the Tevatron*, Phys. Rev. **D 64** (2001) 112006, arXiv: hep-ex/0102049 [hep-ex] (cit. on pp. 12, 13, 32).

[62] A. D. Martin, W. J. Stirling, R. S. Thorne, and G. Watt, *Parton distributions for the LHC*, Eur. Phys. J. C **63** (2009) 189, arXiv: 0901.0002 [hep-ph] (cit. on pp. 12, 13, 30, 64).

[63] S. Alekhin, J. Blumlein, S. Klein, and S. Moch, *The 3, 4, and 5-flavor NNLO Parton from Deep-Inelastic-Scattering Data and at Hadron Colliders*, Phys. Rev. **D 81** (2010) 014032, arXiv: 0908.2766 [hep-ph] (cit. on p. 12).

[64] R. D. Ball et al., *A Determination of parton distributions with faithful uncertainty estimation*, Nucl. Phys. **B 809** (2009) 1, arXiv: 0808.1231 [hep-ph] (cit. on p. 12).

[65] H.-L. Lai et al., *New parton distributions for collider physics*, Phys. Rev. D **82** (2010) 074024, arXiv: 1007.2241 [hep-ph] (cit. on pp. 12, 14).

[66] Richard D. Ball et al., *Precision determination of electroweak parameters and the strange content of the proton from neutrino deep-inelastic scattering*, Nucl. Phys. **B 823** (2009) 195, arXiv: 0906.1958 [hep-ph] (cit. on p. 13).

[67] U. Baur, F. Halzen, S. Keller, M. L. Mangano, and K. Riesselmann, *The Charm content of $W+1$ jet events as a probe of the strange quark distribution function*, Phys. Lett. **B 318** (1993) 544, arXiv: hep-ph/9308370 [hep-ph] (cit. on p. 13).

[68] W. T. Giele, S. Keller, and E. Laenen, *QCD corrections to W boson plus heavy quark production at the Tevatron*, Phys. Lett. **B 372** (1996) 141, arXiv: hep-ph/9511449 [hep-ph] (cit. on p. 13).

[69] T. Aaltonen et al., *First measurement of the production of a W boson in association with a single charm quark in $p\bar{p}$ collisions at $\sqrt{s} = 1.96$ TeV*, Phys. Rev. Lett. **100** (2008) 091803, arXiv: 0711.2901 [hep-ex] (cit. on p. 13).

[70] T. Aaltonen et al., *Observation of the Production of a W Boson in Association with a Single Charm Quark*, Phys. Rev. Lett. **110** (2013) 071801, arXiv: 1209.1921 [hep-ex] (cit. on p. 13).

[71] V. M. Abazov et al., *Measurement of the ratio of the $p\bar{p} \to W^+c^-$ jet cross section to the inclusive $p\bar{p} \to W+$ jets cross section*, Phys. Lett. **B 666** (2008) 23, arXiv: 0803.2259 [hep-ex] (cit. on p. 13).

[72] CMS Collaboration, *Measurement of associated W + charm production in pp collisions at $\sqrt{s} = 7$ TeV*, JHEP **02** (2014) 013, arXiv: 1310.1138 [hep-ex] (cit. on p. 13).

[73] CMS Collaboration, *Measurement of the muon charge asymmetry in inclusive $pp \to W + X$ production at $\sqrt{s} = 7$ TeV and an improved determination of light parton distribution functions*, Phys. Rev. D **90** (2014) 032004, arXiv: 1312.6283 [hep-ex] (cit. on p. 13).

[74] ATLAS Collaboration, *Improved luminosity determination in pp collisions at $\sqrt{s} = 7$ TeV using the ATLAS detector at the LHC*, Eur. Phys. J. C **73** (2013) 2518, arXiv: 1302.4393 [hep-ex] (cit. on pp. 14, 24).

[75] M. L. Mangano et al.,
ALPGEN, a generator for hard multiparton processes in hadronic collisions,
JHEP **07** (2003) 001, arXiv: hep-ph/0206293 (cit. on p. 14).

[76] G. Corcella et al., *HERWIG 6.5 release note*, (2002), arXiv: hep-ph/0210213 [hep-ph]
(cit. on p. 14).

[77] J.M. Butterworth, Jeffrey R. Forshaw, and M.H. Seymour,
Multiparton interactions in photoproduction at HERA, Z. Phys. C **72** (1996) 637,
arXiv: hep-ph/9601371 (cit. on p. 14).

[78] M. L. Mangano, M. Moretti, and R. Pittau, *Multijet matrix elements and shower evolution in hadronic collisions: $Wb\bar{b}$ + n jets as a case study*, Nucl. Phys. **B 632** (2002) 343,
arXiv: hep-ph/0108069 [hep-ph] (cit. on p. 14).

[79] Torbjorn Sjöstrand, Stephen Mrenna, and Peter Z. Skands,
PYTHIA 6.4 physics and manual, JHEP **05** (2006) 026, arXiv: hep-ph/0603175
(cit. on pp. 14, 46).

[80] E. Lohrmann, *A Summary of Charm Hadron Production Fractions*, (2011),
arXiv: 1112.3757 [hep-ex] (cit. on pp. 14, 25, 29).

[81] M. Bähr et al., *Herwig++ physics and manual*, Eur. Phys. J. C **58** (2008) 639,
arXiv: 0803.0883 [hep-ph] (cit. on pp. 14, 29, 46).

[82] J. Beringer et al., *Review of Particle Physics (RPP)*, Phys. Rev. **D 86** (2012) 010001
(cit. on pp. 14, 25).

[83] D. J. Lange, *The EvtGen particle decay simulation package*,
Nucl. Instrum. Meth. A **462** (2001) 152 (cit. on pp. 14, 43).

[84] Paolo Nason,
A new method for combining NLO QCD with shower Monte Carlo algorithms,
JHEP **11** (2004) 040, arXiv: hep-ph/0409146 (cit. on pp. 14, 44).

[85] Stefano Frixione, Paolo Nason, and Carlo Oleari,
Matching NLO QCD computations with parton shower simulations: the POWHEG method,
JHEP **11** (2007) 070, arXiv: 0709.2092 [hep-ph] (cit. on pp. 14, 44).

[86] Simone Alioli, Paolo Nason, Carlo Oleari, and Emanuele Re, *A general framework for implementing NLO calculations in shower Monte Carlo programs: the POWHEG BOX*,
JHEP **06** (2010) 043, arXiv: 1002.2581 [hep-ph] (cit. on pp. 14, 44).

[87] Simone Alioli, Paolo Nason, Carlo Oleari, and Emanuele Re,
NLO vector-boson production matched with shower in POWHEG, JHEP **07** (2008) 060,
arXiv: 0805.4802 [hep-ph] (cit. on p. 14).

[88] Stefano Frixione and Bryan R. Webber,
Matching NLO QCD computations and parton shower simulations, JHEP **06** (2002) 029,
arXiv: hep-ph/0204244 (cit. on pp. 14, 29).

[89] J. Pumplin et al.,
New Generation of Parton Distributions with Uncertainties from Global QCD Analysis,
JHEP **07** (2002) 012, arXiv: hep-ph/0201195 (cit. on p. 14).

[90] B. P. Kersevan and E. Richter-Was, *The Monte Carlo event generator AcerMC version 2.0 with interfaces to PYTHIA 6.2 and HERWIG 6.5*, (2004),
arXiv: hep-ph/0405247 [hep-ph] (cit. on p. 14).

[91] S. Jadach, Z. Was, R. Decker, and Johann H. Kuhn,
The tau decay library TAUOLA: Version 2.4, Comput. Phys. Commun. **76** (1993) 361
(cit. on p. 14).

[92] Piotr Golonka and Zbigniew Was,
PHOTOS Monte Carlo: a precision tool for QED corrections in Z and W decays,
Eur. Phys. J. C **45** (2006) 97, arXiv: hep-ph/0506026 (cit. on p. 14).

[93] Charalampos Anastasiou, Lance Dixon, Kirill Melnikov, and Frank Petriello,
High-precision QCD at hadron colliders: Electroweak gauge boson rapidity distributions at next-to-next-to leading order, Phys. Rev. D **69** (2004) 094008, arXiv: hep-ph/0312266
(cit. on p. 14).

[94] Matteo Cacciari, Michal Czakon, Michelangelo Mangano, Alexander Mitov, and Paolo Nason, *Top-pair production at hadron colliders with next-to-next-to-leading logarithmic soft-gluon resummation*, Phys. Lett. B **710** (2012) 612,
arXiv: 1111.5869 [hep-ph] (cit. on pp. 14, 44).

[95] J. M. Campbell, R. K. Ellis, and C. Williams, *Vector boson pair production at the LHC*,
JHEP **07** (2011) 018, arXiv: 1105.0020 [hep-ph] (cit. on p. 14).

[96] J. M. Campbell, R. K. Ellis, and F. Tramontano,
Single top production and decay at next-to-leading order, Phys. Rev. **D 70** (2004) 094012,
arXiv: hep-ph/0408158 [hep-ph] (cit. on p. 14).

[97] ATLAS Collaboration, *The ATLAS Simulation Infrastructure*,
Eur. Phys. J. C **70** (2010) 823, arXiv: 1005.4568 [physics.ins-det]
(cit. on pp. 14, 43).

[98] GEANT4 Collaboration, S. Agostinelli, et al., GEANT4 – *a simulation toolkit*,
Nucl. Instrum. Meth. A **506** (2003) 250 (cit. on pp. 14, 43).

[99] M. Cacciari and G. P. Salam, *Dispelling the N^3 myth for the k_t jet-finder*,
Phys. Lett. **B 641** (2006) 57, arXiv: hep-ph/0512210 [hep-ph] (cit. on p. 15).

[100] Matteo Cacciari, Gavin P. Salam, and Gregory Soyez, *The anti-k_t jet clustering algorithm*,
JHEP **04** (2008) 063, arXiv: 0802.1189 [hep-ph] (cit. on pp. 15, 41).

[101] Walter Lampl et al., *Calorimeter Clustering Algorithms: Description and Performance*,
ATL-LARG-PUB-2008-002, 2008, URL: https://cds.cern.ch/record/1099735
(cit. on p. 15).

[102] ATLAS Collaboration, *Jet energy measurement with the ATLAS detector in proton–proton collisions at $\sqrt{s} = 7\,TeV$*, Eur. Phys. J. C **73** (2013) 2304, arXiv: 1112.6426 [hep-ex]
(cit. on p. 15).

[103] ATLAS Collaboration,
Identification and Tagging of Double b-hadron jets with the ATLAS Detector,
ATLAS-CONF-2012-100, 2012, URL: https://cds.cern.ch/record/1462603
(cit. on p. 15).

[104] ATLAS Collaboration, *Performance of missing transverse momentum reconstruction in proton–proton collisions at $\sqrt{s} = 7\,TeV$ with ATLAS*, Eur. Phys. J. C **72** (2012) 1844,
arXiv: 1108.5602 [hep-ex] (cit. on p. 15).

[105] ATLAS Collaboration, *Electron performance measurements with the ATLAS detector using the 2010 LHC proton–proton collision data*, Eur. Phys. J. C **72** (2012) 1909,
arXiv: 1110.3174 [hep-ex] (cit. on pp. 15, 24).

[106] ATLAS Collaboration,
Muon Performance in Minimum Bias pp Collision Data at $\sqrt{s} = 7$ TeV with ATLAS,
ATLAS-CONF-2010-036, 2010, URL: https://cds.cern.ch/record/1277675
(cit. on p. 15).

[107] ATLAS Collaboration, *Muon Reconstruction Performance*, ATLAS-CONF-2010-064,
2010, URL: https://cds.cern.ch/record/1281339 (cit. on p. 15).

[108] ATLAS Collaboration, *Muon reconstruction efficiency in reprocessed 2010 LHC
proton–proton collision data recorded with the ATLAS detector*, ATLAS-CONF-2011-063,
2011, URL: https://cds.cern.ch/record/1345743 (cit. on pp. 15, 16).

[109] ATLAS Collaboration,
*Measurement of the top quark pair production cross section with ATLAS in pp collisions at
$\sqrt{s} = 7$ TeV in the single-lepton channel using semileptonic b decays*,
ATLAS-CONF-2012-131, 2012, URL: https://cds.cern.ch/record/1478370
(cit. on pp. 16, 20).

[110] ATLAS Collaboration, *Measurement of the top quark-pair production cross section with
ATLAS in pp collisions at $\sqrt{s} = 7$ TeV*, Eur. Phys. J. C **71** (2011) 1577,
arXiv: 1012.1792 [hep-ex] (cit. on p. 19).

[111] ATLAS Collaboration, *Measurements of top quark pair relative differential cross-sections
with ATLAS in pp collisions at $\sqrt{s} = 7$ TeV*, Eur. Phys. J. C **73** (2013) 2261,
arXiv: 1207.5644 [hep-ex] (cit. on p. 20).

[112] ATLAS Collaboration, *Jet energy scale and its systematic uncertainty in proton–proton
collisions at $\sqrt{s} = 7$ TeV with ATLAS 2011 data*, ATLAS-CONF-2013-004, 2013,
URL: https://cds.cern.ch/record/1509552 (cit. on p. 24).

[113] D Bourilkov, R C Group, and M R Whalley,
LHAPDF: PDF use from the Tevatron to the LHC, (2006),
arXiv: hep-ph/0605240 [hep-ph] (cit. on p. 26).

[114] R. Frederix et al.,
Scalar and pseudoscalar Higgs production in association with a top-antitop pair,
Phys. Lett. **B 701** (2011) 427, arXiv: 1104.5613 [hep-ph] (cit. on p. 26).

[115] F.D. Aaron et al.,
Measurement of the Inclusive ep Scattering Cross Section at Low Q^2 and x at HERA,
Eur. Phys. J. **C 63** (2009) 625, arXiv: 0904.0929 [hep-ex] (cit. on p. 28).

[116] Johan Alwall, Michel Herquet, Fabio Maltoni, Olivier Mattelaer, and Tim Stelzer,
MadGraph 5 : Going Beyond, JHEP **06** (2011) 128, arXiv: 1106.0522 [hep-ph]
(cit. on p. 29).

[117] J. M. Campbell and R. K. Ellis, *MCFM for the Tevatron and the LHC*,
Nucl. Phys. Proc. Suppl. **205-206** (2010) 10, arXiv: 1007.3492 [hep-ph] (cit. on p. 29).

[118] Richard D. Ball et al., *Parton distributions with LHC data*, Nucl. Phys. B **867** (2013) 244,
arXiv: 1207.1303 [hep-ph] (cit. on p. 29).

[119] ATLAS Collaboration, *Measurement of the inclusive $W^{\pm}$ and Z/γ^* cross sections in the e
and μ decay channels in pp collisions at $\sqrt{s} = 7$ TeV with the ATLAS detector*,
Phys. Rev. D **85** (2012) 072004, arXiv: 1109.5141 [hep-ex] (cit. on p. 29).

[120] H1 and ZEUS Collaborations, F. D. Aaron et al., *Combined Measurement and QCD Analysis of the Inclusive $e^{\pm}p$ Scattering Cross Sections at HERA*, JHEP **01** (2010) 109, arXiv: 0911.0884 [hep-ex] (cit. on pp. 29, 35).

[121] S.J. Brodsky, P. Hoyer, C. Peterson, and N. Sakai, *The Intrinsic Charm of the Proton*, Phys. Lett. **B 93** (1980) 451 (cit. on p. 30).

[122] J. Pumplin, H.L. Lai, and W.K. Tung, *The Charm Parton Content of the Nucleon*, Phys. Rev. **D 75** (2007) 054029, arXiv: hep-ph/0701220 [hep-ph] (cit. on p. 30).

[123] Sayipjamal Dulat, Tie-Jiun Hou, Jun Gao, Joey Huston, Jon Pumplin, et al., *Intrinsic Charm Parton Distribution Functions from CTEQ-TEA Global Analysis*, (2013), arXiv: 1309.0025 [hep-ph] (cit. on p. 30).

[124] R. Seuster et al., *Charm hadrons from fragmentation and B decays in e^+e^- annihilation at $\sqrt{s} = 10.6\,GeV$*, Phys. Rev. **D 73** (2006) 032002, arXiv: hep-ex/0506068 [hep-ex] (cit. on p. 30).

[125] R. Barate et al., *Study of charm production in Z decays*, Eur. Phys. J. **C 16** (2000) 597, arXiv: hep-ex/9909032 [hep-ex] (cit. on p. 30).

[126] HERAFitter, *An open source QCD fitting framework*, (2013), URL: http://projects.hepforge.org/HeraFitter (cit. on p. 35).

[127] F.D. Aaron et al., *A Precision Measurement of the Inclusive ep Scattering Cross Section at HERA*, Eur. Phys. J. **C 64** (2009) 561, arXiv: 0904.3513 [hep-ex] (cit. on p. 35).

[128] F. James and M. Roos, *Minuit: A System for Function Minimization and Analysis of the Parameter Errors and Correlations*, Comput. Phys. Commun. **10** (1975) 343 (cit. on p. 35).

[129] H. Abramowicz et al., *Combination of measurements of inclusive deep inelastic $e^{\pm}p$ scattering cross sections and QCD analysis of HERA data*, Eur. Phys. J. C **75** (2015) 580, arXiv: 1506.06042 [hep-ex] (cit. on p. 37).

[130] ATLAS Collaboration, *Determination of the parton distribution functions of the proton using diverse ATLAS data from pp collisions at $\sqrt{s} = 7, 8$ and $13\,TeV$*, Eur. Phys. J. C **82** (2021) 438, arXiv: 2112.11266 [hep-ex] (cit. on pp. 37, 38).

[131] S. Alekhin, J. Blümlein, S. Moch, and R. Placakyte, *Parton distribution functions, α_s, and heavy-quark masses for LHC Run II*, Phys. Rev. D **96** (2017) 014011, arXiv: 1701.05838 [hep-ph] (cit. on p. 38).

[132] Sayipjamal Dulat et al., *New parton distribution functions from a global analysis of quantum chromodynamics*, Phys. Rev. D **93** (2016) 033006, arXiv: 1506.07443 [hep-ph] (cit. on p. 38).

[133] Tie-Jiun Hou et al., *New CTEQ global analysis of quantum chromodynamics with high-precision data from the LHC*, Phys. Rev. D **103** (2021) 014013, arXiv: 1912.10053 [hep-ph] (cit. on p. 38).

[134] L. A. Harland-Lang, A. D. Martin, P. Motylinski, and R. S. Thorne, *Parton distributions in the LHC era: MMHT 2014 PDFs*, Eur. Phys. J. C **75** (2015) 204, arXiv: 1412.3989 [hep-ph] (cit. on p. 38).

[135] S. Bailey, T. Cridge, L. A. Harland-Lang, A. D. Martin, and R. S. Thorne, *Parton distributions from LHC, HERA, Tevatron and fixed target data: MSHT20 PDFs*, Eur. Phys. J. C **81** (2021) 341, arXiv: 2012.04684 [hep-ph] (cit. on p. 38).

[136] Richard D. Ball et al., *Parton distributions for the LHC run II*, JHEP **04** (2015) 040, arXiv: 1410.8849 [hep-ph] (cit. on pp. 38, 44).

[137] Ferran Faura, Shayan Iranipour, Emanuele R. Nocera, Juan Rojo, and Maria Ubiali, *The Strangest Proton?*, Eur. Phys. J. C **80** (2020) 1168, arXiv: 2009.00014 [hep-ph] (cit. on p. 38).

[138] ATLAS Collaboration, *Determination of the parton distribution functions of the proton from ATLAS measurements of differential $W^{\pm}$ and Z boson production in association with jets*, JHEP **07** (2021) 223, arXiv: 2101.05095 [hep-ex] (cit. on p. 38).

[139] ATLAS Collaboration, *Search for the standard model Higgs boson produced in association with top quarks and decaying into a $b\bar{b}$ pair in pp collisions at $\sqrt{s} = 13$ TeV with the ATLAS detector*, Phys. Rev. D **97** (2018) 072016, arXiv: 1712.08895 [hep-ex] (cit. on pp. 39, 80, 120).

[140] ATLAS Collaboration, *Observation of Higgs boson production in association with a top quark pair at the LHC with the ATLAS detector*, Phys. Lett. B **784** (2018) 173, arXiv: 1806.00425 [hep-ex] (cit. on pp. 39, 79, 80).

[141] ATLAS Collaboration, *Observation of $H \to b\bar{b}$ decays and VH production with the ATLAS detector*, Phys. Lett. B **786** (2018) 59, arXiv: 1808.08238 [hep-ex] (cit. on pp. 39, 82).

[142] F. Englert and R. Brout, *Broken Symmetry and the Mass of Gauge Vector Mesons*, Phys. Rev. Lett. **13** (1964) 321 (cit. on p. 39).

[143] Peter W. Higgs, *Broken Symmetries and the Masses of Gauge Bosons*, Phys. Rev. Lett. **13** (1964) 508 (cit. on p. 39).

[144] G.S. Guralnik, C.R. Hagen, and T.B.W. Kibble, *Global Conservation Laws and Mass-less Particles*, Phys. Rev. Lett. **13** (1964) 585 (cit. on p. 39).

[145] C. Englert et al., *Precision measurements of Higgs couplings: implications for new physics scales*, J. Phys. G **41** (2014) 113001, arXiv: 1403.7191 [hep-ph] (cit. on p. 39).

[146] J. N. Ng and P. Zakarauskas, *QCD-parton calculation of conjoined production of Higgs bosons and heavy flavors in p anti-p collisions*, Phys. Rev. D **29** (1984) 876 (cit. on p. 39).

[147] Z. Kunszt, *Associated production of heavy Higgs boson with top quarks*, Nucl. Phys. B **29** (1984) 876 (cit. on p. 39).

[148] S. Dawson, L. H. Orr, L. Reina, and D. Wackeroth, *Associated top quark Higgs boson production the LHC*, Phys. Rev. D **67** (2003) 071503, arXiv: hep-ph/0211438 (cit. on p. 39).

[149] W. Beenakker et al., *Higgs radiation off top quarks at the Tevatron and the LHC*, Phys. Rev. Lett. **87** (2001) 201805, arXiv: hep-ph/0107081 (cit. on pp. 39, 79).

[150] D. de Florian et al., *Handbook of LHC Higgs Cross Sections: 4. Deciphering the Nature of the Higgs Sector*, (2016), arXiv: 1610.07922 [hep-ph] (cit. on pp. 39, 44, 62, 79, 120).

[151] ATLAS Collaboration,
Search for the Standard Model Higgs boson produced in association with top quarks and decaying into $b\bar{b}$ in pp collisions at $\sqrt{s} = 8$ TeV with the ATLAS detector,
Eur. Phys. J. C **75** (2015) 349, arXiv: 1503.05066 [hep-ex]
(cit. on pp. 40, 44, 57, 69, 82).

[152] ATLAS Collaboration,
Search for the Standard Model Higgs boson decaying into $b\bar{b}$ produced in association with top quarks decaying hadronically in pp collisions at $\sqrt{s} = 8$ TeV with the ATLAS detector,
JHEP **05** (2016) 160, arXiv: 1604.03812 [hep-ex] (cit. on p. 40).

[153] CMS Collaboration,
Search for the associated production of the Higgs boson with a top-quark pair,
JHEP **09** (2014) 087, arXiv: 1408.1682 [hep-ex] (cit. on p. 40).

[154] ATLAS Collaboration, *Search for the associated production of the Higgs boson with a top quark pair in multilepton final states with the ATLAS detector*,
Phys. Lett. B **749** (2015) 519, arXiv: 1506.05988 [hep-ex] (cit. on p. 40).

[155] ATLAS Collaboration, *Search for $H \to \gamma\gamma$ produced in association with top quarks and constraints on the Yukawa coupling between the top quark and the Higgs boson using data taken at 7 TeV and 8 TeV with the ATLAS detector*, Phys. Lett. B **740** (2015) 222,
arXiv: 1409.3122 [hep-ex] (cit. on p. 40).

[156] ATLAS Collaboration, *Luminosity determination in pp collisions at $\sqrt{s} = 8$ TeV using the ATLAS detector at the LHC*, Eur. Phys. J. C **76** (2016) 653, arXiv: 1608.03953 [hep-ex]
(cit. on pp. 41, 61).

[157] ATLAS Collaboration, *Electron reconstruction and identification efficiency measurements with the ATLAS detector using the 2011 LHC proton–proton collision data*,
Eur. Phys. J. C **74** (2014) 2941, arXiv: 1404.2240 [hep-ex] (cit. on p. 41).

[158] ATLAS Collaboration, *Electron efficiency measurements with the ATLAS detector using the 2015 LHC proton–proton collision data*, ATLAS-CONF-2016-024, 2016,
URL: https://cds.cern.ch/record/2157687 (cit. on pp. 41, 43, 62).

[159] ATLAS Collaboration, *Muon reconstruction performance of the ATLAS detector in proton–proton collision data at $\sqrt{s} = 13$ TeV*, Eur. Phys. J. C **76** (2016) 292,
arXiv: 1603.05598 [hep-ex] (cit. on pp. 41, 43, 62).

[160] ATLAS Collaboration,
Topological cell clustering in the ATLAS calorimeters and its performance in LHC Run 1,
Eur. Phys. J. C **77** (2017) 490, arXiv: 1603.02934 [hep-ex] (cit. on p. 41).

[161] Matteo Cacciari, Gavin P. Salam, and Gregory Soyez, *FastJet user manual*,
Eur. Phys. J. C **72** (2012) 1896, arXiv: 1111.6097 [hep-ph] (cit. on p. 41).

[162] ATLAS Collaboration, *Jet energy scale measurements and their systematic uncertainties in proton–proton collisions at $\sqrt{s} = 13$ TeV with the ATLAS detector*,
Phys. Rev. D **96** (2017) 072002, arXiv: 1703.09665 [hep-ex] (cit. on pp. 41, 61).

[163] ATLAS Collaboration,
Selection of jets produced in 13 TeV proton–proton collisions with the ATLAS detector,
ATLAS-CONF-2015-029, 2015, URL: https://cds.cern.ch/record/2037702
(cit. on p. 41).

[164] ATLAS Collaboration, *Performance of pile-up mitigation techniques for jets in pp collisions at $\sqrt{s} = 8$ TeV using the ATLAS detector*, Eur. Phys. J. C **76** (2016) 581, arXiv: 1510.03823 [hep-ex] (cit. on p. 42).

[165] ATLAS Collaboration, *Performance of b-jet identification in the ATLAS experiment*, JINST **11** (2016) P04008, arXiv: 1512.01094 [hep-ex] (cit. on pp. 42, 61, 122).

[166] ATLAS Collaboration, *Optimisation of the ATLAS b-tagging performance for the 2016 LHC Run*, ATL-PHYS-PUB-2016-012, 2016, URL: https://cds.cern.ch/record/2160731 (cit. on p. 42).

[167] ATLAS Collaboration, *Reconstruction, Energy Calibration, and Identification of Hadronically Decaying Tau Leptons in the ATLAS Experiment for Run-2 of the LHC*, ATL-PHYS-PUB-2015-045, 2015, URL: https://cds.cern.ch/record/2064383 (cit. on p. 42).

[168] ATLAS Collaboration, *Performance of missing transverse momentum reconstruction with the ATLAS detector in the first proton–proton collisions at $\sqrt{s} = 13$ TeV*, ATL-PHYS-PUB-2015-027, 2015, URL: https://cds.cern.ch/record/2037904 (cit. on p. 42).

[169] ATLAS Collaboration, *Performance of algorithms that reconstruct missing transverse momentum in $\sqrt{s} = 8$ TeV proton–proton collisions in the ATLAS detector*, Eur. Phys. J. C **77** (2017) 241, arXiv: 1609.09324 [hep-ex] (cit. on p. 42).

[170] Benjamin Nachman, Pascal Nef, Ariel Schwartzman, Maximilian Swiatlowski, and Chaowaroj Wanotayaroj, *Jets from jets: re-clustering as a tool for large radius jet reconstruction and grooming at the LHC*, JHEP **02** (2015) 075, arXiv: 1407.2922 [hep-ph] (cit. on p. 42).

[171] ATLAS Collaboration, *Evidence for the associated production of the Higgs boson and a top quark pair with the ATLAS detector*, Phys. Rev. D **97** (2018) 072003, arXiv: 1712.08891 [hep-ex] (cit. on pp. 43, 79, 80).

[172] ATLAS Collaboration, *The simulation principle and performance of the ATLAS fast calorimeter simulation FastCaloSim*, ATL-PHYS-PUB-2010-013, 2010, URL: https://cds.cern.ch/record/1300517 (cit. on p. 43).

[173] T. Sjöstrand, S. Mrenna, and P. Skands, *A brief introduction to PYTHIA 8.1*, Comput. Phys. Commun. **178** (2008) 852, arXiv: 0710.3820 [hep-ph] (cit. on p. 43).

[174] J. Alwall et al., *The automated computation of tree-level and next-to-leading order differential cross sections, and their matching to parton shower simulations*, JHEP **07** (2014) 079, arXiv: 1405.0301 [hep-ph] (cit. on p. 44).

[175] ATLAS Collaboration, *ATLAS Pythia 8 tunes to 7 TeV data*, ATL-PHYS-PUB-2014-021, 2014, URL: https://cds.cern.ch/record/1966419 (cit. on p. 44).

[176] Pierre Artoisenet, Rikkert Frederix, Olivier Mattelaer, and Robbert Rietkerk, *Automatic spin-entangled decays of heavy resonances in Monte Carlo simulations*, JHEP **03** (2013) 015, arXiv: 1212.3460 [hep-ph] (cit. on p. 44).

[177] Risto Raitio and Walter W. Wada, *Higgs-boson production at large transverse momentum in quantum chromodynamics*, Phys. Rev. D **19** (1979) 941 (cit. on pp. 44, 62, 79).

[178] W. Beenakker et al., *NLO QCD corrections to $t\bar{t}H$ production in hadron collisions*, Nucl. Phys. B **653** (2003) 151, arXiv: hep-ph/0211352 (cit. on pp. 44, 62, 79).

[179] S. Dawson, C. Jackson, L. H. Orr, L. Reina, and D. Wackeroth, *Associated Higgs boson production with top quarks at the CERN Large Hadron Collider: NLO QCD corrections*, Phys. Rev. D **68** (2003) 034022, arXiv: hep-ph/0305087 (cit. on pp. 44, 62, 79).

[180] Yu Zhang, Wen-Gan Ma, Ren-You Zhang, Chong Chen, and Lei Guo, *QCD NLO and EW NLO corrections to $t\bar{t}H$ production with top quark decays at hadron collider*, Phys. Lett. B **738** (2014) 1, arXiv: 1407.1110 [hep-ph] (cit. on pp. 44, 62, 79).

[181] S. Frixione, V. Hirschi, D. Pagani, H.-S. Shao, and M. Zaro, *Electroweak and QCD corrections to top-pair hadroproduction in association with heavy bosons*, JHEP **06** (2015) 184, arXiv: 1504.03446 [hep-ph] (cit. on pp. 44, 62, 79).

[182] A. Djouadi, J. Kalinowski, and M. Spira, *HDECAY: A program for Higgs boson decays in the Standard Model and its supersymmetric extension*, Comput. Phys. Commun. **108** (1998) 56, arXiv: hep-ph/9704448 (cit. on p. 44).

[183] John M. Campbell, R. Keith Ellis, Paolo Nason, and Emanuele Re, *Top-pair production and decay at NLO matched with parton showers*, JHEP **04** (2015) 114, arXiv: 1412.1828 [hep-ph] (cit. on p. 44).

[184] ATLAS Collaboration, *Studies on top-quark Monte Carlo modelling for Top2016*, ATL-PHYS-PUB-2016-020, 2016, URL: https://cds.cern.ch/record/2216168 (cit. on p. 44).

[185] Michal Czakon and Alexander Mitov, *Top++: A program for the calculation of the top-pair cross-section at hadron colliders*, Comput. Phys. Commun. **185** (2014) 2930, arXiv: 1112.5675 [hep-ph] (cit. on pp. 44, 62).

[186] Michal Czakon and Alexander Mitov, *NNLO corrections to top-pair production at hadron colliders: the all-fermionic scattering channels*, JHEP **12** (2012) 054, arXiv: 1207.0236 [hep-ph] (cit. on p. 44).

[187] Michal Czakon and Alexander Mitov, *NNLO corrections to top pair production at hadron colliders: the quark-gluon reaction*, JHEP **01** (2013) 080, arXiv: 1210.6832 [hep-ph] (cit. on p. 44).

[188] Michal Czakon, Paul Fiedler, and Alexander Mitov, *Total Top-Quark Pair-Production Cross Section at Hadron Colliders Through $O(\alpha_S^4)$*, Phys. Rev. Lett. **110** (2013) 252004, arXiv: 1303.6254 [hep-ph] (cit. on p. 44).

[189] Fabio Cascioli, Philipp Maierhoefer, Niccolo Moretti, Stefano Pozzorini, and Frank Siegert, *NLO matching for $t\bar{t}b\bar{b}$ production with massive b-quarks*, Phys. Lett. B **734** (2014) 210, arXiv: 1309.5912 [hep-ph] (cit. on p. 45).

[190] T. Gleisberg et al., *Event generation with SHERPA 1.1*, JHEP **02** (2009) 007, arXiv: 0811.4622 [hep-ph] (cit. on p. 45).

[191] Fabio Cascioli, Philipp Maierhöfer, and Stefano Pozzorini, *Scattering Amplitudes with Open Loops*, Phys. Rev. Lett. **108** (2012) 111601, arXiv: 1111.5206 [hep-ph] (cit. on p. 45).

[192] Emanuele Re, *Single-top Wt-channel production matched with parton showers using the POWHEG method*, Eur. Phys. J. C **71** (2011) 1547, arXiv: 1009.2450 [hep-ph] (cit. on p. 45).

[193] Simone Alioli, Paolo Nason, Carlo Oleari, and Emanuele Re, *NLO single-top production matched with shower in POWHEG: s- and t-channel contributions*, JHEP **09** (2009) 111, arXiv: 0907.4076 [hep-ph] (cit. on p. 45), Erratum: JHEP **02** (2010) 011.

[194] Stefano Frixione, Eric Laenen, Patrick Motylinski, Chris White, and Bryan R. Webber, *Single-top hadroproduction in association with a W boson*, JHEP **07** (2008) 029, arXiv: 0805.3067 [hep-ph] (cit. on pp. 46, 65).

[195] Peter Zeiler Skands, *Tuning Monte Carlo generators: The Perugia tunes*, Phys. Rev. D **82** (2010) 074018, arXiv: 1005.3457 [hep-ph] (cit. on p. 46).

[196] Nikolaos Kidonakis, *Two-loop soft anomalous dimensions for single top quark associated production with a W^- or H^-*, Phys. Rev. D **82** (2010) 054018, arXiv: 1005.4451 [hep-ph] (cit. on pp. 46, 65).

[197] Nikolaos Kidonakis, *NNLL resummation for s-channel single top quark production*, Phys. Rev. D **81** (2010) 054028, arXiv: 1001.5034 [hep-ph] (cit. on pp. 46, 65).

[198] Nikolaos Kidonakis, *Next-to-next-to-leading-order collinear and soft gluon corrections for t-channel single top quark production*, Phys. Rev. D **83** (2011) 091503, arXiv: 1103.2792 [hep-ph] (cit. on pp. 46, 65).

[199] Tanju Gleisberg and Stefan Höche, *Comix, a new matrix element generator*, JHEP **12** (2008) 039, arXiv: 0808.3674 [hep-ph] (cit. on p. 46).

[200] Steffen Schumann and Frank Krauss, *A parton shower algorithm based on Catani–Seymour dipole factorisation*, JHEP **03** (2008) 038, arXiv: 0709.1027 [hep-ph] (cit. on p. 46).

[201] Stefan Höche, Frank Krauss, Marek Schönherr, and Frank Siegert, *QCD matrix elements + parton showers. The NLO case*, JHEP **04** (2013) 027, arXiv: 1207.5030 [hep-ph] (cit. on p. 46).

[202] ATLAS Collaboration, *Measurement of $W^\pm$ and Z Boson Production Cross Sections in pp Collisions at $\sqrt{s} = 13$ TeV with the ATLAS Detector*, ATLAS-CONF-2015-039, 2015, URL: https://cds.cern.ch/record/2045487 (cit. on p. 46).

[203] ATLAS Collaboration, *Multi-boson simulation for 13 TeV ATLAS analyses*, ATL-PHYS-PUB-2016-002, 2016, URL: https://cds.cern.ch/record/2119986 (cit. on pp. 46, 65).

[204] ATLAS Collaboration, *Estimation of non-prompt and fake lepton backgrounds in final states with top quarks produced in proton–proton collisions at $\sqrt{s} = 8$ TeV with the ATLAS Detector*, ATLAS-CONF-2014-058, 2014, URL: https://cds.cern.ch/record/1951336 (cit. on p. 46).

[205] Andreas Hoecker et al., *TMVA - Toolkit for Multivariate Data Analysis*, 2007, arXiv: physics/0703039 [physics.data-an] (cit. on p. 55).

[206] V. Barger, J. Ohnemus, and R. Phillips, *Event shape criteria for single lepton top signals*, Phys. Rev. D **48** (1993) 3953, arXiv: hep-ph/9308216 (cit. on pp. 58, 59).

[207] ATLAS Collaboration, *Jet mass and substructure of inclusive jets in $\sqrt{s} = 7$ TeV pp collisions with the ATLAS experiment*, JHEP **05** (2012) 128, arXiv: 1203.4606 [hep-ex] (cit. on p. 60).

[208] ATLAS Collaboration, *Search for flavour-changing neutral current top quark decays $t \to Hq$ in pp collisions at $\sqrt{s} = 8$ TeV with the ATLAS detector*, JHEP **12** (2015) 061, arXiv: 1509.06047 [hep-ex] (cit. on p. 57).

[209] M. R. Whalley, D. Bourilkov, and R. C. Group, "The Les Houches accord PDFs (LHAPDF) and LHAGLUE", *HERA and the LHC: A Workshop on the implications of HERA for LHC physics. Proceedings, Part B*, 2005, arXiv: hep-ph/0508110 (cit. on p. 57).

[210] G. P. Lepage, *A New Algorithm for Adaptive Multidimensional Integration*, Journal of Computational Physics **27** (1978) 192 (cit. on p. 57).

[211] Doug Schouten, Adam DeAbreu, and Bernd Stelzer, *Accelerated matrix element method with parallel computing*, Comput. Phys. Commun. **192** (2015) 54, arXiv: 1407.7595 [physics.comp-ph] (cit. on p. 57).

[212] ATLAS Collaboration, *Measurement of the Inelastic Proton–Proton Cross Section at $\sqrt{s} = 13$ TeV with the ATLAS Detector at the LHC*, Phys. Rev. Lett. **117** (2016) 182002, arXiv: 1606.02625 [hep-ex] (cit. on p. 61).

[213] Johannes Bellm et al., *Herwig 7.0/Herwig++ 3.0 release note*, Eur. Phys. J. C **76** (2016) 196, arXiv: 1512.01178 [hep-ph] (cit. on p. 62).

[214] ATLAS Collaboration, *Studies on top-quark Monte Carlo modelling with Sherpa and MG5_aMC@NLO*, ATL-PHYS-PUB-2017-007, 2017, URL: https://cds.cern.ch/record/2261938 (cit. on p. 64).

[215] ATLAS Collaboration, *Studies of $t\bar{t}c\bar{c}$ production with* MadGraph5_aMC@NLO *and* Herwig++ *for the ATLAS experiment*, ATL-PHYS-PUB-2016-011, 2016, URL: https://cds.cern.ch/record/2153876 (cit. on p. 64).

[216] John M. Campbell and R. Keith Ellis, *$t\bar{t}W^{\pm}$ production and decay at NLO*, JHEP **07** (2012) 052, arXiv: 1204.5678 [hep-ph] (cit. on p. 65).

[217] Glen Cowan, Kyle Cranmer, Eilam Gross, and Ofer Vitells, *Asymptotic formulae for likelihood-based tests of new physics*, Eur. Phys. J. C **71** (2011) 1554, arXiv: 1007.1727 [physics.data-an] (cit. on pp. 66, 69), Erratum: Eur. Phys. J. C **73** (2013) 2501.

[218] Alexander L. Read, *Presentation of search results: the CL_S technique*, J. Phys. G **28** (2002) 2693 (cit. on p. 66).

[219] Thomas Junk, *Confidence level computation for combining searches with small statistics*, Nucl. Instrum. Meth. A **434** (1999) 435, arXiv: hep-ex/9902006 (cit. on p. 66).

[220] Z. Kunszt, *Associated Production of Heavy Higgs Boson with Top Quarks*, Nucl. Phys. B **247** (1984) 339 (cit. on p. 79).

[221] S. Dawson, L.H. Orr, L. Reina, and D. Wackeroth, *Next-to-leading order QCD corrections to $pp \to t\bar{t}h$ at the CERN Large Hadron Collider*, Phys. Rev. D **67** (2003) 071503, arXiv: hep-ph/0211438 (cit. on p. 79).

[222] S. Frixione, V. Hirschi, D. Pagani, H. S. Shao, and M. Zaro, *Weak corrections to Higgs hadroproduction in association with a top-quark pair*, JHEP **09** (2014) 065, arXiv: 1407.0823 [hep-ph] (cit. on p. 79).

[223] ATLAS Collaboration, *Measurements of the Higgs boson production and decay rates and coupling strengths using pp collision data at $\sqrt{s} = 7$ and 8 TeV in the ATLAS experiment*, Eur. Phys. J. C **76** (2016) 6, arXiv: 1507.04548 [hep-ex] (cit. on p. 79).

[224] ATLAS Collaboration, *Search for the $b\bar{b}$ decay of the Standard Model Higgs boson in associated $(W/Z)H$ production with the ATLAS detector*, JHEP **01** (2015) 069, arXiv: 1409.6212 [hep-ex] (cit. on pp. 82, 121).

[225] ATLAS Collaboration, *Search for Higgs bosons produced via vector-boson fusion and decaying into bottom quark pairs in $\sqrt{s} = 13$ TeV pp collisions with the ATLAS detector*, Phys. Rev. D **98** (2018) 052003, arXiv: 1807.08639 [hep-ex] (cit. on p. 82).

[226] ATLAS Collaboration,
Search for the Standard Model Higgs boson produced by vector-boson fusion and decaying to bottom quarks in $\sqrt{s} = 8$ TeV pp collisions with the ATLAS detector,
JHEP **11** (2016) 112, arXiv: 1606.02181 [hep-ex] (cit. on p. 82).

[227] G. Aad et al.,
The Phase-I trigger readout electronics upgrade of the ATLAS Liquid Argon calorimeters,
JINST **17** (2022) P05024, arXiv: 2202.07384 [physics.ins-det]
(cit. on pp. 84, 86, 88, 89, 91, 92, 124).

[228] G. Aad et al., *Artificial Neural Networks on FPGAs for Real-Time Energy Reconstruction of the ATLAS LAr Calorimeters*, Comput Softw Big Sci **5** (2021) 19
(cit. on pp. 84, 102, 105, 125).

[229] G. Aad et al., *Firmware implementation of a recurrent neural network for the computation of the energy deposited in the liquid argon calorimeter of the ATLAS experiment*,
JINST **18** (2023) P05017, arXiv: 2302.07555 [physics.ins-det] (cit. on pp. 84, 125).

[230] D. Axen et al., *Signal feedthroughs for the ATLAS barrel and endcap calorimeters*,
Rev. Sci. Instrum. **76** (2005) 063306 (cit. on p. 86).

[231] W.E. Cleland and E.G. Stern, *Signal processing considerations for liquid ionization calorimeters in a high rate environment*, NIM A **338** (1994) 467 (cit. on pp. 87, 101, 102).

[232] ATLAS Collaboration,
Readiness of the ATLAS liquid argon calorimeter for LHC collisions,
Eur. Phys. J. C **70** (2010) 723, arXiv: 0912.2642 [hep-ex] (cit. on p. 87).

[233] J. Anderson et al., *FELIX: a PCIe based high-throughput approach for interfacing front-end and trigger electronics in the ATLAS Upgrade framework*,
JINST **11** (2016) C12023 (cit. on p. 90).

[234] J. Duarte et al., *Fast inference of deep neural networks in FPGAs for particle physics*,
JINST **13** (2018) P07027, arXiv: 1804.06913 [physics.ins-det] (cit. on p. 101).

[235] R. Ospanov et al., *Development of a resource-efficient FPGA-based neural network regression model for the ATLAS muon trigger upgrades*, Eur. Phys. J. C **82** (2022) 576,
arXiv: 2201.06288 [physics.ins-det] (cit. on p. 101).

[236] C. Sun et al., *Fast muon tracking with machine learning implemented in FPGA*,
Nucl. Instrum. Meth. A **1045** (2023) 167546, arXiv: 2202.04976 [physics.ins-det]
(cit. on p. 101).

[237] M. Migliorini et al., *Muon trigger with fast Neural Networks on FPGA, a demonstrator*,
J. Phys. Conf. Ser. **2374** (2022) 012099, arXiv: 2105.04428 [hep-ex] (cit. on p. 101).

[238] N. Nottbeck et al., *Implementation of high-performance, sub-microsecond deep neural networks on FPGAs for trigger applications*, JINST **14** (2019) P09014, arXiv: 1903.10201 [physics.ins-det] (cit. on p. 101).

[239] N. Madysa, *AREUS: a software framework for ATLAS readout electronics upgrade simulation*, EPJ Web Conf **214** (2019) 02006 (cit. on p. 101).

[240] A. Sherstinky, *Fundamentals of Recurrent Neural Network (RNN) and Long Short-Term Memory (LSTM) network*, Physica D: Nonlinear Phenomena **404** (2020) 132306, arXiv: 1808.03314 (cit. on p. 102).

[241] S. Hochreiter and J. Schmidhuber, *Long Short-Term Memory*, Neural Computation **9** (1997) 1735, arXiv: 1808.03314 (cit. on p. 102).

[242] François Chollet et al., *Keras*, 2015, URL: https://keras.io (cit. on p. 102).

[243] M. Abadi et al., *TensorFlow: Large-Scale Machine Learning on Heterogeneous Systems*, https://www.tensorflow.org/, 2015 (cit. on p. 102).

[244] *Mentor Graphics Algorithmic C (AC) data types*, provided under the Apache license as part of the Intel HLS Compiler (cit. on pp. 111, 112).

[245] ATLAS Collaboration, *Measurement of Higgs boson decay into b-quarks in associated production with a top-quark pair in pp collisions at $\sqrt{s} = 13$ TeV with the ATLAS detector*, JHEP **06** (2021) 097, arXiv: 2111.06712 [hep-ex] (cit. on p. 120).

[246] ATLAS Collaboration, *Measurements of inclusive and differential fiducial cross-sections of $t\bar{t}$ production with additional heavy-flavour jets in proton–proton collisions at $\sqrt{s} = 13$ TeV with the ATLAS detector*, JHEP **04** (2019) 046, arXiv: 1811.12113 [hep-ex] (cit. on p. 121).

[247] ATLAS Collaboration, *Measurement of the cross section for the production of a W boson in association with b-jets in pp collisions at $\sqrt{s} = 7$ TeV with the ATLAS detector*, Phys. Lett. B **707** (2012) 418, arXiv: 1109.1470 [hep-ex] (cit. on p. 122).

[248] ATLAS Collaboration, *Charged-particle multiplicities in pp interactions measured with the ATLAS detector at the LHC*, New J. Phys. **13** (2011) 053033, arXiv: 1012.5104 [hep-ex] (cit. on p. 122).